UNIVERSIDAD AUTÓNOMA DE MADRID

FACULTAD DE CIENCIAS

TESIS DOCTORAL

In-beam gamma-ray spectroscopy of nuclei near doubly-magic ^{132}Sn

MEMORIA PARA OPTAR AL GRADO DE DOCTOR

PRESENTADA POR

Víctor Vaquero Soto

Directora:

Andrea Jungclaus

Madrid, 2018

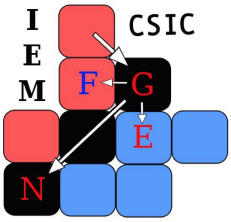

Grupo de Física
Nuclear Experimental

In-beam gamma-ray spectroscopy of nuclei near doubly-magic ^{132}Sn

Memoria que presenta para optar al grado
de Doctor en Ciencias Físicas

Víctor Vaquero Soto

Universidad Autónoma de Madrid
Instituto de Estructura de la Materia (IEM-CSIC)

Dirigida por:

Dr. Andrea Jungclaus

Instituto de Estructura de la Materia (IEM-CSIC)

Madrid, Noviembre de 2018
Departamento de Física Teórica
Universidad Autónoma de Madrid

A mi familia y amigos.

Abstract

This thesis is focussed on the region around the doubly magic nucleus ^{132}Sn (Z=50 and N=82). The nuclei situated in this region of the nuclear chart are of great interest both for nuclear structure investigations and nuclear astrophysics. By studying these systems, information about the evolution of nucleon-nucleon correlations, quadrupole collectivity and single-particle energies can be obtained. New experimental information allows the test of different nuclear models and examine their validity in this region of the nuclear chart.

In order to study the neutron-rich nuclei located in the vicinity of ^{132}Sn, in April 2015 an experiment was carried out at the Radioactive Isotope Beam Factory at the RIKEN Nishina Center, Japan. The radioactive beam was produced by the in-flight abrasion fission of a primary beam of ^{238}U at 345 MeV/u bombarding a 4-mm-thick beryllium target. The exotic nuclei to be investigated were selected and identified using the BigRIPS in-flight separator. After the selection and identification, the neutron-rich radioactive isotopes were transported to the focal point, F8, where they impinged on two different reaction targets of carbon and gold. Surrounding these targets was the DALI2 spectrometer, which was used to detect the γ rays emitted by the decay of excited states in several N=82-84, Z$\geq$50 isotopes. Finally, the reaction products exited the target and were identified by the ZeroDegree spectrometer.

The reduced transition probability B($E2; 0_1^+ \rightarrow 2_1^+$) for the first excited 2^+ state of the neutron-rich ^{136}Te nucleus, with two protons and two neutrons outside the ^{132}Sn core, was determined via Coulomb excitation in inverse kinematics at intermediate energies. A value of B(E2) = 0.191(26) e^2b^2 was extracted from measured differential cross sections on gold and carbon targets in order to take into account both the Coulomb and the nuclear excitation contributions. Our experimental B(E2) value is compared to the previous values from literature and to different theoretical calculations. In addition, ^{133}Sn was studied via the one-neutron knockout from a ^{134}Sn projectile. Besides the known γ rays emitted from the decay of the single-particle states, additional γ-ray strength was observed above the neutron separation energy, extending up to about 5.5 MeV. These excited states are interpreted as neutron-hole states that are populated through the removal of a neutron from the closed N=50-82 shell of the ^{134}Sn projectile. The ability of γ-ray emission to compete with neutron decay is explained taking into account the structure of the initial and final states, and the resultant wave-function overlap. Lastly, experimental inclusive cross sections for the multiple knockout of neutrons and protons were derived from different projectiles at energies around 165 MeV/u. The experimental values have been compared to predictions from state-of-the-art calculations based on a Monte Carlo description of the cascade and evaporation processes obtained with the INCL-ABLA reaction code.

Contents

List of Figures

List of Tables

Chapter 1

Introduction

Atomic nuclei form the majority of the known matter in the universe lending great importance to understanding their origin, properties and structure. The nucleus is a quantum system composed of a finite number of fermions. These fermions, known as nucleons, have two types of similar mass: protons and neutrons. Protons are particles with a positive electric charge of +e, whereas neutrons have no net electric charge. Therefore, if only the electromagnetic interaction were present in the atomic nucleus, it would be an unbound system due to the electromagnetic repulsion between the protons. Thus there must be another force that binds protons and neutrons together to form the nucleus, this force is known as the strong interaction.

Since the discovery of the atomic nucleus by E. Rutherford [1] in 1911, many advances and discoveries, both experimental and theoretical, have occurred in the field of nuclear physics. Of these, it is worth highlighting the work carried out by W. Elsasser [2–4] in 1934, who observed sudden drops in binding energies at certain nucleon numbers, giving rise to the term “magic numbers”. To explain this phenomenon, W. Elsasser drew upon on the shell model applied to atomic electrons and identified the more bound nuclei as having closed shells of protons and neutrons. In his shell model, each nucleon moved in a global potential well at degenerated energy levels without interacting with each other. However, this model was not able to reproduce the limited experimental information at that time. It was later, in 1949, when M. Goeppert-Mayer [5, 6] and O. Haxel, J. Jensen and H. Suess [7] found a solution that reproduced the experimental information. They showed that by including a spin-orbit term in the potential the shell model was able to reproduce the experimental energy gaps observed between the different shells at 2, 8, 20, 28, 50, 82 and 126 thus explaining the magic numbers. This model represented a great advance since it was able to predict correctly different properties of nuclei and still represents our most fundamental understanding of nuclear structure.

For a long time, investigations of nuclei were limited to the valley of stability of the nuclear chart, i.e, naturally abundant nuclei, and its vicinity. However, in the last decades, the development of facilities capable of producing radioactive ion beams (RIBs), has enabled the study

of nuclei with large imbalances of protons and neutrons with respect to the valley of stability. These nuclei far from the valley of stability are known as “exotic nuclei”. One of the main discoveries made when studying exotic nuclei was that the magic numbers observed near the valley of stability change dramatically for extreme N/Z ratios. This phenomenon is caused by shell evolution as a function of protons and neutrons and has been widely studied recently both experimentally and theoretically. Examples of these effects are the disappearance of the N = 20 [8] and N = 28 [9–11] shell gaps and the appearance of new magic numbers N = 32 [12] and N = 34 [13, 14] in Ca isotopes. Another important reason for the study of these exotic systems is the impact of individual nuclear properties on the astrophysical rapid neutron capture process (r-process). The r-process is the responsible for the production of about half of the elements heavier than Fe. Calculations of r-process nucleosynthesis need as input different nuclear properties such as masses, lifetimes, β-decay and neutron capture rates. While these properties are well known for nuclei situated near stability, many are not yet known for nuclei far from stability which may have a strong impact on the r-process [15].

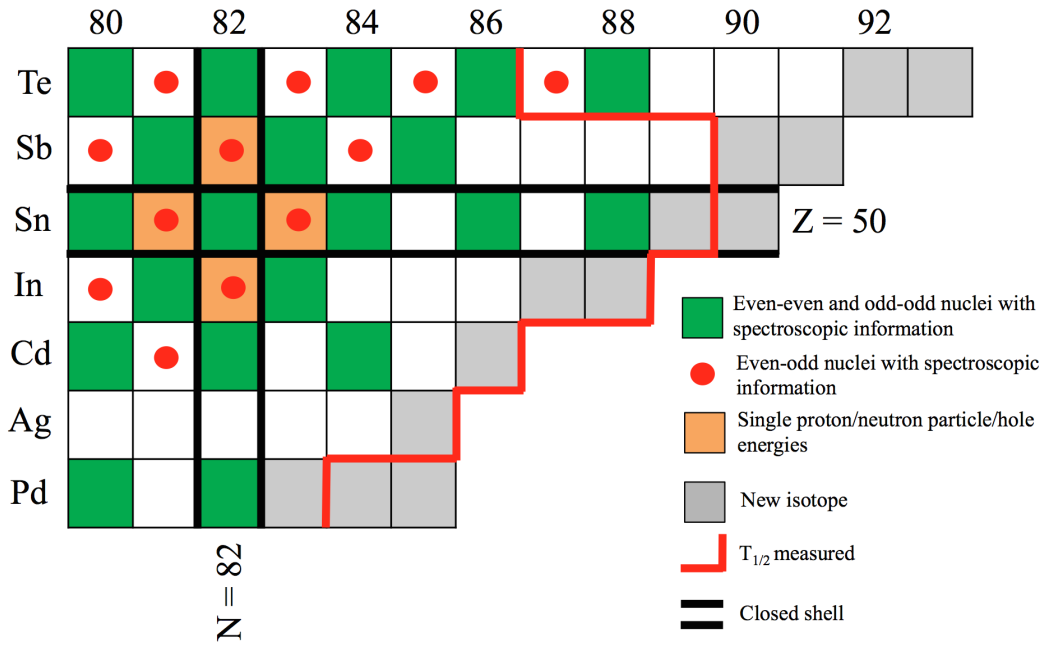

Figure 1.1: Sketch of the region around the doubly magic ^{132}Sn showing the experimental information available to date of this work.

In this work we will focus on the region of the nuclear chart around doubly-magic ^{132}Sn, Z=50 and N=82. This region is of great importance for nuclear structure investigations since it is the only region around a heavy, doubly-magic nucleus that is far-off stability and experimentally accessible today (8 neutrons more than the last stable tin isotope, ^{124}Sn). The study of nuclei with a few nucleons outside doubly-magic closed-shells provides direct information about the nucleon-nucleon correlations, quadrupole collectivity and single particle energies. New experimental information allows to test different nuclear models and examine their validity in this region of the nuclear chart. This region is also very important for nucleosynthesis calculations

due to the connection between the nuclear structure effects and the solar r-process abundances. For example, the abundance peak at A $\approx$ 130 arises from the N=82 shell closure while a N=82 shell quenching below ^{132}Sn improves the r-process abundances in the regions around A $\approx$ 120 and 140 [16]. Figure 1.1 displays the region around the doubly-magic ^{132}Sn and the experimental information available at time of writing. In this figure, the red lines indicate the limit of nuclei with known half-lives. Many of these half-lives were recently measured by G. Lorusso *et al*. [17] at the Radioactive Isotope Beam Factory (RIBF), which when included into r-process calculations, alleviated the previous under-prediction of isotopes just below and above the peak at A $\approx$ 130. As indicated by the gray boxes in Fig. 1.1, many of these neutron-rich isotopes have been identified for the first time only very recently. This is the case for the ^{129,130,131}Pd, ^{132}Ag, ^{134}Cd, ^{136,137}In, ^{139,140}Sn, ^{141,142}Sb and ^{144,145}Te isotopes, which were produced using the in-flight fission of a ^{238}U beam again at the RIBF [18]. Regarding the spectroscopic information, the situation is very different in each of the quadrants around ^{132}Sn. While the quadrant north-west has been widely studied during last years, more limited experimental information is available for the rest of quadrants. In fact, the first spectroscopic informations for nuclei situated in the quadrant south-east have only been reported very recently in 2016. First, A. Jungclaus *et al*. [19] measured for first time γ rays emitted by ^{132}In following the β-delayed neutron emission from ^{133}Cd. These γ rays were identified as members of the $\pi g_{9/2}^{-1} \otimes \nu f_{7/2}$ multiplet. Soon after, H. Wang *et al*. [20] reported the first experimental information about excited states from an even-even nucleus situated in the south-east quadrant, i.e ^{132}Cd, placing the 2_1^+ state at 618(8) keV. With respect to the remaining quadrants, significant progress has been achieved with respect to spectroscopic information. This is the case of the isotopic and isotonic chains (Z=50 and N=82, respectively) of ^{132}Sn, where new experimental information has been obtained using the technique of isomer spectroscopy. In the isotonic side, in 2007, A. Jungclaus *et al*. [21] observed for the first time a $\pi(0g_{9/2})\ 8^+$ seniority isomer in the waiting-point nucleus ^{130}Cd and later, in 2013, H. Watanabe *et al*. [22] reported the analog 8^+ isomer in the waiting-point nucleus ^{128}Pd. With respect to the isotopic tin chain, G. S. Simpson *et al*. [23] have reported the existence of 6^+ isomeric states in the neutron-rich semi-magic ^{136,138}Sn nuclei. These 6^+ isomeric states were proposed to have a dominant $\nu(1f_{7/2})^2$ configuration. Also in the south-west quadrant the experimental information has been recently extended, by the study of isomeric states in ^{126}Pd [24], ^{129}Cd [25] and ^{128}Cd [26] and β decays of neutron-rich ^{129,130,131}Cd isotopes [27–29]. Finally, the first experimental information about excited states for the heaviest isotopes of the ^{132}Sn region such as ^{140}Te [30] has been obtained from β-decay of ^{140}Sb. All this new experimental information is used as a test for the different shell-model calculations employed in each quadrant.

In Fig. 1.1, the orange boxes represent the one valence particle/hole nuclei, possessing, or lacking only one proton/neutron with respect to ^{132}Sn, namely ^{131}Sn, ^{133}Sn, ^{133}Sb and ^{131}In. Figure 1.2 shows the proton and neutron single-particle/hole energy levels in ^{132}Sn, where the

position of each state is normalized to the middle of the shell gap (λ_f) eliminating the Coulomb energy difference (ΔE_C). These single-particle/hole energies are used as input for shell model calculations. ^{133}Sn consists of a single neutron coupled to the doubly-magic nucleus ^{132}Sn and provides information about the position of the neutron single-particle orbitals situated in the N = 82-126 major shell. The lowest-energy neutron single-particle states expected above the N = 82 shell closure are the $1f_{7/2}$, $2p_{3/2}$, $2p_{1/2}$, $0h_{9/2}$, $1f_{5/2}$ and $0i_{13/2}$ orbitals. Candidates for all of these states have been identified in ^{133}Sn. First, Hoff *et al.* [31] studied the low lying single-neutron states in ^{133}Sn populated through the emission of a delayed neutron following the β decay of ^{134}In. The energies of the $2p_{3/2}$, $0h_{9/2}$ and $1f_{5/2}$ states were found to be 854, 1561 and 2004 keV, respectively, relative to the $1f_{7/2}$ orbital. Later, Jones *et al.* [32, 33] used the neutron transfer reaction ^{132}Sn(d,p) to study the single-particle states in ^{133}Sn. They measured a new state at 1363 keV, which was identified as the single-particle $2p_{1/2}$ state. Regarding the position of the $0i_{13/2}$ orbital, first Allmond *et al.* [34] proposed a candidate for this state at an energy of 2792 keV but the evidence for this candidate was inconclusive and later an energy range of 2360-2600 keV was stablished by Reviol *et al.* [35] based on the systematics of the $13/2^+_1$ and $13/2^+_2$ levels in ^{137}Xe and neighboring N=83 nuclei. Regarding the one-neutron hole nucleus, ^{131}Sn, the first experimental information was available for the $2s_{1/2}$ and $0g_{7/2}$ orbitals placed at 333 and 2433 keV relative to the $1d_{3/2}$ orbital, respectively, and populated from β decay of ^{131}In [36]. Later, the full one-neutron hole spectrum was completed with the energies of the $0h_{11/2}$ and $1d_{5/2}$ orbits at 242 and 1655 keV, respectively, again from the β-decay spectroscopy of ^{131}In [37, 38]. The single-proton nucleus ^{133}Sb provides information about the proton orbitals belonging to the Z = 50-82 major shell, i.e, the $0g_{7/2}$, $1d_{5/2}$, $1d_{3/2}$, $2s_{1/2}$ and $0h_{11/2}$ orbitals. From the β-decay of ^{133}Sn, the $1d_{5/2}$ and $0h_{11/2}$ single proton states were established at 962 and 2791 keV relative to the $0g_{7/2}$ orbital [39, 40], respectively. Later, a new single-proton state was found at 2440 KeV corresponding to the $1d_{3/2}$ orbital [41]. With respect to the position of the $2s_{1/2}$, this single-proton level is still experimentally unknown. Lastly, in the one-proton hole nucleus ^{131}In, the position of the single-proton hole $1p_{1/2}$ relative to the $0g_{9/2}$ hole in the ^{131}In nucleus was determined to be 363 keV [42] and the single-hole energy of the $1p_{3/2}$ orbital has been determined to be 1353 KeV [43]. In contrast, no experimental candidates are available for the $0f_{5/2}$ proton-hole orbital.

In the even-even nuclei, the most elucidating experimental signatures are the excitation energy $E(2^+_1)$, the ratio $R_{42} = E(4^+_1)/E(2^+_1)$, and the reduced transition probability $B(E2; 0^+_1 \rightarrow 2^+_1)$, in short $B(E2)$. These directly relate to the degree and type of collectivity present in the nucleus and, in general, are found to be well described by simple empirical relations and shell model calculations. In Fig. 1.3 the energies of the first excited 2^+_1 states (left) and the B(E2) values (right) for several isotopic chains around the neutron shell gap N=82 are displayed. As expected, the energy of the 2^+_1 states increases towards the neutron shell closure at N=82, peaks sharply at N=82 and then drops rapidly afterwards. The B(E2) values show the opposite

behavior, decreasing towards the shell gap and then increases afterwards. However, there are a limited number of cases where these trends are not adhered to in the ^{132}Sn region. One of them is the anomalous behaviour of the 2_1^+ energies in the Cd isotopes another is the extremely low B(E2) value of the first excited state in ^{136}Te.

Regarding the unusual behavior observed in the Cd isotopes, the 2_1^+ state in ^{128}Cd (N=80) is situated at an excitation energy of 645 keV, 7 keV lower than the same state in ^{126}Cd. Different shell model calculations tried to reproduce the trend of the 2_1^+ energies in the Cd chain but none were successful. The origin of this anomaly was revealed through modern beyond-mean-field calculations employing the Gogny force [44], to be consequence of the doubly-magic character of this nucleus for oblate deformation which favors prolate configurations close to the N=82 shell closure.

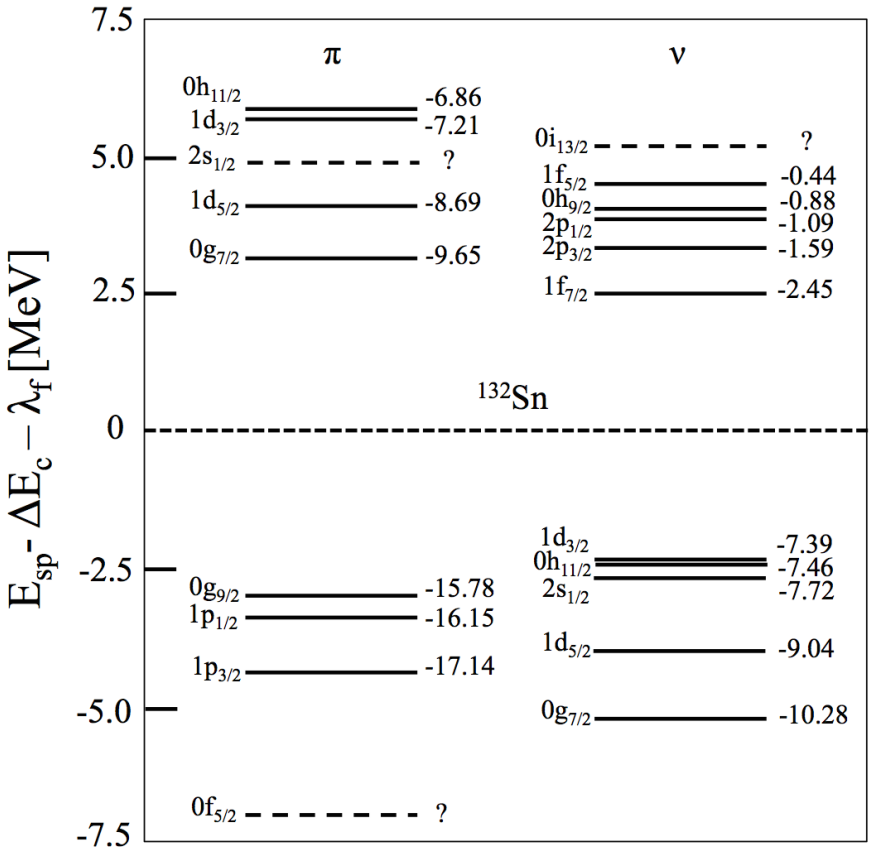

Figure 1.2: Experimental single-particle/hole proton (π) and neutron (ν) energies in the doubly-magic ^{132}Sn. The energies, E_{sp}, are normalized to the middle of the shell gap (λ_f), eliminating the Coulomb energy difference (ΔE_C). The numbers quoted next to each orbital are the absolute single-particle energies including the Coulomb shift. The 0f$_{5/2}$ proton-hole, 0i$_{13/2}$ neutron-particle and 2s$_{1/2}$ proton-particle orbitals are represented by a dashed-line to show their positions are still unknown.

The second anomaly is related to the low B(E2) value in the ^{136}Te nucleus, with just one pair

of protons and neutrons outside the doubly-magic core. Firstly, D. C. Radford *et al.* [45] reported a value of B(E2)↑=0.103(15) e^2b^2 for the excitation of the 2_1^+ state in ^{136}Te. Later, this low value was confirmed by L. M. Fraile *et al.* [46] from the preliminary results of a fast timing experiment, giving a value of B(E2)↑=0.122(24) e^2b^2. In 2011, M. Danchev *et al.* [47] reported that a wrong target thickness was used in the results presented in Ref. [45], being the corrected value B(E2)↑=0.122(18) e^2b^2. This value does not agree with the empirical Grodzins rule [48] and, as a result, this value has attracted considerable theoretical and experimental investigation. Different shell model calculations (SM), which in principle are the most appropriate to describe properties of nuclei with a few valence nucleons, have tried to reproduce the experimental B($E2$) value, but always obtained higher values [49, 50]. Only calculations performed with the quasiparticle random phase approximation (QRPA) [51, 52] were able to reproduce this low B($E2$). All calculations (SM and QRPA) agree to attribute such behaviour as a consequence of a strong proton-neutron asymmetry in the wave function of the 2_1^+ state in ^{136}Te, which is neutron-dominated, leading to a reduced B($E2$) value.

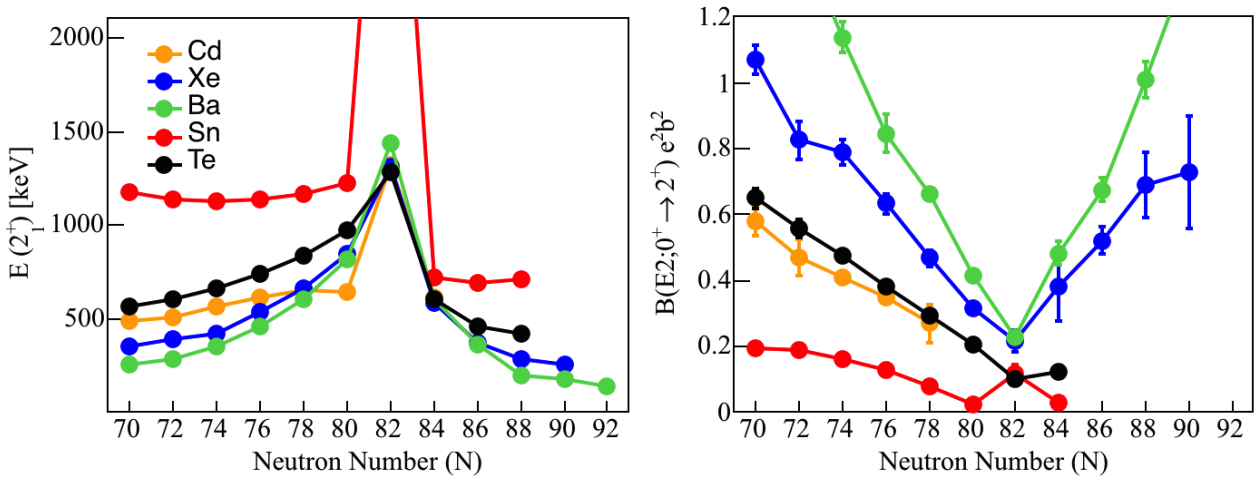

Figure 1.3: Experimental values of 2_1^+ excitation energies (left) and $B(E2; 0_1^+ \rightarrow 2_1^+)$ (right) for even-even nuclei in the ^{132}Sn region: Cd (orange), Xe (blue), Ba (green), Sn (red) and Te (black).

One possible approach to probe the proton-neutron balance of the 2_1^+ wave function is to study the decay properties of its isovector analogue, the one-phonon state with mixed proton-neutron symmetry, 2_{ms}^+. Due to the two-fluid nature of nuclear matter, in even-even nuclei the 2^+ states with vibrational character appear as a symmetric or an antisymmetric configuration of the proton and neutron configurations and hence, in the case of ^{136}Te, the 2_{ms}^+ state is expected to be proton dominated. SM calculations predict a 2_{ms}^+ at an excitation energy around 1.5 MeV [50] or 1.7 MeV [49], while a QRPA calculation predicts the 2_{ms}^+ state at 2.0 MeV [52]. In Ref. [50] a value of B($E2$; $0_1^+ \rightarrow 2_{ms}^+$) = 0.03 e^2b^2 is quoted, while in Ref. [52] this value is B($E2$; $0_1^+ \rightarrow 2_{ms}^+$) = 0.074 e^2b^2. This 2_{ms}^+ state would decay strongly to the first 2^+ via an M1 transition and via a weak E2 transition to the ground state.

Given the importance of the B(E2) value in ^{136}Te, a Coulomb excitation experiment at intermediate energies was conducted in 2015 at the RIBF, RIKEN, Japan, with the following goals:

- Determination of the B($E2; 0_1^+ \rightarrow 2_1^+$) value in ^{136}Te using the Coulomb excitation technique at intermediate energies with the aim of confirming the low values previously reported. Furthermore, it is worth mentioning that during the development of this thesis, a recent work [53] has reported a new B(E2)=0.181(15) e^2b^2 value for ^{136}Te, which is only $\sim$16% smaller than the B(E2) value for ^{132}Te (if we take the B(E2) for ^{132}Te from Ref. [47]) or only $\sim$ 5% smaller than the B(E2) value for ^{132}Te (if we take the B(E2) for ^{132}Te from Ref. [54]). This work concludes that the wave function of the 2_1^+ state in ^{136}Te is dominated by excited valence neutron configurations, but not to the extent previously suggested. Therefore, an ambiguity around the B(E2) value of ^{136}Te has been established and a new experimental measurement of this value using a different technique is necessary.

- Study the excitation and decay of the 2^+ mixed-symmetry state in ^{136}Te. The excitation of these kind of states has usually been carried out using Coulomb excitation below the Coulomb barrier. At low beam energies, the excitation cross section depends strongly on the excitation energy of the state, higher state energies have lower cross-section. Mixed-symmetry states have small transition probabilities to the ground state and are located at energies around 2 MeV, therefore, sub-barrier Coulomb excitation is not an optimal technique to study the mixed-symmetry states. In contrast, at intermediate energies the excitation cross section is practically independent on the excitation energy of the state of interest and depends only on the transition strength to the state, i.e its B(E2) value. The present experiment was the first time that intermediate-energy Coulomb excitation was applied to study mixed-symmetry states. The aim was to obtain its $E(2_{ms}^+)$ and $B(E2; 0_1^+ \rightarrow 2_{ms}^+)$ values and determine which of the theoretical calculations is able to reproduce these experimental values, such information would provide the correct composition of the wave functions for the 2_1^+ and 2_{ms}^+ states.

- To perform a model analysis with high statistics for the determination of B(E2) values from measured differential cross sections at intermediate energies. At intermediate energies, the shape of the measured differential cross section for a given state shows three different contributions: Coulomb excitations, nuclear excitations and feeding from higher lying states. A good knowledge of the different components will show whether it is possible to obtain information about the spin of unknown states from the shape of the differential cross section.

- To obtain new spectroscopic information from the decay of excited states in several N=82-84, Z$\geq$50 isotopes. As the RIBF is an in-flight facility with a large acceptance spectrom-

eter, besides ^{136}Te, the secondary beam is composed of other nuclei that can also be studied.

The thesis is organized as follows. An overview of the different theoretical and experimental considerations will be presented in chapter 2. Chapter 3 shows the procedure to produce the isotopes of interest as well as an explanation of the experimental setup. The different analysis steps are explained in chapter 4. In chapter 5 we will illustrate how the experimental results are obtained then discuss and compare these results with various theoretical models. Chapter 6 provides the conclusions of the thesis and future perspectives. Finally, a Spanish summary is presented in chapter 7.

Chapter 2

Theoretical and Experimental Considerations

In this chapter, a brief description of the theoretical topics relevant to this thesis are presented. In addition, the different experimental considerations necessary for the measurement of interest will be discussed. Firstly, in section 2.1 the nuclear shell model, employed to treat the many-body problem of the nucleus, is briefly described. In later chapters, these shell model calculations will be compared to our experimental measurements. Section 2.2 describes the Coulomb excitation theory necessary to understand this type of inelastic scattering reaction, which, in our case, is used to measure the B(E2) of ^{136}Te. Finally, section 2.3 gives a brief overview of knockout reactions and the theoretical formalism behind this type of reaction.

2.1 Shell model

The nuclear shell model is based on the atomic model, in which the particles do not move randomly as they do in a Fermi gas. Instead, they are found in orbitals following the quantum mechanical laws. Each nucleon moves independently under the influence of an average potential created by the interactions of all the nucleons. The description of such a quantum system is given by the Schrödinger equation for single-particle states [55]:

$$H\phi_i(r) = \epsilon_i\phi(r) \tag{2.1}$$

$$\big(-\frac{\hbar^2}{2m}\nabla^2 + U(r)\big)\phi_i(r) = \epsilon_i\phi(r) \tag{2.2}$$

where the first term of the Hamiltonian represents the kinetic energy while the second one is an effective potential. Different shapes of $U(r)$ have been historically used in the nuclear shell model, notably [56]:

i): Woods-Saxon:

$$U(r) = -\frac{V_0}{1 + e^{(r-R_0)/a}} \tag{2.3}$$

ii): Harmonic oscillator:

$$U(r) = \frac{1}{2} m\omega^2 r^2 \tag{2.4}$$

iii): Square well:

$$U(r) = \begin{cases} -V_0 & \text{if } r \leq R_0 \\ +\infty & \text{if } r > R_0 \end{cases} \tag{2.5}$$

Solving the Schrödinger equation with these potentials, the energy levels (eigenvalues of the Schrödinger equation) obtained do not reproduce all the experimental magic numbers. Finally, the solution to this problem was given by M. Goeppert-Mayer [5,6] and O. Haxel, J. Jensen and H. Suess [7] who had the idea to incorporate a strong spin-orbit term in the Hamiltonian:

$$V_{s.o.} = f(r)\vec{l} \cdot \vec{s} \tag{2.6}$$

This term splits the degeneracy of the levels according to $\epsilon(j_>{=}l + 1/2){<}\epsilon(j_<{=}l - 1/2)$. The inclusion of this term allows to reproduce the experimental magic numbers (2, 8, 20, 28, 50, 82, 126 and 184). The order of levels within different shells depends on the degree of energy splitting induced by eq. 2.6 and, therefore, the form of $f(r)$. An often used form of $f(r)$ is the derivative of the effective $U(r)$ potential [56]:

$$f(r) = \lambda \frac{1}{r} \frac{dU(r)}{dr} \tag{2.7}$$

A more sophisticated treatment of the shell model requires a many-body approach. The assumption is made that only two-body interactions are relevant, while the three and more body interactions are small enough to be neglected. The description of such system is now given by the many-body Schrödinger equation [55,56]:

$$H\phi = \Big\{ \sum_{i=1}^{A} -\frac{\hbar^2}{2m}\nabla_i^2 + \sum_{i<j}^{A} V(i,j) \Big\} \phi(1, ..., A) = E\phi(1, ..., A) \tag{2.8}$$

where i represents the coordinates of the i-th nucleon. Introducing a mean field potential $U(r_i)$ to the Hamiltonian of eq. 2.8, the many-body problem is reduced to a single-particle Hamiltonian plus a residual interaction which is treated as perturbation of the full system:

$$H = \underbrace{\Big[\sum_{i=1}^{A} \Big(-\frac{\hbar^2}{2m}\nabla_i^2 + U(r_i) \Big) \Big]}_{H_0} + \underbrace{\Big[\sum_{i<j}^{A} V(i,j) - \sum_{i=1}^{A} U(r_i) \Big]}_{H_{res}} \tag{2.9}$$

where the first term H_0 represents the single-particle Hamiltonian and the second one, H_{res}, considers the residual effects of the internucleon interactions. The eigenvalues of the H_0 Hamil-

tonian are the single-particle/hole energies (SPE) which are used as inputs to the shell model calculations. These SPE can be directly taken from experimental values, or derived from empirically adjusted central potentials such as Woods-Saxon, harmonic oscillator or folded Yukawa.

The size of the H_{res} Hamiltonian depends on the number of nucleons that form the nucleus. For light nuclei, the dimension of the configuration space is small enough for all possible nucleon couplings to be calculated. For heavier systems, due to computational restrictions, the configuration space needs to be truncated. Three types of configuration space are defined: the inert core, where all orbitals are full and the nucleons do not interact between each other; the valence space, consisting of all orbitals available for occupation by the valence nucleons; and the external space, which refers to high-lying orbitals whose occupation by valence nucleons is energetically very unlikely and, therefore, are not considered in the calculations. As a consequence of these space restrictions, different model spaces are required for different regions of the nuclear chart. The mutual interaction between the valence nucleons is characterized by the two-body matrix elements (TBME) of the residual interaction H_{res}. The energy shift induced by the residual interaction depends on the TBME:

$$\Delta E(j_1 j_2; J) = \langle j_1 j_2; JM | V_{12} | j_1 j_2; JM \rangle \tag{2.10}$$

and therefore the residual part will split the energy degeneracy in J for the $(j_1 j_2)J$ multiplet of states. These TBME can be extracted in three different ways [55, 57]:

i) Empirical interactions: the TBME are derived from experimental binding energies (BE) of doubly-closed shell (CS) nucleus and its neighbours. For the case of a single-j shell:

$$\left\langle j^2; JM \right| V_{12} \left| j^2; JM \right\rangle = BE(CS \pm 2; j^2, I = J) - BE(CS; g.s.) - 2\epsilon_j \tag{2.11}$$

where ϵ_j are the single-particle/hole energies. For small model spaces it is also possible to use a χ^2-fitting method to calculate the single-particle energies and the TBME from experimental data.

ii) Schematic interactions: in this model a simple spatial form of the interaction is assumed and the TBME are numerically calculated. The main potentials used in this approach are the Yukawa, Gaussian, square-well, δ (contact) and surface-δ forms.

iii) Realistic interactions: the TBME are obtained from experimental nucleon-nucleon (NN) scattering data, with NN potentials adjusted to the data. The NN interaction is used to determine the G-matrix and, thus, eliminate the strong repulsive core of the NN interaction. Afterwards, the TBME are calculated for a specific space with a mass dependence. With this approach it is not possible to get reliable single-particle energies and, therefore, they are taken from the

experimental values. A new method has been developed [58], which is based on the construction of a low-momentum NN potential, V_{low-k}, that preserves the physics of the original V_{NN} up to a certain momentum cutoff, Λ. The deuteron binding energy and low-energy scattering phase-shifts of V_{NN} are reproduced with the V_{low-k} potential.

The observation of the evolution of the single-particle/hole energies from one closed shell to the next one is well established. To reproduce this effect, more sophisticated shell model calculations that consider three-body forces are necessary [59]. However, there are regions in the nuclear chart where no effective three-body forces are available yet. In these cases, the evolution of the SPE throughout a shell is determined by the monopole part of the residual interaction given by [57, 60, 61]:

$$V^m_{jj'} = \frac{\sum_J (2J+1) \langle jj'J| V |jj'J\rangle}{\sum_J (2J+1)} \tag{2.12}$$

for a specific multiplet (j, j'). The relation between the SPE of a CS and the next higher closed shell (CS') is expressed as:

$$\epsilon^{CS}_j = \epsilon^{CS'}_j + \sum_{j'} (2j'+1-\delta_{jj'}) V^m_{jj'} \tag{2.13}$$

This monopole drift is the responsible for shell-structure changes when we move away from the valley of stability making some magic numbers disappear and giving rise to new ones.

2.2 Coulomb excitation

Coulomb excitation is a process of inelastic scattering in which a nucleus is excited by means of electromagnetically interacting with another charged particle. This process is very useful since the interaction mechanism is perfectly known. It forms the basis of an experimental technique of the same name that has been used since the 1950s (first with stable beams and targets, but nowadays using fast RI beams and stable targets). Since the strength of the Coulomb interaction is proportional to the charges of the nuclei involved in the process, heavy targets (usually gold or lead) are used to increase the Coulomb strength.

2.2.1 Theoretical formalism

The Coulomb potential between a system of i point-like charges can be written as [62]:

$$V(r) = \sum_i \frac{e_i}{|r - r_i|} \tag{2.14}$$

where e_i is the electric charge of the particle i situated at the point r_i. Using the Legendre polynomials and the multipole expansion, the potential of eq. 2.14 can be expressed as:

$$V(r) = \sum_{L\,M} \frac{4\pi}{2L+1} \frac{1}{r^{L+1}} Y^*_{L\,M}(n) \mathcal{M}(EL, M) \tag{2.15}$$

with n being the direction of r and $\mathcal{M}(EL, M)$ the electric multipole moment given by:

$$\mathcal{M}(EL, M) = \sum_i e_i r_i^L Y_{L\,M}(n_i) \tag{2.16}$$

For a charge density distribution, the electric multipole moment can be written as:

$$\mathcal{M}(EL, M) = \int d^3 r \rho(r) r^L Y_{L\,M}(n) \tag{2.17}$$

where $\rho(r)$ is the charge density operator expressed as $\rho(r) = \sum_i e_i \delta(r - r_i)$. In an analogous way, one can obtain the magnetic multipole moment $\mathcal{M}(ML, M)$ [62]:

$$\mathcal{M}(ML, M) = \sum_i (g_i^s + \frac{2}{L+1} g_i^L \mathbf{l}_i).\nabla(r_i^L Y_{L\,M}(n_i)) \tag{2.18}$$

with s_i being the spin, $\mathbf{l}_i$ the orbital angular momentum, g_i^s and g_i^L the gyromagnetic factors of the spin and orbital angular momentum, respectively, of a particle i.

For the case of a radiative transition between an initial nuclear state, i, and a final nuclear state, f, the probability for the radiative decay is given by:

$$w_{fi} = \frac{8\pi(L+1)}{L\left[(2L+1)!!\right]^2 \hbar} \kappa^{2L+1} \sum_{L\,M} \left\{ \left| \Big(\mathcal{M}(EL, M) \Big)_{fi} \right|^2 + \left| \Big(\mathcal{M}(ML, M) \Big)_{fi} \right|^2 \right\} \tag{2.19}$$

with $\kappa = \omega/c$ and $\omega = (E_f - E_i)/\hbar$. We can define the reduced transition probability as:

$$B(EL; i \to f) = \sum_{M\,M_f} \left| \Big(\mathcal{M}(EL, M) \Big)_{fi} \right|^2 \tag{2.20}$$

Using the *Wigner-Eckart theorem*:

$$B(EL; i \to f) = \frac{1}{2J_i + 1} \left| \langle f | \, | \mathcal{M}(EL) | \, | i \rangle \right|^2 \tag{2.21}$$

For the inverse transition ($f \to i$), the reduced transition probability can be calculated as:

$$B(EL; f \to i) = \frac{2J_i + 1}{2J_f + 1} B(EL; i \to f) \tag{2.22}$$

From this reduced transition probability we can evaluate the partial lifetime of a specific initial state:

$$\frac{1}{\tau_{i\to f}} = \sum_{M_f} w_{fi} = \frac{8\pi(L+1)}{L\left[(2L+1)!!\right]^2\hbar}\kappa^{2L+1}B(EL;i\to f) \tag{2.23}$$

For the case of ion-ion collisions, the probability that the Coulomb excitation process occurs has to be studied separately for three different cases: low energy collisions, relativistic collisions and intermediate-energy collisions, since different approximations can be applied to each of these energy regimes.

2.2.1.1 Low-energy collisions

The theory of Coulomb excitation in low-energy collisions was formulated by K. Alder and A. Winther [63] and since then has been applied to and tested in many experiments. Here, the term "low energy" refers to energies of the projectile below the Coulomb barrier. In this case, the process of excitation is purely Coulomb since the minimum distance between the two ions is larger than the range where the two nuclei interact through nuclear interactions.

The semiclassical approach of Coulomb excitation at low energy considers the projectile moving along a classical Rutherford trajectory. The differential excitation cross section for this process can be written as:

$$\left(\frac{d\sigma}{d\Omega}\right)_{fi} = \left(\frac{d\sigma}{d\Omega}\right)_{Ruth} w_{fi} \tag{2.24}$$

where the probability, w_{fi}, can be expressed in terms of the amplitudes, a_{fi} [62, 64]:

$$w_{fi} = \sum_{M_f\,M_i} \frac{1}{2J_i+1}\left|a_{fi}\right|^2 \tag{2.25}$$

Under most experimental conditions, these amplitudes are small and can be expressed using first-order time-dependent perturbation theory:

$$a_{fi} = \frac{1}{i\hbar}\int_{-\infty}^{\infty}\langle f|\,H_{fi}(t)\,|i\rangle\, e^{i\omega t}dt \tag{2.26}$$

The interaction Hamiltonian in the case of low-energy collision is given by [64]:

$$H_{fi}(t) = \int \rho_n(\mathbf{r})\phi(\mathbf{r},t)d\tau \tag{2.27}$$

with:

$$\phi(\mathbf{r},t) = \frac{Z_1 e}{|\mathbf{r}-\mathbf{r}_p(t)|} - \frac{Z_1 e}{\mathbf{r}_p(t)} \tag{2.28}$$

and $\rho_n(\mathbf{r})$ being the nuclear charge-density operator. One of the charged particles is considered as a point charge and its position $\mathbf{r}_p(t)$ is measured from the nuclear center of mass. In addition, in the eq. 2.28, the interaction between the mass center is not considered since it does not

contribute to the intrinsic excitations. Expanding the Hamiltonian in multipole components we obtain the following expression:

$$H_{fi}(t) = 4\pi Z_1 e \sum_{L=1}^{\infty} \sum_{M=-L}^{M=L} \frac{1}{2L+1} \frac{1}{r_p^{L+1}} Y^*_{L\,M}(\theta_p, \varphi_p) \mathcal{M}(EL, M) \tag{2.29}$$

Inserting this Hamiltonian into eq. 2.26 and using the definition of the electric multipole moment in eq. 2.17, we can get the amplitudes, a_{fi}:

$$a_{fi} = \frac{4\pi Z_1 e}{i\hbar} \sum_L \frac{1}{(2L+1)^{3/2}} \langle f| \, |\mathcal{M}(EL)| \, |i\rangle \sum_M I_{L\,M}(w_{fi}) \tag{2.30}$$

and the probability, w_{fi}:

$$w_{fi} = \Big(\frac{4\pi Z_1 e}{\hbar}\Big)^2 \sum_L \frac{B(EL; i \to f)}{(2L+1)^3} \sum_M \big|I_{L\,M}(w_{fi})\big|^2 \tag{2.31}$$

where we have defined the orbital integrals, $I_{L\,M}(w_{fi})$, as:

$$I_{L\,M}(w_{fi}) = \int_{-\infty}^{\infty} r_p(t)^{-L-1} Y_{L\,M}(\theta_p, \varphi_p) e^{i\omega t} dt \tag{2.32}$$

Using eq. 2.24 we can derive the cross section as a function of multipolarity, L:

$$\Big(\frac{d\sigma(L)}{d\Omega}\Big)_{fi} = \Big(\frac{\pi Z_1 e a}{\hbar sin^2(\theta/2)}\Big)^2 \frac{B(EL; i \to f)}{(2L+1)^3} \sum_M \big|I_{L\,M}(w_{fi})\big|^2 \tag{2.33}$$

where a is the distance of closest approach defined as, $a = 2a_0 = \frac{2Z_1 Z_2 e^2}{\mu v^2}$. Expression 2.33 corresponds to the differential cross section for collisions at low energy only considering the electrostatic interaction. A more rigorous description of Coulomb excitation needs to consider the magnetic interaction and the Coulomb recoil of the classical trajectories. The differential cross section taking into account these factors is given by [62, 64]:

$$\frac{d\sigma_{fi}}{d\Omega} = \Big(\frac{\pi Z_1 e a \epsilon^2}{\hbar}\Big)^2 \sum_{\pi\, L\, M} \frac{B(\pi L; i \to f)}{(2L+1)^3} |S(\pi L, M)|^2 \tag{2.34}$$

with π = E or M, for electric or magnetic transitions, respectively, ϵ being the eccentricity parameter defined as, $\epsilon = \sqrt{1 + \frac{b^2}{a_0^2}}$, and the orbital integrals expressed as:

$$S(EL, M) = \int_{-\infty}^{\infty} r_p(t)^{-L-1} Y_{L\,M}(\theta_p, \varphi_p) e^{i\omega t} dt \tag{2.35}$$

$$S(ML, M) = -\frac{1}{L\mu c} \mathbf{L}_0 \int_{-\infty}^{\infty} \nabla\{r_p(t)^{-L-1} Y_{L\,M}(\theta_p, \varphi_p)\} e^{i\omega t} dt \tag{2.36}$$

where we have used the parametrization of the Rutherford trajectory:

$$x = a_0[cosh\chi + \epsilon] \qquad y = a_0\sqrt{\epsilon^2 - 1}sinh\chi \qquad z = 0 \tag{2.37}$$

According to virtual photon theory, the excitation of the target nucleus can be considered as the absorption of virtual photons whose spectrum is determined by [62]:

$$\frac{d\sigma_C}{d\Omega} = \sum_f \int \frac{d\sigma_{fi}}{d\Omega}\rho_f(E_\gamma)dE_\gamma \tag{2.38}$$

where $\rho_f(E_\gamma)$ represents the density of final states of the target nucleus with energy $E_f = E_i + E_\gamma$. Inserting eq. 2.34 into eq. 2.38:

$$\frac{d\sigma_C}{d\Omega} = \sum_{\pi L} \int \frac{dE_\gamma}{E_\gamma}\frac{dn_{\pi L}}{d\Omega}(E_\gamma)\sigma_\gamma^{\pi L}(E_\gamma) \tag{2.39}$$

with $\sigma_\gamma^{\pi L}$ and $n_{\pi L}$ being the photonuclear cross sections and the virtual photon numbers, respectively, given by:

$$\sigma_\gamma^{\pi L} = \frac{(2\pi)^3(L+1)}{L\left[(2L+1)!!\right]^2}\sum_f \rho_f(E_\gamma)\kappa^{2L-1}B(\pi L; i \to f) \tag{2.40}$$

$$\frac{dn_{\pi L}}{d\Omega} = \frac{Z_p^2\alpha}{2\pi}\frac{L\left[(2L+1)!!\right]^2}{(L+1)(2L+1)^3}\frac{c^2a_o^2\epsilon^4}{\kappa^{2(L-1)}}\sum_M |S(\pi L, M)|^2 \tag{2.41}$$

2.2.1.2 Relativistic collisions

Now, we consider the case of collisions at very high kinetic energy, that is $\gamma >> 1$. The semi-classical theory for this regime of energy was written by, again, A. Winther and K. Alder [65]. At these energies, well above the Coulomb barrier, the charge distributions of the two nuclei involved in the process can overlap during the collision. As a result, the strong and Coulomb interactions play a role. For the case of low-energy collisions, the projectile is assumed to move on a Rutherford trajectory. Whereas, in the high energy regime, the projectile is considered to move on a straight-line trajectory with an impact parameter, b, which is the distance of closest approach between the center of mass of the two ions at t=0. In order to consider only Coulomb contributions, this impact parameter is always assumed larger than the sum of the two nuclear radii, $R = R_1 + R_2$, and, therefore, the charge distributions of the two nuclei do not overlap. To get the probability of excitation we follow the same procedure as in the previous subsection. The relativistic electromagnetic field for a charged particle moving on a straight line is given by the Lienar-Wiechert expression [62, 65, 66]:

$$\phi(\mathbf{r}, t) = \frac{\gamma Ze}{\sqrt{(x-b)^2 + y^2 + \gamma^2(z-vt)^2}} \tag{2.42}$$

The Fourier component of this field is:

$$\phi(\mathbf{r},\omega) = \int \phi(\mathbf{r},t)e^{i\omega t}dt = \frac{2Ze}{v}e^{i\omega v/z}K_0(\frac{\omega}{v}q) \tag{2.43}$$

where K_0 is the modified Bessel function of zero order and $q = 1/\gamma^2[(b-x)^2+y^2]$. Expanding in multipole components:

$$\phi(\mathbf{r},\omega) = \sum_{L\,M} W_{LM}(\mathbf{r},\omega)Y^*_{L\,M}(\hat{\mathbf{r}}) \tag{2.44}$$

with:

$$\begin{aligned} W_{LM}(\mathbf{r},\omega) = \sqrt{16\pi(2L+1)}\Big(\frac{(L-M)!}{(L+M)!}\Big)^2(2M-1)!!\times \\ i^{L+M}\frac{Ze}{v}\Big(\frac{c}{\gamma v}\Big)^M K_M\Big(\frac{\omega b}{\gamma v}\Big)C^{M+1/2}_{L-M}(\frac{c}{v})j_L(\kappa r) \end{aligned} \tag{2.45}$$

The excitation amplitudes, a_{fi}, can be calculated using eq. 2.26:

$$a_{fi} = -i\frac{Ze}{\hbar v\gamma}\sum_{\pi L M} G_{\pi L M}(\frac{c}{v})(-1)^M K_M\Big(\frac{\omega b}{\gamma v}\Big)\sqrt{2L+1}\kappa^L\mathcal{M}_{fi}(\pi L,-M) \tag{2.46}$$

The functions $G_{\pi L M}$ have analytical expressions. From the amplitude in eq. 2.46 the total cross section is given by [62, 65, 66]:

$$\sigma_{fi} = \Big(\frac{Ze}{\hbar c}\Big)^2\sum_{\pi L M}\kappa^{2(L-1)}B(\pi L; i\to f)\big|G_{\pi L M}(\frac{c}{v})\big|^2 g_M(\xi(R)) \tag{2.47}$$

with $\xi(R) = \frac{\omega R}{\gamma v}$. As in the case of the low energy theory, the result can be written in terms of virtual photon theory using eq. 2.38, where, now, the total number of virtual photons is given analytically by (for the cases of E1 and E2 excitations) [62]:

$$N_{E1}(E_\gamma) = \frac{2Z^2\alpha}{\pi}(\frac{c}{v})^2\Big[\xi K_0K_1 - \frac{v^2\xi^2}{2c^2}(K_1^2-K_0^2)\Big] \tag{2.48}$$

$$N_{E2}(E_\gamma) = \frac{2Z^2\alpha}{\pi}(\frac{c}{v})^4\Big[\frac{2}{\gamma^2}K_1^2 + \frac{\xi}{\gamma^4}K_0K_1 + \frac{v^4\xi^2}{2c^4}(K_1^2-K_0^2) + \xi^2(2-v^2/c^2)^2K_1^2\Big] \tag{2.49}$$

where K_M are the modified Bessel functions.

2.2.1.2.1 Quantum approach: the eikonal approximation

For relativistic energy collisions, if we want to describe correctly the angular distribution, the absorption and diffraction effects due to the presence of Coulomb and nuclear interactions, we have to employ a quantum mechanical approach. This can be done using the eikonal approximation. The movement of a free-particle is given by the wavefunction:

$$\psi \sim e^{i\mathbf{k}.\mathbf{r}} \tag{2.50}$$

This wavefunction is distorted in the presence of a potential. The distorted function is calculated solving the Schrödinger equation:

$$\Big[\frac{d^2}{dr^2} + \Big\{\frac{2\mu}{\hbar^2}\Big[E - V(r) - \frac{l(l+1)\hbar^2}{2\mu r^2}\Big]\Big\}^2\Big]\xi_l(r) = 0 \tag{2.51}$$

In high energy collisions, the excitations energies, ΔE, are much lower than the energy, E, of the projectile and, as a consequence, the scattering angles are very small $\theta << 1$. Under this condition, the wavefunction can be written as [62]:

$$\psi(r) = e^{ikz}\phi(z, \mathbf{b}) \tag{2.52}$$

where ϕ changes slowly with the coordinate along the beam direction z and the impact parameter, b, satisfying:

$$\big|\nabla^2\phi\big| << k\big|\nabla\phi\big| \tag{2.53}$$

Under this condition, the Schrödinger equation is reduced to:

$$\frac{\partial\phi}{\partial z} = -\frac{i}{\hbar v}V(\mathbf{r})\phi \tag{2.54}$$

The solution of eq. 2.54 is:

$$\phi = exp\Big\{-\frac{i}{\hbar v}\int_{-\infty}^{z} V(\mathbf{b}, z')dz'\Big\} \tag{2.55}$$

and inserting this solution in the eq. 2.52:

$$\psi(\mathbf{r}) = exp\big\{ikz + i\chi(\mathbf{b}, z)\big\} \tag{2.56}$$

where we have introduced the eikonal phase:

$$\chi(\mathbf{b}, z) = -\frac{i}{\hbar v}\int_{-\infty}^{z} V(\mathbf{b}, z')dz' \tag{2.57}$$

Defining now **r** as the distance between the center of mass of two nuclei and **r′** as the intrinsic coordinate of the target nucleus, the inelastic scattering amplitude to first-order can be written as:

$$f(\theta) = \frac{ik}{2\pi\hbar v}\int d^2r d^3r' \left\langle \Phi^{(-)}_{\mathbf{k'}}(\mathbf{r})\phi_f(\mathbf{r'})\right| H_{int}(\mathbf{r}, \mathbf{r'}) \left|\Phi^{(+)}_{\mathbf{k}}(\mathbf{r})\phi_i(\mathbf{r'})\right\rangle \tag{2.58}$$

where we have defined the functions $\Phi^{(-)}_{\mathbf{k'}}(\mathbf{r})$ and $\Phi^{(+)}_{\mathbf{k}}(\mathbf{r})$ as the incoming and outgoing distorted waves for the scattering of the center of mass. Using the eikonal approximation (eq. 2.56):

$$\Phi^{(-)*}_{\mathbf{k'}}(\mathbf{r})\Phi^{(+)}_{\mathbf{k}}(\mathbf{r}) = exp\big\{-i\mathbf{q}.\mathbf{r} + i\chi(b)\big\} \tag{2.59}$$

where now the eikonal phase is given by the expression:

$$\chi(b) = -\frac{i}{\hbar v}\int_{-\infty}^{\infty} U_N^{opt}(z', b)dz' + i\chi_C(b) \tag{2.60}$$

with $\mathbf{q} = \mathbf{k}' - \mathbf{k}$, U_N^{opt} the nuclear potential and $\chi_C(b)$ the Coulomb eikonal phase expressed as:

$$\chi_C(b) = \frac{2Z_pZ_te^2}{\hbar v} ln(kb) \tag{2.61}$$

The interaction Hamiltonian in the eq. 2.58 (considered to be purely Coulomb) is given by [62]:

$$H_{int}(\mathbf{r}, \mathbf{r}') = \frac{v^\mu}{c^2} j_\mu(\mathbf{r}') \frac{e^{ik|\mathbf{r}-\mathbf{r}'|}}{|\mathbf{r}-\mathbf{r}'|} \tag{2.62}$$

Inserting all these expressions into eq. 2.58, we get:

$$f(\theta) = \frac{iZek}{\gamma\hbar v}\sum_{\pi LM} i^M \Big(\frac{\omega}{c}\Big)^L \sqrt{2L+1} e^{-iM\phi}\Omega_M(q) G_{\pi LM}\big(\frac{c}{v}\big)\mathcal{M}_{fi}(\pi L, -M) \tag{2.63}$$

where πLM denotes the multipolarity, $G_{\pi LM}$ are the Winther-Alder relativistic functions previously introduced [65] and $\Omega_M(q)$ are functions given by:

$$\Omega_M(q) = \int_0^\infty db\ \ b\ \ J_M(qb)\ \ K_M\Big(\frac{\omega b}{\gamma v}\Big) exp\{i\chi(b)\} \tag{2.64}$$

with $q = 2ksin(\theta/2)$ being the momentum transfer. Once the inelastic amplitudes are calculated, following the same procedure as in the previous subsection, we can get the differential cross section:

$$\frac{d^2\sigma_C}{d\Omega dE_\gamma}(E_\gamma) = \frac{1}{E_\gamma}\sum_{\pi L}\frac{dn_{\pi L}}{d\Omega}\sigma_\gamma^{\pi L}(E_\gamma) \tag{2.65}$$

where $\frac{dn_{\pi L}}{d\Omega}$is the virtual photon number per solid angle given by:

$$\frac{dn_{\pi L}}{d\Omega} = Z^2\alpha\Big(\frac{\omega k}{\gamma v}\Big)^2 \frac{L[(2L+1)!!]^2}{(2\pi)^3(L+1)}\sum_M |G_{\pi LM}|^2 |\Omega_M(q)|^2 \tag{2.66}$$

Using the hypothesis of small scattering angles, we can get the total cross section for the Coulomb excitation and the total number of virtual photons:

$$\frac{d\sigma_C}{dE_\gamma}(E_\gamma) = \frac{1}{E_\gamma}\sum_{\pi L} N_{\pi L}(E_\gamma)\sigma_\gamma^{\pi L}(E_\gamma) \tag{2.67}$$

$$N_{\pi L} = Z^2\alpha\frac{L[(2L+1)!!]^2}{(2\pi)^3(L+1)}\sum_M |G_{\pi LM}|^2 g_M(\omega) \tag{2.68}$$

with:

$$g_M(\omega) = 2\pi\Big(\frac{\omega}{\gamma v}\Big)^2 \int db\ \ b\ \ K_M^2\ \ \Big(\frac{\omega b}{\gamma v}\Big) exp\{-2\chi_I(b)\} \tag{2.69}$$

with $\chi_I(b)$ being the imaginary part of $\chi(b)$ defined in eq. 2.60.

2.2.1.3 Intermediate energy collisions

At low energies, the movement of ions is characterized by Rutherford trajectories, whereas at relativistic energies one assumes straight-line motions. In the case of intermediate-energy collisions, it is necessary to consider the recoil and retardation effects. The solution of this collision process is given by the solution of the classical problem of the motion of two relativistic charged particles. It was shown that the solution to this problem is very well approximated assuming the following trajectories [62, 67, 68]:

$$x = a'[cosh\chi + \epsilon] \qquad y = a'\sqrt{\epsilon^2 - 1}sinh\chi \qquad z = 0 \tag{2.70}$$

with $\epsilon = 1/sin(\theta/2)$ and the impact parameter expressed as $b = a'cot(\theta/2)$. The trajectory of eq. 2.70 corresponds to a Rutherford trajectory, as in the case of non-relativistic energies, but the half-distance of closest approach, a_0, has been replaced by $a' = a_0/\gamma$. The excitation amplitudes, a_{fi}, for the intermediate-energy Coulomb excitation of a nucleus from the initial state, i, to the final state, f, moving along a modified Rutherford trajectory are given by the same expressions as the low-energy excitation, but replacing a_0 by a_0/γ. Thus the differential cross section is calculated from:

$$\frac{d\sigma_{i\to f}}{d\Omega} = \frac{4\pi^2 Z_p^2 e^2}{\hbar^2} a'^2 \epsilon^4 \sum_{\pi\lambda\mu} \frac{B(\pi\lambda, I_i \to I_f)}{(2\lambda+1)^3} \left|S(\pi\lambda,\mu)\right|^2 \tag{2.71}$$

and in terms of virtual photon numbers:

$$\frac{dn_{\pi\,L}}{d\Omega} = \frac{Z_p^2\alpha}{2\pi} \frac{L\left[(2L+1)!!\right]^2)}{(L+1)(2L+1)^3} \frac{c^2 a'^2 \epsilon^4}{\kappa^{2(L-1)}} \sum_M \left|S(\pi L, M)\right|^2 \tag{2.72}$$

2.2.2 Angular distribution of γ rays

Once the state of interest has been excited from a lower-lying state due to the Coulomb interaction, the de-excitation of this state occurs via the emission of γ rays. The angular distribution of these γ rays depends on the frame of reference considered. Considering the z axis as the direction of the incident beam, the angular distribution can be expressed as a function of the excitation amplitudes, a_{fi}, discussed previously for each of the energy regimes [64]:

$$W_{\theta,\varphi}(\Omega_\gamma) = \sum_{\sigma M_i M_F} \left| \sum_{M_f} a_{fi} \left\langle I_F M_F \right| H_\gamma(\Omega_\gamma, \sigma) \left| I_f M_f \right\rangle \right|^2 \tag{2.73}$$

where i is the initial state, f is the state excited via the Coulomb interaction, F is the state populated once the γ-ray emission takes place, σ is the polarization and $H_\gamma(\Omega_\gamma, \sigma)$ is the interaction Hamiltonian. Considering the case in which the excitation occurs by a transition of pure

multipole order λ:

$$W_{\theta,\varphi}(\Omega_\gamma) = \sum_{k\kappa} a^{\lambda}_{k\kappa}(\theta,\varphi,\xi)\, A^{\lambda}_{k} Y_{k\kappa}(\Omega_\gamma) \tag{2.74}$$

where the definition of the coefficients $a^{\lambda}_{k\kappa}$ and A^{λ}_{k} can be found in Refs. [64, 68] and $Y_{k\kappa}(\Omega_\gamma)$ are the normalized spherical harmonics. The total angular distribution of the γ rays, integrating over all the scattering angles of the projectile, is given by:

$$W_{c.m}(\theta_{c.m}) = \sum_{k} a^{\lambda}_{k}(\xi)\, A^{\lambda}_{k}\, P_k(cos(\theta_{c.m})) = 1 + \sum_{k=2,4...} a^{\lambda}_{k}(\xi)\, A^{\lambda}_{k}\, P_k(cos(\theta_{c.m})) \tag{2.75}$$

where $P_k(cos(\theta_{c.m}))$ are the Legendre polynomials. In eq. 2.75, the angular distribution is expressed in the center-of-mass system. In the laboratory frame, the angular distribution is enhanced in the forward direction due to the Lorentz boost:

$$W_{lab}(\theta_{lab}) = W_{c.m}(\theta_{c.m}) \frac{d\Omega^{c.m}_{\gamma}}{d\Omega^{lab}_{\gamma}} \tag{2.76}$$

with:

$$d\Omega^{c.m}_{\gamma} = \frac{1-\beta^2}{(1-\beta cos(\theta_{lab}))^2} d\Omega^{lab}_{\gamma} \qquad cos(\theta_{c.m}) = \frac{cos(\theta_{lab})-\beta}{1-\beta cos(\theta_{lab})} \tag{2.77}$$

2.2.3 Experimental considerations

The Coulomb cross section of a final nuclear state, f, from an initial state, i, is large if the adiabacity parameter (ratio of the time scales for Coulomb excitation and for the nuclear contribution) satisfies the condition:

$$\xi = \frac{E_{exc} a_0}{\hbar v} < 1 \tag{2.78}$$

where a_0 is the half distance of closest approach, v is the velocity of the projectile and E_{exc} is the excitation energy. This condition implies that the maximum excitation energy is given by:

$$E^{max}_{exc} \approx \frac{\gamma \hbar v}{b} \tag{2.79}$$

Thus for a low-energy Coulomb excitation experiment the maximum energy of excitation is limited to 1-2 MeV while for an intermediate/relativistic energy Coulomb excitation experiment the reaction mechanism favors the excitation of collective states at higher energies, i.e pigmy, or giant resonances. Figure 2.1 shows the dependence of the Coulomb excitation cross section on the beam energy for the reaction studied in this work, ^{136}Te+^{197}Au. The calculations were performed using a new computer code called nuco [69] and developed in Ref. [70]. The cross sections were calculated up to the maximum scattering angle of θ_{max}=1.2°, corresponding to a minimum impact parameter of b_{min} =15.7 fm ($b_{min} = R^{1/3}_{projectile} + R^{1/3}_{target} + 2fm$). The cross section for the 2^+_1 state at 0.606 MeV with B(E2)↑=0.18 e^{2}b^2 were calculated as a function of the beam energy. We also assumed a 3^- octupole state at 1.5 MeV and with a reduced transition probability of B(E3)↓=20 W.u. We also calculated the Coulomb excitation cross sections for a

possible pigmy resonance set of states centered at 10 MeV with a total strength of B(E1)↑=0.5 e^2fm. As one can see in Fig. 2.1, the study of low-lying states is better performed at low beam energies since the cross sections are higher, while the excitation of higher energy states, such as pigmy, or giant dipole/quadrupole resonances, are only possible with high beam energies.

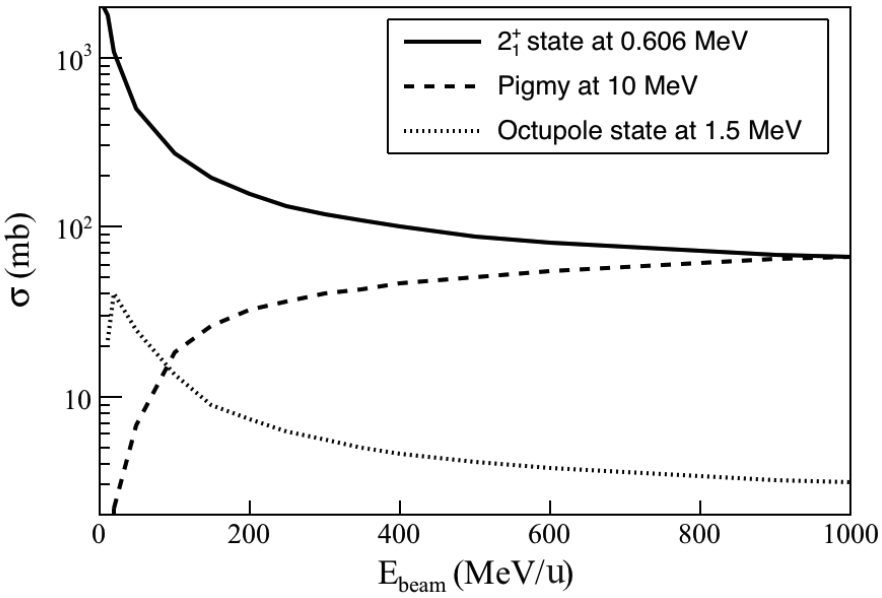

Figure 2.1: Calculated Coulomb excitation cross sections as a function of the beam energy for different collective states in ^{136}Te for the ^{136}Te+^{197}Au reaction with a minimum impact parameter of b_{min} = 15.7 fm.

Another important difference between the low and intermediate/high energy regimes is that at low beam energies, due to the adiabacity cutoff, the excitation cross section depends strongly on the excitation energy of the state. In contrast, at intermediate/high energies, the excitation cross sections for E2 and E3 multipolarities are practically independent of the excitation energy of the state of interest and only depend on the strength of the state, i.e B(E2) and B(E3) values. Figure 2.2 displays the calculated Coulomb excitation cross sections at low (5 MeV/u) and intermediate (150 MeV/u) beam energies for multipolarities E2 (left), E1 (middle) and E3 (right) as a function of the energy of a hypothetical state in ^{136}Te for the ^{136}Te+^{197}Au reaction. Fixed values of B(E2)↑=0.18 e^2b^2, B(E3)↓=20 W.u and B(E1)↑=0.5 e^2fm were used in the calculations. Again, a minimum impact parameter of $b_{min} = 15.7$ fm was used. As is visible, for the case of Coulomb excitation at low beam energy, the cross sections strongly fall with the energy of the state independently of the multipolarity and the direct excitation of states is very suppressed above $\sim$ 2 MeV, whereas at intermediate beam energy the Coulomb excitation cross sections are almost constant for E2 and E3 excitations over the whole range of energies.

At low energies multiple-step Coulomb excitation occurs and many low-lying states are excited, while at intermediate/high energies multi-step excitations are highly suppressed since the time

of interaction between the projectile and the target is very fast. Instead, the direct excitation of collective E1, E2 and E3 states is possible at high beam energies, which is not possible at low beam energies, as shown in Fig. 2.2. A consequence of multiple-step Coulomb excitation is that the feeding from low-lying states is suppressed in intermediate/high-energy Coulomb excitation compared to low-energy Coulomb excitation, although at intermediate/high-energy beam energies it is possible to have considerable feeding (maybe unobserved) from higher-lying 1^-, 2^+ and 3^- excited states.

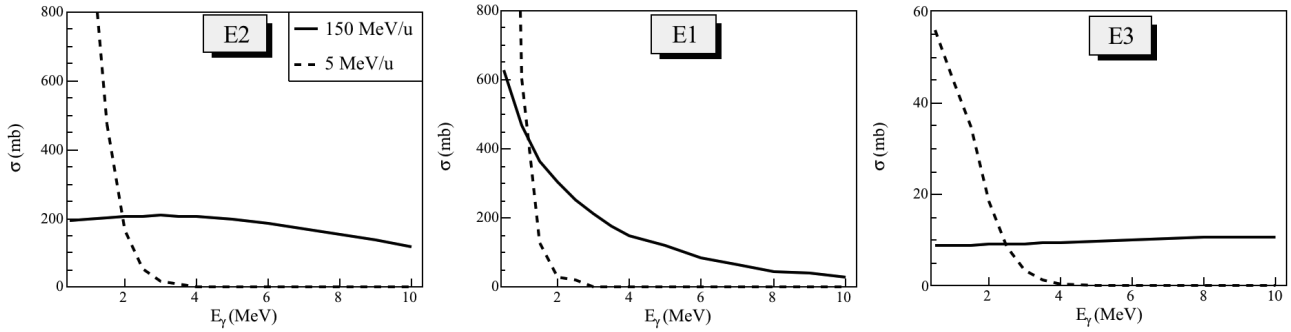

Figure 2.2: Calculated Coulomb excitation cross sections at 5 MeV/u (dashed line) and 150 MeV/u (continuous line) beam energies for multipolarities E2 (left), E1 (middle) and E3 (right) as a function of the energy of a state in ^{136}Te for the ^{136}Te+^{197}Au reaction. Values of B(E2)↑=0.18 e^{2}b^2, B(E3)↓=20 W.u and B(E1)↑=0.5 e^{2}fm were used in the calculations. A minimum impact parameter of b_{min} = 15.7 fm was used.

An aspect that simplifies the analysis of Coulomb excitation experiments at low energies is that the excitation mechanism is purely electromagnetic and nuclear contributions are negligible while at intermediate/high energies the total cross section includes Coulomb and nuclear excitations. Pure electromagnetic interaction is considered if the distance of closest approach is at least of the order of the sum of the nuclear radii, $R = R_P + R_t + 2fm$. In low-energy Coulomb excitation, this condition is satisfied for all scattering angles, while at intermediate/high energies peripheral collisions are selected in the analysis in order to suppress the nuclear contributions [71, 72]. Therefore, only events with an extreme forward scattering angle, corresponding to a large impact parameter, are studied, consequently leading to statical losses. It is possible to avoid the rejection of events in the analysis of high-energy Coulomb experiments, but in this case the analysis is more complicated since the nuclear contribution has to be considered with the help of optical potentials [73, 74]. Lastly, in the case of low-energy Coulomb excitation, the angular distribution of the scattered projectile ions has a large range and, therefore, if we are interested in measuring the whole angular distribution an experimental setup covering the 0-180° angular range is required. Conversely, for intermediate/high energy Coulomb excitation, since the scattering angles are very small, detectors sensitive to only the forward angles are necessary to measure the entire angular distribution.

Table 2.1 summarizes the main differences between low- and intermediate/high-energy Coulomb

excitation experiments previously explained in this section.

Table 2.1: Differences between low- and intermediate/high-energy Coulomb excitation experiments. See the text for more details.

	Low energy	Intermediate/Relativistic energy
Energy (MeV/u)	$<$30	$>$30
Interaction	Coulomb	Coulomb+Nuclear
Maximum excitation energy (MeV)	$\sim$ 2	-
Multi-step excitation	✓	✗
Direct E1, E2 and E3 excitation of high energy states	✗	✓
σ independent on the E_γ	✗	✓(E2 and E3)
Scattering angles θ	Large	Small
Approach of angular cut and loss of statistics	✗	✓
Codes	GOSIA/CLX/ ECIS/FRESCO	DWEIKO/COULINT/ ECIS

2.3 Nucleon removal reactions

Nucleon removal reactions, also known by the name of nucleon breakup or nucleon knockout reactions, are processes in which the projectile and the target interact causing one, or both, to lose one or more nucleons. The nature of this interaction can be mainly nuclear or Coulomb depending on the masses of the projectile and target. These type of reactions have been widely used since 1980 as spectroscopic tool and to obtain nuclear structure information about a wide variety of isotopes. At low beam energies ($<$20-30 MeV/u), transfer reactions are used to populate states of interest due to their high cross sections, whereas intermediate/high beam energies ($>$50 MeV/u), nucleon removal cross sections are favored and, therefore, used to populate states of interest. The latter experiments are carried out at NSCL/MSU (first laboratory to use the nucleon-knockout technique), GANIL, GSI and RIKEN.

The nucleon removal process can occur in the collision of a fast moving projectile beam with a low mass target (typically ^{9}Be or ^{12}C). The projectile (A) loses one nucleon, this nucleon is scattered at large angles and the core-fragment ($A-1$) continues moving along its initial trajectory with almost the same energy. The wave function of the projectile $|\varphi_A\rangle$ can be expressed as [75]:

$$|\varphi_A\rangle = \sum C^2S(|\varphi_{A-1}\rangle \otimes |\varphi_{removed}\rangle) \tag{2.80}$$

where $|\varphi_{A-1}\rangle$ and $|\varphi_{removed}\rangle$ are the wave-function of the core-fragment and removed nucleon, respectively, and C^2S are the spectroscopic factors of each orbital configuration. A detailed

description of these terms is given below.

2.3.1 Theoretical formalism

At high beam energies, two different approximations permit the use of a semiclassical description of the reaction process. The first one is related to the fact that the internal degrees of freedom (relative motion of the fragment and removed nucleon) can be considered as frozen during the collision since the interaction time is short. This approximation is called the "sudden approximation", or "adiabatic approximation" and implies that the momentum of the recoiling fragment after the one-nucleon knockout provides information about the wave function of the removed nucleon. The second approximation is based on the fact that, due to the high beam energy, the scattering process of the projectile is concentrated at very forward angles and thus the projectile follows straight-line trajectories. This approximation is known by the name of the "eikonal approximation" [76].

The cross section, $\sigma(J^\pi)$, for the removal of a nucleon from a single-particle orbital with quantum numbers (n, l, j) which populates a final state J^π in the fragment can be expressed as a function of the single-particle cross sections, σ_{sp}, and the spectroscopic factors, C^2S, through the equation [76, 77]:

$$\sigma(J^\pi) = \sum_j C^2S(J^\pi, nlj)\sigma_{sp}(S_N + E_x(J^\pi), nlj) \tag{2.81}$$

where the sum $S_N + E_x(J^\pi)$ is the effective binding energy of the removed nucleon, with S_N being the proton/neutron separation energy of the projectile and $E_x(J^\pi)$ the excitation energy of the final state J^π. The single-particle cross section, σ_{sp}, represents three different contributions [76–78]:

$$\sigma_{sp} = \sigma_{sp}^{str} + \sigma_{sp}^{diff} + \sigma_{sp}^{Cou} \tag{2.82}$$

The three terms on the right of eq. 2.82 are defined below.

σ_{sp}^{str}/*Stripping cross section*: also called inelastic breakup, it is the process in which the removed nucleon interacts with the target and is scattered to large angles, or absorbed by the target, while the target is excited from the ground state. The stripping single-particle cross sections are calculated within the "spectator-core" model applied to the many-body eikonal theory:

$$\sigma_{sp}^{str} = \frac{1}{2I+1}\int d\vec{b}\sum_M \langle\varphi_{IM}|\left(1 - \left|S_n\right|^2\right)\left|S_c\right|^2|\varphi_{IM}\rangle \tag{2.83}$$

with $I = j + J^\pi$ being the total angular momentum, φ_{IM} the removed nucleon-fragment relative motion wave-functions, and S_c and S_n the S-matrices of the fragment-target and removed nucleon-target systems, respectively. These S-matrices can be obtained from empirical poten-

tials such as Woods-Saxon well, folding approaches, or multiple scattering theory in the optical limit of the Glauber theory, while the wave-functions φ_{IM} are derived from an effective two-body Hamiltonian based on an effective local potential adjusted to reproduce the separation energy of the removed nucleon from the projectile.

σ_{sp}^{diff}/*Diffraction cross section*: also called elastic breakup, here the target remains in its ground state and the removed nucleon moves in the same direction and at the same velocity as the beam. The expression of the diffractive cross sections σ_{sp}^{diff} in the spectator eikonal model is given by:

$$\sigma_{sp}^{diff} = \frac{1}{2I+1} \sum_{\sigma,M} \int \vec{k}d \int d\vec{b} \left| \left\langle \varphi_{\vec{k}\sigma} \right| 1 - S_c S_n \left| \varphi_{IM} \right\rangle \right|^2 \tag{2.84}$$

where $\varphi_{\vec{k}\sigma}$ represents the continuum breakup states. Eliminating the integration over the continuum, the previous expression is transformed into:

$$\sigma_{sp}^{diff} = \frac{1}{2I+1} \int d\vec{b} \sum_{MM'} \left[\left\langle \varphi_{IM} \right| \left| 1 - S_c S_n \right|^2 \left| \varphi_{IM} \right\rangle \delta_{MM'} - \left| \left\langle \varphi_{IM'} \right| \left(1 - S_c S_n\right) \left| \varphi_{IM} \right\rangle \right|^2 \right] \tag{2.85}$$

σ_{sp}^{Cou}/*Coulomb breakup cross section*: also called Coulomb dissociation, a nucleon is evaporated due to the electromagnetic excitation of resonant states, or non-resonant transitions above the nucleon separation energy of the projectile. As a consequence of the smaller effective charge for higher multipolarities, the dipole excitations dominate the Coulomb breakup cross section. The Coulomb dissociation cross section plays a minor role for light targets and, as normally light targets are used to induce nucleon knockout reactions, this contribution is not considered in the eikonal theory although it may be important for projectiles with low nucleon separation energies despite the use of a light target.

Nuclear structure is incorporated in the cross section calculations via the C^2S spectroscopic factors. These express the parentage of the initial state of the projectile with respect to a specific state in the remaining fragment coupled to a nucleon with quantum numbers (ℓ, j). Spectroscopic factors can be derived from shell model calculations. In this case a center-of-mass correction has to be applied to the calculated cross sections [79]:

$$\sigma(J^\pi) = \left(\frac{A}{A-1}\right)^N \sum_j C^2S(J^\pi, n\ell j)\sigma_{sp}(S_N + E_x(J^\pi), n\ell j) \tag{2.86}$$

where N is the major oscillator quantum number shell.

2.3.2 Experimental considerations

Knockout reactions are normally induced from a high-energy secondary beam produced via fragmentation/fission of a heavy primary beam. Therefore, these type of experiments are performed in inverse kinematics, meaning that the projectile is heavier than the target. During the

interaction of the secondary beam and the light target, many multi-nucleon removal reactions can occur and a clean identification of the reaction product is required. The first stage of a typical configuration used to study knockout reactions consists in a spectrometer used to separate the different isotopes of the secondary beam and to transport the isotope(s) of interest. The second stage of the same spectrometer is used to perform the identification of the secondary beam and deliver it to the reaction target where the multi-nucleon removal reactions will take place. A second spectrometer is installed after the reaction target in order to perform the identification of the ^{A-n}X fragments. As the experiments are performed in inverse kinematics, all fragments are emitted in the forward direction, with velocities similar to that of the projectile and small scattering angles, which makes it possible to detect most of the fragments at the same time. A light target is chosen to induce the knockout reactions for two main reasons. The first one is to minimize the Coulomb breakup cross section (third term in the eq. 2.82) which is usually not considered in the eikonal model and depends on the atomic numbers Z of the target and projectile. Therefore, with light targets the reaction can be considered to be mediated only by the strong interaction. The second reason is due to the requirement that the fragment must survive the collision with the target and that the nucleon knockout must occur from a very peripheral collision. This is possible only with light absorptive targets such as ^{9}Be, or ^{12}C. Additionally, at high energies it is possible to use relatively thick targets of the order of hundreds of mg/cm^2, such a thickness increases the yields.

One of the main experimental observables of nucleon removal reactions is the inclusive cross section. This is calculated from the ratio between the number of projectile ions at the entrance of the target and the number of knockout residues at the exit of the target. Additional factors such as the transmission of the fragments through the second spectrometer, the detector efficiency, reaction losses or dead time have to be considered in the determination of the cross sections. For the determination of exclusive cross sections of individual, bound, excited states of the fragment, a γ-ray detection array must be installed surrounding the secondary reaction target. Then the exclusive cross section is determined from the γ-ray yields measured in coincidence with the fragment of interest and considering the possible feeding from higher-lying states. The cross section to the ground state is calculated from the difference between the inclusive cross section and the total exclusive cross sections of the different bound excited states. The experimental spectroscopic factors, C^2S_{exp}, for the one-nucleon removal reaction are derived from the experimental exclusive cross section of a specific orbital and the theoretical single-particle values [79]:

$$C^2S_{exp} = \frac{\sigma_{exp}(J^\pi)}{\sigma_{sp}(S_N + E_x(J^\pi), n\ell j)} \tag{2.87}$$

for the knockout to an odd-A nucleus. For the cases of knockout to odd-odd or even-even nuclei, the final state configurations present mixed configurations and have to be separated into single-particle configurations. The theoretical cross sections are found to be systematically too high for deeply bound nucleons in compassion with the experimental values. A quenching

factor to account for this is defined as:

$$R_s = \frac{\sigma_{exp}}{\sigma_{th}} \tag{2.88}$$

Gade *et al.* [80] reported a correlation between this factor and the asymmetry of the system defined as $\Delta S = \pm(S_n - S_p)$, where the sign $+$ is for neutron knockout and the sign $-$ for proton removal. At the extremes of nuclear binding, this factor is as small as $R_s \approx$ 0.25-0.4.

Another important experimental observable is the momentum distribution of the remaining fragment. In the "sudden approximation" mentioned previously, in the rest frame the modulus of the momentum of the fragment is equal to the momentum of the removed nucleon and with opposite sign [75, 78]. This momentum distribution of the fragment corresponds to the Fourier transform of the radial wave function and the spatial extension of this radial wavefunction depends on the orbital angular momentum of the removed nucleon, ℓ. Again this momentum distribution can be measured in coincidence with discrete γ-ray transitions and, through the comparison of the experimental and theoretical momentum distributions, we can obtain the angular momentum ℓ of the removed nucleon. The experimental momentum distribution is determined by measuring the velocity shift caused by the reaction target while the theoretical one can be obtained from computer programs such as MOMDIS [81].

Chapter 3

Experimental Setup

The experiment reported on this thesis was conducted at the Radioactive Isotope Beam Facility (RIBF), RIKEN, Japan. It took place in April, 2015 and lasted 2.5 days. It was focused on the Coulomb excitation of ^{136}Te and knockout reactions to study excited states of more exotic species. In this chapter, we will describe the steps of the production, separation and identification of the radioactive ion (RI) beam. Additionally, the different experimental components of the setup shall be described in detail: the RIBF accelerating system, the BigRIPS and ZeroDegree spectrometers, the DALI2 scintillator array and the multiple beam-line detectors used to perform the particle identification.

3.1 Radioactive Isotope Beam Factory

The RIBF facility became operational in 2007 at RIKEN Nishina center. The production of the RI beam is based on the in-flight method, in which a stable projectile is accelerated to several hundreds of MeV/nucleon and collides with a primary stable target. This method is capable of producing RI beams of wide variety of elements both proton and neutron rich. Currently, the RIBF provides the most intense RI beams in the world from light to medium masses.

3.1.1 Primary beam production

As previously mentioned, the exotic cocktail is produced through the in-flight mechanism. The RIBF has different primary beams depending on the mass and proton-to-neutron ratio of the exotic nuclei that we want to study. Usually, a ^{238}U beam is used to generate neutron-rich nuclei in the medium mass region, while ^{48}Ca and ^{70}Zn primary beams are used to produce neutron-rich nuclei in lighter-mass regions. In the present experiment, we were interested in studying nuclei in the ^{132}Sn region, therefore, ^{238}U was used as the primary beam. The super conducting electron cyclotron resonance ion source (SC-ECRIS) [82, 83] was used to extract ^{238}U from an uranium compound and provide initial acceleration. After the extraction, the primary beam was transported into the RIBF accelerating system. Figure 3.1 displays a schematic picture of the accelerator setup at RIBF. The RIBF accelerating system has three modes [84]. Mode(1): the

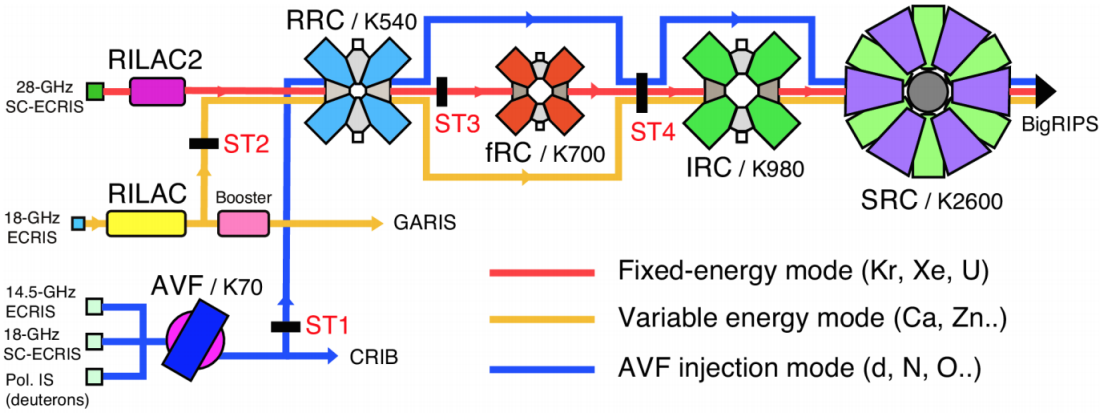

Figure 3.1: Scheme of the RIBF accelerator system indicating the three acceleration modes. The fixed-energy mode was used for the acceleration of ^{238}U at 345 MeV/nucleon. The image is taken from the reference [85].

line RILAC2→RRC→fRC→IRC→SRC is used for the acceleration of the primary beam to a fixed energy of 345 MeV/u (red line of Fig. 3.1). Mode (2): RILAC→RRC→IRC→SRC is used for variable energy experiments (yellow line of Fig. 3.1). Mode (3): AVF→RRC→SRC is used for providing deuteron beams at 880 MeV (blue line of Fig. 3.1). Mode(1) was used in our experiment. Firstly, the ^{238}U beam is injected in RILAC2. At the output of RILAC2, the ^{238}U beam is injected to the RRC of an energy of approximately 670 keV/u. In the RRC, the ^{238}U ions reach energies of 11 MeV/u and are transported to the fRC where they are accelerated up to 50.7 MeV/u. After the fRC, the primary beam enters the IRC where it can reach a maximum energy of 127 MeV/u. The last acceleration stage occurs in the SRC (the first superconducting ring cyclotron with the largest bending power at time of writing) in which the ^{238}U ions are accelerated to 345 MeV/u. After leaving the SRC, the ^{238}U primary beam was guided to the BigRIPS separator, where a 4-mm ^{9}Be target was installed at its entrance. The mean intensity of the ^{238}U beam was 2.5 and 15 pnA for the Coulomb excitation and knockout parts of the experiment, respectively.

3.1.2 Secondary beam production: separation and identification

When the ^{238}U primary beam impinges on the ^{9}Be target, two different reactions can occur, both contribute to the production of the exotic beam [86]. Both reactions are two-step processes:

Fragmentation: this process is dominant at energies above 100 MeV/u. Its reaction mechanism is described with the abrasion-ablation model [87]. In the first step, called abrasion, the ^{238}U beam interacts with the target and abrades nucleons (participants). The remaining nucleons belonging to the primary beam (spectators) continue traveling in the forward direction but gain excitation energy due to the shape change of the abraded fragment. The time scale of this first process is around 10^{-23} s. In the second step, called ablation, the excited remnant nucleus

de-excites by emitting low-energy particles (n, p and γ), or, if possible, by fissioning. The time scale for the de-excitation process is much longer (10^{-16} s) than the abrasion process. Figure 3.2 shows a schematic view of the fragmentation process.

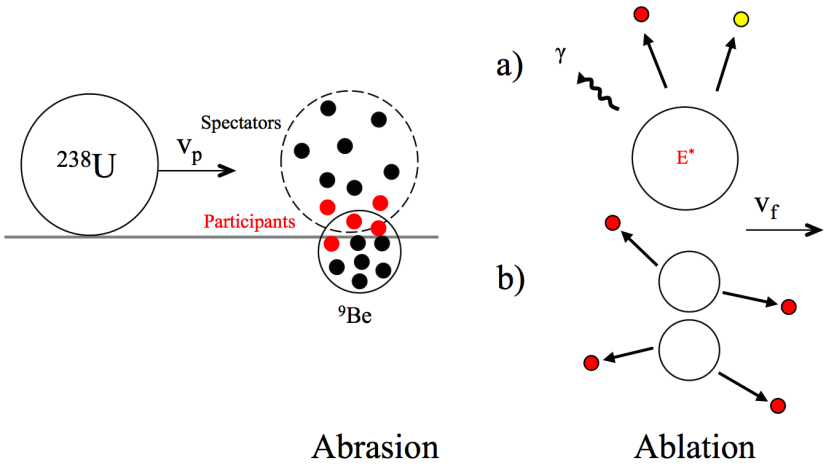

Figure 3.2: Illustration of the fragmentation process. The de-excitation is carried out through the a) emission of low-energy particles, or b) fission and neutron emission. See text for details.

Coulomb fission: this process is dominant at energies around 1 A·GeV with a heavy primary target. Since the energy of our ^{238}U primary beam is 345 MeV/u and we use a light target, it contributes negligibly to the production of the exotic isotopes in this experiment. First, the ^{238}U is Coulomb excited. The Coulomb field of relativistic heavy ions with large proton numbers mainly excites the giant dipole resonance [86]. Then, one, or two neutrons are evaporated after which the uranium will undergo fission. The fission products tend to have similar masses and a neutron-to-proton ratio similar to the primary beam due to shell effects. Figure 3.3 shows a schematic view of the Coulomb-fission process.

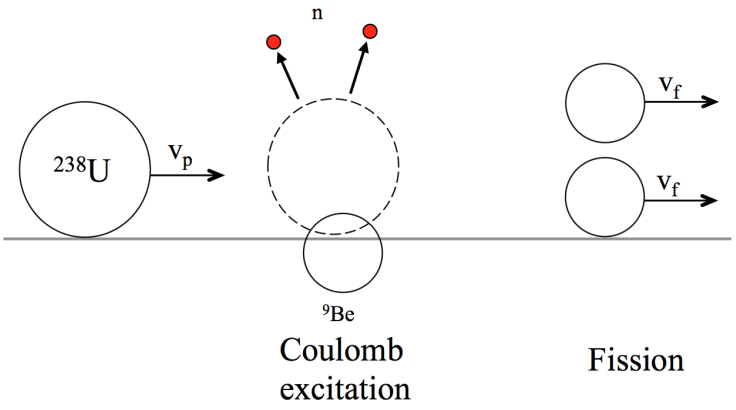

Figure 3.3: Illustration of the Coulomb-fission process. See text for details.

The secondary beam produced in the fragmentation or fission of the ^{238}U primary beam was then delivered to the BigRIPS spectrometer.

3.1.2.1 BigRIPS spectrometer

The Big RIKEN projectile-fragment separator (BigRIPS) [88–90] is characterized by three main features: large ion-optical acceptances, two-stage structure and an excellent particle identification. The large acceptance allows efficient collection of isotopes produced from the fragmentation and fission of a ^{238}U primary beam. This large acceptance is required since the secondary beam is produced with large angular and momentum spreads, particularly after fission. Figure 3.4 shows a schematic of the BigRIPS separator. The first stage of BigRIPS extends from the production target to the F2 focal plane while the second stage starts at the F2 focal plane and ends at F7. Along the beam line there are seven focal planes (labeled as F1-F7), fourteen superconducting triplet quadrupoles (STQs) and six room-temperature dipoles each with a bending angle of 30° (indicated as D1-D6). The length of the BigRIPS separator is 78.2 m, 31.6 m of which corresponds to the first stage and 46.6 m to the second one [90].

The first stage of BigRIPS is used to separate and select the RIB. With the fragmentation and fission of the ^{238}U primary beam, many isotopes with very different masses and neutron-to-proton ratios are produced and we need to select only the nuclei in which we are interested. The separation in the BigRIPS spectrometer is performed following the momentum-loss achromat method ($B\rho$-ΔE-$B\rho$ selection). This method is based on two principles. Firstly, when an ion is moving in a region of a constant magnetic field, B, its trajectory inside this region depends on its mass, A, its charge, Q, and its momentum, P, through the following expression:

$$B\rho = \frac{P}{Q} = \frac{uc}{e}\beta\gamma\frac{A}{Q} \tag{3.1}$$

where ρ is the radius of curvature of the ion, $u \approx 931.5$ MeV the atomic mass unit, c is the speed of light, $\beta = v/c$ and $\gamma = (1-\beta^2)^{-1/2}$ is the Lorentz factor. Isotopes with different A/Q ratios follow different trajectories within the same magnetic field B. Therefore, tuning the magnetic field of the D1 dipole of the first stage of BigRIPS we can perform the first $B\rho$ selection. A high-power beam dump is situated after the first dipole D1 to stop the primary heavy ion beam. The second principle relied upon in the separation of the RIBs, is that the energy loss of a nucleus inside a material depends on its atomic number, Z, through the Bethe-Bloch equation:

$$\Delta E \propto Z^2 f(\beta) \tag{3.2}$$

with $f(\beta)$ being a function that depends on β. A wedge-shaped aluminum degrader was installed after the D1 dipole of thickness at the central trajectory of 6 mm. This degrader, induces isotopic separation. After this degrader, the magnetic field of the D2 dipole is used to perform a second $B\rho$ selection as well as centering the nuclei of interest. In the second stage of the BigRIPS spectrometer, there are 4 dipoles (D3-D6) and eight quadrupoles installed, forming a four-bend achromatic system, which is used to deliver the beam to the F8 focal plane. An additional degrader, 3 mm of Al at the central trajectory, was placed at F5 to improve the separation

of the secondary beam. In addition, vertical and horizontal slits are located along the beam line to block the trajectories of those ions not of interest.

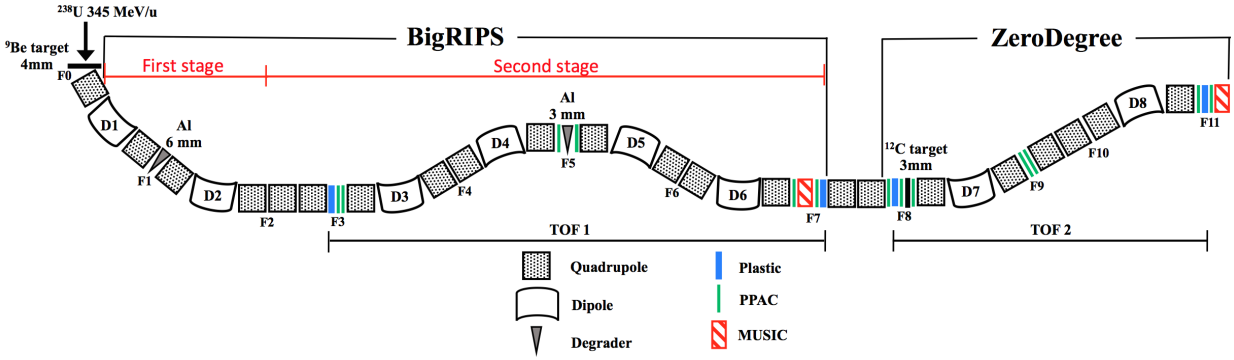

Figure 3.4: Schematic of the BigRIPS and ZeroDegree spectrometers. The two-stage structure of the BigRIPS spectrometer is indicated by the red lines. The different quadrupoles, dipoles and detectors used in the experiment are also labelled in the figure.

Angular acceptances of the BigRIPS spectrometer are $\pm$40 mr horizontally and $\pm$50 mr vertically, while the momentum acceptance is $\pm$3%. The angular and momentum spreads of fragments produced at 345 MeV/u are estimated to be around $\pm$50 mr and $\pm$5%, meaning approximately half of the produced fragments are accepted by the BigRIPS spectrometer. Figure 3.5 shows the ionic separation in the BigRIPS spectrometer calculated by the COSY INFINITY code, it is evident that the focal planes F1, F4, F5 and F6 are momentum dispersive, F2 and F3 are achromatic and F7 is doubly achromatic [84, 90].

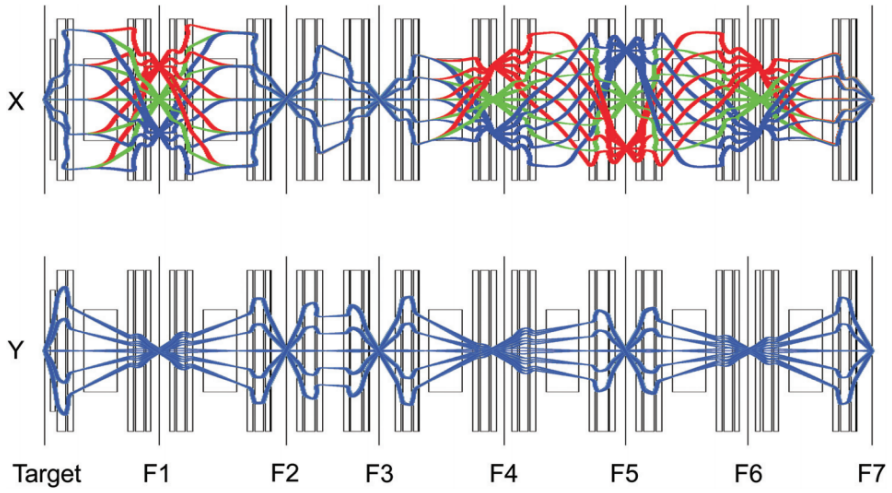

Figure 3.5: First-order ion optics of the BigRIPS separator in the horizontal (top) and vertical (bottom) planes. Source [90].

The second stage of BigRIPS (from F3 to F7) is used to perform the particle identification of the secondary beam. The identification was performed event-by-event by following the TOF-$B\rho$-ΔE method. In this method an ion's mass-to-charge ratio, A/Q, and its atomic number, Z,

are determined by its time of flight (TOF), magnify rigidity ($B\rho$) and energy loss (ΔE). Along the BigRIPS beam line there are several detectors that are used to measure and reconstruct an ion's TOF, $B\rho$ and ΔE. Energy loss is measured with a multi-sampling ionization chamber (MUSIC) installed at the F7 focal plane and TOF is determined as the time difference between two plastic scintillation counters situated at F3 and F7, between which the ions travel a flight path of 46.6 m. The $B\rho$ is reconstructed from the ion's positions and angles measured at the F3, F5 and F7 focal planes. The (x,y,θ,ϕ) coordinates are measured with two sets of position-sensitive double parallel plate avalanche counters (PPACs) installed in the aforementioned focal planes. More details about this method will be given in section 4.1. With this method, an excellent A/Q resolution is achieved which allows unambiguous particle identification. After the identification, the secondary beam was transported to the reaction target.

3.1.2.2 ZeroDegree spectrometer

On the right of Fig 3.4, we show a schematic picture of the ZeroDegree spectrometer. At the F8 focal plane we placed the secondary reaction target with which the RIB will interact. The reaction target was placed on a frame to centralize it with respect to the incident RIB. Two different reaction targets were used, a 948.34-mg/cm^2-thick ^{197}Au target and a 534.44-mg/cm^2-thick ^{12}C target. The gold target was used to induce the Coulomb excitation of the projectiles, since it has a high atomic number (Z=79), while the carbon target, with low atomic number (Z=6), was used to extract the nuclear contribution to the inelastic scattering cross section measured with the Au target. In addition, the carbon target was also used to induce knockout reactions and study the γ rays emitted from the decay of excited states from different fragments. Once the ions exit the secondary target they are separated and identified with the ZeroDegree spectrometer. This spectrometer is a two-bend achromatic system with anti-mirror symmetry. It consists of two dipoles (D7-8) and six STQs. These magnets have been designed with the same characteristics as those of BigRIPS. The total length of the ZeroDegree spectrometer is 36.5 m. Depending on the experimental conditions, the ZeroDegree spectrometer can be configured to different ion-optics modes. For our experiment the standard configuration, known as large acceptance achromatic mode, was used. Figure 3.6 shows the ionic separation of the standard configuration in the ZeroDegree spectrometer calculated, again, with the COSY INFINITY code. We can observe from Fig. 3.6 that the focal planes F9 and F10 are momentum dispersive, while F11 is fully achromatic. With the standard configuration, the angular acceptances of the ZeroDegree spectrometer are $\pm$45 mr horizontally and $\pm$30 mr vertically, while the momentum acceptance is $\pm$3%.

As in BigRIPS, the particle identification in ZeroDegree is achieved following the TOF-$B\rho$-ΔE method, where now the TOF is measured with two plastic scintillator counters installed at F8 and F11, the $B\rho$ values are determined from the positions measured at the F8, F9 and F11 focal planes and ΔE is measured with a MUSIC detector placed at F11. Instead of two PPACs, three

sets of PPACS were installed at the F8 focal plane, two before and one after the secondary target. These PPACs were used to determine the scattering angle of the ions. Lastly, behind the F11 MUSIC, a total kinetic energy (TKE) detector was installed to measure the kinetic energy of the reaction fragments with the aim of improving the particle identification. However, this detector was not used in the analysis.

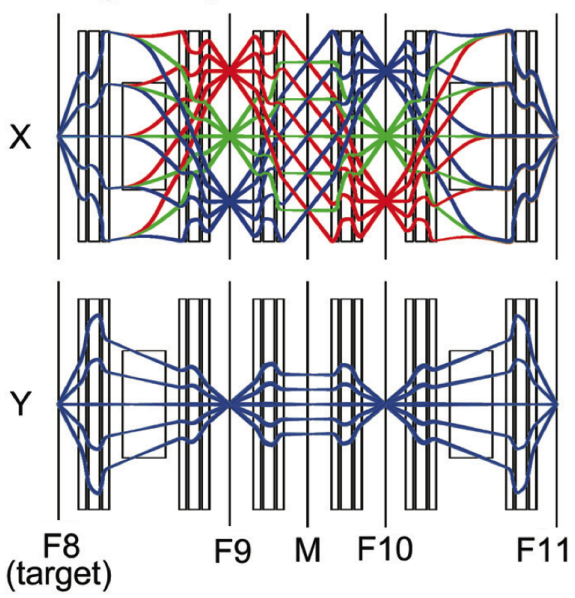

Figure 3.6: First-order ion optics of the large acceptance achromatic mode of the ZeroDegree separator in the horizontal (top) and vertical (bottom) planes. Source [90].

3.2 Beam-line detectors

In this section, we will describe the different detectors positioned along the BigRIPS and ZeroDegree spectrometers which are used for the particle identification. As previously mentioned, the PID is done measuring the ΔE with the MUSIC detector, the TOF is determined with two plastic scintillator counters and $B\rho$ values are obtained from positions and angles measured by the PPACs. Additionally, a TKE detector was placed at the final focus of the ZeroDegree spectrometer. In table 3.1 the detectors installed at the different focal planes are summarized. In the following sections the different types of detectors are described in detail.

3.2.1 Parallel Plate Avalanche Counters (PPACs)

The trajectory of each ion was measured with Parallel Plate Avalanche Counters (PPACs). The use of this type of detector is well established [91, 92]. The basic structure of these detectors is an anode plate located between two cathodes. The PPACs used at the RIBF use 2.5-μm-thick anode films and cathode film thickness of 4 μm. The cathode is formed by 2.4-mm wide strips with 0.15-mm inter-strip-spacing. The number of strips is 40 in both X and Y directions, resulting in an effective area of 240 mm x 150 mm. The spacing between the anode and

cathode electrodes is 4.3 mm [93]. Figure 3.7 shows a schematic view of one PPAC (left) and a photograph of two of the PPACs used in our experiment (right).

Table 3.1: Locations of the detectors used for the particle identification along the BigRIPS and ZeroDegree spectrometers.

Detector	Focal planes
PPAC (x2)	F3, F5, F7, F9 and F11
PPAC (x3)	F8
Plastic scintillator	F3, F7, F8 and F11
MUSIC	F7 and F11
TKE	F11

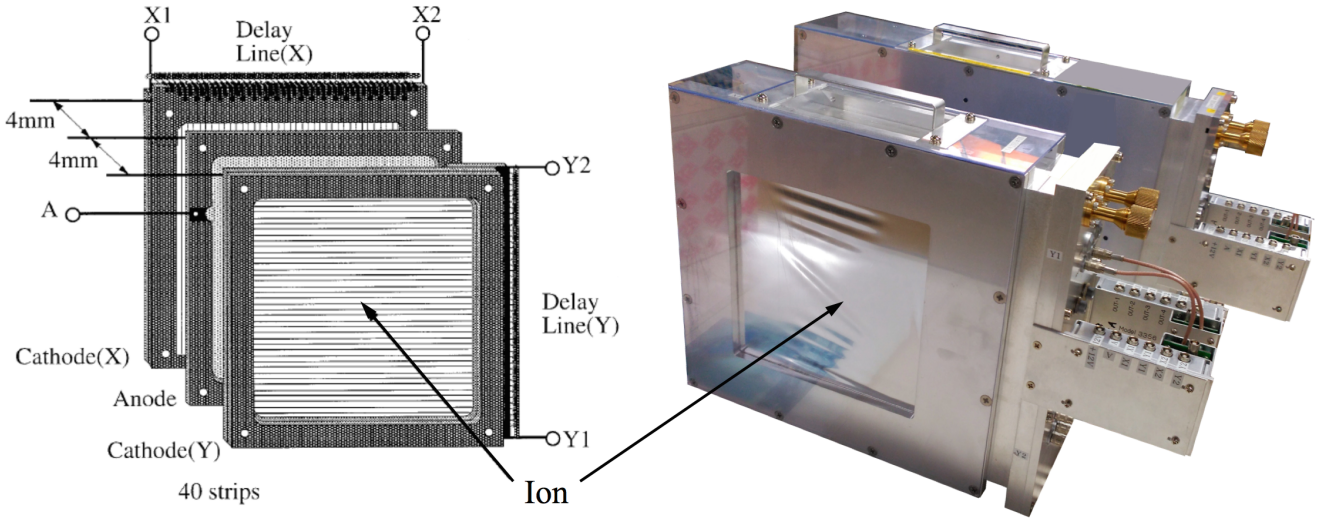

Figure 3.7: Left: schematic view of the PPAC. The image is taken from Ref. [94]. Right: photograph of two sets of double PPACs used during the experiment.

The anode and cathode were encapsulated in a chamber filled with a perfluoropropane (C_3F_8) gas. The advantages of using this gas are a large energy deposition of the ion when passing through it, a fast rise time of the signal and it is not flammable. A voltage of around 700 V was applied between the anode and the cathode. When an ion traverses the gas, it ionizes C_3F_8 molecules, the liberated electrons motion due to the voltage induces an electron avalanche. The avalanches are terminated at their respective cathode strips which are connected to multi-tapped delay lines. The cathode signals are separated into right and left (and up and down) directions shown as X1 and X2 (and Y1 and Y2) in Fig. 3.7 and the delay time is determined with a time-to-digital converter (TDC). The positions can be calculated from the difference of

delay times using the following expressions [93, 94]:

$$X = k_x \frac{T_{x1} - T_{x2}}{2} + X_{off} \qquad Y = k_y \frac{T_{y1} - T_{y2}}{2} + Y_{off} \tag{3.3}$$

where k_x and k_y are the slope factors for the X and Y delay-lines, T_{x1} and T_{x2} (T_{y1} and T_{y2}) are the delay-times between the two signals in the X (Y) direction, and X_{off} and Y_{off} are geometrical offsets. The sum of the delay times, $T_{sum} = T_1 + T_2$, is a constant value and can be used to remove inconsistent events detected in the PPACs.

Two sets of double PPACs were situated at the F3, F5, F7, F9 and F11 focal planes, while the F8 focal planes had an extra double PPAC used to determine the scattering angle of ions off the secondary target. This configuration allows for a twofold position measurement and an efficiency of around 100%. The focal plane position uncertainty reduces with the number of valid PPAC position measurement, consequently enhancing its resolution. Furthermore we can discriminate inconsistent events through correlations between the different PPACs.

3.2.2 Plastic scintillators

The time of flight in both BigRIPS and ZeroDegree was measured using two thin plastic scintillator counters. These detectors were chosen due to their fast timing properties [95]. In the case of BigRIPS, the two plastics were placed at the F3 and F7 focal planes (distance of flight 46.6 m), while in ZeroDegree they were installed at F8 and F11 (flight distance, 36.5 m). The thickness of each plastic was 0.2 mm. The scintillation photons that constitute the signal produced when the ion traverses the plastic scintillator are collected with two photomultiplier tubes (PMT), one of them coupled to the left side and the other one to the right side of the plastic. The amplified signal is converted into charge and time measurements with the help of a QDC and a TDC, respectively. The time signal in each of the focal planes is given by:

$$T_{focal\ plane} = \frac{t_R + t_L}{2} \tag{3.4}$$

where t_L and t_R are the timing signals from the left and right PMTs, respectively. Averaging the left and right times, the position dependence of the ion hit is eliminated. The TOFs in BigRIPS and ZeroDegree are given by:

$$\begin{aligned} TOF_{BigRIPS} &= T_{F7} - T_{F3} + offset_{37} \\ TOF_{ZeroDegree} &= T_{F11} - T_{F8} + offset_{811} \end{aligned} \tag{3.5}$$

where the offset parameters are experimentally determined.

3.2.3 Multi-sampling ionization chamber (MUSIC)

Multiple sampling ionization chambers (MUSICs) were used to measure the energy loss, ΔE, of the incident particles. This type of detector has been widely applied for particle identification

of high-energy heavy ions [96, 97]. The ΔE detectors requiere excellent energy resolution and high counting rate capacity. The MUSIC detectors used at the RIBF [98] consist of twelve anode planes and thirteen cathode planes which are alternately placed in 20-mm steps resulting in a 48-cm chamber. Figure 3.8 displays a schematic of the detector. The chamber is filled with a gas mixture (Ar 90%+CH_4 10%), which is ionized as an ion passes through it, creating pairs of electrons and positive ions along its trajectory. A voltage is applied (around 500 V) between the anode and cathodes to which the electrons and positive ions are attracted to, respectively. As shown in Fig. 3.8, the anodes and cathodes are tilted by 30° to avoid the recombination of electrons and positive ions, since the electrons and positive ions drift in opposition directions. Since the time for the electron drift is lower than the time for the drift of positive ions (100 ns compared to 1 ms), only the signal generated in the anode was read out. Therefore, all cathode electrodes were connected together and grounded, while pairs of anode plates were connected together and six separate signals were generated and read by six channels of a peak-sensitive ADC.

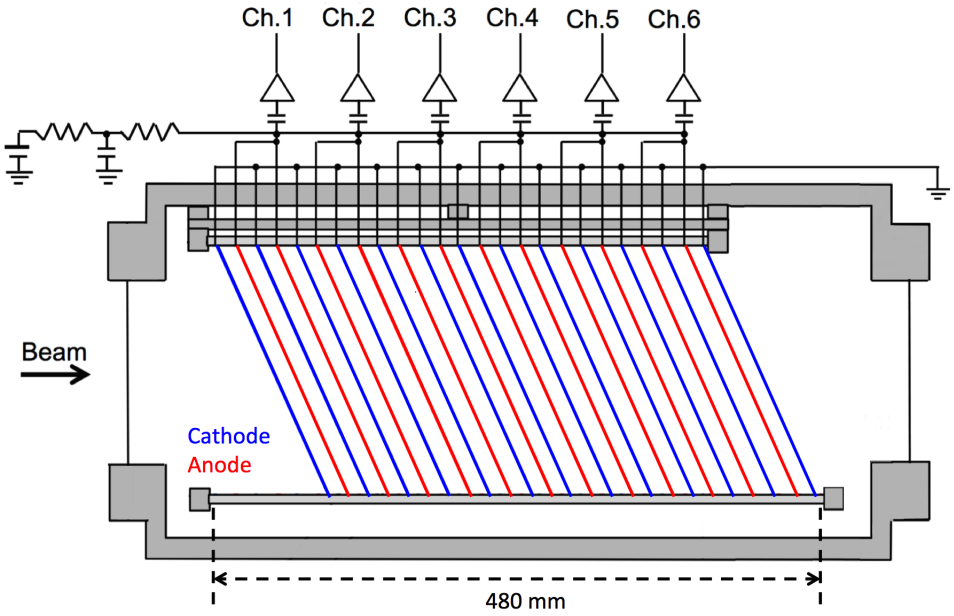

Figure 3.8: Schematic view of the MUSIC detector used at the RIBF for the measurement of the energy loss.

Two different MUSIC detectors were used in the present experiment. The first one, placed at the F7 focal plane, was used to measure the energy loss of the incoming ions in BigRIPS while the second one, installed at the F11 focal plane, was used to determine the ΔE of the outgoing products in ZeroDegree. In both MUSICs, the ΔE of each ion was obtained as the average of the six signals of each anode. The geometric and arithmetic averages were used to determine ΔE:

$$\Delta E_{Geo} = \Big(\prod_{i=1}^{6} \Delta E_i\Big)^{1/6} \qquad \Delta E_{Arith} = \frac{1}{6}\Big(\sum_{i=1}^{6} \Delta E_i\Big) \tag{3.6}$$

where ΔE_i is the signal from the i^{th} anode. The geometric average was used to determine ΔE since with it naturally removes background events in which an ion is stopped within the chamber, causing the signal of the subsequent anodes to be zero and therefore $\Delta E_{Geo} = 0$.

3.2.4 Total kinetic energy (TKE)

In order to improve the quality of the particle identification in the ZeroDegree spectrometer, a total kinetic energy (TKE) detector was installed downstream of the F11 MUSIC. From the total kinetic energy an ion deposits into the detector it is possible to determine its mass number, A. This kind of detector is primarily used in the heavy ion region, A$\geq$100, where the mass-to-charge ratios of several fully stripped and hydrogen-like isotopes are very similar and the TOF-$B\rho$-Δ-E method is not sufficient to distinguish them [99]. Because of the high counting rate at F11, the detector must have a short decay time and be resilient to radiation damage. For this reason, a $LaBr_3$(Ce) scintillator detector (Fig. 3.9) with a fast light-decay time ($\sim$ 15 ns) was used. The light signal generated when the ion stopped inside the detector was read-out with a PMT. Unlike the light yield for γ rays which is almost proportional to energy, the light yield for heavy ions does not follow a simple relationship. In the case of heavy ions, the light yield per energy deposition of the incident beam decreases as a function of Z, so that to optimize the use of this type of detector the degree of the quenching phenomenon must be well known. Finally, the quality achieved in the particle identification in the ZeroDegree spectrometer was good enough to separate the different charge states and we did not use this detector in the analysis. However, this detector has been successfully used in other RIBF experiments [100, 101].

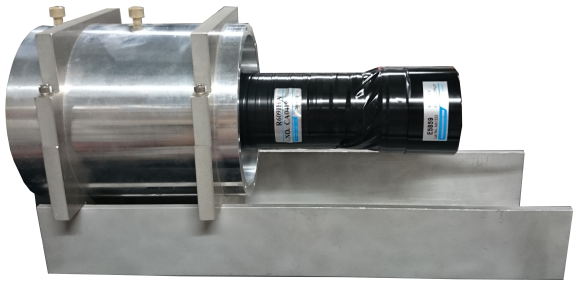

Figure 3.9: Total kinetic energy (TKE) detector used in the experiment.

3.3 Detector for in-beam γ-ray spectroscopy

Placed at the F8 focal plane and surrounding the secondary target, a γ-ray spectrometer was installed in order to detect γ rays emitted by the decay of excited states in several isotopes. This spectrometer is called DALI2 and is explained in this section.

3.3.1 DALI2

The Detector Array for Low Intensity radiation 2 (DALI2) spectrometer is an array formed of 186 NaI(Tl) detectors. Its configuration is based on the original DALI array [102] but with improvements for the detection of γ rays emitted with velocities around β=0.6. The array covers polar angles in the range of 20° to 150° and is composed of three different types of crystal. The first type consists of 88 crystals manufactured by Saint-Gobain with a volume of 45x80x160 mm^3, the second type is composed of 66 crystals manufactured by Scionix with dimensions of 40x80x160 mm^3 and, lastly, the third type, with 32 crystals, fabricated by Bicron with a volume of 60x60x120 mm^3. Each DALI2 crystal is encapsulated in a 1-mm-thick aluminum housing and coupled to a HAMAMATSU PMT. The first 122 crystals are distributed in eleven layers set perpendicularly to the beam axis, while the remaining 64 detectors are installed in a forward wall [103, 104]. Figure 3.10 shows a schematic DALI2 view obtained with the GEANT4 code (left) and a picture of the DALI2 array looking downstream (right). A beam pipe enclosed by 1-mm lead and 1-mm tin shields is installed inside the DALI2 spectrometer (green tube in Fig. 3.10) with the aim of stopping atomic background and radiation with very low energy.

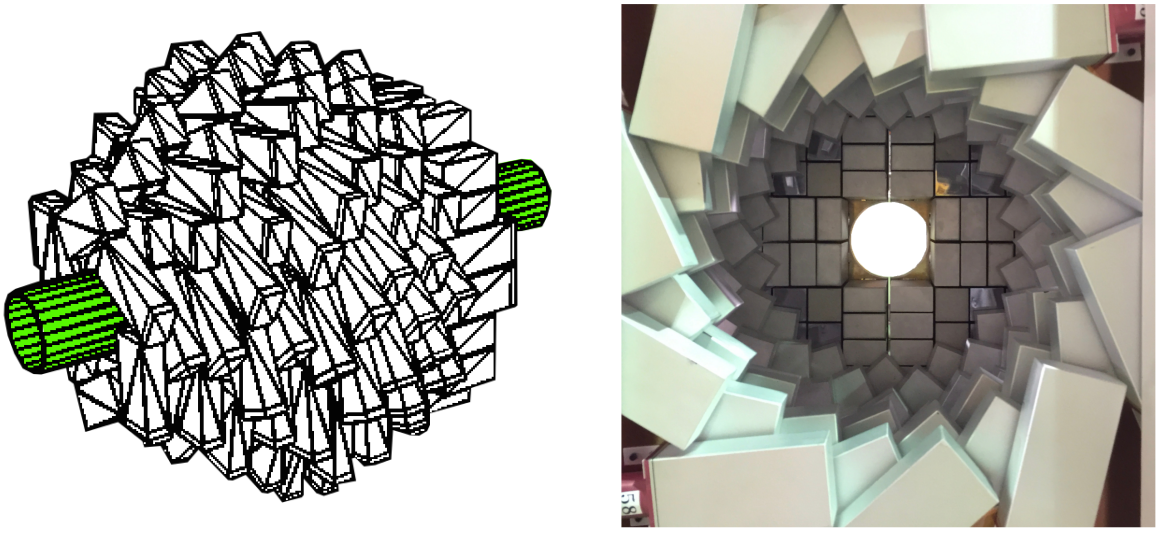

Figure 3.10: Left: schematic view of the DALI2 array. The secondary beam crosses the array from the left to the right. Right: picture of DALI2 looking downstream through the array.

High voltage was applied to each PMT, such that all PMTs had the same gain. To achieve the gain-matched condition, a ^{137}Cs source was placed inside the DALI2 array and we observed the amplified peak signal of the 662-keV transition with an oscilloscope. The voltage of each PMT was selected to produce the same amplitude of the signal. The amplification of the PMT signal was performed with a shaping amplifier which split it into two signals, one for energy and one for time measurements. The energy branch was delivered to a peak-sensing analog to digital converter (ADC) while the time signals were processed by a constant-fraction discriminator (CFD) and delivered to a time-to-digital converter (TDC). In order to suppress low-energy

background events, a threshold of 150-200 keV was applied to the CFD.

The standard configuration of the DALI2 array offers a reasonably good angular resolution and a high detection efficiency necessary to study secondary beams far from stability. As the energy of γ rays emitted at velocities $\beta \simeq$0.3-0.6 are Doppler shifted, the high granularity of DALI2 is required to perform a precise Doppler correction. Besides that, due to the Lorentz boost, the γ-ray angular distribution in the laboratory system is enhanced in the forward direction necessitating the forward wall. Below, we will describe the spectral aspects of the DALI2 array such as its γ-ray response, Doppler correction, energy resolution and γ-ray efficiency.

Figure 3.11 displays the DALI2 response function for the detection of 2.5 MeV γ rays emitted at rest. This DALI2 response was generated with a GEANT4 [105] simulation which will be described in the following chapter. A threshold of 150 keV was incorporated to the GEANT4 simulation. The spectrum shows different components which will be explained now [95]:

■: the photopeak is produced when the incident γ ray is converted to an electron through the photoelectric process. The electron carries off the full energy of the γ ray and, therefore, the position of the photopeak corresponds to the energy of the γ ray.

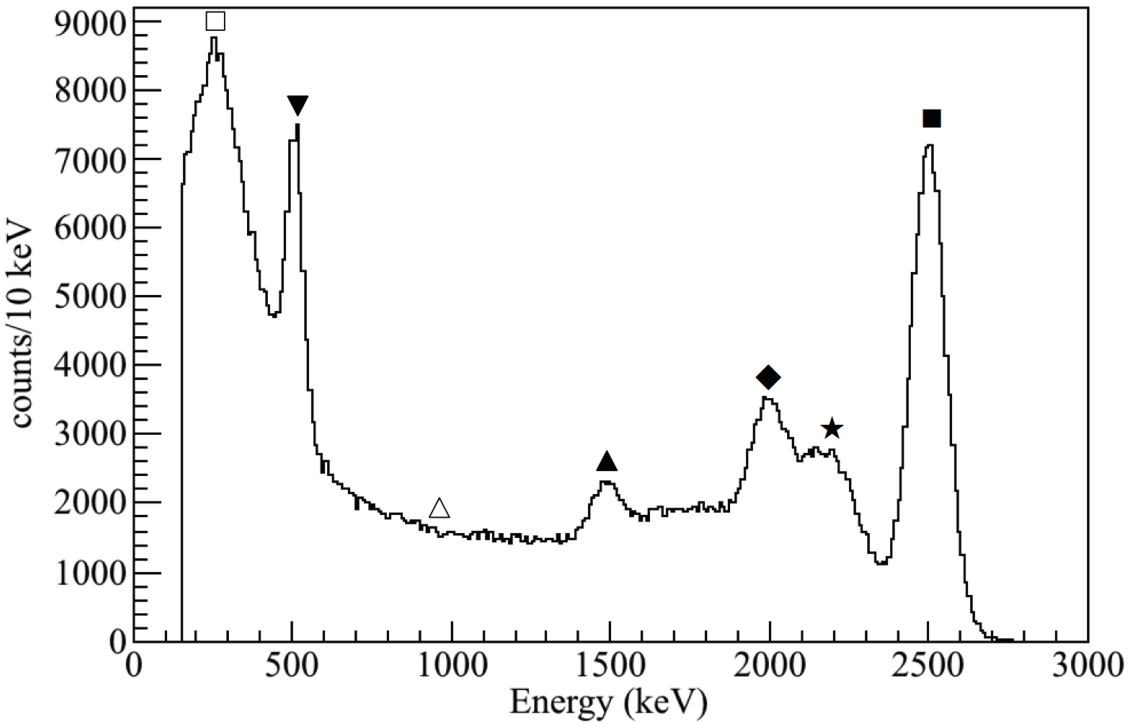

Figure 3.11: Simulated DALI2 response function for a γ ray with an energy of 2.5 MeV emitted by a source at rest ($\beta = 0$). The symbols on the spectrum indicate the most important parts of the spectrum and are explained in the text.

△: the γ ray can suffer Compton scattering with the electrons of the crystal. The result of this interaction is the creation of a scattered photon and a recoil electron. The energies of the γ ray and the electron are given by:

$$E'_\gamma = \frac{E_\gamma}{1 + \frac{E_\gamma}{m_e c^2}(1 - cos\theta)} \qquad E_e^- = E_\gamma - E'_\gamma \tag{3.7}$$

where E_γ is the initial energy of the γ ray (2.5 MeV in the present case), m_e is the electron rest mass and θ is the scattering angle. Therefore, a continuum of energies is transferred to the electron, this behavior observed as the continuum below the symbol, △. The maximum energy transferred to the electron is given when the energy of the scattered photon is minimum ($\theta = \pi$):

$$E_{e^-\ max} = E_\gamma - \frac{E_\gamma}{1 + \frac{2E_\gamma}{m_e c^2}} \tag{3.8}$$

For the γ ray at 2.5 MeV, this maximum, called the Compton edge, is placed at 2.27 MeV and is represented by the symbol ★ in the Fig. 3.11.

▲: for γ rays with energies higher than $2m_ec^2$ (1.02 MeV), pair production is also a significant process. In this interaction, an electron-positron pair is created from the γ ray, where the excess in energy is transferred to the electron-positron pair as kinetic energy:

$$E_{e^+} + E_{e^-} = E_\gamma - 2m_e c^2 \tag{3.9}$$

As a consequence of this process and once the positron has been annihilated and the two photons with energies of 0.511 MeV escape outside the detector, a peak with an energy of $E = E_\gamma - 2m_e c^2$ is observed in the spectrum. This peak is called the double escape peak and for the γ ray with an energy of 2.5 MeV is placed at 1.478 MeV (symbol ▲).

♦: when pair production takes place, once the kinetic energy of the positron is very low, it will annihilate with an electron and create a pair of photons each with an energy of 0.511 MeV. If both photons escape outside the detector, the double escape peak will appear in the spectrum. However, it is also possible that one of the annihilation photons is totally absorbed in the detector, leading to the single escape peak at an energy of E_γ-0.511 MeV. For the case of a 2.5 MeV γ ray, the single escape peak is situated at 1.99 MeV, as denoted by the symbol ♦.

▼: the peak at 0.511 MeV is produced when one of the photons emitted in the annihilation of a positron escapes and is detected in another detector of the array.

□: the peak positioned between 0.2-0.25 MeV is called the backscatter peak. It is produced when a γ ray first interacts by Compton scattering with any of the materials surrounding the detector, or another detector. From eq. 3.7, we can extract that scattering angles greater than

110°-120° produce scattering photons with a nearly identical energy independently of the initial energy of the photon. Therefore the backscatter peak always occurs at an energy of 0.25 MeV or less.

When the γ-ray source is moving at high velocities, as is the case at the RIBF facility where the typical velocities are $\beta \simeq$0.3-0.6, the observed γ-ray energy in the laboratory system, E_{lab}, is shifted relative to the γ-ray energy in the center-of-mass system, E_{CM}, in which the source is at rest. These energies are related through the following expression:

$$E_{CM} = \gamma(1 - \beta cos\theta_{lab})E_{lab} \tag{3.10}$$

where θ_{lab}, β and γ are the γ-ray emission angle, the velocity of the source and the Lorentz factor, respectively. How to perform the Doppler correction of the γ-ray energy spectrum measured with DALI2 will be explained in the following chapter. The energy resolution of γ rays emitted in flight is given by [103, 104]:

$$\left(\frac{\Delta E_{CM}}{E_{CM}}\right)^2 = \underbrace{\left(\frac{\beta sin\theta_{lab}}{1 - \beta cos\theta_{lab}}\right)^2 (\Delta\theta_{lab})^2}_{Angular\ resolution} + \underbrace{\left(\frac{\beta - cos\theta_{lab}}{(1-\beta^2)(1 - \beta cos\theta_{lab})}\right)^2 (\Delta\beta)^2}_{Uncertainty\ beam\ velocity} + \underbrace{\left(\frac{\Delta E_{lab}}{E_{lab}}\right)^2}_{Intrinsic\ resolution} \tag{3.11}$$

The first term is related to the uncertainty in the detection angle of the γ ray and depends on the solid angle of the detector. The second term represents the uncertainty of the beam velocity and is due to the beam-energy spread and target thickness. Finally, the third term reflects the intrinsic energy resolution of the array (resolution when the emission occurs at rest). Figure 3.12 displays the energy resolution as a function of the emission angle for a 1-MeV γ ray emitted from a source moving with a velocity of $\beta = 0.5$ at the moment of the emission. An uncertainty in the emission angle and a velocity spread of 7° (FWHM) and $\Delta\beta/\beta$=0.1 were considered in the calculation, respectively. Regarding the intrinsic energy resolution, as will be shown in the next chapter, it follows a square root dependence with the energy, i.e, ΔE_{lab} = 2.3$\sqrt{E}$. As can be seen from Fig. 3.12, the relative resolution is better for low θ_{lab} angles, although the overall contribution follows the same behavior as the intrinsic resolution.

The energy resolution and the photopeak efficiency of the array for the γ-ray emission at rest were obtained with standard ^{60}Co, ^{88}Y and ^{137}Cs sources. In the next chapter we will show the experimental and simulated values for the energy resolution and the photopeak efficiency. However, for the case of the in-flight γ-ray emission, due to the Lorentz boost and other experimental aspects, it is very complicated to obtain efficiencies. For this reason, the expected resolution and the efficiency of the array for in-flight γ-emission were estimated using the GEANT4 code. Figure 3.13 shows the energy resolution and the photopeak efficiency as a function of the energy of the γ ray as obtained with GEANT4 [105]. In this plot, the γ emission takes place from a ^{136}Te beam at β=0.5. A square root dependence of the intrinsic resolution with the energy

($\Delta E_{intr} = a \cdot E_{\gamma}^{0.5}$(keV)) was used. As is visible in the plot, the photopeak efficiency decreases and the energy resolution worsens with the increase of the energy. Moreover, the photopeak efficiency does not depend on the beam velocity and is only sensitive to the γ-ray energy and its angular distribution [104].

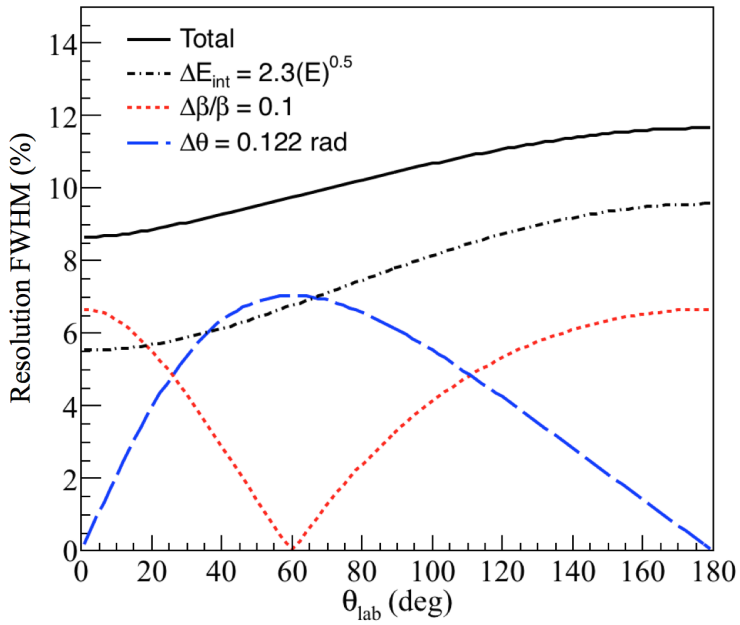

Figure 3.12: Doppler broadening of a γ ray with an energy of 1 MeV in the center-of-mass system as a function of γ-ray emission angle, θ_{lab} (black solid curve). The contribution stemming from the detector opening angle (blue dashed curve), the uncertainty in the velocity (red dashed line) and the intrinsic resolution (black dashed-point line) are also included.

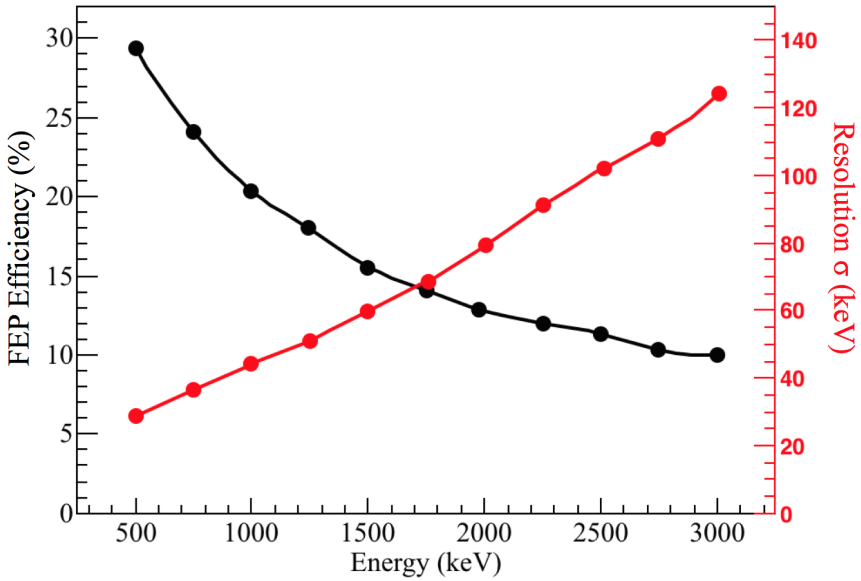

Figure 3.13: DALI2 simulated photo-peak efficiency (black) and energy resolution σ (red). The γ rays are emitted from a beam of ^{136}Te moving at β=0.5. No addback was applied.

3.4 Data Acquisition and Trigger

The information provided by all detectors installed along the BigRIPS and ZeroDegree spectrometers was processed with a data-acquisition system called ”RIBF DAQ” [106]. Due to the large number of detectors and electronic channels, there is a large data throughput. To reduce dead time and use disk space efficiently it is necessary to have a fast and intelligently designed DAQ system. The main features of the RIBF DAQ are that it can provide hierarchical event building online and parallel data readout of all beam-line detectors from their front-end computers (FECs). It is worth mentioning that all these functions are performed with commercial computers, network equipment and standard VME and CAMAC modules. The whole DAQ system is organized into different sub-DAQ systems, each one of them with its own event builder, and all connected by the master event builder.

Due to the large number of CAMAC and VME modules associated with the detectors, a common trigger is required in order to determine the dead time of the system. The common trigger logic was performed with a General Trigger Operator (GTO). The GTO receives the End-of-Busy signals from the different FECs of each detector and the next event does not start until the GTO receives all the End-of-Busy signals. Finally, the dead time of the system is determined by the slowest FEC. In our experiment, the slowest FEC (200 μs) corresponded to a beam-line detector while the dead time of DALI2 was around 100 μs.

With the aim of selecting the events of interest, some specific trigger conditions were used to initialize the data acquisition (Fig. 3.14 displays a diagram of the trigger configuration used during the experiment):

F7DS trigger: this trigger is generated when the ion produces a signal in the F7 plastic detector. Then, the signal is input into a rate divider module, where the total number of signals is downscaled (DS) by a factor due to the high secondary beam intensity.

F7DSxF11 trigger: if besides the F7 plastic signal the ion also produces a signal in the F11 plastic detector, the F7DSxF11 trigger is generated which means that the ion reached the end of the ZeroDegree spectrometer.

F7DSxF11xDALI2 trigger: if in addition to the F7 and F11 plastics signals, at least one γ ray is detected in DALI2, the F7DSxF11xDALI2 trigger is activated.

F7xF11xDALI2 trigger: same trigger as before but without the downscaling of the F7 plastic signal.

3.5 Settings and run conditions

The experiment was carried out over 2.5 days employing three different BigRIPS and ZeroDegree settings. The first setting used the gold and carbon targets, while the other two were only performed with the carbon target. The secondary beam was always produced from a primary beam of ^{238}U at 345 MeV/u, but for the first setting, where the secondary beam was less exotic, the primary intensity had to be limited due to the rate limit of the beam-line detectors. Also, the down-scale factor of the F7 trigger was changed from 1/60 for the first setting to 1/40 for the other two. Table 3.2 shows a summary of the parameters used for each setting. The optimization of these parameters was performed prior to the experiment using LISE^{++} simulations [107]. The experiment ran without problem during the 2.5 days. During beam stoppages DALI2 energy calibrations were made.

Table 3.2: Summary of the conditions of the three different BigRIPS and ZeroDegree settings.

	Setting 1	Setting 2	Setting 3
Primary beam	^{238}U	^{238}U	^{238}U
Primary intensity (pnA)	2.5	15	15
Beam energy (MeV/u)	345	345	345
Production target	^{9}Be 4 mm	^{9}Be 4 mm	^{9}Be 4 mm
Bρ_{01} (D1) (T.m)	7.500	7.500	7.500
Degrader at F1	Al 6 mm	Al 6 mm	Al 6 mm
F1 slits (mm)	[-47.1,64.2]	[-15,64.2]	[-10,64.2]
Bρ_{12} (D2) (T.m)	6.2658	6.2658	6.2658
F2 slits (mm)	[-2,3]	[-3,3]	[-3.5,3]
Bρ_{35} (D3,D4) (T.m)	6.2178	6.2178	6.2178
Degrader at F5	Al 3 mm	Al 3 mm	Al 3 mm
F5 slits (mm)	[-120,120]	[-120,120]	[-120,120]
Bρ_{57} (D5,D6) (T.m)	5.3721	5.3721	5.3721
F7 slits (mm)	[-50,50]	[-50,50]	[-50,50]
F7DS factor	1/60	1/40	1/40
Bρ_{89} (D7) (T.m)	4.0897	4.221	4.221
Bρ_{1011} (D8) (T.m)	4.0502	4.194	4.194
Target	Au and C	C	C
Run duration (h)	13 and 4	9	13

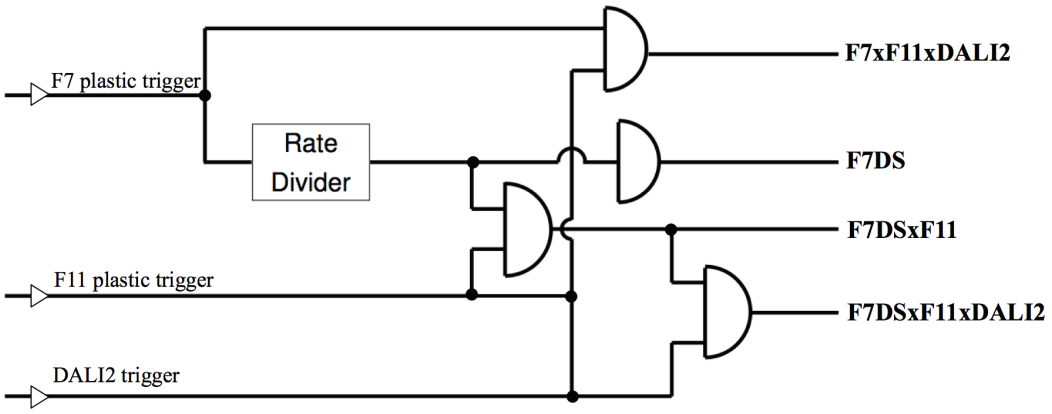

Figure 3.14: Schematic view of the trigger configuration used during the experiment. Two different scaling factors of 40 and 60 were employed by the rate divider module during different parts of the experiment.

Chapter 4

Data analysis

In this chapter, we will describe the data analysis procedures employed to obtain the experimental quantities of interest. Firstly, the particle identification method for the incoming (BigRIPS) and outgoing (ZeroDegree) ions will be explained, as well as its optimization to improve A/Q and Z resolutions. Secondly, the analysis related to the DALI2 array will be discussed in terms of its energy and time calibration, efficiency calibration, Doppler correction, the addback algorithm and the GEANT4 simulations of the array. Finally, we will describe the procedure to obtain the scattering angle of ions off the secondary target and the associated F8-PPAC calibrations.

4.1 Particle identification

The particle identification of the incoming ions impinging on the reaction target was performed with the BigRIPS spectrometer while the identification of the outgoing fragments produced in the secondary target was carried out with the ZeroDegree spectrometer. In both cases, the particle identification was performed event-by-event using the TOF-Bρ-ΔE method.

4.1.1 TOF-Bρ-ΔE method

The particle identification procedure used at the RIBF is based on the TOF-B$_\rho$-ΔE method. With this method, an ion's mass-to-charge ratio, A/Q, and its atomic number, Z, are deduced from its time of flight (TOF), magnetic rigidity (Bρ), and energy loss (ΔE) using the following equations:

$$TOF = \frac{L}{\beta c} \tag{4.1}$$

$$B\rho = \frac{\beta\gamma m_u}{c}\frac{A}{Q} \tag{4.2}$$

$$\Delta E = \frac{4\pi e^4 Z^2}{m_e v^2} N z \Big[ln\frac{2m_e v^2}{I} - ln(1-\beta^2) - \beta^2 \Big] \tag{4.3}$$

In the eqs. 4.1-4.3, L is the flight-path length, $\beta = v/c$ is the velocity of the ion, $\gamma = 1/\sqrt{1-\beta^2}$ is the Lorentz factor, $m_u = 931.494$ MeV is the atomic mass unit, m_e is the electron mass and e is the elementary charge. N, z and I are the atomic density, the atomic number and the mean excitation potential of the counter gas of the MUSIC detector, respectively. Z and A/Q are the atomic number and mass to charge ratio of the ion, respectively. The A and Q numbers can not be deduced separately since the total kinetic energy is not measured with this method.

4.1.2 Particle identification in BigRIPS

The particle identification in the BigRIPS spectrometer starts at the F3 focal plane and ends at the F7 focal plane. The Bρ values are deduced from the position measurements from the double PPAC detector configurations situated at the F3, F5 and F7 focal planes. The TOF is measured with two plastic scintillation counters installed at F3 and F7, with the central flight-path between them being 46.6 m. Energy loss, necessary to deduce the Z of the ion, was measured in the MUSIC placed at the F7 focal plane. Applying eqs. 4.1-4.3 to the measurements made in the BigRIPS spectrometer, we obtain the following expressions:

$$TOF = \frac{L_{35}}{\beta_{35}c} + \frac{L_{57}}{\beta_{57}c} \tag{4.4}$$

$$\left(\frac{A}{Q}\right)_{35} = \frac{B\rho_{35}}{\beta_{35}\gamma_{35}}\frac{c}{m_u} \tag{4.5}$$

$$\left(\frac{A}{Q}\right)_{57} = \frac{B\rho_{57}}{\beta_{57}\gamma_{57}}\frac{c}{m_u} \tag{4.6}$$

$$Z = C_1\beta_{57}c\sqrt{\frac{\Delta E}{\left[ln(\frac{2m_ec^2}{I}\beta_{57}^2) - ln(1-\beta_{57}^2) - \beta_{57}^2\right]}} + C_2 \tag{4.7}$$

where the subscripts 35 and 57 correspond to the quantities measured in the F3-F5 and F5-F7 subsections of BigRIPS, respectively. We need to separate the F3-F5 and F5-F7 measurements since an energy degrader was placed at F5, which changes the velocity of the ions. Assuming no charge state change at F5, the A/Q ratio determined in F3-F5 and F5-F7 will be equal, and therefore, from eqs. 4.5 and 4.6:

$$\frac{\beta_{35}\gamma_{35}}{\beta_{57}\gamma_{57}} = \frac{B\rho_{35}}{B\rho_{57}} \tag{4.8}$$

Combining the eqs. 4.4 and 4.8 we can obtain the velocities β_{35} and β_{57} from the Bρ_{35}, Bρ_{57} and TOF measurements, providing all the necessary variables to deduce the Z and A/Q numbers. Figure 4.1 a) shows the energy loss in the F7 MUSIC, Fig. 4.1 b) displays the β_{57} parameter and Fig. 4.1 c) shows the energy loss in the F7 MUSIC as a function of the TOF between the F3 and F7 focal planes. In Fig. 4.1 c), the different distributions correspond to different atomic numbers, Z. Figures 4.2 a) and b) show the uncorrected spectra of atomic number, Z, and the

A/Q ratio of each ion measured in BigRIPS, respectively.

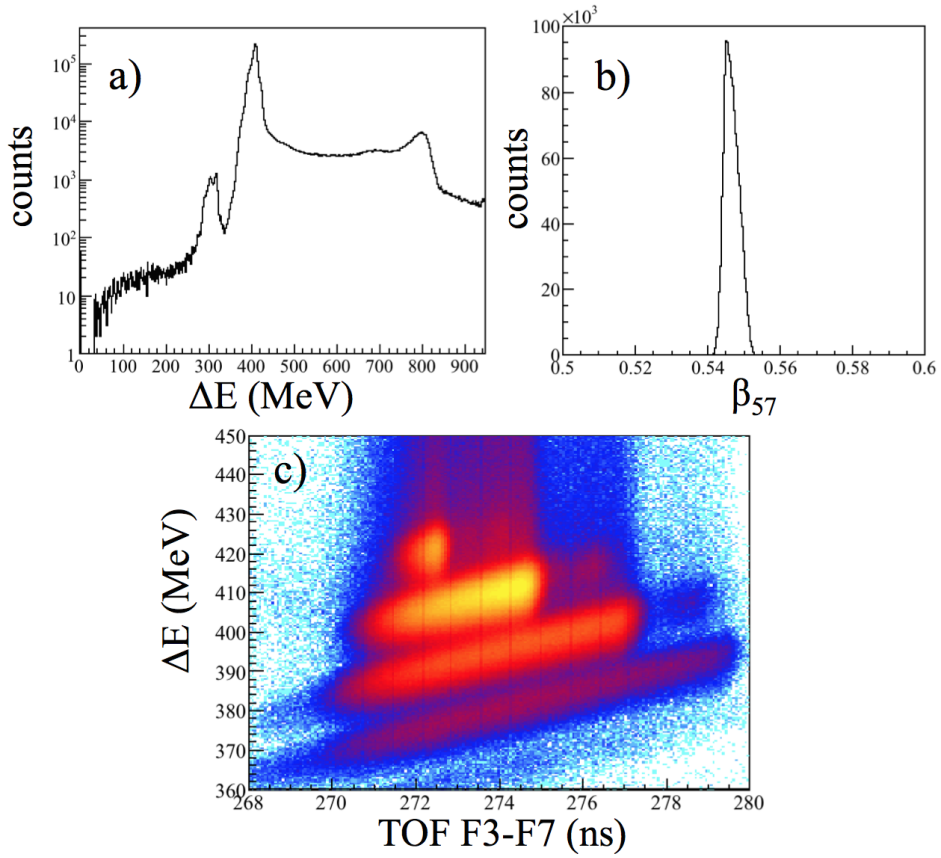

Figure 4.1: a) Energy loss (in MeV) in the F7 MUSIC detector. b) Velocity β_{57} of the ions after passing through the F5 degrader. c) Energy loss in the F7 MUSIC as a function of the TOF between the F3 and F7 focal planes. All these parameters were used to deduce the Z and A/Q numbers in BigRIPS.

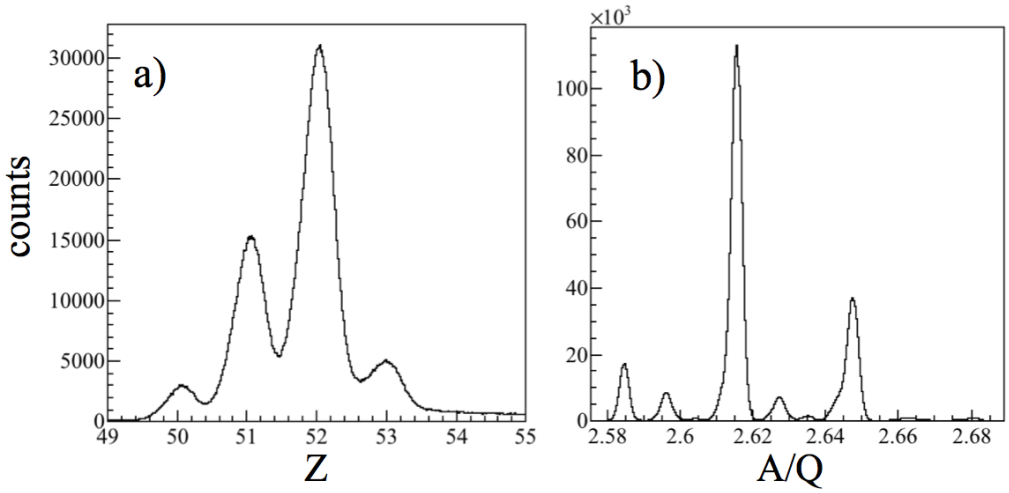

Figure 4.2: a) Atomic number, Z, and b) A/Q ratio in BigRIPS. These distributions are directly obtained from the measured TOF, $B\rho$ and ΔE variables without any corrections.

4.1.3 Particle identification in ZeroDegree

The particle identification in the ZeroDegree spectrometer was performed following the same method as in the BigRIPS spectrometer, but starting now at the F8 focal plane and ending at the F11 focal plane. As there is no degrader in ZeroDegree, we do not have to distinguish any region where the velocity of the ion changes significantly, therefore, the equations of the TOF-Bρ-ΔE method applied to the ZeroDegree spectrometer are:

$$TOF = \frac{L_{811}}{\beta_{811} c} \tag{4.9}$$

$$\left(\frac{A}{Q}\right) = \frac{B\rho_{911}}{\beta_{811}\gamma_{811}} \frac{c}{m_u} \tag{4.10}$$

$$Z = C_1 \beta_{811} c \sqrt{\frac{\Delta E}{\left[ln(\frac{2m_e c^2}{I}\beta_{811}^2) - ln(1-\beta_{811}^2) - \beta_{811}^2\right]}} + C_2 \tag{4.11}$$

where, now, the TOF is measured between two plastic scintillation counters installed at F8 and F11, between which an ion travels on the central trajectory 36.5 m. The energy loss is measured with a MUSIC detector placed at the F11 focal plane and we use the last magnetic stage, F9-F11, to deduce the Bρ_{911} value. Figure 4.3 a) shows the energy loss in the F11 MUSIC, Fig. 4.3 b) displays the β_{911} parameter and Fig. 4.3 c) shows the energy loss in the F11 MUSIC as a function of the TOF between the F8 and F11 focal planes. Figures 4.4 a) and b) show the uncorrected atomic number, Z, of each ion and the A/Q ratio of the reaction residues of the ^{136}Te isotopes measured in ZeroDegree, respectively.

4.1.4 Background reduction

In order to improve the resolutions of the Z and A/Q distributions measured in the BigRIPS and ZeroDegree spectrometers, we can exclude background events by applying certain conditions to the parameters used in the particle identification. The background exclusion is mainly based on Ref. [108] and will now be explained in detail.

4.1.4.1 Background in the plastic scintillation counters

The TOF is measured in both BigRIPS and ZeroDegree using two plastic scintillation counters where the signals produced when the ion passes through them are amplified by two photomultiplier tubes (PMTs) placed at the left and right ends of each detector. The signals of each side are related with the following expression [108]:

$$\lambda ln\left(\frac{q_L}{q_R}\right) = V(t_R - t_L) \tag{4.12}$$

where q_L and q_R are the charges measured in the left and right PMTs, respectively, t_L and t_R represent the time recorded on the left and right side, respectively, and V is the propagation

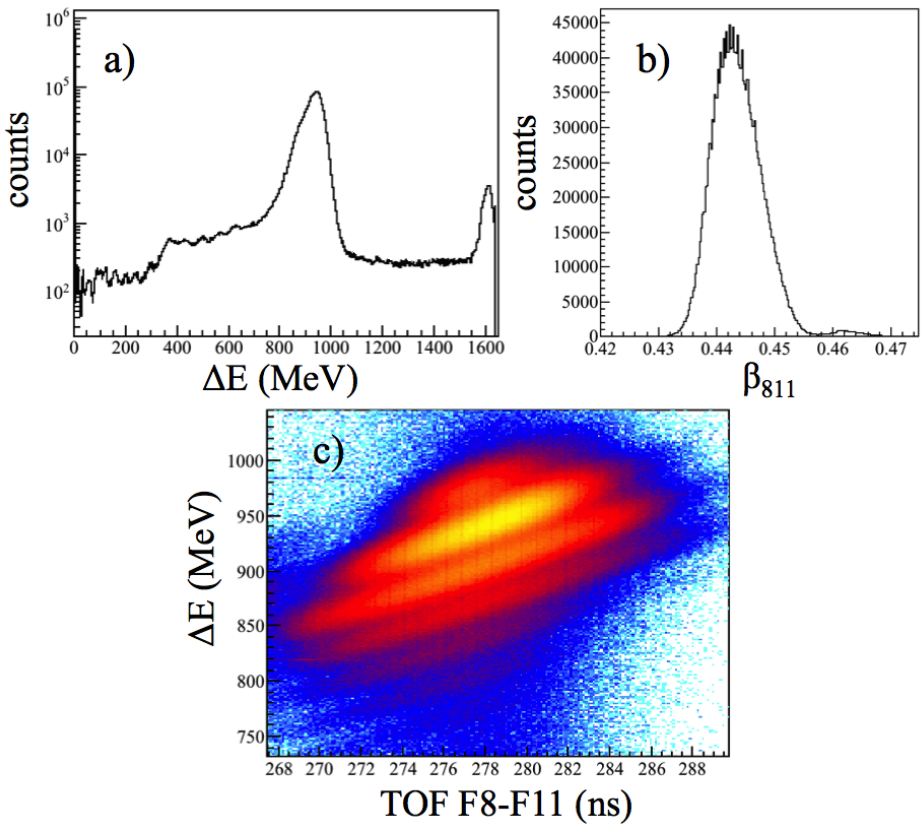

Figure 4.3: a) Energy loss (in MeV) in the F11 MUSIC. b) Velocity β_{811} of the ions after passing through the target. c) Energy loss in the F11 MUSIC as a function of the TOF between the F8 and F11 focal planes. All these parameters were used to deduce the Z and A/Q numbers in ZeroDegree.

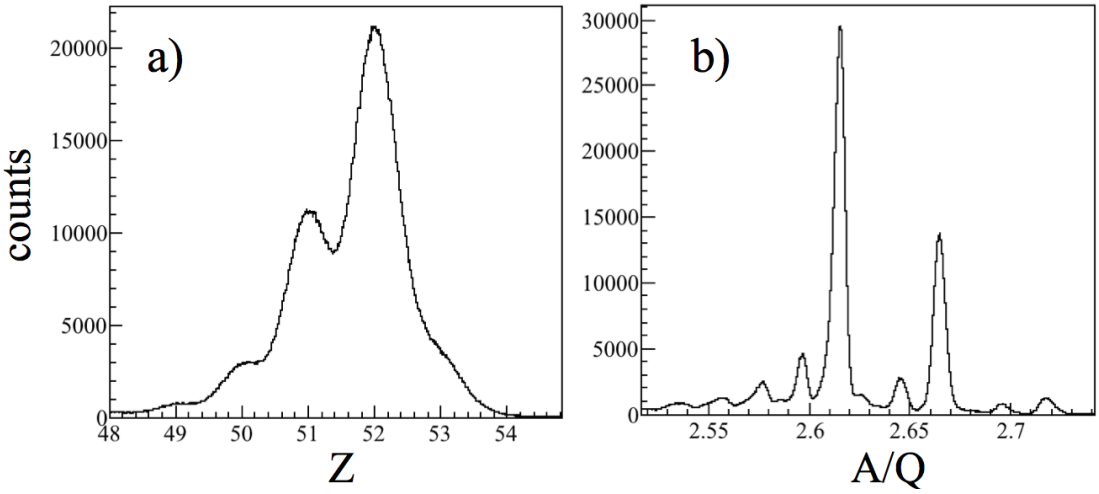

Figure 4.4: a) Atomic number Z and b) A/Q ratio in ZeroDegree (a gate on ^{136}Te on BigRIPS was applied). Again, no corrections have been applied to the displayed distributions.

speed of the light in the plastic counters. Equation 4.12 shows that events with good q_L, q_R, t_L and t_R measurements should be linearly related on plot of $ln\left(\frac{q_L}{q_R}\right)$ versus $t_R - t_L$. Figure 4.5 shows such plots for the four plastic counters used in the particle identification. In them, events which lie along the correlation line are clearly distinguished from those that are not.

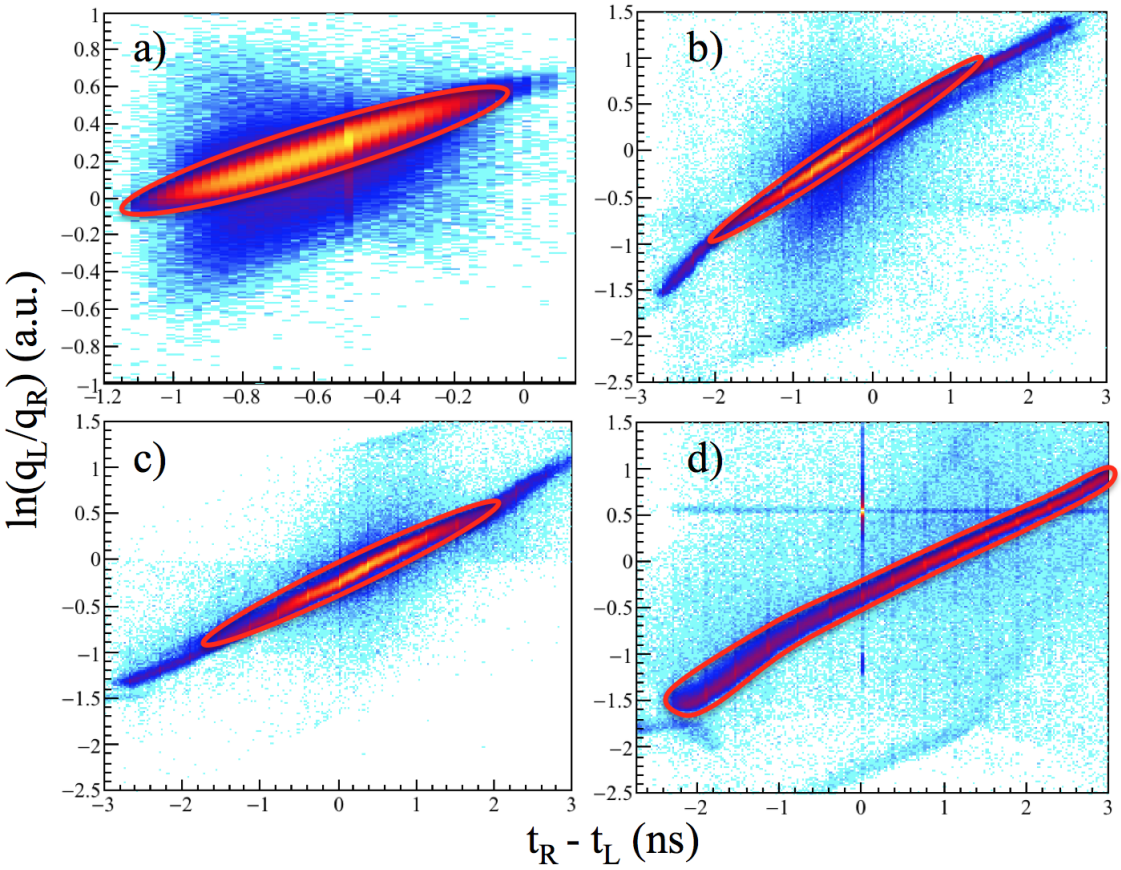

Figure 4.5: Correlation plots between $ln\left(\frac{q_L}{q_R}\right)$ and $t_R - t_L$ for the plastic detectors situated at the a) F3, b) F7, c) F8 and d) F11 focal planes. The red curves represent the background removal gates.

It is possible to identify and remove background events from correlation plots between the charge signals of left and right PMTs of each plastic and correlation plots between the total charge signals, $q = \sqrt{q_L \cdot q_R}$, of the plastic counters of different focal planes. Figure 4.6 a) shows the correlation plot between the total charge signals of the plastics F3 and F7 and Fig. 4.6 b) displays the correlation plot between the charge-integrated left and right signals of the F3 plastic counter. The same kind of correlation plots were produced for the other focal planes and plastic counters.

4.1.4.2 Background in the PPAC detectors

The positions of ions in the PPAC layers were determined from the time difference between two signals, T_1 and T_2 (left and right or up and down), obtained with the delay–line read-out

method. Occasionally, a pile-up, or multi-hit event occurs in the PPAC detectors, resulting in incorrect positions being derived. To avoid this, we define the variable $T_{sum} = T_1 + T_2$, which should correspond to the time required for the signal to traverse the entire delay line. This value should, therefore, be constant and events with T_{sum} values differing from the measured constant value are assigned as background events. Figures 4.7 a) and b) show the T_{sum} distributions for the first PPAC at F5 and for the second PPAC at F7, respectively. Although this background removal method based on the T_{Sum} value has been explained here, it was not applied in the analysis since a large fraction of ^{136}Te ions were lost (approx. 40%) after applying this condition.

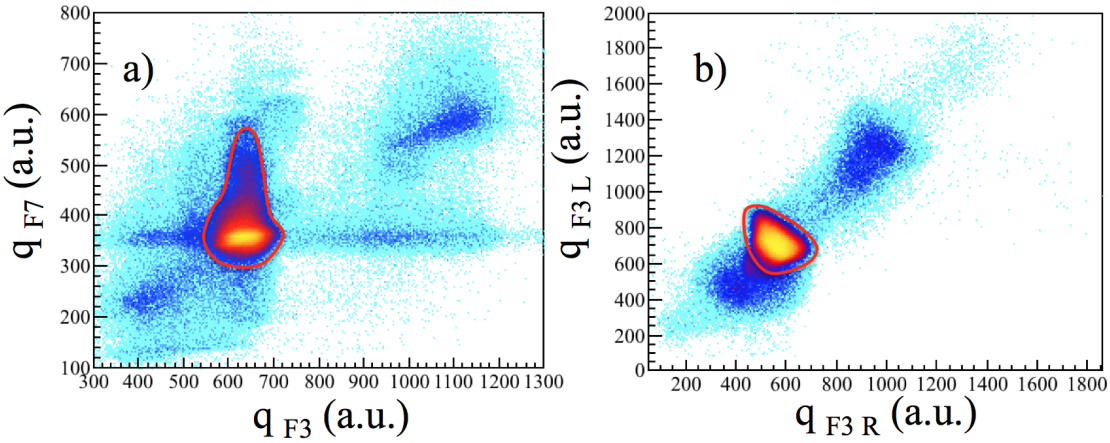

Figure 4.6: a) Correlation plot between the charge-integrated signals of the plastic counters F3 and F7. b) Correlation plot between the left and right signals of the plastic counter at F3. The red curves indicate the gates used to reject the background events.

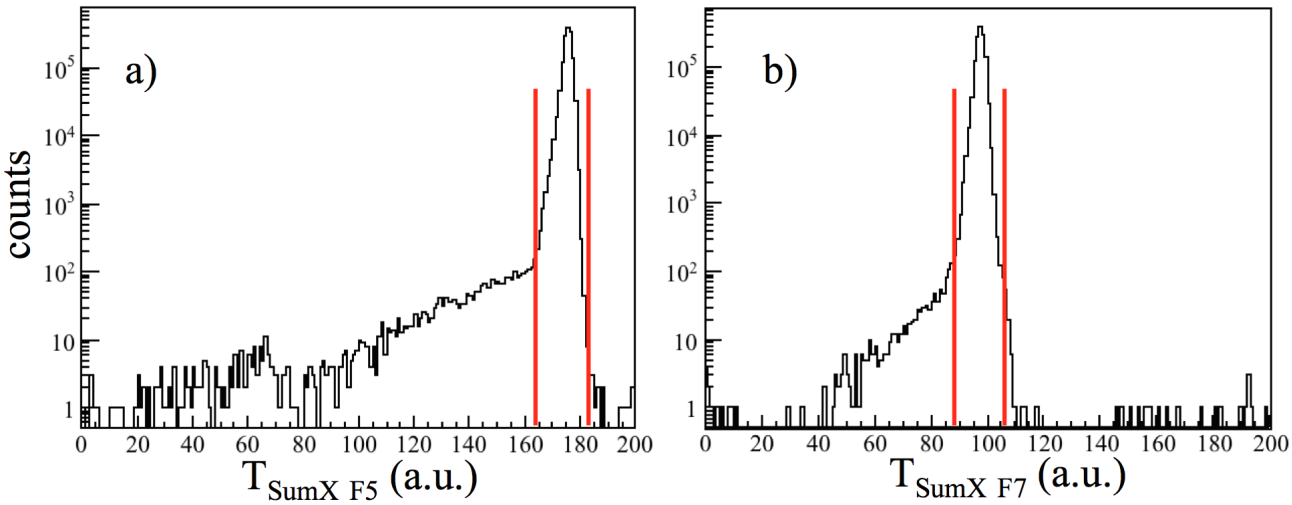

Figure 4.7: Example of T_{SumX} plots for a) the first PPAC at F5 and b) the second PPAC at F7. The red lines represent the selection of events with good T_{SumX} values.

4.1.4.3 Background in the MUSIC detectors

The energy loss, ΔE, needed to calculate the atomic number, Z, was obtained from an average value of the six independent signals measured with the six anodes of the MUSIC detector. Nuclear reaction events in the electrodes and counter gas can be removed through the correlations between the individual and the averaged signals. Figure 4.8 a) shows the individual signals measured with each anode in the F7 MUSIC. Figure 4.8 b) displays the difference between the energy loss measured in each anode and the average ΔE value. Events with $|\Delta E_{ave} - \Delta E_i| >$ 20 MeV were considered as background.

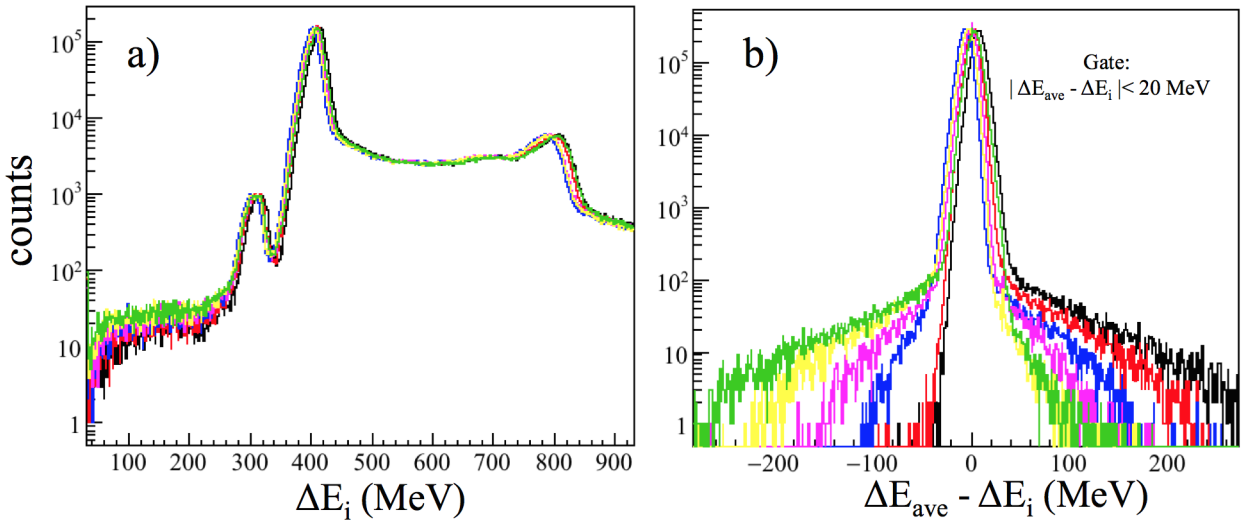

Figure 4.8: a) Energy losses measured in the six individual anodes of the F7 MUSIC. b) Difference between the energy loss measured in each anode and the average ΔE value. Only events with values $|\Delta E_{ave} - \Delta E_i|$ smaller than 20 MeV were considered in the analysis. The different colors distinguish the anodes.

4.1.5 Resolution improvement for PID

Besides background rejection, the resolutions of the atomic number, Z, and mass to charge ratio, A/Q, can be improved with some experimental corrections. The first of them is related with the gain factor of the MUSIC detector, which depends strongly on the temperature of the fill gas. Figure 4.9 shows the relative energy loss measured in the F7 MUSIC (normalized to run number 4) as a function of run number. As is evident in the figure, the relative gain factor changed during the experiment and, as a consequence, so did the measured Z number. To correct for this, the energy losses measured during each run with the MUSIC detector were aligned to run number 4, which was taken as the reference.

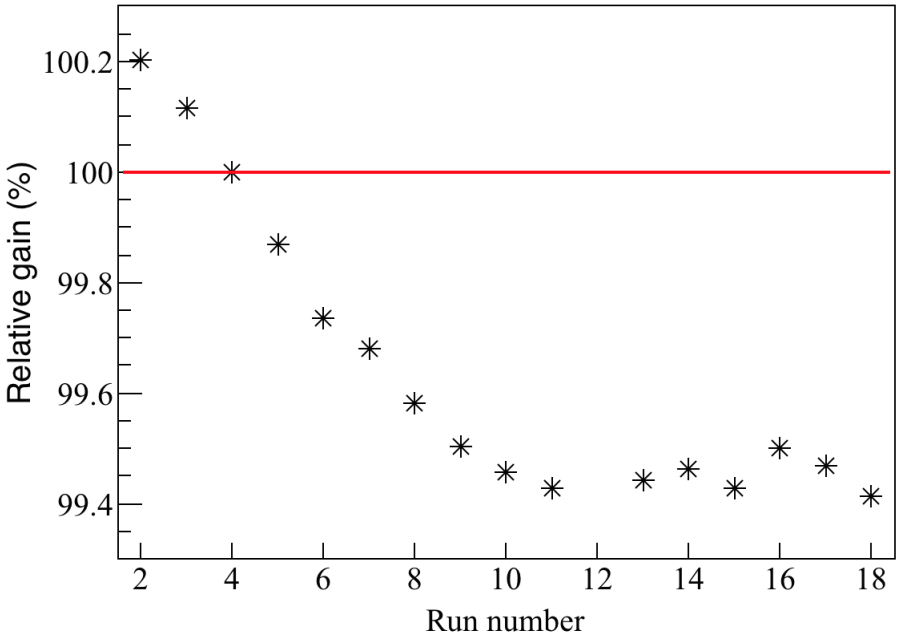

Figure 4.9: Relative gain factor (%) of the F7 MUSIC for the first 18 runs (Au target). The gain factor is normalized to run number 4. This gain shift was caused by a dependence with the temperature of the fill gas of the MUSIC.

Additionally, checking the individual signals measured with the six anodes of the MUSIC, we observed that the first anode of the F11 MUSIC behaved strangely (the energy loss spectrum obtained with this anode had a different shape as compared to the signals of the other five anodes). Figure 4.10 shows the individual signals of the six anodes measured with the MUSIC placed at F11, clearly, the first anode behaves differently from the others. Therefore, for the determination of the Z number in ZeroDegree we use an average energy which does not consider the first anode:

$$\Delta E_{F11} = \Big(\prod_{i=2}^{6} \Delta E_i\Big)^{1/5} \tag{4.13}$$

The last correction applied to improve the resolution of the Z number was related to a dependence of Z on the velocity, β, of the ions. This dependence on the velocity was only observed for the ZeroDegree spectrometer. Figure 4.11 a) shows the dependence of Z on β_{811} for the F11 MUSIC. The dependence on the velocity was corrected with the following expression:

$$Z_{new} = a[Z + k(\beta_{811} - \beta_p)] + b \tag{4.14}$$

where Z is the atomic number directly deduced from eq. 4.13, β_{811} is the velocity of the ions in ZeroDegree, k is the parameter which corrects the β dependence, β_p is the β value from which we change the degree of rotation, finally, a and b are calibration parameters to calibrate the corrected Z value to the known Z values. Figure 4.11 b) displays Z versus β_{811} once the correction has been applied.

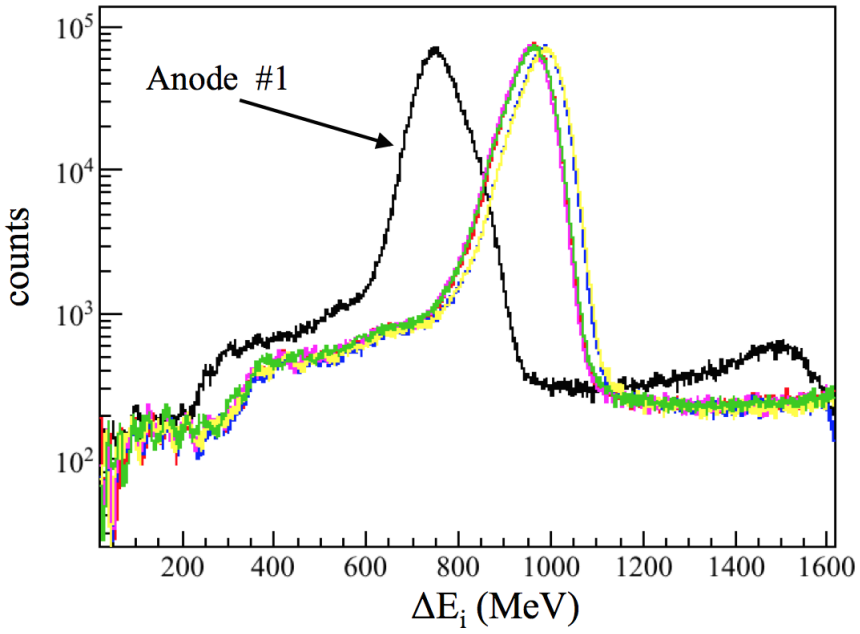

Figure 4.10: Energy losses measured in the six individual anodes of the F11 MUSIC, where the first anode exhibited a strange behavior. Finally, this anode was removed in the calculation of the ΔE_{F11} value. The different colors distinguish the anodes.

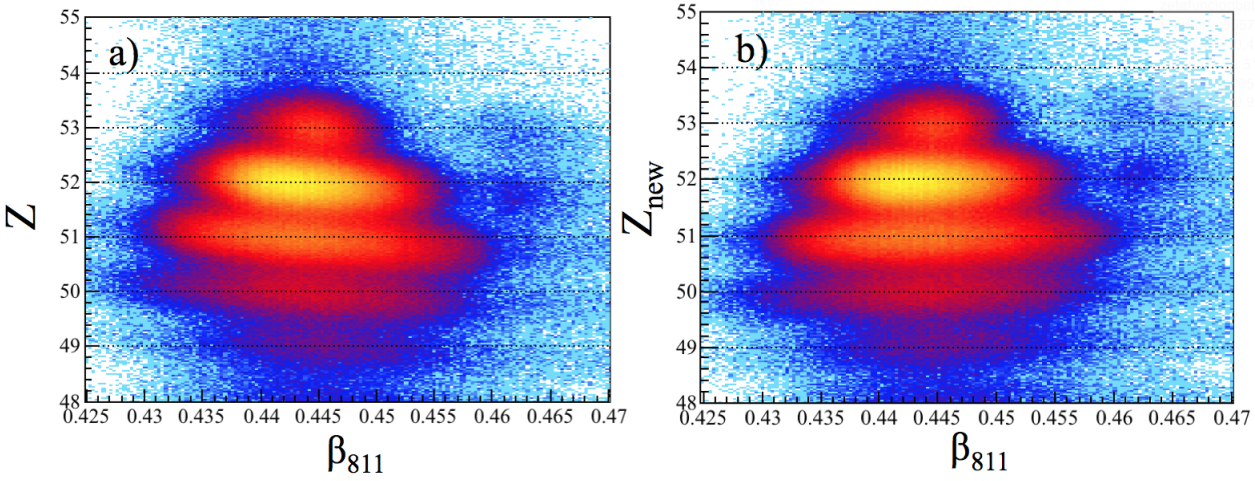

Figure 4.11: Atomic number, Z, versus β_{811} for ZeroDegree: a) before applying the corrections to remove the dependence on the velocity and b) after applying the corrections.

In order to improve the A/Q resolution, the approach discussed in Ref. [108] was followed. The A/Q ratio is obtained from the Bρ values derived from the trajectory of the ion at each focal plane. The trajectory reconstruction is performed by combining the measured trajectory with the ion-optical transformation between the initial and the final coordinate vectors. The optical transformations are applied with first-order transfer matrix elements. In some cases, first-order matrix elements are not sufficient to compensate for aberrations, and therefore, higher order matrix elements are needed to improve A/Q resolutions. The higher order matrix elements

are experimentally determined through checking the dependence of A/Q with the horizontal and vertical positions, and angles at the different focal planes. If the trajectory were perfectly reconstructed, the A/Q ratio of an isotope would be independent of its position and angle. Therefore, different corrections have to be applied for each focal plane with the aim of removing these dependencies. Figure 4.12 a) shows the dependence of A/Q with the x position in the F7 focal plane. This dependence was corrected by applying the polynomial, $(A/Q)_{new} = A/Q + 0.00014 * F7X + 0.000002 * F7X^2$. Figure 4.12 b) displays the corrected A/Q ratio versus F7X. The same procedure was applied to the remaining positions and angles for the all focal planes in BigRIPS.

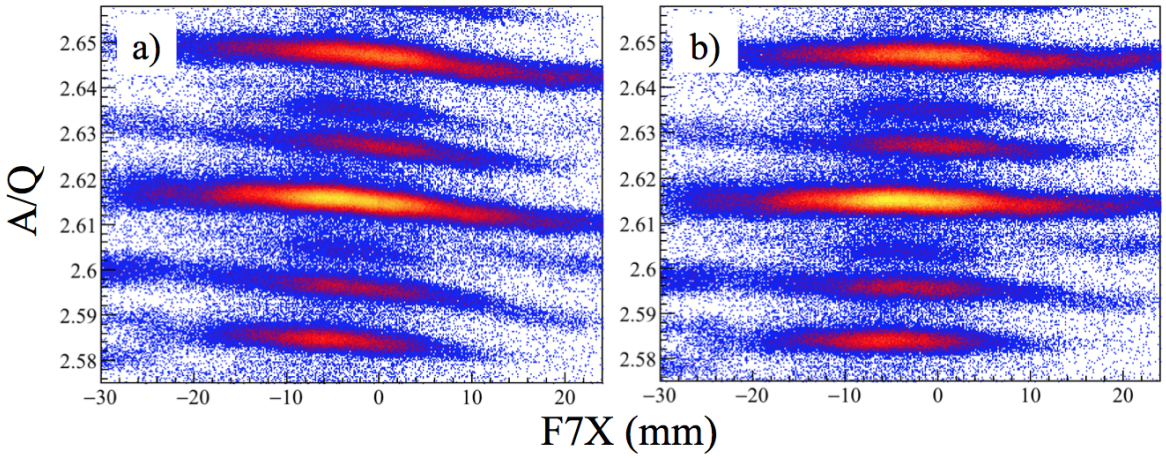

Figure 4.12: a) Dependence of the A/Q of incoming ions (BigRIPS) on the measured F7X horizontal position. b) Dependence after corrections with higher order matrix elements.

For the case of ZeroDegree, the A/Q corrections discussed above are more complicated since a large number of the ions suffered charge state changes between the F8-F9 and F9-F11 focal planes, consequently, the measured positions and angles in the F11 focal plane exhibit different components. Up to the F9 focal plane, the same corrections are applied to all outgoing isotopes in ZeroDegree since there are no charge state changes between F8 and F9. Figures 4.13 a) and b) show the A/Q dependence on the F9X position and the correction of this dependence, respectively, for the outgoing ions gated on ^{136}Te in BigRIPS. As mentioned before, between the F8-F9 and F10-F11 focal planes charge state changes were observed. These charge state changes are shown in the plot a) of the Fig. 4.14, where we show δ_{89} versus δ_{911}, where δ is the fractional Bρ deviation from the central Bρ_0 value expressed as $\delta = (B\rho - B\rho_0)/B\rho_0$. The central distribution corresponds to no charge state changes between F8-F9 and F10-F11, while the upper and lower distributions correspond to charge state changes of $\pm$e unit, where e is the electron charge. Figure 4.14 b) displays the difference, $\delta_{89} - \delta_{911}$, versus the x position in the F11 focal plane. Since each charge state component has a different position in the F11 focal plane, we have to apply corrections for each component separately. Figure 4.15 a) shows the dependence of A/Q on the F11X position for the ions which did not suffer charge state changes

and Fig. 4.15 b) shows the same for ions which suffer a charge state change of $-e$ between F8-F9 and F9-F11. Again, polynomial corrections were applied to remove the dependence on the position. The new corrected A/Q values were calibrated to their known values. Figures 4.15 b) and d) show the A/Q ratio as a function of the F11X for the cases of no charge change and a change of $-e$, respectively, after the dependence has been corrected for. The same procedure was applied to the remaining charge state changes.

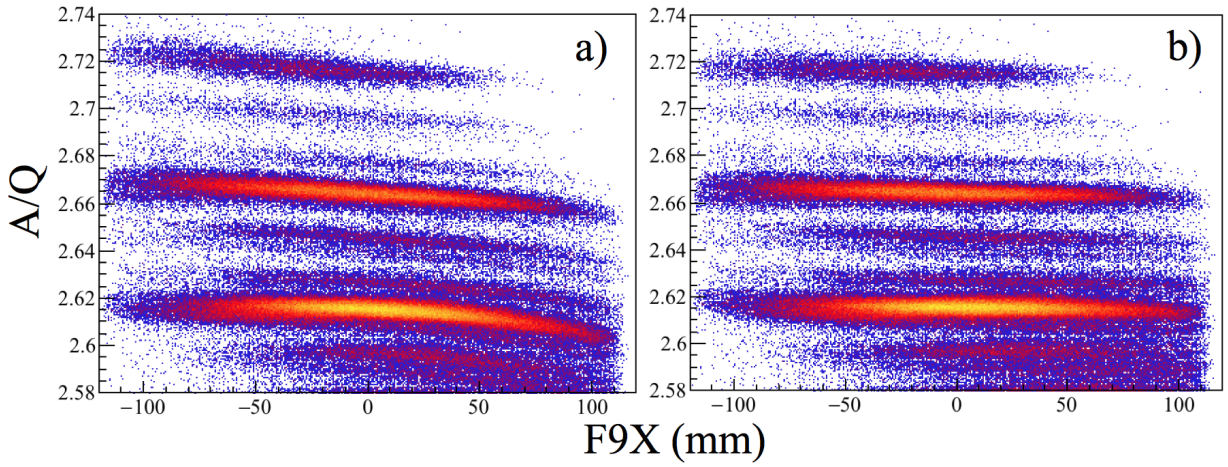

Figure 4.13: a) Dependence of A/Q of outgoing ions (ZeroDegree) on the measured F9X horizontal position. b) Dependence after corrections with higher order matrix elements. Both plots are gated on ^{136}Te in BigRIPS.

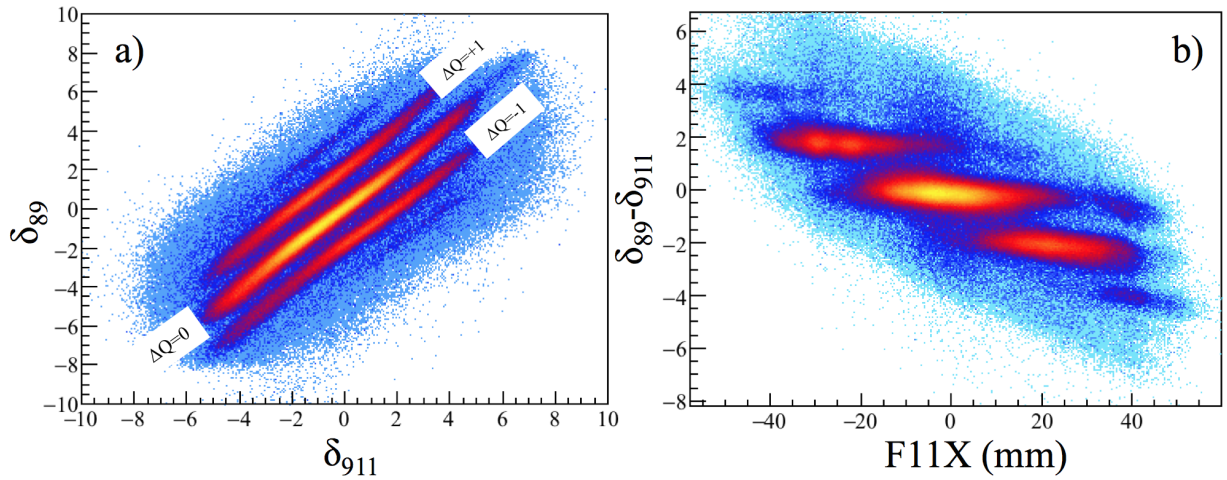

Figure 4.14: a) δ_{89} versus δ_{911}. Each distribution corresponds to a charge state change between the F8-F9 and F9-F11 focal planes. b) The difference, $\delta_{89} - \delta_{911}$, is plotted versus the x position in the F11 focal plane.

4.1.6 PID Resolution

Figures 4.16 a) and c) show the PID plots for the BigRIPS and ZeroDegree spectrometers without any correction, or background subtraction, respectively. For the particle identification in

ZeroDegree we gated on ^{136}Te in BigRIPS. Once all corrections and background removal gates are applied, we obtain the BigRIPS and ZeroDegree PID plots shown in Figs. 4.16 b) and d), respectively, where the resolution in ZeroDegree has been improved to such a degree that we can now identify the charge states of the reaction products. Figures 4.17 a) and b) show the raw Z and A/Q distributions measured in ZeroDegree (black curves) and the distributions once we apply all corrections and background removals explained in the text (red curves). Table 4.1 contains the final resolutions of Z and A/Q for both spectrometers after applying all corrections and background removal.

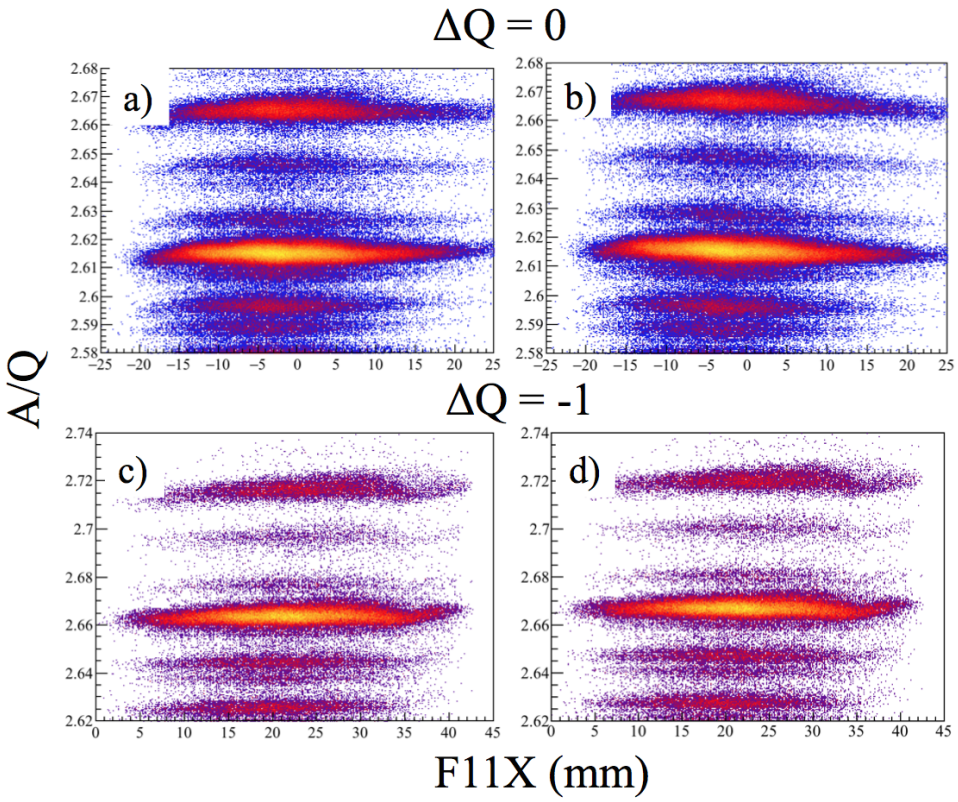

Figure 4.15: a) Dependence of A/Q on the F11X position for the ions which did not suffer a charge state change between F8-F9 and F9-F11. b) Elimination of the previous dependence. c) Dependence of A/Q on the F11X position for the ions which suffered a charge state change of $-e$ between F8-F9 and F9-F11. d) Elimination of the previous dependence.

Table 4.1: Resolutions (σ) of A/Q and Z for the BigRIPS and ZeroDegree spectrometers. The resolutions were obtained for the ^{136}Te^{52+} ions in both spectrometers.

	BigRIPS	ZeroDegree
A/Q resolution (%)	0.045	0.082
Z resolution (%)	0.44	0.55

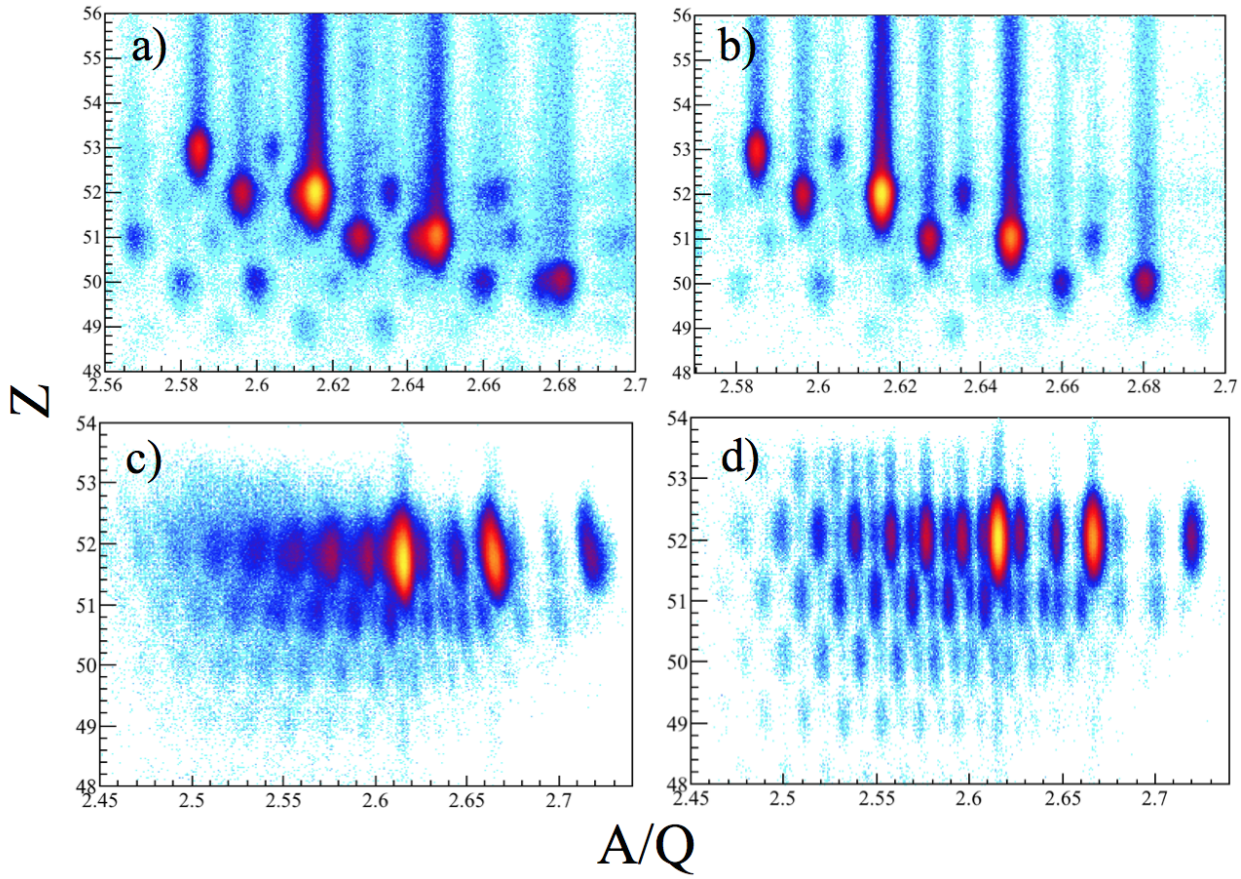

Figure 4.16: BigRIPS PID plots (C target): a) before and b) after corrections and background removal. ZeroDegree PID plots (C target): c) before and d) after corrections and background removal. The ZeroDegree plots are obtained with a gate on ^{136}Te in BigRIPS.

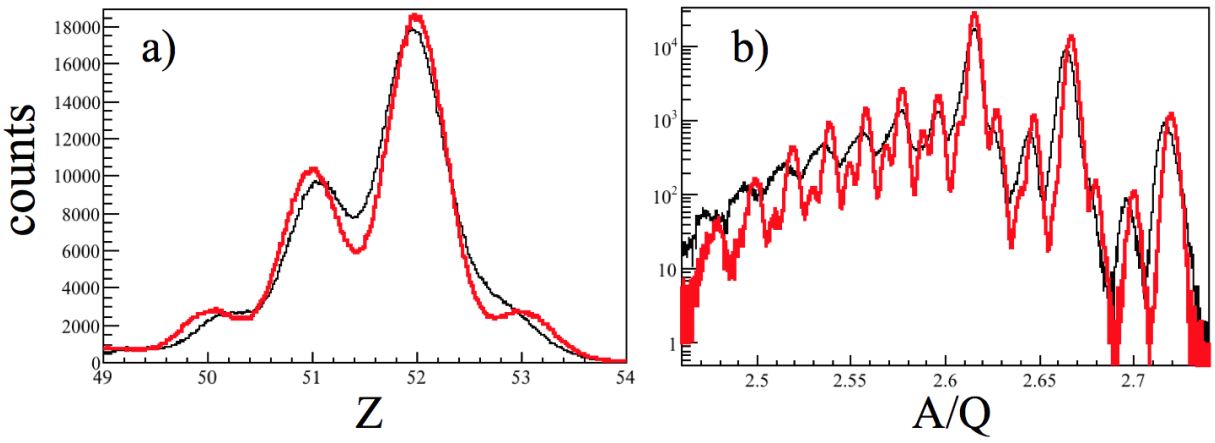

Figure 4.17: a) Atomic number, Z, determined for the ZeroDegree spectrometer (C target) without corrections (black curve) and with the corrections explained in the text (red curve). b) A/Q ratio for ZeroDegree gated on ^{136}Te in BigRIPS (C target) and for the Te isotopes (the condition 51.5<Z<52.5 was applied to the atomic number in ZeroDegree) without corrections (black curve) and with corrections (red curve). After the corrections, the resolutions of both distributions improve considerably.

4.2 The DALI2 γ-ray spectrometer

4.2.1 DALI2 Energy calibration

The energy calibration of the DALI2 array was performed with three different γ-ray sources: ^{60}Co, ^{88}Y and ^{137}Cs. The ^{60}Co source emits two γ rays with energies of 1173.23 and 1332.49 keV, the ^{88}Y source also emits two γ rays at 898.04 and 1836.07 keV, and ^{137}Cs emits a 661.66 keV γ ray [109]. The sources were placed at the target position and data for each calibration source was accumulated for approximately 30 min. Two calibrations were carried out at the beginning and at the end of the experiment.

The gains of the ADC modules used to record the DALI2 signals were adjusted to reach energies up to $\sim$ 12 MeV over 4096 channels. It is well known that the raw ADC signal of a NaI(Tl) scintillator is proportional to the energy deposited in the crystal. For each crystal, the five transitions described in the previous paragraph observed in the raw spectrum were fitted with a Gaussian function to determine the centroid of the photopeak and with an exponential function to describe the background underneath the peak. Once the positions of the raw ADC photopeaks were determined, a linear fit between the tabulated energies and the ADC channels was performed. Figure 4.18 shows such a calibration for the DALI2 crystal number 90.

The same procedure shown in Fig. 4.18 was applied to the remaining 185 DALI2 detectors. On the left of Fig. 4.19 we show 2D plots between the raw ADC signal and the DALI2 detector ID for the three different sources, while on the right of the same figure we display the calibrated energy versus the detector ID, again, for the three different sources. As is visible, the detector number 168 does not produce signal and was inoperable during the entire experiment. Furthermore, there were some detectors (number 32 and 64) which presented strange line-shapes of the photopeaks and non-linear behavior and, therefore, they were removed from the analysis.

To verify the quality of the calibration, we study the differences between the measured and tabulated energies of the five γ-ray transitions used in the calibration. The measured energies were obtained from a fit of the energy spectra for the three γ-ray sources, where again we used a Gaussian+exponential functions to describe the response. Figure 4.20 shows the difference between the experimental and tabulated energies of the γ rays used in the calibration for all DALI2 crystals. For most of the crystals, this difference is below 1%. The biggest discrepancies between the measured and tabulated energies are observed for the detectors with ID between 121 and 145. These detectors received far fewer statistics since they were situated in the outer part of the forward wall and were shadowed by the last layer. Note that, with this in mind, the detectors with worse resolution and linearity were intentionally positioned there.

A second calibration setting was carried out at the end of the experiment with the aim of study-

ing the possible gain drifts of the DALI2 crystals. These gain drifts happen because DALI2 is close to the magnetic field of the downstream quadrupole and dipole magnets, and the PMTs are very sensitive to the magnetic field. The gain drifts can also be caused by radiation damage in the detectors since they are exposed to highly energetic particles. Comparing the calibrated spectra at the beginning and at the end of the experiment (using in both cases the calibration parameters derived from the first calibration run) we observed that the gain drift was negligible for all detectors and the use of one calibration was sufficient for the whole experiment.

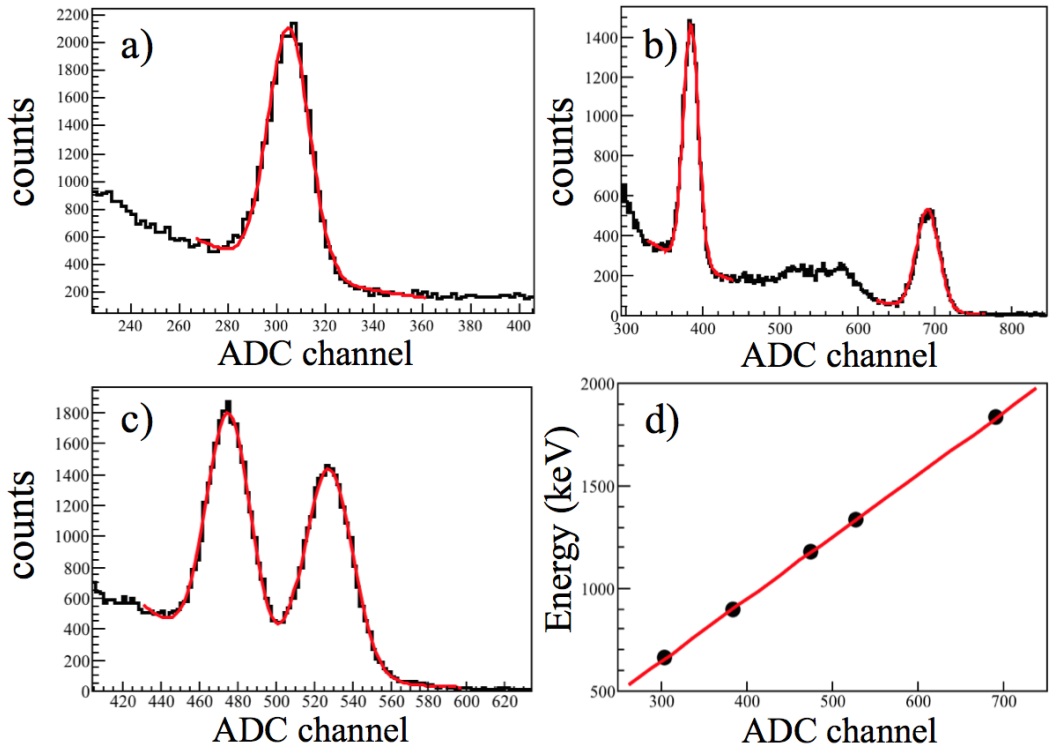

Figure 4.18: Example of the DALI2 calibration. a) Raw spectrum of ^{137}Cs. b) Raw spectrum of ^{88}Y. c) Raw spectrum of ^{60}Co. The spectra (black histograms) were fitted with a Gaussian function to describe the photopeak and an exponential function to describe the background underneath the peak (red line). d) Linear fit between the ADC channels and the tabulated energies. The spectra correspond to the detector number 90.

The energy resolution (σ) of each DALI2 crystal was also determined for the different γ-ray transitions. The resolutions were obtained from the Gaussian fit of the photopeak observed in the energy spectrum. Figure 4.21 a) shows the energy resolution of each crystal. As expected, the resolution worsens with the increase of the γ-ray energy. The first detectors have worse resolution and they were situated in the backward layers and, as a consequence of the Lorentz boost, they accumulated fewer statistics. Furthermore, the Doppler shift reduces the energy in the laboratory system for these detectors. Again, it is also visible that the detectors between 121 and 145 have the poorest resolution. In a NaI(Tl) scintillator, the energy resolution is proportional to the square-root of the energy [95], so the resolution of each detector as a

function of the energy was fitted using the following expression:

$$\sigma_E = a\sqrt{E} \tag{4.15}$$

where the parameters, a, were used as input of the GEANT4 simulation. Figure 4.21 b) displays the $\sigma_E = a\sqrt{E}$ functions for all DALI2 detectors.

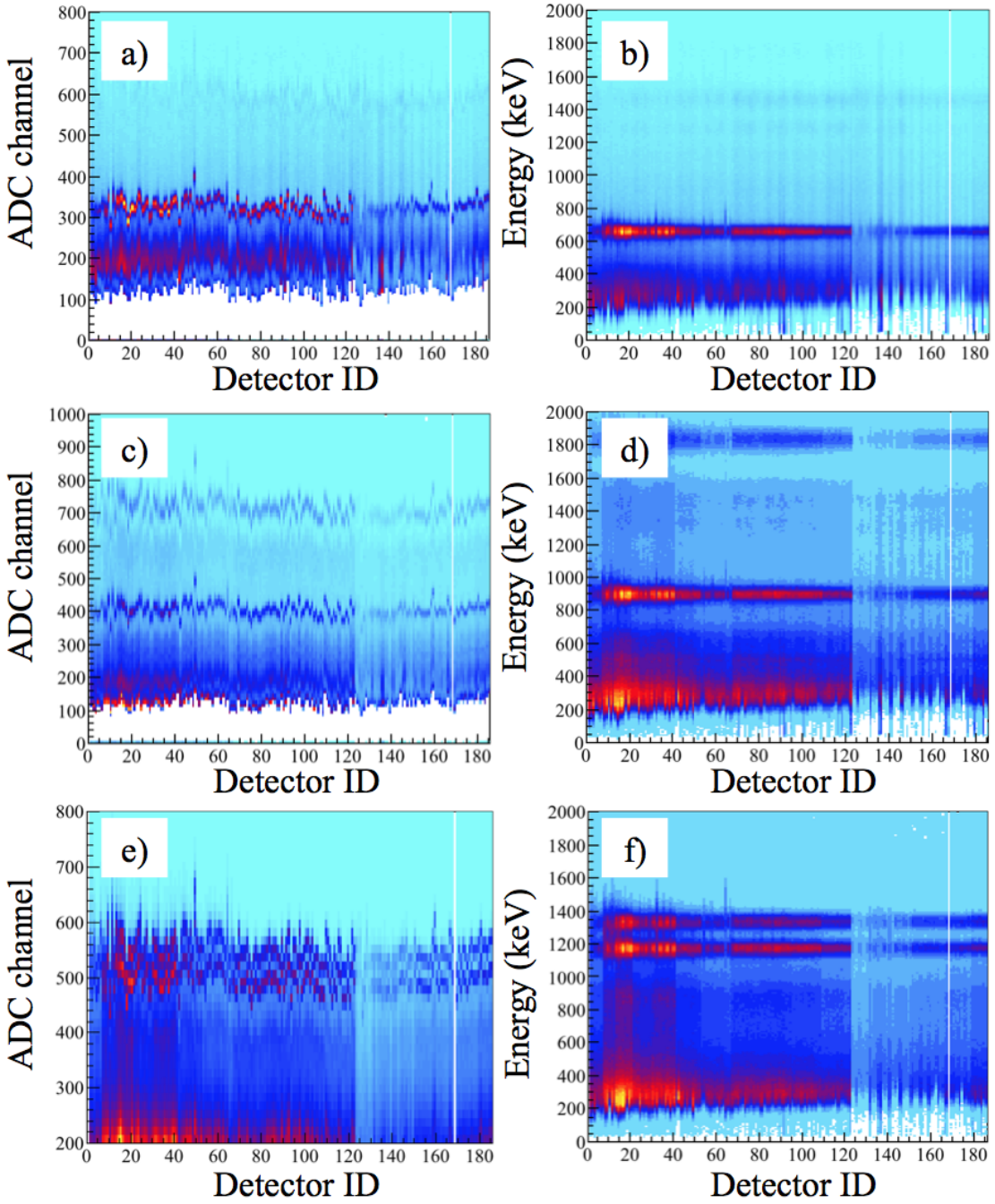

Figure 4.19: Left: raw energy spectra for the a) ^{137}Cs, c) ^{88}Y and e) ^{60}Co sources. Right: calibrated energy spectra for the b) ^{137}Cs, d) ^{88}Y and f) ^{60}Co sources. The detector number 168 did not work during the entire experiment.

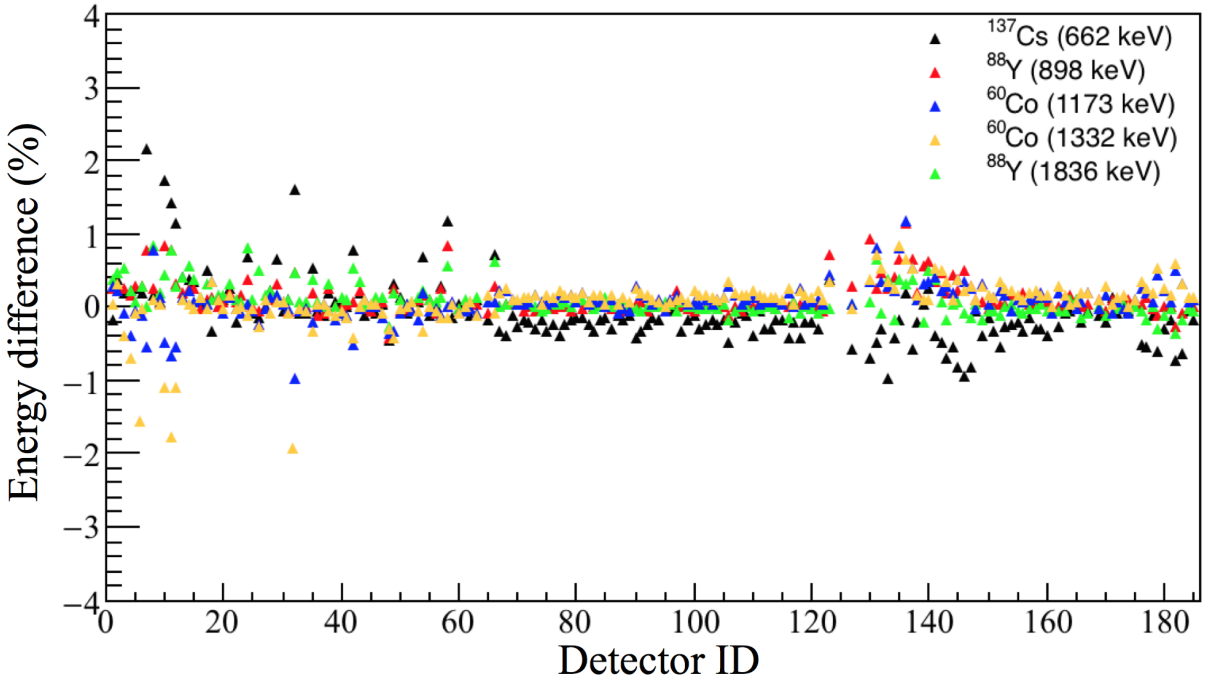

Figure 4.20: Difference between the measured and tabulated energies of the transitions used in the calibration for each DALI2 crystal.

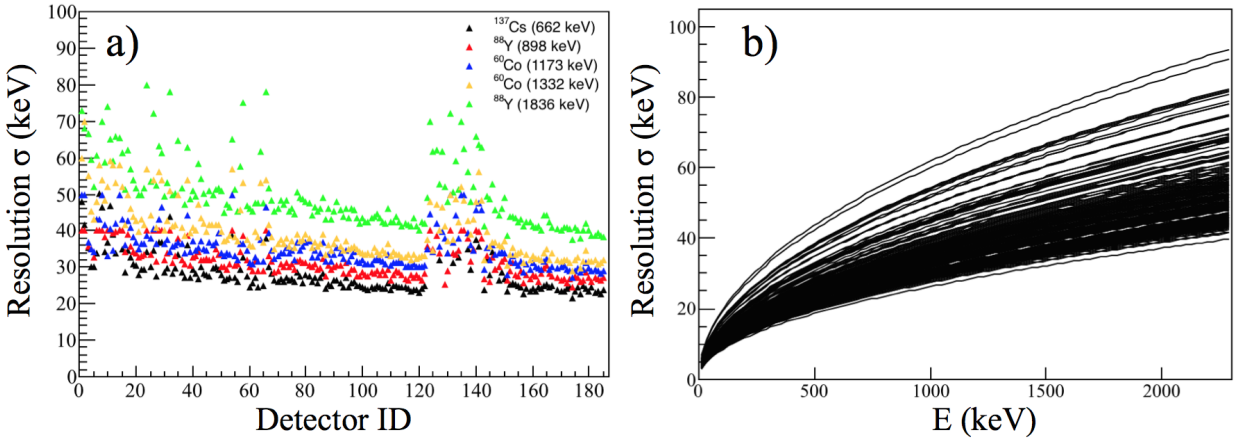

Figure 4.21: a) Energy resolution (σ) of each crystal for the transitions used in the energy calibration. b) Energy resolution functions, $\sigma_E = a\sqrt{E}$, of each crystal. Each function was obtained from a fit of the experimental resolutions as a function of the energy for each crystal.

4.2.2 DALI2 time calibration

The time information of the DALI2 array requieres calibration. The time signal starts when the F7 plastic produces a signal due to an ion passing through it and ends when a DALI2 crystal detects a γ ray. Time delay is added to the DALI2 signals such that their signals falls within the acquisition window of the electronics. As in the case of the energy, each crystal has an individual time signal. Figure 4.22 a) shows the raw time spectrum of the DALI2 crystal number

90. To obtain the centroid of the time distributions, a Landau function was used (red line). Once determined, the time centroids of each detector were aligned to the same mean value by applying an offset. This mean value is arbitrary since the time information is relative to the F7 plastic, but it has to be the same for all detectors. Once the alignment is performed, we can plot the time signal of the full array versus the energy of the γ ray; shown in Fig. 4.22 b). On average, the time passed between the start and stop of the time signal is:

$$T \approx t + t_{1/2} + b \tag{4.16}$$

where t is the time that the ions need to reach the target from the F7 plastic (the velocity of the ions is $\beta \approx 0.5$ and the distance between F7 and the target is around 12 m, so $t \approx 80$ ns), $t_{1/2}$ is the half-life of each γ ray emitted by the ions and b is the time offset applied to take into account the electronic delay. Usually, the time signal is of the order of t ($T \approx t$) since the half-life $t_{1/2}$ is of the order of ps (except isomeric states). Uncorrelated background events can be removed with a temporal gate $t \pm \Delta t$, named the prompt time gate, illustrated by the red lines in Fig. 4.22 b).

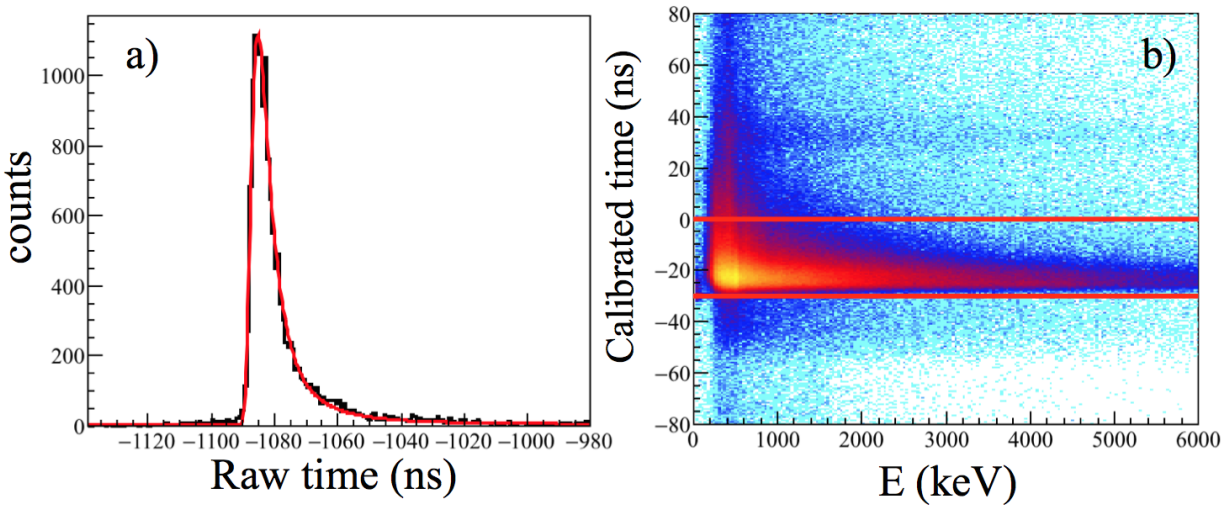

Figure 4.22: a) Raw time spectrum of the DALI2 crystal number 90. The centroid of the spectrum was obtained from a fit using a Landau function (red line). b) Aligned DALI2 time as a function of γ-ray energy. The red lines shown the time cut applied in the analysis to remove uncorrelated events.

4.2.3 DALI2 efficiency

To obtain the efficiency of the DALI2 spectrometer as a function of γ-ray energy, two different methods were used.

4.2.3.1 Method 1

In the first method, we use the typical definition of efficiency, namely the ratio between the number of events detected and the number of events emitted. This definition corresponds to the absolute efficiency, where the geometry and characteristics of the detector are included in the definition:

$$\epsilon = \frac{Number\ of\ \gamma\ detected}{Number\ of\ \gamma\ emitted} = \frac{n(\gamma)}{Act \cdot t \cdot \epsilon_{livetime} \cdot I_\gamma} \tag{4.17}$$

where $n(\gamma)$ is the number of counts in the photopeak area for a specific energy, Act is the activity of the source at the measurement date, t is the length of time of the measurement, $\epsilon_{livetime}$ is the live time of the DALI2 data acquisition system and I_γ is the absolute intensity of a specific γ ray emitted from the source.

The quantity $n(\gamma)$ was obtained from the number of counts in the photopeak of the transitions of interest. Instead of considering an exponential function to describe the background, we could directly subtract the experimental background since we took a measurement with DALI2 with an empty frame in order to characterize the natural background. For each source, the background spectrum was normalized to reproduce the high energy region of the source spectrum, where no γ-ray transitions corresponding to the source are observed, then the normalized background spectrum was subtracted from the source spectrum. Then, $n(\gamma)$ was determined from the number of counts in the photopeak after the background was subtracted. For the sources with two γ-ray transitions (^{60}Co and ^{88}Y), the transition at lower energy has a contribution to its photopeak from the Compton continuum of the transition at higher energy, which is also subtracted. Figure 4.23 shows the experimental spectra of the three different sources (black histogram) together with the normalized background (blue histogram).

The activity of the source at the measurement date, Act, was calculated from the following expression:

$$Act = A_0 \cdot e^{-\lambda \Delta t} \tag{4.18}$$

where A_0 is the known activity of the source at some specific date, λ is the decay constant of each source and Δt is the time passed between the measurement date of A_0 and the calibration date of the experiment. Table 4.2 contains A_0, the measurement date of this parameter for each source and Act.

The time, t, of the respective measurement was obtained from the start of the DALI2 data acquisition system with the source placed inside the array and the stop of the acquisition of data. The live time, $\epsilon_{livetime}$, of the DALI2 array was calculated as the ratio between the accepted triggers and the offered triggers. Table 4.2 contains the $\epsilon_{livetime}$ parameter for each source. It was lowest for the ^{60}Co source since this source had the highest activity at the date of the experiment. Lastly, the intensities, I_γ, were taken from Ref. [109].

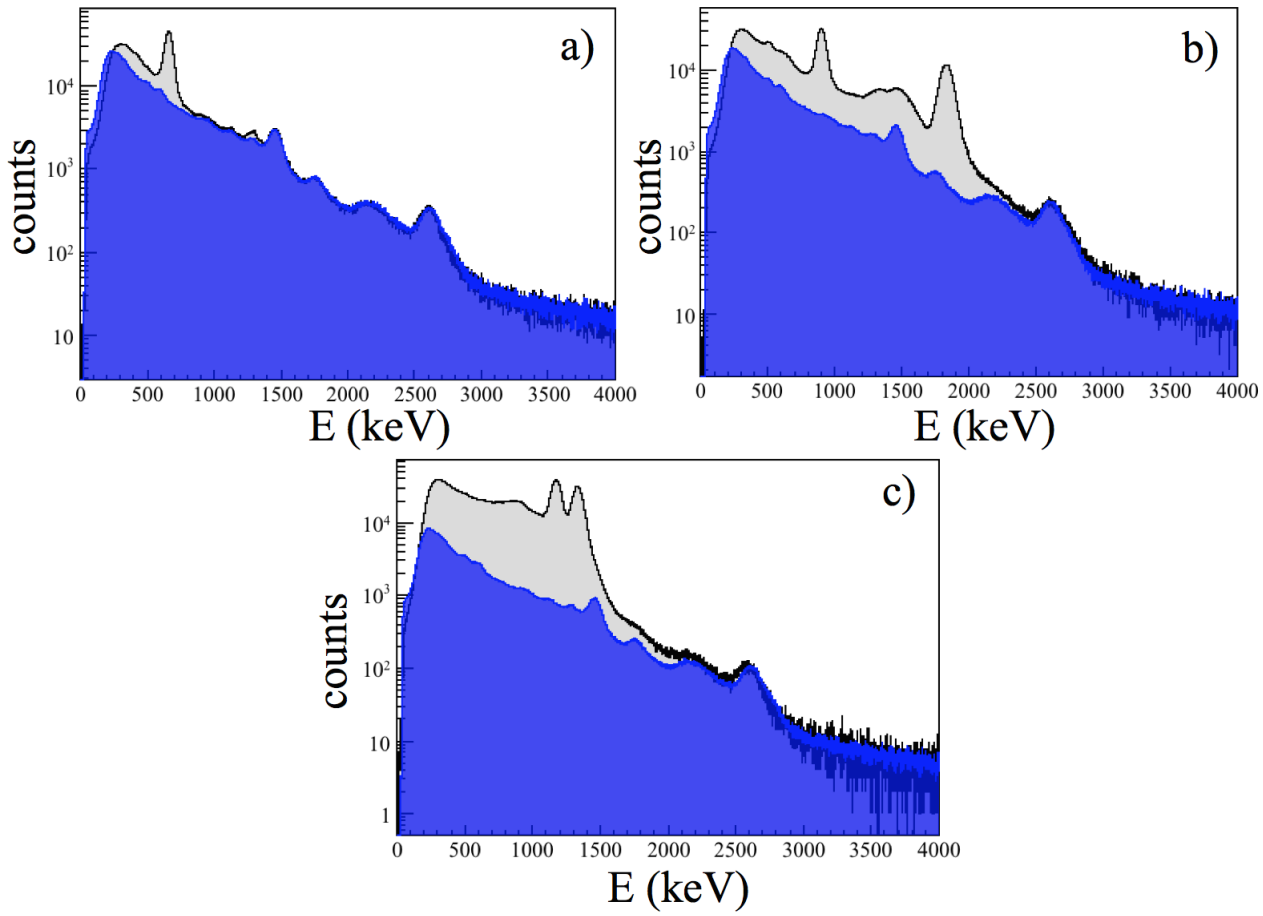

Figure 4.23: Comparison between the experimental source (black histogram) and normalized background (blue histogram) spectra for a) ^{137}Cs, b) ^{88}Y and c) ^{60}Co sources.

Table 4.2: List of the sources used for the determination of the absolute efficiency of DALI2. The table includes the reference activity, A_0, the measurement date of A_0, the activity of the source at date of the experiment, Act, and the live time of the DALI2 data acquisition system for each source.

Isotope	A_0 (Bq)	measurement date	Act (Bq)	$\epsilon_{livetime}$
^{60}Co	8.81·10^4	16-3-2010	4.52·10^4	0.26
^{88}Y	8.52·10^5	17-6-2013	1.13·10^4	0.51
^{137}Cs	8.23·10^3	16-3-2010	7.32·10^3	0.64

Table 4.3 summarizes the efficiencies obtained with this method for the γ-ray transitions emitted by the three sources. The error in the efficiency includes the error on the number of counts in the peak, the error in the activity at the measurement date (a 5% error was considered), the error in the intensities, I_γ [109], and the error in the estimation of the live time of the acquisition system.

4.2.3.2 Method 2

The second method used to determine the DALI2 efficiency can only be applied to the sources with two γ-ray transitions in coincidence, which is the case for the ^{60}Co and ^{88}Y sources. When two γ-ray transitions are in coincidence, if we gate on one of them, the number of events of the other transition should be the same. Any reduction of the events in the coincident peak compared to the gated peak would correspond to the energy-dependent efficiency of the array. With this method, the efficiency is given by:

$$\epsilon_{\gamma_2} = \frac{Number\ of\ events\ in\ the\ peak\ \gamma_2\ after\ the\ gate}{Number\ of\ events\ in\ the\ peak\ \gamma_1} \tag{4.19}$$

The β decay of the ^{60}Co source (see Fig. 4.24) always populates the state at 2505.7 keV in ^{60}Ni. This state emits a γ ray with an energy of 1173 KeV with a branching ratio of 100% to an excited state at 1333 keV which decays to the ground state emitting a γ ray of 1333 keV (again with a branching ratio of 100%). So, for the ^{60}Co source the two transitions should have the same intensity. However, in the case of the ^{88}Y source (see Fig. 4.24), 94.3% of the electron capture strength goes to the state placed at higher energy (2734.14 keV) and 5.7% to the first excited state (1836.09 keV). The state at higher energy feeds the first excited state with a branching ratio of 100%, but this first state already has intensity due to direct excitation from the electron capture decay. Therefore, for the ^{88}Y source we have to take into account the intensity due to feeding of the cascade and the intensity of the first excited state due to direct population of this state [109].

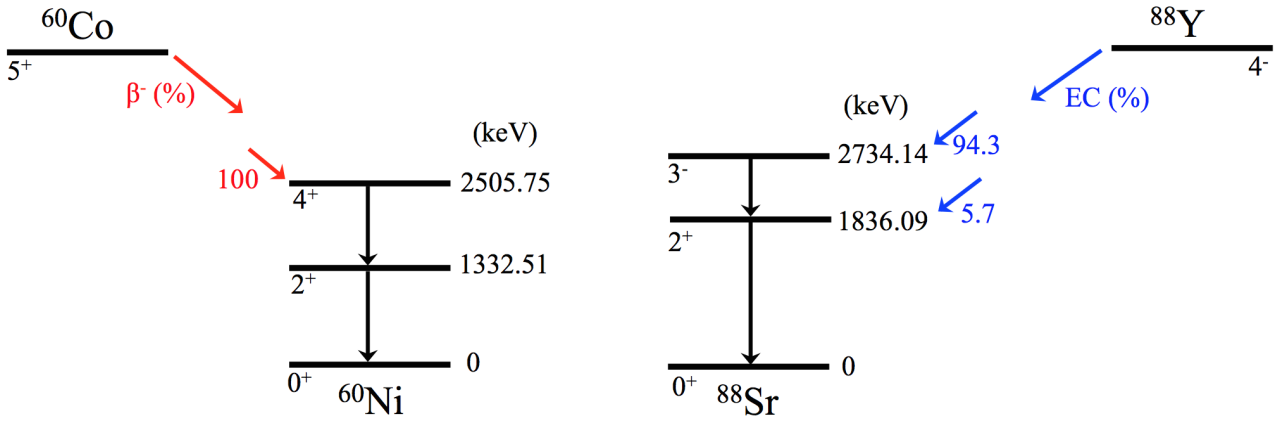

Figure 4.24: Left: decay scheme of the ^{60}Co source. Right: decay scheme of the ^{88}Y source.

Figure 4.25 a) shows the singles spectrum measured with the ^{60}Co source. In Fig. 4.25 b) we show the $\gamma\gamma$ coincidence spectrum when we gate on the transition at 1333 keV and in Fig. 4.25 c) that obtained when we gate on the transition at 1173 keV. In both cases, the transition on which we gate is observed in self coincidence. This auto-coincidence could be due to random coincidences, or coincidences from the Compton component of the higher-energy transition.

Figure 4.26 displays the same kind of spectra but now for the ^{88}Y source: a) experimental singles spectrum, b) spectrum gated on the transition at 898 keV and c) spectrum gated on the transition at 1836 keV.

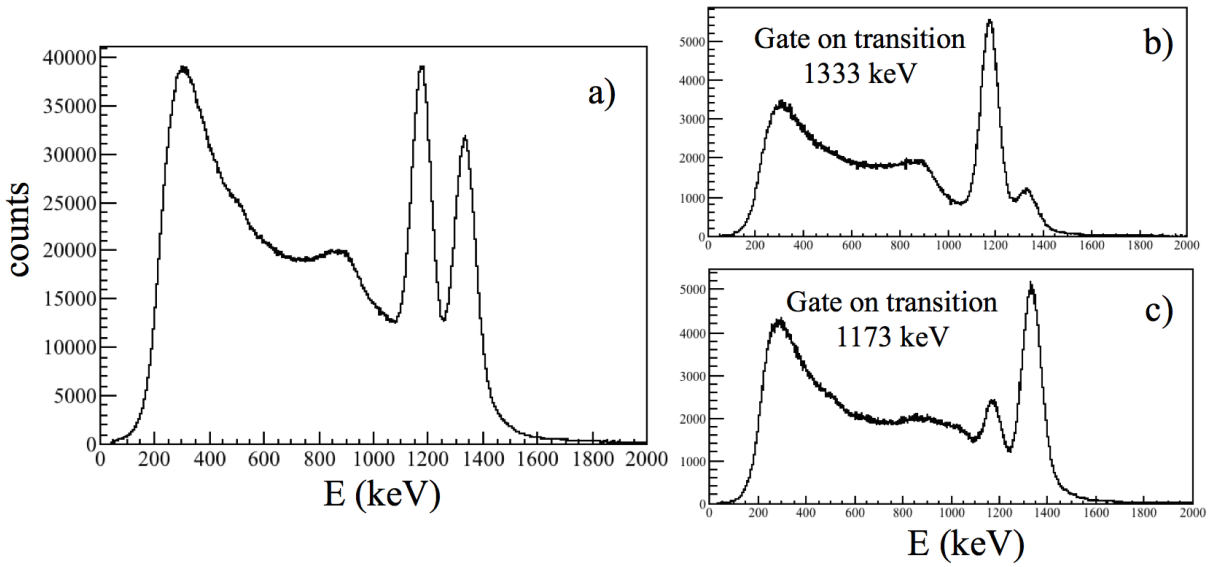

Figure 4.25: a) Experimental singles γ-ray spectrum measured with the ^{60}Co source. b) $\gamma\gamma$ coincidence spectrum for the ^{60}Co source gated on the transition at 1333 keV. c) $\gamma\gamma$ coincidence spectrum for the ^{60}Co source gated on the transition at 1173 keV.

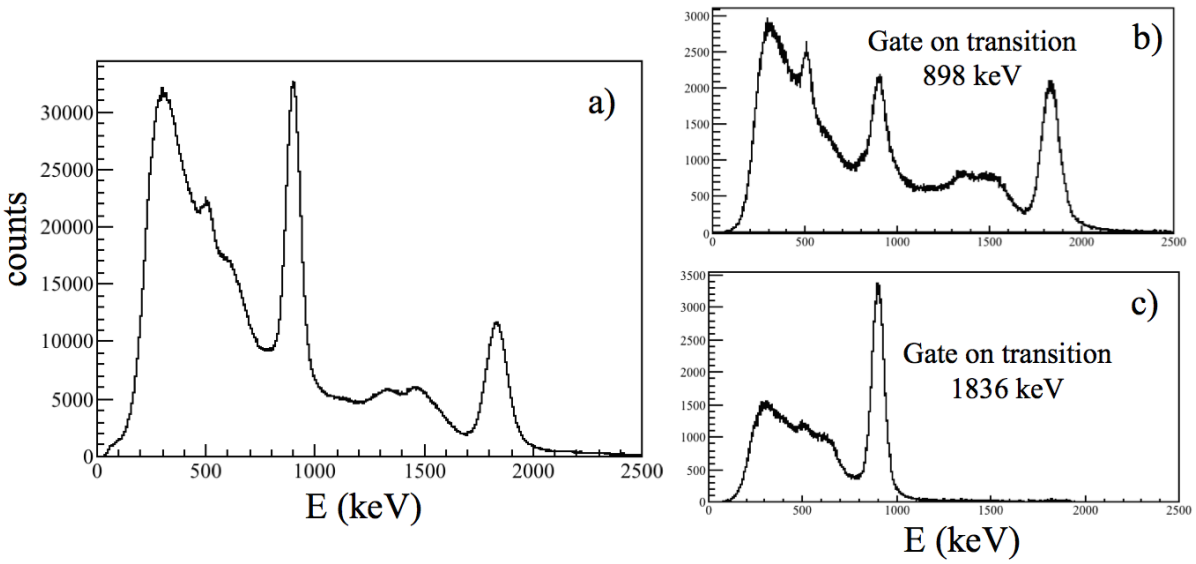

Figure 4.26: a) Experimental singles γ-ray spectrum measured with the ^{88}Y source. b) $\gamma\gamma$ coincidence spectrum for the ^{88}Y source gated on the transition at 898 keV. c) $\gamma\gamma$ coincidence spectrum for the ^{88}Y source gated on the transition at 1836 keV.

Table 4.3 contains the experimental efficiencies obtained with this method, where now the error in the efficiency is only due to the error in the determination of the number of counts in the

photopeak and, as a consequence, the errors are smaller as compared to the first method.

Table 4.3: Efficiency of the DALI2 array for the energies of the five γ-ray transitions from the sources (^{60}Co, ^{88}Y and ^{137}Cs). The efficiencies were obtained with the two methods explained in the text.

Energy (KeV)	M1 Efficiency (%)	M2 Efficiency (%)
661.66	24.1(12)	-
898.04	20(1)	20.78(8)
1173.23	15.7(8)	16.01(7)
1332.49	15.6(8)	15.62(6)
1836.07	11.5(6)	11.87(5)

4.2.4 Addback

In the spectrum taken with a γ-ray detector, the photopeak area corresponds to events in which the photoelectric absorption process has taken place (also multiple scattering of the γ ray within the same crystal but with much less probability). However, the probability of the photoelectric process decreases strongly with the energy of the γ ray, it only being the dominant process at energies below a few hundred of keV. For energies between 250-4000 keV, the Compton scattering process becomes the dominant interaction process [95]. When the γ ray suffers a Compton scatter, the deposition of its energy can take place in different detectors. The addback routine is an algorithm which tries to recover the full energy of the γ ray scattered between several crystals. The basic idea of the addback algorithm is the following: if two or more energy depositions are registered in neighboring detectors, these events are identified as a single γ ray and its energy is obtained as the sum of the individual energies ($E_\gamma = E_1 + E_2 +$ ...). The detector with the largest energy deposition is assigned as the first interaction of the γ ray and its angle is then used to perform the Doppler correction. Neighboring detectors are those whose mean interaction point is located within a certain radius. The mean interaction point of each detector was calculated with GEANT4 simulations. Figure 4.27 shows the spectrum measured with the ^{88}Y source without (black histogram) and with (red histogram) addback. The considered maximum distance between neighboring detectors was 15 cm. This value was obtained from GEANT4 simulations and it will be explained later. As shown in Fig. 4.27, the reconstruction of the addback has a greater effect for the transition at higher energy.

4.2.5 Doppler analysis

The Doppler effect is the change in frequency (wavelength) of light, caused by the relative motion of the source and the observer. In our case, the ions are traveling with velocities around $\beta \approx 0.5$ when they emit γ radiation. The γ radiation is detected with DALI2, which is at rest with respect to the ions. Therefore, the γ rays emitted by the nuclei are subject to relativistic

Doppler shifts. The relation between the energy in the laboratory system of γ rays emitted from fast-moving ions, E_{lab}, and its energy in the center of mass, E_{CM}, is given by:

$$E_{CM} = \gamma(1 - \beta cos\theta_{lab})E_{lab} \tag{4.20}$$

with θ_{lab} being the γ-ray emission angle with respect to the direction of the ion, β is the velocity of the ion at the moment of the emission and γ is the Lorentz factor. Figure 4.28 a) shows the ratio between the energies in the laboratory and the CM systems as a function of the emission angle for different velocities of the projectile. For emission at rest ($\beta = 0$), the energies are the same for all angles and as β increases the ratio, E_{lab}/E_{CM}, varies more with respect to the emission at rest. Figure 4.28 b) displays the γ-ray energy spectrum (black histogram) measured by DALI2 for the Coulomb excitation of ^{136}Te on the Au target. The spectrum in the laboratory system does not show any peak. In the same figure we also display the same spectrum but Doppler corrected (red spectrum). The peak at around 600 keV corresponds to the transition from the first excited 2^+ state to the 0^+ ground state in ^{136}Te. This spectrum was Doppler-corrected with the velocity and angles outside the target since this 2^+ state is known to have a lifetime of several picoseconds and, therefore, the emission of the γ ray happens mostly downstream of the target.

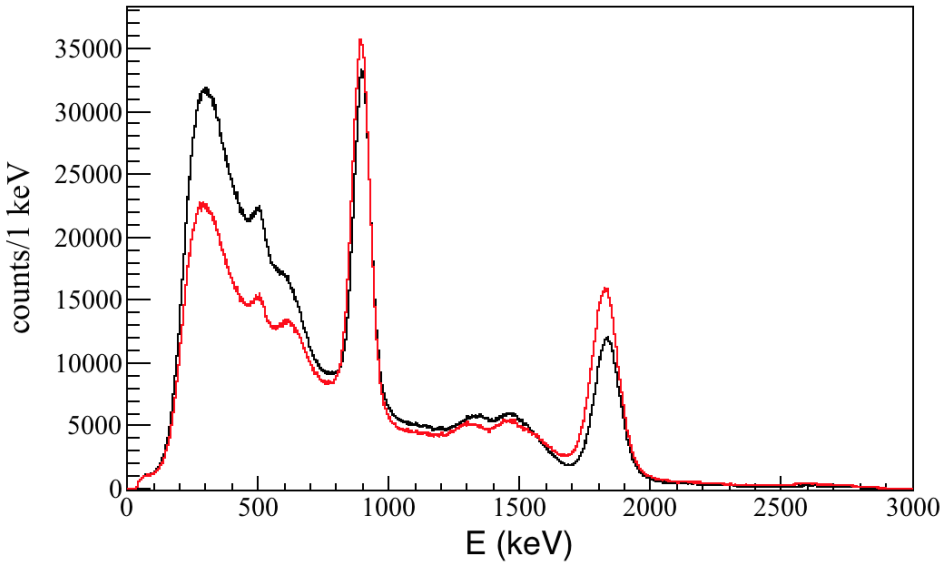

Figure 4.27: Comparison between the experimental γ spectrum measured with the ^{88}Y source without (black histogram) and with addback (red histogram). A maximum distance of 15 cm was considered in the addback algorithm.

In eq. 4.20, the angle, θ_{lab}, is defined as the angle between the γ-ray emission and the direction of the emitting nucleus. The angle of detection was obtained through GEANT4 simulations to determine the mean interaction point of each detector in which the γ ray is detected. The angle of the trajectory of the emitting nucleus was obtained with three PPACs placed at F8, two PPACs before the target to calculate the incoming angle and one extra PPAC behind the

target to obtain the outgoing angle. The scattering angle of the projectiles was negligible as compared to the angle of the γ-ray detection and we did not observe an improvement of the Doppler correction when the angle of the scattered ion was also considered. Another factor on which the angle, θ_{lab}, depends is the offset of the target from its nominal position, z_{off}. This offset was obtained through an optimization of the Doppler correction for states of different nuclei with well known energies and lifetimes. Different z_{off} parameters were employed in the Doppler correction, we chose the z_{off} parameter with which we got the correct energy and the best resolution for all transitions. The z_{off} values obtained were -21.75 and -10.5 mm for the C and Au targets, respectively.

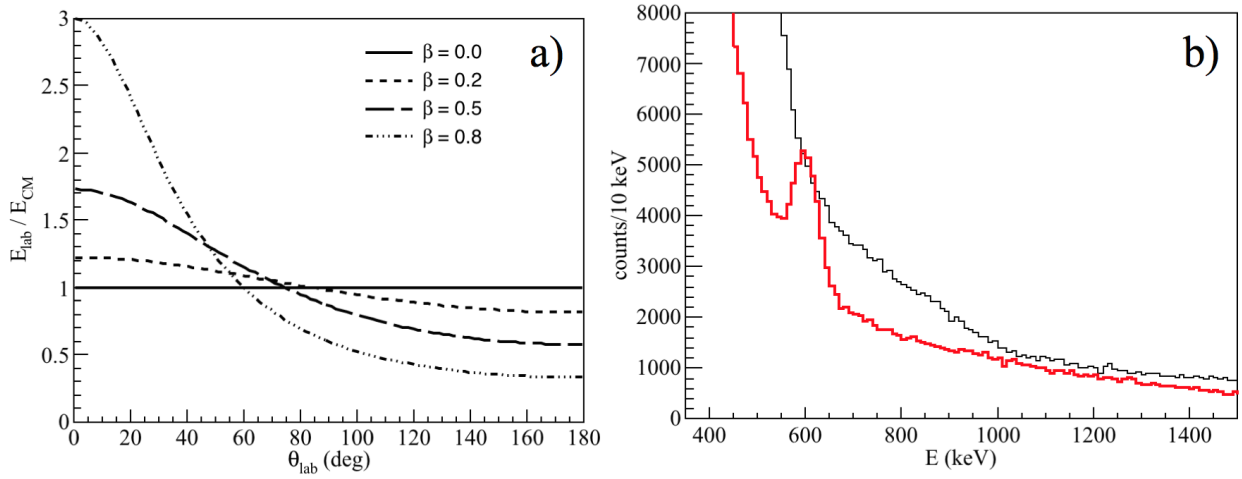

Figure 4.28: a) Ratio between the energies in the laboratory system and in the CM system as a function of the γ-ray emission angle for different velocities of the projectile. b) γ-ray energy spectrum obtained for the Coulomb excitation of ^{136}Te on the Au target without the correction for Doppler shift effects (black histogram) and with Doppler correction (red histogram).

The velocity, β, in eq. 4.20 corresponds to the velocity of the ions at mid-target (assuming that the γ-ray emission occurs at mid-target). Experimentally, we measure the velocity in BigRIPS, β_{BR}, which corresponds to the velocity of the ions after the F5 degrader. Similarly, we measure the velocity in ZeroDegree, β_{ZD}, which corresponds to the velocity after the F10 PPAC. However, between the F5 degrader and the target there are several layers of material which cause the β_{BR} value to change up until the ions reach the target (the same happens in ZeroDegree). To obtain the velocities before, after and at mid target we use LISE^{++} simulations. First, we take the mean value of the β_{BR} distribution and we introduce this velocity in LISE^{++} as the velocity after the F5 degrader. Then we calculate the velocity before, in the middle and after the target considering all beam-line materials. We also calculate the velocity in ZeroDegree and verify that this velocity is similar to the experimentally measured β_{ZD}. In addition, we also check the consistency of the energy-loss calculation with the empty target run. The energy loss in the target was also verified with GEANT4 simulations. Table 4.4 contains the experimental velocity of several ions in BigRIPS and ZeroDegree, and the calculated velocities with LISE^{++}

before, in the middle and after the target and at the end of ZeroDegree. As can be seen in this table, a good agreement is observed between the calculated and the measured velocities in ZeroDegree.

Table 4.4: Average velocity of the isotopes in BigRIPS (experimental), at the entrance, middle and end of the target (calculated), and in ZeroDegree (calculated and experimental).

Isotope BR	Isotope ZD	Target	β_{BR}	$\beta_{before\ target}$	$\beta_{mid\ target}$	$\beta_{after\ target}$	$\beta_{ZD\ LISE++}$	$\beta_{ZD\ exp}$
^{136}Te	^{136}Te	no	0.5465	-	-	-	0.5237	0.5243
^{135}Sb	^{135}Sb	no	0.5440	-	-	-	0.5215	0.5222
^{134}Sn	^{134}Sn	no	0.5418	-	-	-	0.5197	0.5204
^{136}Te	^{136}Te	Au	0.5466	0.5275	0.4930	0.4477	0.4411	0.4455
^{136}Te	^{136}Te	C	0.5467	0.5277	0.4942	0.4503	0.4437	0.4437
^{135}Sb	^{135}Sb	C	0.5440	0.5257	0.4928	0.4498	0.4435	0.4432
^{134}Sn	^{134}Sn	C	0.5424	0.5240	0.4918	0.4501	0.4439	0.4427

4.2.6 GEANT4 simulations

The GEANT4 package of DALI2 was developed by P. Doornenbal. The main aim of this package is to characterize the response of the DALI2 spectrometer. The typical simulation is divided into three steps as discussed in the following.

EventGenerator: in the first step we simulate the projectile impinging on the reaction target, or the sources at rest used in the calibration. For that, we define in the input of the EventGenerator the mass, A_P, the atomic number, Z_P, and the charge state, Q_P, of the isotope. The energy of the isotope before the target, E_P, and the resolution of this distribution, ΔE_P, are also defined and provided according to the experimental ones. Also, the target material and its thickness are defined in this step. Lastly, the energy and lifetime of the γ-ray transition and its angular distribution (uniform, prolate or oblate) are included in the input. The number of events to be simulated is also a variable in the input. From this part of the simulation we can obtain some results such as the velocity of the ions after the target. The obtained velocities after the target are in good agreement with the ones calculated with LISE^{++}. In addition, from the first part of the simulation we can also determine the average velocity at the moment of γ-ray emission. For short-lived excited states, this average value corresponds to the velocity at mid-target and for excited states with lifetimes of several picoseconds the average β is approximately the velocity downstream of the target. Figure 4.29 shows the β distribution at the moment of γ-ray emission for the case of the ^{136}Te beam impinging with 165 MeV/u on a 534 mg/cm^2 ^{12}C target. The number of γ rays emitted downstream of the target increases with increasing lifetime. For γ-ray transitions decaying from states with lifetimes of several ps, the Doppler correction was performed with the velocity downstream of the target to shift the energy to the proper value.

EventBuilder: in the second step, we simulate the interaction of the γ rays generated in the

first step with the DALI2 detectors. The geometry of the DALI2 array is defined as a plain text file. The individual resolution of each detector was also included as an input. The parameters, a_i, of each crystal ($\sigma_E = a\sqrt{E}$) obtained with the calibration sources were used. The beam pipe surrounding the target is also included. Finally, the z_{off} offset with respect to the nominal target position was taken into account.

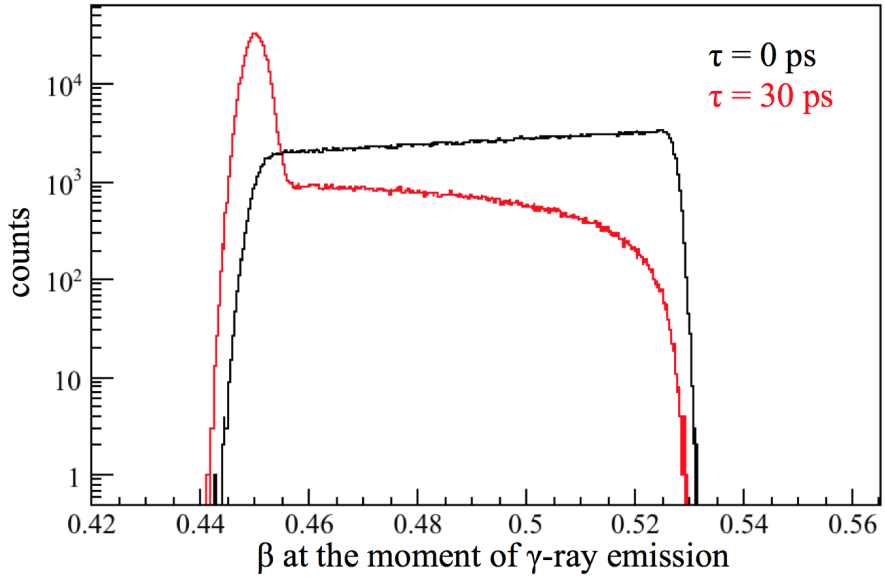

Figure 4.29: β distribution at the moment of γ-ray emission for a ^{136}Te beam impinging with 165 MeV/u on a 534 mg/cm^2 ^{12}C target and assuming lifetimes of 0 (black) and 30 ps (red), respectively.

Reconstructor: in the last step, the analysis of the simulated data is carried out. The analysis in the reconstructor was performed identically as in for treatment of the experimental data which will be described in the next chapter.

Once the three steps are performed, we can extract different information about the DALI2 response. We will start with the response functions of DALI2 for different energies of γ rays. Figure 4.30 a) displays the DALI2 response for γ-ray energies from 0 to 3.5 MeV in steps of 0.5 MeV and assuming vanishing lifetime of the excited state. The γ rays were emitted in flight by ^{136}Te ions moving at β=0.5. As shown in this figure, as the γ energy increases the efficiency decreases and the resolution worsens. Furthermore, for γ-ray transitions with energies higher than 3 MeV we are not able to separate the photopeak and the Compton edge. Figure 4.30 b) shows the DALI2 responses for excited states with an energy of 1.5 MeV and lifetimes of 0, 100 and 500 ps. The lifetime of the excited state shifts the average emission point of the γ ray compared to the center of the target where, on average, the emission of γ rays from excited states without lifetimes occurs. If we perform the Doppler correction with the velocity and angles at mid-target, the photopeak of a γ-ray transition from an excited state with lifetime is moved towards lower energies and the resolution gets worse.

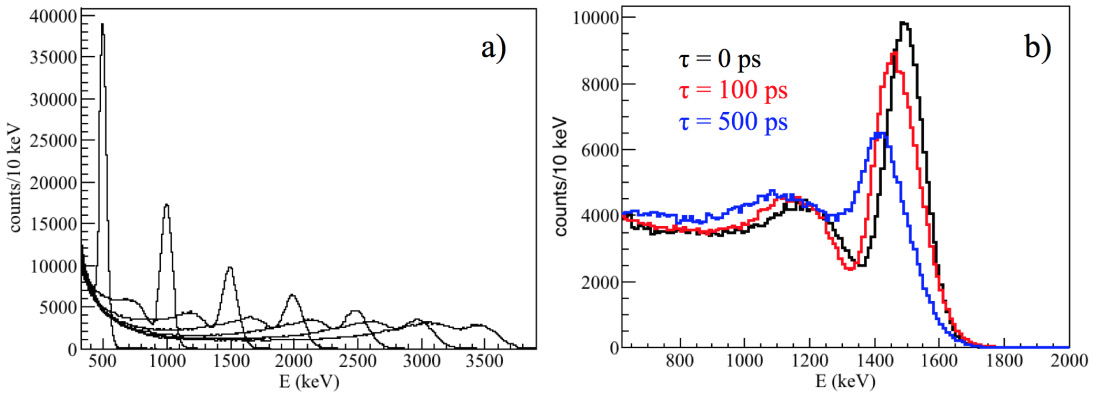

Figure 4.30: a) DALI2 response functions without addback for γ-ray transitions with energies between 0.5 and 3.5 MeV in steps of 0.5 MeV. These γ rays were emitted in-flight by ^{136}Te ions moving at $\beta = 0.5$. b) Simulated 1.5 MeV γ-ray transition responses for 0, 100 and 500 ps lifetimes. Again, the γ rays were emitted by ^{136}Te ions moving at $\beta = 0.5$. The Doppler correction was performed with the velocity and angles at mid-target and the addback was not applied.

We used the GEANT4 simulations to obtain the optimal value of maximum distance to be used in the addback algorithm. Figure 4.31 a) displays the photopeak response of DALI2 for a γ ray at 1.33 MeV when different addback distances are used in the reconstruction of the energy. The distance, d=0 cm, is equivalent to not applying any addback (black histogram). We do not include the distance d=5 cm because at this distance we are still inside the same detector. As we increase the distance, d, there are more counts in the photopeak up to a point where the intensity of the photopeak does not increase. This effect is shown in Fig. 4.31 b), where we plot the number of counts in the photopeak relative to the number of counts in the photopeak for d=0 cm as a function of the addback distance. As is evident, from d=15 cm we do not gain counts in the photopeak and, therefore, d=15 cm was the distance used in the analysis and GEANT4 simulations when the addback algorithm was applied.

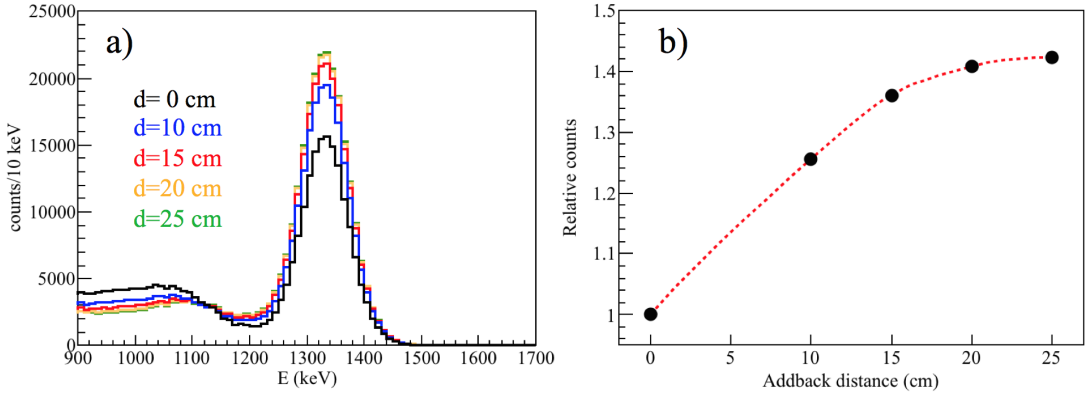

Figure 4.31: a) Effect of the addback procedure when different addback distances are used in the reconstruction of the energy. b) Number of counts in the photopeak relative to the same number for d=0 cm as a function of the addback distance, d. From d=15 cm the number of counts in the photopeak starts to plateau, we use this distance in the addback routine.

The response functions of DALI2 obtained with GEANT4 will be used to fit the Doppler-corrected γ-ray spectra of different isotopes and to extract the intensity of each transition. Therefore, we need to verify that the simulations are in good agreement with experimental measurement. For that we use the data obtained with the γ-ray sources. Figure 4.32 shows a comparison between the experimental (black histograms) and simulated (red histograms) spectra for the three different sources. The simulated spectra were obtained as the sum of the fitted experimental background (blue dashed line) and the simulated DALI2 response for the different γ rays (black dashed line). Good agreement between the experimental and simulated spectra is observed which indicates that the resolution calibration of each detector was performed correctly. We also verified that the efficiency of the DALI2 array in the GEANT4 simulation is consistent with the experimental one. For that, again, we use the efficiencies obtained with the γ-ray sources. In addition, we have also calculated the experimental efficiencies when the addback algorithm was applied to the energy spectra measured with the three different sources. The addback efficiencies were calculated using the method 1 explained in section 4.2.3.1. Regarding the GEANT4 efficiencies, we simulated γ-ray transitions with the experimental energies and compared the number of counts in the photopeak to the number of simulated transitions. In table 4.5, the experimental and simulated efficiencies of the DALI2 array without and with addback are quoted for the five γ rays emitted from the sources. In Fig. 4.33, we show a comparison between the experimental and GEANT4 simulated γ-ray efficiencies with and without addback. For the case without addback, the GEANT4 efficiencies are in perfect agreement with the experimental ones, while for the case with addback, in general, the GEANT4 efficiencies are higher than the experimental ones. This might be because in the GEANT4 simulation we are not considering background and, as a consequence, the reconstruction of the energy is always between two, or more "good" Compton events. However, in the experiment there was significant background and these background events also enter in the reconstruction of the γ-ray energy, lowering the photopeak efficiency. For this reason, we always used specta without addback to determine cross sections in coincidence with γ rays.

As previously mentioned, the angles of the DALI2 detectors were obtained from the GEANT4 simulation. The angles were derived from the mean interaction point of each detector where the γ rays were detected. We investigated the dependence of the detector angles from both the γ-ray energy and the beam energy, we found negligible changes. The only change observed in the angles is when we consider different lifetimes of the excited state since the average position at the moment of the γ-ray emission depends on the lifetime resulting in the angles changing.

Table 4.5: Summary of the experimental and simulated DALI2 efficiencies without and with addback.

	γ efficiency (%)				
	No-addback			Addback	
	Exp		GEANT4	Exp	GEANT4
Energy (KeV)	method 1	method 2		method 1	
661.66	24.1(12)	-	23.5	27.7(14)	27.7
898.04	20(1)	20.78(8)	19.8	23.3(12)	24.9
1173.23	15.7(8)	16.01(7)	16.7	20.7(10)	22.2
1332.49	15.6(8)	15.62(6)	15.2	20.1(10)	20.7
1836.07	11.5(6)	11.87(5)	11.9	16.3(8)	17.3

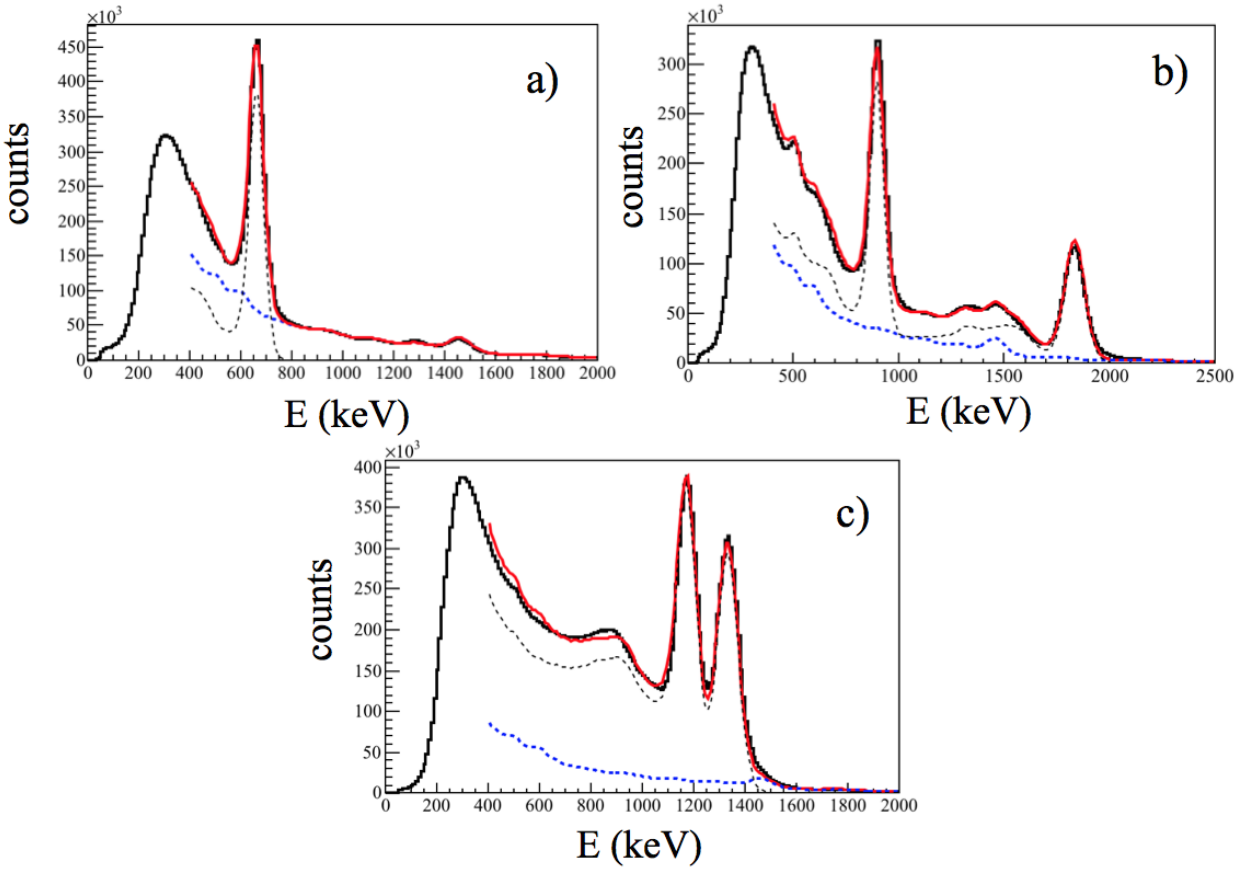

Figure 4.32: Comparison between the experimental specta measured with the three different sources and the GEANT4 simulations for the a) ^{137}Cs, b) ^{88}Y and c) ^{60}Co sources. The experimental spectra correspond to the black histograms, the GEANT4 simulations of the DALI2 response are the black dashed line and the experimental background is the blue dashed line. The sum of the GEANT4 simulation and the experimental background is represented by the red line. No addback was applied.

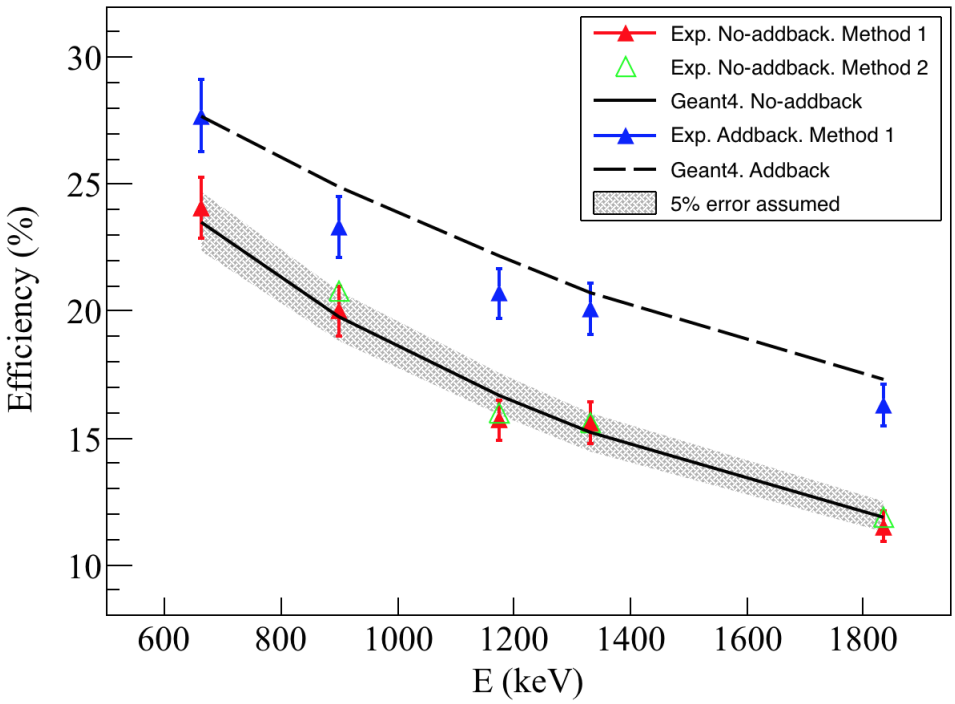

Figure 4.33: Experimental (points) and simulated GEANT4 (lines) efficiencies with and without addback. The efficiencies are quoted in table 4.5. The shaded area represents the 5% error we consider in the analysis.

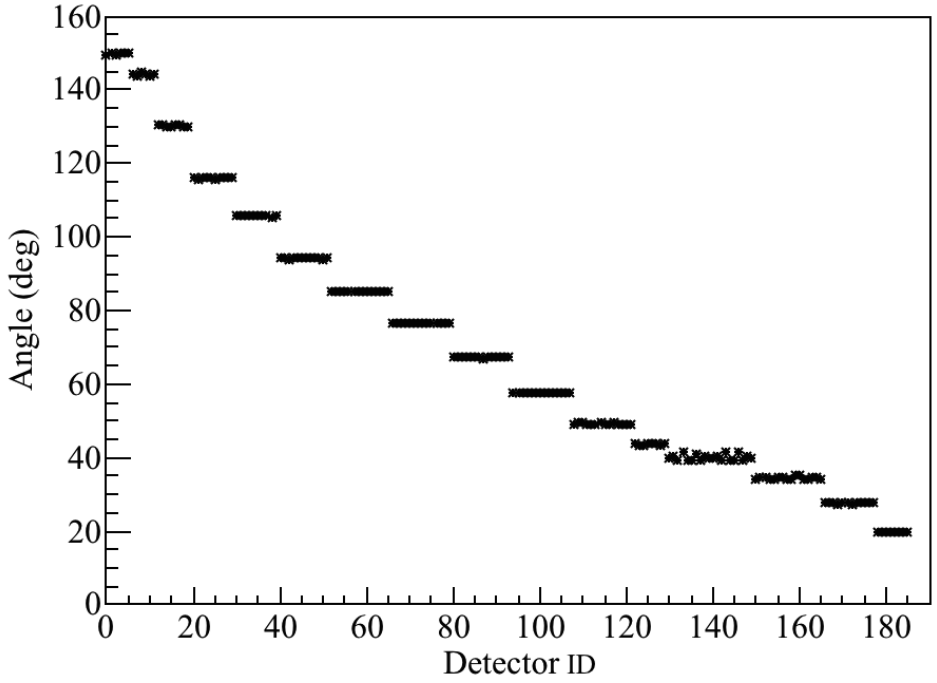

Figure 4.34: Average detection angle of each DALI2 detector simulated with GEANT4. The angles were obtained assuming no lifetime of the excited state so that the angles are with respect to the center of the target.

4.3 Scattering Angle reconstruction and calibration of the PPACs

To obtain the differential inelastic scattering cross sections, we need to know the angular distribution of the scattered ions. The scattering angle is defined as the change in direction of the ion due to its interaction with the target. To determine this angle we need to know the position of the ions before and after the target. In Fig. 5.6 of the next chapter, where we discuss in detail the analysis procedure to obtain differential cross sections, we show a schematic picture of the PPAC positions at the F8 focal plane. The position of the ions in the F8 focal plane was measured with two PPACs situated upstream of the secondary target and extrapolated to the target position. The PPAC positioned downstream from the target was used to measure the deviation from the F8 position and obtain the angle of the outgoing ion with respect to the beam axis. Since the determination of the scattering angle is only of importance in Coulomb excitation experiments, usually these PPACs are not used and, the F8 PPAC, situated after the target, usually removed from the beam line. Therefore, their positions along the beam line are not fixed. To compensate, we introduce horizontal (x_{off}) and vertical (y_{off}) offsets with respect to their nominal positions. To determine these offsets we use the empty target run, since without the target at F8 the ion's trajectory will be unchanged between different focal planes.

The offsets, x_{off} and y_{off}, of the first PPAC at F8 were kept to 0 mm since the determination of the scattering angle is done with respect to the incident position in this PPAC. To obtain x_{off} and y_{off} for the second PPAC situated before the target, we know that without target the following relation between the positions in the F8 and F11 focal planes must be fulfilled:

$$\frac{F8X}{F11X} \approx -1 \qquad\qquad \frac{F8Y}{F11Y} \approx -1 \tag{4.21}$$

where X and Y refer to the horizontal and vertical positions, respectively. This relation was calculated with the GICOSY code and corresponds to the transfer matrix properties. So, we modified the offsets of the second PPAC such that these conditions are satisfied. Figure 4.35 a) displays the correlation between the horizontal positions of $^{136}Te^{52+}$ ions at the F8 and F11 focal planes for the run without target and obtained with the final x and y offsets of the second PPAC at F8. As is visible in this plot, the condition, $F8X = -F11X$, is satisfied.

Once the position at the F8 focal plane is well defined, we can fix the offsets x_{off} and y_{off} of the third PPAC situated after the target. Again, we use the empty target run. As we know the position (X and Y) at F8, and there is no target between the first two PPACs and the third, we can extrapolate these positions to the third PPAC. The positions measured with the third PPAC must be consistent with the extrapolated ones. Figure 4.35 b) shows a correlation plot between the extrapolated and measured horizontal positions at the place of the third PPAC at F8. This plot was generated, again, for $^{136}Te^{52+}$ ions without target and with the final x_{off} and y_{off} values of the third PPAC. Table 4.6 lists the final x_{off} and y_{off} offsets of the three PPACs

at F8.

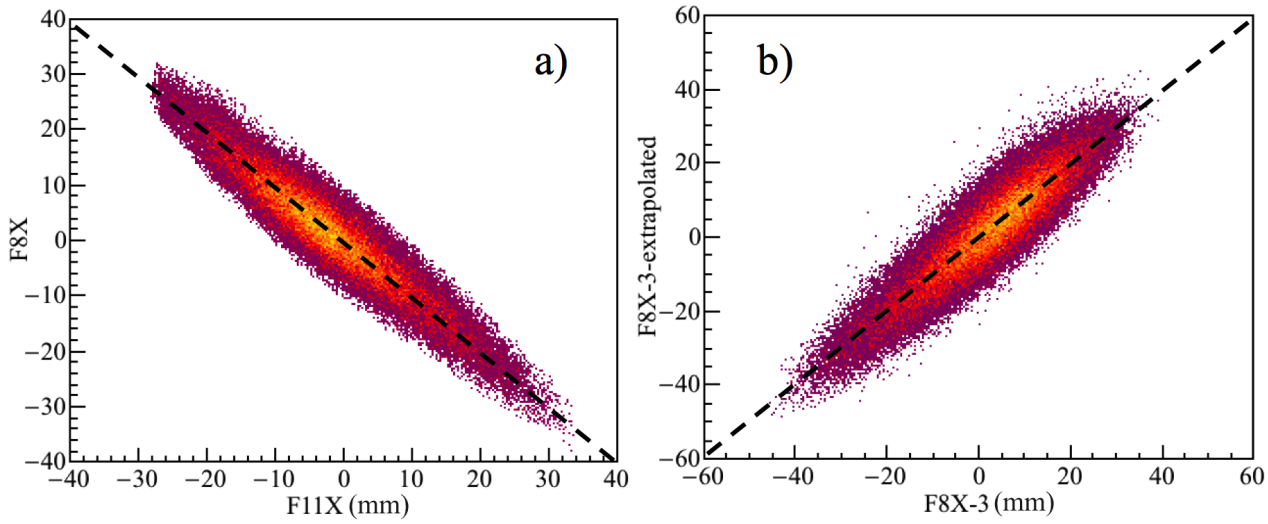

Figure 4.35: a) Correlation plot between the horizontal positions at the F8 and F11 focal planes. b) Correlation plot between the extrapolated and measured horizontal positions at the place of the third PPAC at F8. Both plots were obtained with empty run, gated on ^{136}Te $^{52+}$ ions in BigRIPS and ZeroDegree and with the final set of offsets.

Table 4.6: Final set of horizontal, x_{off}, and vertical, y_{off}, offsets of the three PPACs at F8 with respect to their nominal position.

PPAC	F8-1	F8-2	F8-3
x_{off} (mm)	0	0	-1.72
y_{off} (mm)	0	-1.6	-2.45

Once we have fixed the offsets, x_{off} and y_{off}, we can verify that they have been optimized correctly checking the θ and φ scattering angular distributions. The resolution of the θ scattering distribution should be the most enhanced and more importantly the azimuthal scattering distribution has to be uniform between [$-\pi$,π], since the ions are uniformly scattered in the azimuthal direction. In Fig. 4.36 we show the raw φ angular distribution (black histogram) measured without target and any optimization. As is visible, this distribution is not uniform and presents a pronounced asymmetry. In the same figure we also show the φ angular distribution after the optimization of the PPACs offsets (red histogram). Now the azimuthal angle is nearly constant in the range [$-\pi$,π] as expected.

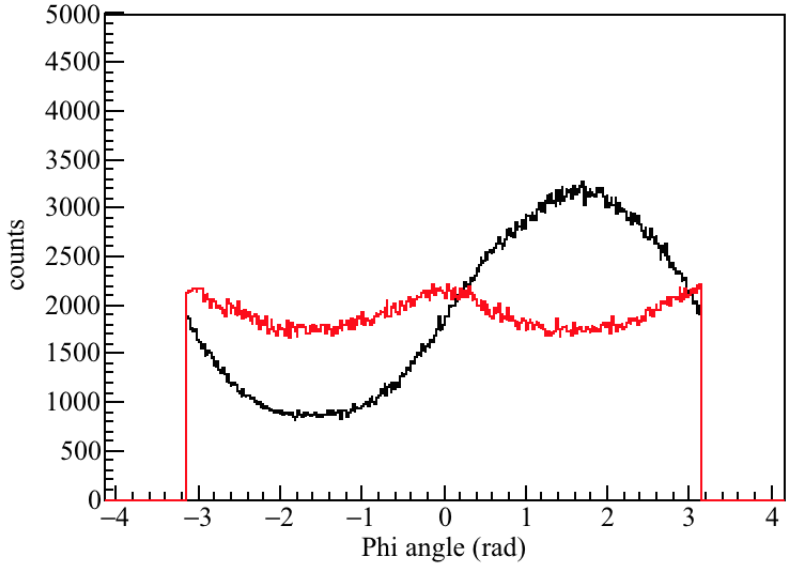

Figure 4.36: φ azimuthal scattering angle distribution of all ions measured with empty target before (black curve) and after (red curve) the optimization of the x_{off} and y_{off} offsets. After the optimization, a flat distribution of the azimuthal scattering angle is observed.

Chapter 5

Experimental Results and Discussion

In this chapter, the experimental results are presented and discussed. In section 5.1, the data analysis of the intermediate-energy Coulomb excitation of ^{136}Te is presented. The experimentally derived B(E2) value is compared to previous results reported in literature and to different theoretical calculations. Section 5.2 shows the analysis of the cross sections and the obtained cross section systematics for the multi-nucleon knockout from different projectiles at energies around 165 MeV/u. The experimental cross sections are compared to predictions obtained with the Liège intranuclear cascade model. Finally, section 5.3 describes the results obtained for ^{133}Sn, which were recently published in Ref. [110].

5.1 Intermediate-energy Coulomb excitation of ^{136}Te

In this section we will explain in detail the different steps which we have followed in the analysis of the Coulomb excitation data at intermediate-energy for the ^{136}Te nucleus to obtain the B(E2) value of the first excited 2^+ state. This value will be compared to the previous experimental values from literature [46, 47, 53] and with different theoretical calculations, mainly shell model calculations using realistic effective interactions [111]. Finally, we discuss a new excited state observed at 4.2 MeV and assign its spin.

5.1.1 Experimental conditions and PID plots

Since the aim of this part of the experiment was to measure the Coulomb excitation of the ^{136}Te nucleus, the BigRIPS and ZeroDegree settings were optimized for the transmission of this isotope. The energy of the ^{136}Te ions before the secondary target was around 165 MeV/u. At these energies, besides the electromagnetic interaction between the projectile and the target, also the nuclear interaction contributes to the excitation cross section. To quantify both processes, two different targets were installed at F8. A gold target (950 mg/cm^2) was used to induce the Coulomb excitation, while a carbon target (535 mg/cm^2) was used to extract the nuclear contributions to the total cross sections measured for the inelastic scattering reactions with the gold target. The measurement time was around 13 and 4 h for the Au and C targets,

respectively. Table 5.1 contains the energies of the ^{136}Te ions before, after and at mid-target for both targets.

Table 5.1: Energies of the ^{136}Te ions before, after and at mid-target for the two different targets used in this part of the experiment.

Target	E_{beam} before-target (MeV/u)	E_{beam} mid-target (MeV/u)	E_{beam} after-target (MeV/u)
Carbon	165	140	112
Gold	165	139	110

Regarding the F7 downscaled trigger, the scaling factor was set to 1/60 due to the high secondary beam intensity. Figures 5.1 a) and c) show the particle identification obtained with the BigRIPS spectrometer for the gold and carbon targets, respectively. The total number of ions detected in BigRIPS for each nucleus is summarized in table 5.2. Figures 5.1 b) and d) show the pid plots for the ZeroDegree spectrometer with a gate on ^{136}Te ions in BigRIPS. After the target, the ^{136}Te ions are observed in three charge states, due to electron pickup from the target (also with the materials of the detectors). The probability of electron pickup depends on the charges of the projectile and the target. For the gold target (Z=79), the directly measured (without transmission corrections) charge state distribution was 50% fully stripped ions, 42% hydrogen-like ions and 8% helium-like ions, while for the carbon target (Z=6), 64% of the ions were fully stripped ions, 33% hydrogen-like ions and 3% helium-like ions. As the carbon target has a lower atomic number, less electrons were captured by the projectile meaning more ions were observed fully stripped.

Table 5.2: Total number of ions detected in BigRIPS for the two different targets.

Nucleus	Number of ions in BigRIPS Gold	Carbon
^{136}Te	$2.36{\cdot}10^{8}$	$6.72{\cdot}10^{7}$
^{135}Sb	$1.02{\cdot}10^{8}$	$2.82{\cdot}10^{7}$
^{137}I	$2.80{\cdot}10^{7}$	$8.86{\cdot}10^{6}$
^{134}Sn	$1.33{\cdot}10^{7}$	$3.47{\cdot}10^{6}$
^{134}Sb	$1.10{\cdot}10^{7}$	$4.74{\cdot}10^{6}$
^{135}Te	$1.01{\cdot}10^{7}$	$4.71{\cdot}10^{6}$
^{137}Te	$7.78{\cdot}10^{6}$	$9.62{\cdot}10^{5}$

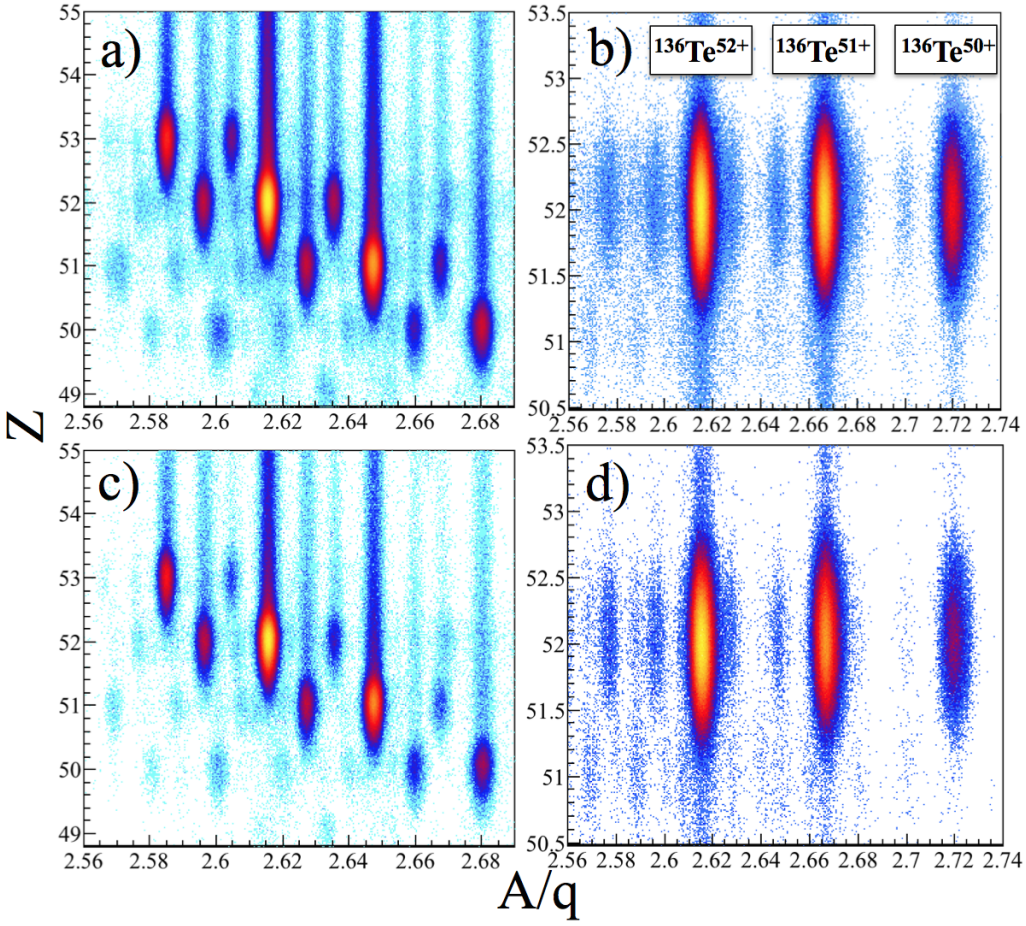

Figure 5.1: Particle identification plots for the BigRIPS spectrometer a) for the gold target and c) for the carbon target. Same identification plots, but now for the ZeroDegree spectrometer b) with the gold target and d) with the carbon target. The plots for ZeroDegree were obtained requiring the identification of ^{136}Te ions in BigRIPS.

5.1.2 γ-ray spectra

The γ rays emitted by the decay of excited states populated through the inelastic scattering reactions with the gold and carbon targets were detected using the DALI2 spectrometer, which was introduced previously in section 3.3. For in-beam γ-ray spectroscopy experiments performed at relativistic energies, the γ-energy spectrum always presents a background component which is caused by atomic processes and strongly depends on the atomic number of the projectile and the target [104]. In the case of our Coulomb excitation experiment, due to the high atomic numbers of the projectile and target (Z=52 and Z=79), a strong background was expected. For this reason, during this part of the experiment, the most downstream detectors (DALI2 ID lower than 52, which corresponds to angles larger than 94° in the laboratory frame) were deactivated (the energy thresholds were set very high). These detectors do not contribute significantly to the statistics for the γ-ray transitions of interest since the γ-ray angular distribution is enhanced in the forward direction in the laboratory frame due to the Lorentz

boost. Figure 5.2 shows the Doppler-corrected γ-ray energy plotted versus the DALI2 detector number for the ^{136}Te ions obtained with the Au target. In this figure, we can see that the detectors with ID lower than 52 were effectively deactivated. In addition, in the analysis, only the detectors with ID higher than 90 were considered since they have a large peak-to-background ratio. Under this condition, the efficiency was reduced from 24% (total DALI2 array) to 13% (DALI2 ID higher than 90) for γ rays at 600 keV emitted from ions moving with velocities around β = 0.5.

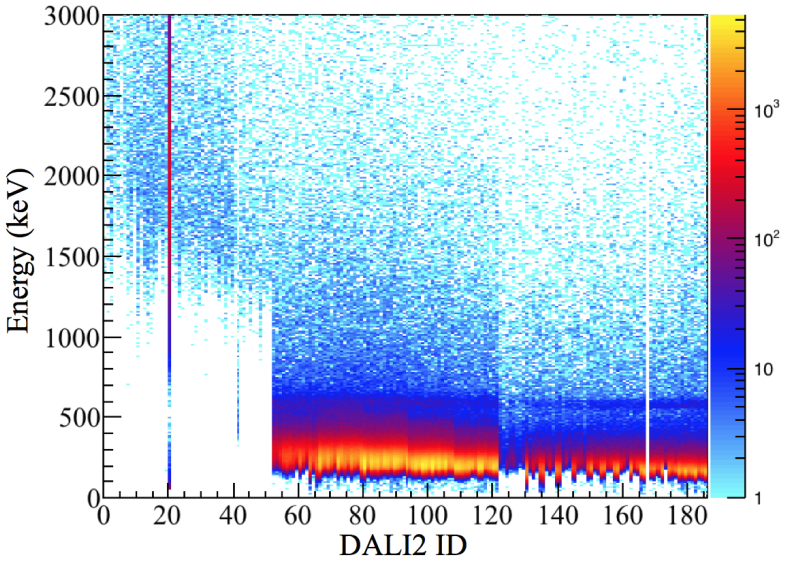

Figure 5.2: Doppler-corrected γ-ray spectrum for ^{136}Te from the inelastic scattering on the Au target plotted against the DALI2 detector number.

Figures 5.3 a) and b) show the Doppler-corrected γ-ray spectra measured in coincidence with ^{136}Te ions detected in BigRIPS and with the fully stripped (52+), hydrogen-like (51+) and helium-like (50+) ^{136}Te ions measured in ZeroDegree for the Au and C targets, respectively. Both spectra were obtained considering only the most upstream detectors (DALI2 ID higher than 90). The 2_1^+ state of the ^{136}Te has a lifetime of several ps (τ=41(6) ps [46, 47] or τ=27(2) ps [53]) and, as a result of this lifetime, the decay of the 2_1^+ state occurs mostly after the target. The mid-target velocities (β=0.4912 for the Au target and β=0.4924 for the C target) were used to perform the Doppler-correction and, as a consequence, the 2_1^+ γ-ray transition energy is shifted to smaller energies with respect to the nominal value. The addback algorithm was not applied to the spectrum with the Au target since the experimental background was very high leading to a considerable incorrectly reconstructed γ-ray energies. The experimental spectra shown in Fig. 5.3 were fitted with the DALI2 response functions simulated using the GEANT4 code (red area) and two exponentials for the background (blue dashed line). For the spectrum obtained with the C target (Fig. 5.3 b)), the background was folded with a step function to reproduce the low energy cut-off. The total fit is shown by the black line for both targets.

As is visible in the spectrum shown in Fig. 5.3 a) obtained with the gold target, only one γ ray with an energy around 600 keV was observed in the energy range up to 2 MeV. This transition corresponds to the γ-ray decay of the 2_1^+ state. The literature value for the $2_1^+ \rightarrow 0^+$ transition is 607 keV, we observe it at slightly lower energies due to the lifetime of the 2_1^+ state. Later, a procedure to obtain the lifetime from this energy shift will be explained. Regarding the observation of the decay of the mixed-symmetry 2_{ms}^+ state, there is no evidence of such a transition in the experimental spectrum and only an upper limit for the B(E2;$0^+ \rightarrow 2_{ms}^+$) value can be determined taking into account the experimental sensitivity. This will be done in subsection 5.1.10.

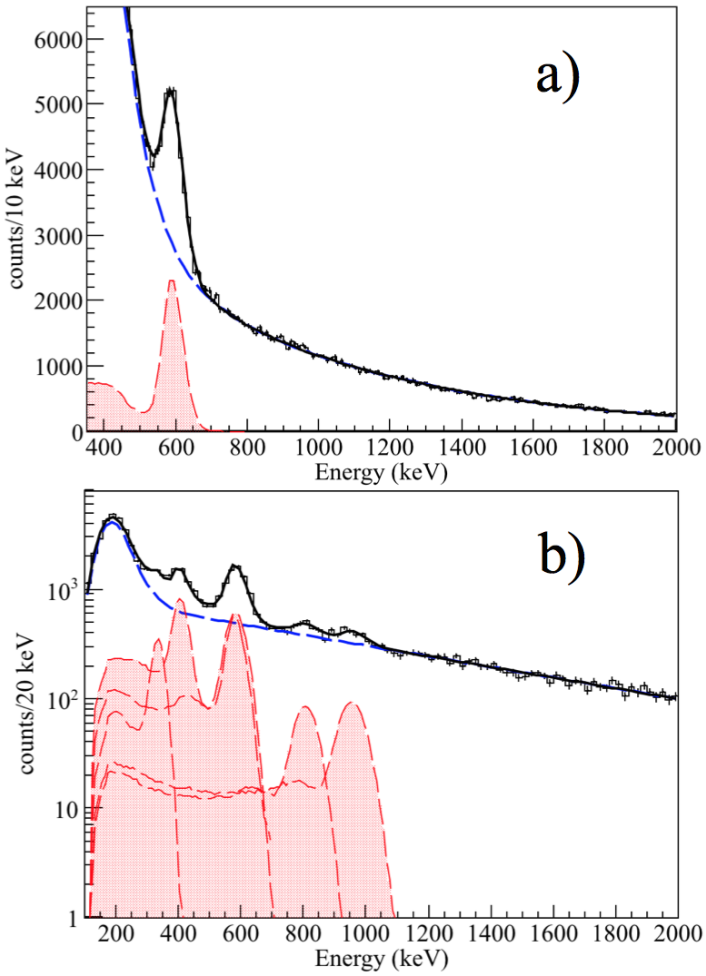

Figure 5.3: Doppler-corrected γ-ray spectrum for the ^{136}Te from inelastic scattering a) on the Au target and b) on the C target.

Besides the $2_1^+ \rightarrow 0^+$ transition, two more γ rays were observed in the spectrum measured with the gold target. Figure 5.4 a) shows the Doppler-corrected γ-ray spectrum for ^{136}Te on the Au target in the energy range from 0 to 7 MeV and considering only events with γ-ray multiplicity lower than 4. There, two γ rays with energies of 3.6(1) and 4.2 (1) MeV are clearly visible, moreover, their intensities are almost equal. This is the first observation of these transitions. To

place them in the level scheme, different conditions were applied to the γ-ray spectrum. Note that, due to the moderate energy resolution of DALI2 at high energies, no γ-γ coincidences were used. Instead, the multiplicity of the γ-ray events, M_γ, was iterated. Figures 5.4 b) and c) show the γ-ray spectra for M_γ=1 and 2, respectively. For the case of M_γ=1, the transition situated at 4.2 MeV is observed stronger than the transition at 3.6 MeV, suggesting that it corresponds to a decay directly to the ground state. In contrast, in the case of M_γ=2, the γ ray at 3.6 MeV has a greater intensity than the γ ray at 4.2 MeV, which suggests that it corresponds to a decay to an excited state. If, for the events with M_γ=2, we sum the energies of two γ rays measured in coincidence, we obtain the spectrum shown in Fig. 5.4 d), where the peak at high energy is well reproduced considering only one γ ray with an energy of 4.2 MeV. All these observations suggest that the transition at 3.6 MeV populates the 2_1^+ state (0.6 MeV+3.6 MeV = 4.2 MeV). The newly observed excited state at an energy of 4.2 MeV has two different branches with roughly the same intensity: one to the 2_1^+ state (γ ray at 3.6(1) MeV) and the other one to the ground state (γ ray at 4.2(1) MeV). The spin and parity of this new state will be discussed later.

As an additional comment, the spectra shown in Fig. 5.4 were fitted considering three exponentials for the background (blue dashed line): the first exponential for the low energy region 350-800 keV (Bremsstrahlung background), the second one for the background situated between 0.8-4 MeV (originated from unresolved high energy transitions emitted by the projectile) and the third one for the background placed between 4-8 MeV (produced by excitations of the target). The procedure of considering three exponential functions to reproduce the background was validated with other nuclei for which no discrete γ rays were observed over the full energy range. This was the case, for example, for ^{135}Sb from inelastic scattering on the Au target. The shape of the background was fixed and a scaling factor was introduced to take into account the different number of ions in BigRIPS. The fixed shape of the background well reproduced the experimental γ-ray spectrum for the ^{135}Sb nucleus. A more precise treatment of the shape of the background would require a statistical model calculation as shown in Ref. [112].

Looking at the γ-ray spectrum measured for inelastic scattering of ^{136}Te on the C target shown in Fig. 5.3 b), besides the $2_1^+ \rightarrow 0_1^+$ transition at 607 keV, four additional peaks with energies around 330, 400, 810 and 960 keV are visible. The first two were already reported in Refs. [113, 114] with energies of 353 and 423 keV, corresponding to the $6_1^+ \rightarrow 4_1^+$ (353 keV) and $4_1^+ \rightarrow 2_1^+$ (423 keV) transitions. Also for these transitions the energies are shifted to smaller values due to lifetime effects. Regarding the transition at 960 keV, in Ref. [115] a γ ray with 962 keV was observed for the first time and was assigned as the $2_2^+ \rightarrow 2_1^+$ transition from a 2_2^+ state placed at 1568 keV. No evidence of the 810(15)-keV transition was found in the literature and we conclude that it was observed for the first time in the present experiment. To get place the 810-keV transition in the level scheme, a γ-γ coincidence analysis was performed. Fig-

ure 5.5 shows the γ-ray coincidences with the 607-keV transition, revealing that all transitions are in coincidence with the first-excited 2^+ state. Also the 607 keV transition is observed in self-coincidence due to Compton events of high energy transitions. Figure 5.5 also shows the γ-ray coincidences with the 962 keV transition. This γ-γ coincidence spectrum is very clean due to the low background in the energy gating region and since there are no coincidences with Compton events originating from higher-energy transitions, showing that the transition at 962(18) keV is clearly in coincidence with the transition at 607 keV and with the transition observed at 810(15) keV. Based on this γ-γ coincidence analysis, the level scheme shown in Fig. 5.5 is proposed, where the new γ ray at 810 keV is situated on the top of the 2_2^+ state.

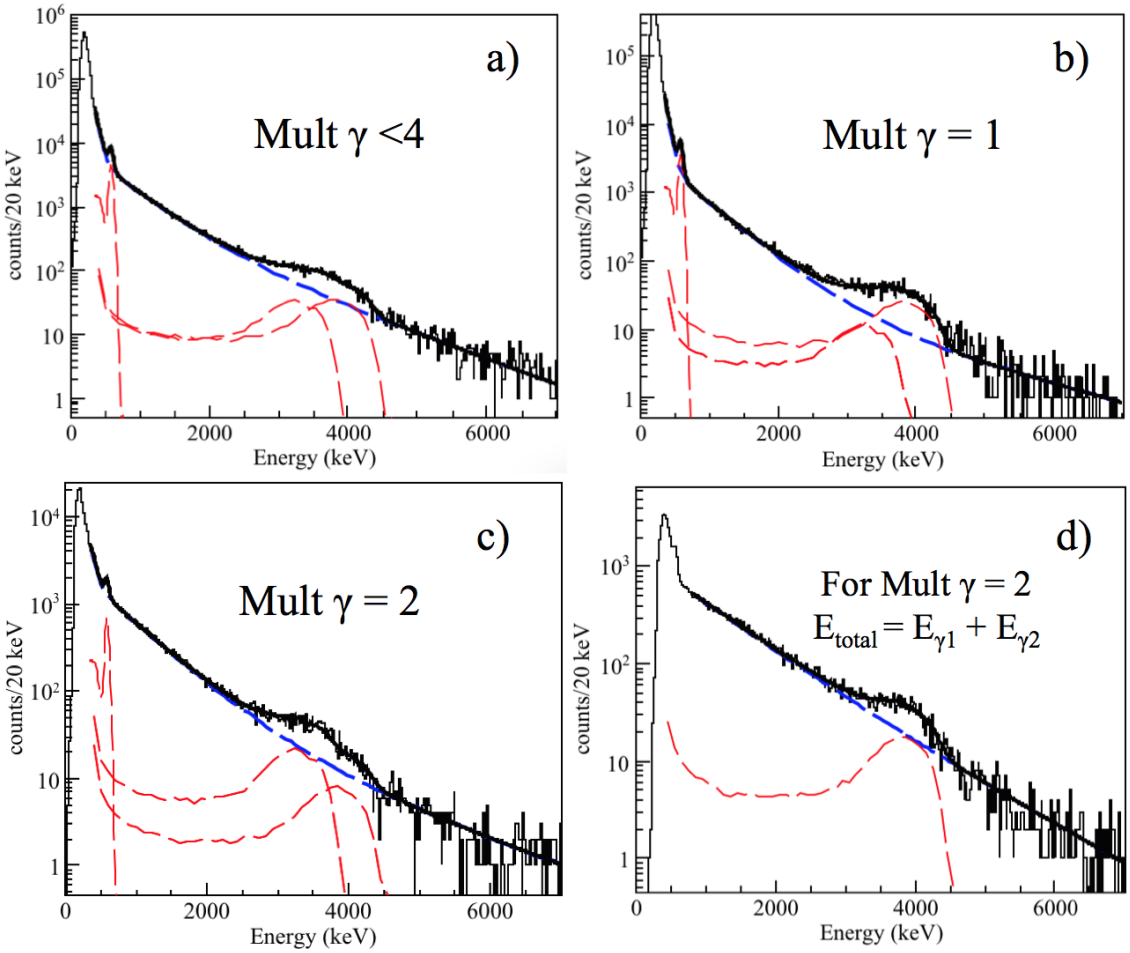

Figure 5.4: Doppler-corrected γ-ray spectra in the energy range from 0 to 7 MeV for ^{136}Te from inelastic scattering on the gold target for a) γ-ray multiplicity < 4, b) γ-ray multiplicity = 1, c) γ-ray multiplicity = 2 and d) γ-ray multiplicity = 2 and the energies of the two γ rays were summed.

5.1.3 Determination of the scattering angle θ and angular resolution

In order to obtain the differential cross section, the scattering angle of the ^{136}Te ions on the target needs to be measured. The scattering angle was measured with two PPACs installed

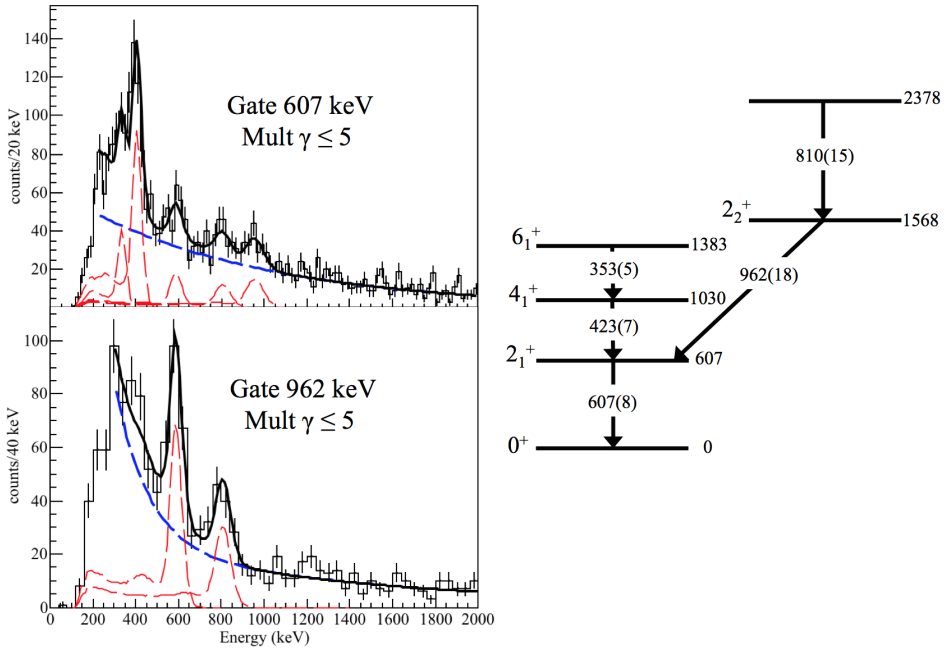

Figure 5.5: Left: γ-γ coincidence spectra for ^{136}Te on the C target gated on the 607-keV (top) and on the 962-keV (bottom) transitions. Right: experimental level scheme of ^{136}Te established from the γ-γ analysis. The energies are quoted in keV.

before the target (to obtain the incoming angle) and one extra PPAC situated behind the target (to get the outgoing angle). A schematic view of this part of the setup is shown in Fig. 5.6, where the positions of the PPACs were varied until a constant distribution for the φ angle was obtained (see section 4.3). The experimental distributions of scattering angles measured for the ^{136}Te without a target and with the C and Au targets are shown in Fig. 5.7 a). The former distributions can be fitted with the function $f(\theta) = A \cdot e^{-\frac{\theta^2}{2\sigma_\theta^2}} \cdot sin(\theta)$, where the first term, A, is a constant factor, the second term, $e^{-\frac{\theta^2}{2\sigma_\theta^2}}$, is a Gaussian function centered at θ=0° and with σ_θ being the experimental angular resolution and the third term, $sin(\theta)$, takes into account the effect of the solid angle. A fit of the experimental angular distribution of ^{136}Te measured with the Au target is shown in Fig. 5.7 b). The resolution parameters obtained from the fits are 4.8 mrad (0.275°) for the empty target, 5.4 mrad (0.31°) with the C target and 8.8 mrad (0.504°) with the Au target. Each of these resolution values include different contributions. For the case of the empty target, the measured angular resolution is due to the uncertainty of the position measurements in the PPACs. To obtain the resolution in the X and Y directions, a Monte Carlo simulation was performed in which the positions in each of the PPACs were randomly chosen from Gaussian functions with resolutions, $\sigma_{x,y}$, and then the scattering angle was calculated in the same way as done in the analysis. The same resolutions, $\sigma_x = \sigma_y$, were considered for all three PPACs involved in the reconstruction of the scattering angle. Finally, the resolutions $\sigma_{x,y}$ were adjusted until the experimental distribution without a target was reproduced. The $\sigma_{x,y}$ value with which we reproduce the experimental distribution is σ =

0.73 mm. Figure 5.7 c) shows the comparison between the experimental angular resolution without a target and the Monte Carlo simulation performed to get the $\sigma_{x,y}$ resolution values. For the runs with C and Au targets, the experimentally measured resolutions have two contributions: one from the uncertainty of the position measurements (measured directly without target) and one stemming from the angular straggling caused by the multiple scattering in the target. This angular straggling can be calculated using the ATIMA code [116], which provides values of 2.3 and 8.0 mrad for the C and Au targets, respectively. The effect of both contributions on the final resolution can be estimated from, $\sigma = \sqrt{\sigma^2_{position} + \sigma^2_{straggling}}$, yielding values in agreement with the directly measured ones.

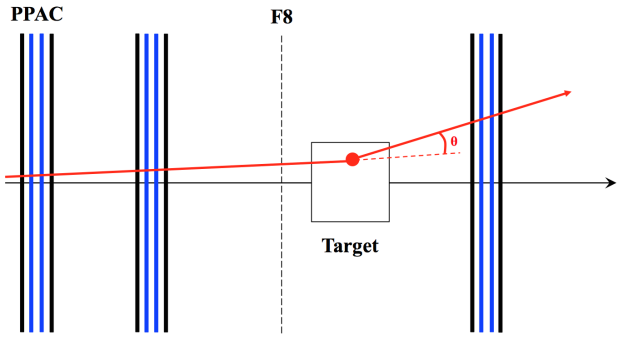

Figure 5.6: Schematic view of the setup used to determine the scattering angle of the outgoing ions.

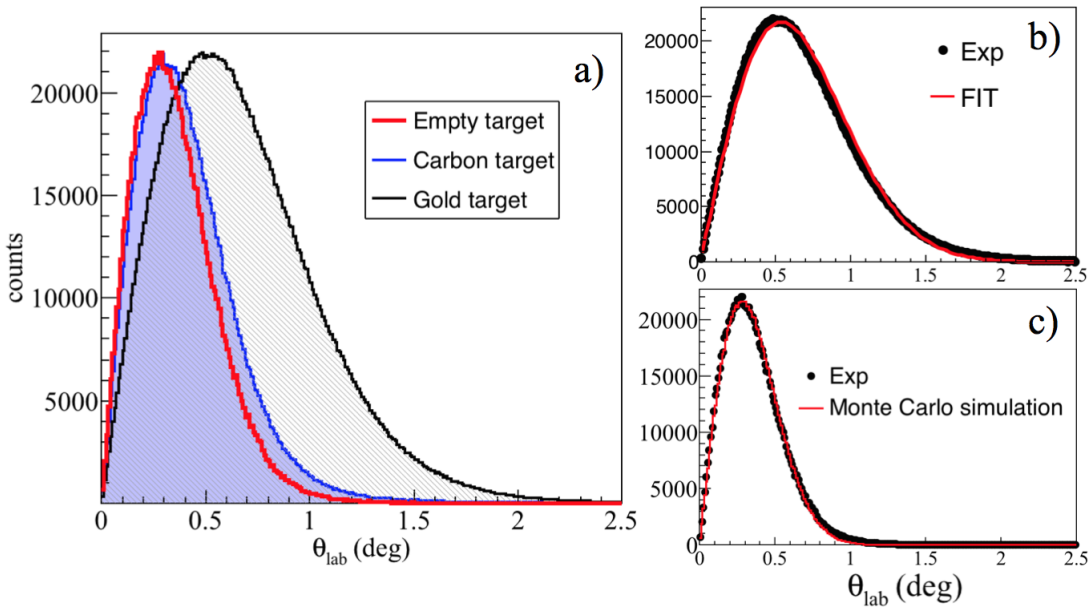

Figure 5.7: a) Experimental angular distributions with a gate on ^{136}Te in BigRIPS without a target and with the C and Au targets. b) Fit of the experimental angular distribution measured with the Au target. c) Comparison between the angular distribution without target and a Monte Carlo simulation where the resolution in the position measurements was fixed to reproduce the experimental resolution observed without target.

5.1.4 Differential and total cross sections

With the scattering angle, the differential inelastic scattering cross section for the different excited states can be calculated. For that, we need to know the intensity of the γ-ray transition as a function of the scattering angle. Figure 5.8 shows the γ-ray energy spectra produced for ^{136}Te gating on different ranges of the scattering angle for the Au (top part) and C (bottom part) targets. These spectra were obtained requiring the identification of ^{136}Te in BigRIPS and the fully-stripped ^{136}Te in the ZeroDegree spectrometer. Since for both targets the $2_1^+ \rightarrow 0^+$ transition was measured with high statistics, a small angular bin size of $\Delta\theta$=0.15° was used to obtain the differential inelastic cross sections for the 2_1^+ state in ^{136}Te. For the different ranges of the scattering angle, the energy spectrum was fitted with the DALI2 response and two exponential functions. The intensity of the 2_1^+ state was extracted from the fit. Since the excitation mechanism is different for the C (mainly nuclear excitations) than for the Au target (mainly Coulomb excitations), the different angular distributions of γ rays of each process have to be considered in the GEANT4 simulations of the DALI2 response. For intermediate-energy Coulomb excitation the nucleus exhibits a prolate alignment while for nuclear excitations an oblate alignment is observed [117]. Figure 5.9 shows three different γ-ray angular distributions for a quadrupole transition, a) no alignment is considered, which results in uniform emission, b) a prolate alignment is considered which corresponds to Coulomb excitation at intermediate energies and, finally, c) an oblate alignment is presented which is assumed for the nuclear excitation. The distributions displayed in the Figs. 5.9 b) and c) were used in the GEANT4 simulations for the excitation of the 2_1^+ state with the Au and C targets, respectively. The effect of considering an isotropic γ-ray emission would lead to about 10% higher cross sections for both cases.

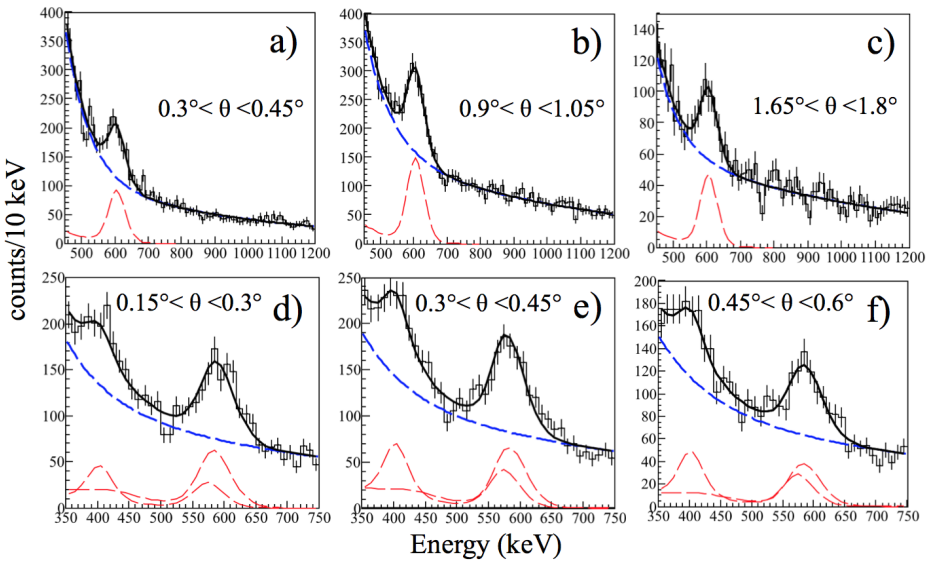

Figure 5.8: Doppler-corrected γ-ray energy spectra produced gating on different ranges of the scattering angle for the Au (a, b, c) and for the C (d, e, f) targets. The plots are labeled by their angular ranges. Note that, for the spectra obtained with the C target, the 4_1^+ state and its feeding to the 2_1^+ state were included in the fit to better describe the experimental spectra.

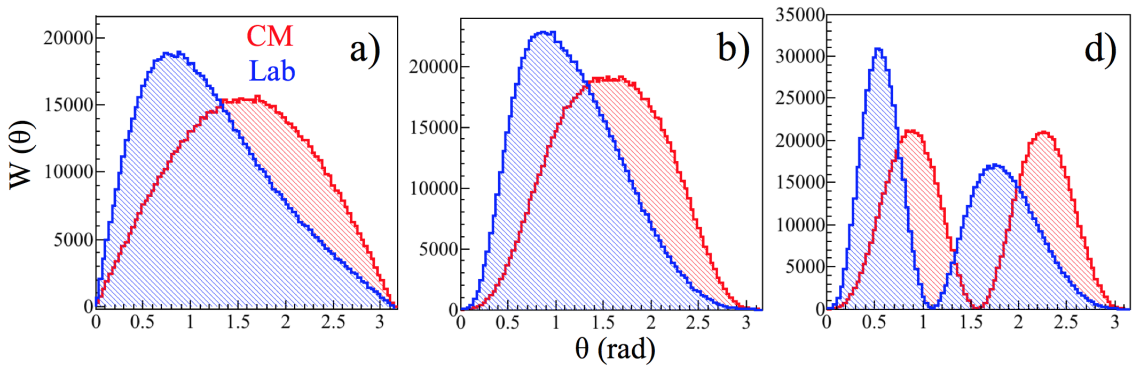

Figure 5.9: γ-ray angular distribution, W(θ), for the 2_1^+ state in ^{136}Te considering different alignments: a) no alignment, b) prolate alignment and c) oblate alignment. The distributions are shown in the center of mass system (red curves) and in the laboratory system (blue curves).

Since the transmission of the ZeroDegree spectrometer is not 100%, but depends on the scattering angle, θ, the observed γ-ray intensity for each angular gate has to be corrected with the average transmission of the angular bin. To get the transmission of each angular bin, we have to compare the number of ^{136}Te ions measured in BigRIPS to the number of ^{136}Te ions detected in ZeroDegree (either the fully-stripped, or the hydrogen-like), so that the transmission is given by $T(bin) = N_{ions\ ZD}(bin)/N_{ions\ BR}(bin)$. This way of determining the transmission does not only include the losses due to the acceptance of the ZeroDegree spectrometer, but also includes the distribution of charge states and the reaction losses. Figure 5.10 a) shows the transmissions for the fully-stripped (for the C and Au targets) and hydrogen-like (only for the Au target) ^{136}Te ions. Figure 5.10 b) shows the angular distributions that have been used to determine the transmission of the fully-stripped ions with the C target. For the curve gated only on BigRIPS (red curve), a tail is observed at large angles. This tail is not due to ^{136}Te ions and it might be produced by light particles originating from reactions between the ^{136}Te ions and the material situated between F7 music (where the identification is done) and the PPAC situated after the target (last detector needed to measure the scattering angle). In the present experiment these fragments were not detected in ZeroDegree since they were not inside the ZeroDegree acceptance. The same tail was observed in another Coulomb excitation experiment performed at the RIBF [118], but, there, the reaction fragments were also detected in the ZeroDegree spectrometer and, therefore, the tail could be experimentally subtracted. In our case, to fit the tail we considered an exponential function (shape of the tail) multiplied by $sin(\theta)$ (to take into account the solid angle). The parameters of the exponential function were adjusted to reproduce the tail at large angles. This function was then subtracted from the original curve and the new $T(bin)$ values were calculated. Figures 5.11 a) and b) show the fit in the region of large scattering angles for the C and Au targets, respectively. Furthermore, also the extreme case of a flat transmission curve was considered to see the effect on the points situated at larger angles and try to get realistic errors for these points. Figure 5.12 shows the three considered cases for the fully-stripped ^{136}Te ions with the Au target: transmission obtained from the directly

measured angular distributions, transmission calculated once the tail has been removed and lastly considering a flat transmission. All differential cross sections were obtained considering the transmission once the tails have been removed from the experimental angular distributions and the errors were increased for the points at large scattering angles where the effect of the tail is more pronounced.

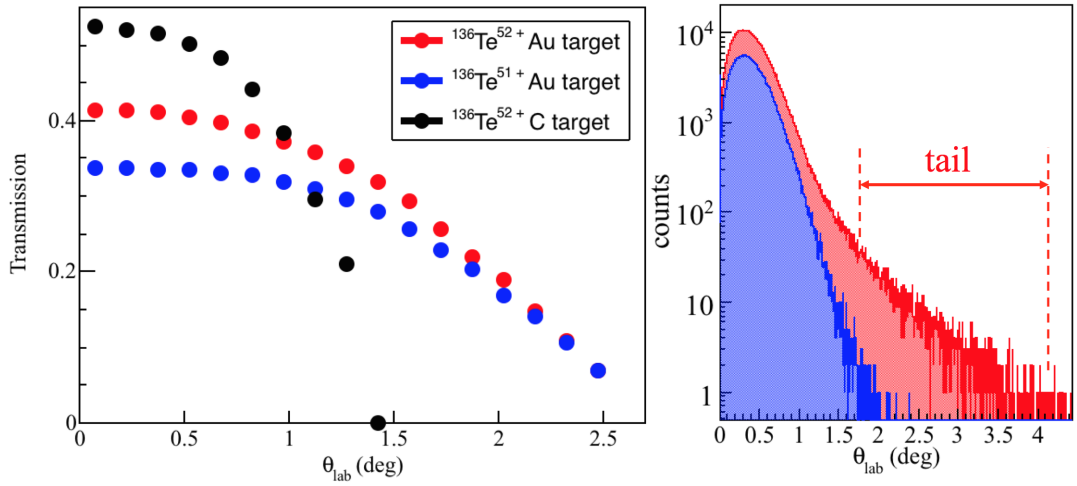

Figure 5.10: a) Transmissions for the fully-stripped ^{136}Te ions with the C (black points) and Au (red points) targets and for the hydrogen-like ions with the Au (blue points) target. b) Angular distributions of the ions identified as ^{136}Te in BigRIPS (red curve) and with an additional gate on ^{136}Te ions detected in the fully-stripped component in ZeroDegree (blue curve) with the C target.

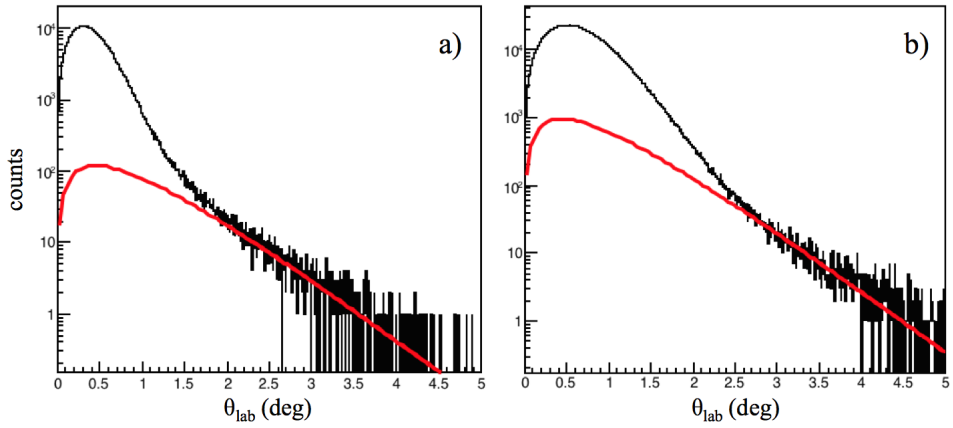

Figure 5.11: Fit of the tail observed at large scattering angles for the a) C and b) Au targets. A exponential function multiplied by $sin(\theta)$ was used in the fit.

The expression used to calculate differential cross section is:

$$\frac{d\sigma}{d\Omega}(bin) = \frac{N_\gamma(bin)}{T(bin) \cdot N_{ions\ BR} \cdot d\Omega(bin) \cdot N_{target} \cdot \epsilon_{\gamma\ losses}} \tag{5.1}$$

where $N_\gamma(bin)$ is the number of γ rays in each bin, $T(bin)$ is the transmission of the angular

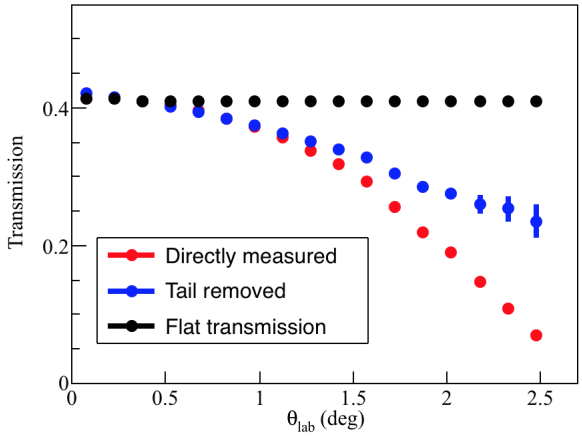

Figure 5.12: Transmission points for the fully-stripped ^{136}Te ions with the Au target. The red points correspond to the transmission obtained from the directly measured angular distribution. The blue points are obtained once the tail observed at large angles is subtracted from the experimental angular distribution. The black points represent the extreme case where a constant transmission curve is assumed.

bin, $N_{ions\ BR}$ is the total number of ions detected in BigRIPS for the nucleus of interest (^{136}Te in our case), $d\Omega$ is the differential solid angle given by $d\Omega = sin(\theta)d\theta d\varphi$, N_{target} is the number of target atoms per cm^2 and $\epsilon_{\gamma\ losses}$ is an experimentally determined correction factor due to a trigger effect during the experiment. The left of Fig. 5.13 shows the experimental angular distributions, $d\sigma$ ($d\sigma = \frac{d\sigma}{d\Omega} * d\Omega$), for the 2_1^+ state in ^{136}Te measured with the Au target for both the fully-stripped and hydrogen-like ions. A good agreement is observed between both curves and the average of them is used as the final angular distribution, shown on the right of Fig. 5.13.

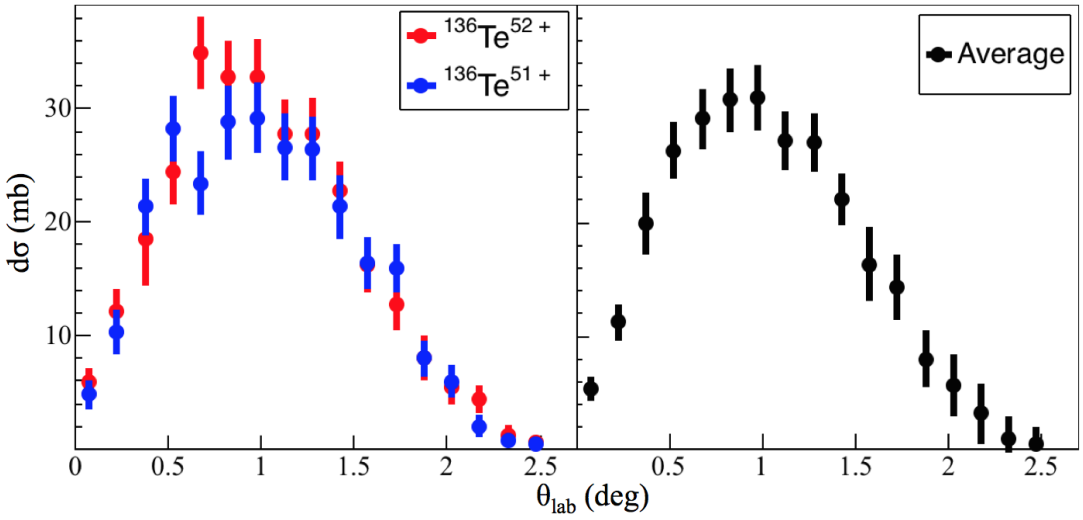

Figure 5.13: Experimental angular distributions obtained for the 2_1^+ state in ^{136}Te with the Au target. Left: separately for the fully-stripped (red points) and hydrogen-like (blue points) ions. Right: after averaging both components. A bin size of 0.15° has been used.

Figure 5.14 shows the angular distribution for the excitation of the 2_1^+ state of ^{136}Te on the C target obtained in the same way as the distributions displayed in Fig. 5.13. Note that for the C target, the angular distribution is concentrated at very small scattering angles. Figure 5.15 a) displays the angular distribution measured for the Au target in coincidence with the transitions at 3.6(1) and 4.2(1) MeV emitted from the newly discovered state at 4.2(1) MeV. Due to the limited statistics, a larger angular bin size of $\Delta\theta$=0.255° was used to calculate the differential inelastic cross section. Since the angular bin is larger, the points shown in Fig. 5.15 a) correspond to the angle that covers half of the total solid angle contained in the angular bin. Since the angular bin sizes of the distributions presented in Fig. 5.13 and Fig. 5.14 is small ($\Delta\theta$=0.15°), there is practically no difference between placing the point at half angle or at the angle that covers half of the total solid angle. For the other transitions observed in Fig. 5.3 b), unfortunately, there are too few statistics to determine differential cross sections. It is worth mentioning that the excited state at 4.2(1) MeV measured on the Au target should also be excited on the C target. However, the high energy region (2-4.5 MeV) of the γ-ray spectrum is contaminated by excitations of the C target and, therefore, it is not possible to deduce the angular distribution of the γ rays depopulating the 4.2(1) MeV state on the C target. This contamination is visible in the energy spectrum shown in Fig. 5.15 b).

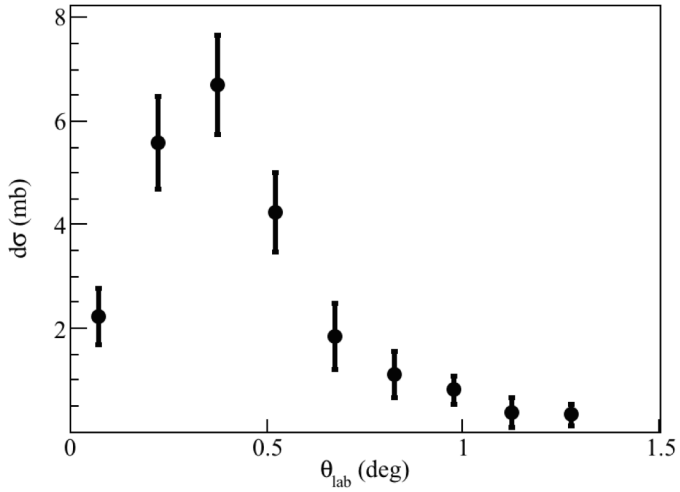

Figure 5.14: Experimental angular distribution of the 2_1^+ state in ^{136}Te on C target. A bin size of 0.15° has been used.

From the differential inelastic scattering cross sections, the absolute cross section can be calculated as the sum over all bins, that is $\sigma_{total} = \sum_{bin=1}^{n} d\sigma(bin)$, where n is the total number of angular bins. For the weaker transitions, the absolute cross section can be determined by comparing their intensities to the γ-ray intensity of the $2_1^+ \rightarrow 0_1^+$ transition (both corrected for the energy-efficiency of DALI2), where we are assuming that the shapes of the angular distributions are similar. Table 5.3 contains the deduced cross sections for the γ-ray transitions observed with the Au and C targets. The quoted errors of the cross sections include the uncertainties due to the transmission, the number of γ rays extracted from the fit, the number of ions in BigRIPS,

the target thickness (5% error), the downscaled trigger factor, the error in the determination of the $\epsilon_{\gamma\ losses}$ factor and the uncertainty of the DALI2 efficiency from the GEANT4 simulation (5% error).

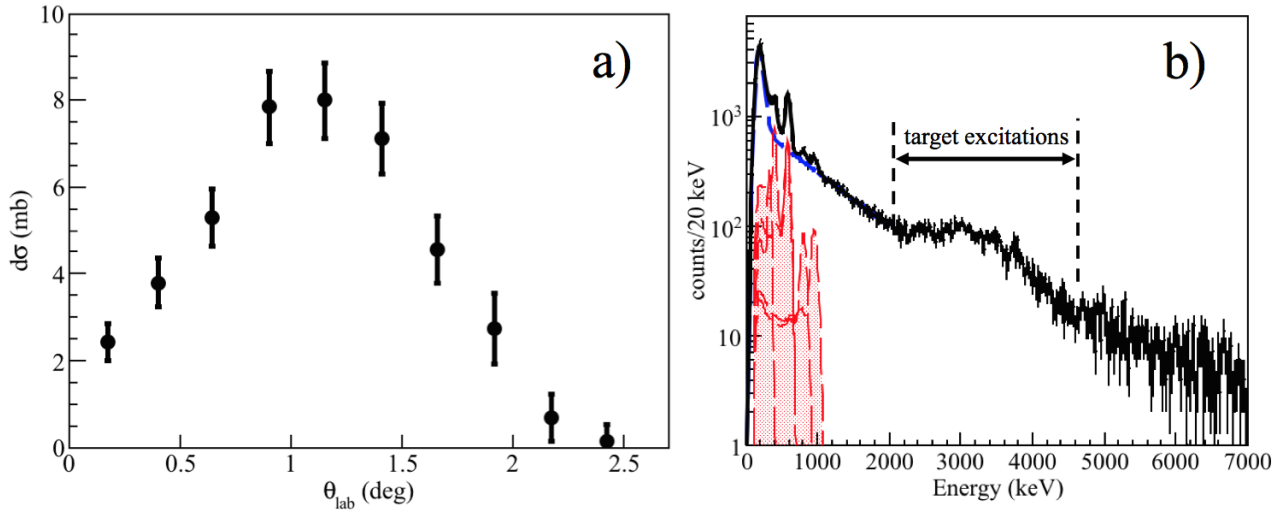

Figure 5.15: a) Experimental angular distribution for the state observed at 4.2(1) MeV in ^{136}Te on the Au target. A bin of 0.255° has been used. b) Doppler-corrected γ-ray spectrum in the energy range from 0 to 7 MeV for ^{136}Te from inelastic scattering on the C target. The spectral strength between 2-4.5 MeV is produced by C excitations, in particular by the $2_1^+ \rightarrow 0_1^+$ transition at 4.438 MeV, which after the Doppler correction is moved to lower energies.

Table 5.3: Absolute cross sections for the different γ-ray transitions observed with the Au and C targets.

E_γ (MeV)	0.353	0.423	0.607	0.810	0.962	3.6	4.2
σ_{Au} (mb)	-	-	279(22)	-	-	21(3)	21(3)
σ_C (mb)	5.1(7)	10.7(11)	23(3)	2.1(3)	2.8(4)	-	-

5.1.5 Feeding corrections

Since we want to determine the B(E2) of the first excited 2^+ state, the different contributions which do not correspond to the direct excitation of the 2_1^+ state have to be considered. These contributions come from the excitation of higher-lying states which partially, or totally decay to the 2_1^+ state. This feeding can take the form of observed γ-ray transitions decaying to the the 2_1^+ state, or unobserved transitions. The first type of feeding is calculated from the measured cross sections of each transition and considering the feeding from inspection of the level scheme. For the C target, the cross section measured for the 2_1^+ state includes feeding from two different sequences: $6_1^+ \rightarrow 4^+ \rightarrow 2_1^+$ and $x \rightarrow 2_2^+ \rightarrow 2_1^+$, while for the Au target the new excited state at 4.2(1) MeV was found to have one decay branch to the 2_1^+ state and the corresponding cross

section (21(3) mb) has therefore to be subtracted from the measured cross section for the 2^+_1 state.

The feeding from unobserved higher-lying states (mainly 2^+ states) was estimated in two different ways. Firstly, an evaluation of this feeding in the nuclei ^{142}Ce and ^{144}Nd, the stable N=84 isotones, was performed. For that, all 2^+ states located above the 2^+_1 state up to the neutron separation energy, and whose half-lives and branching ratios are known were considered. From the half-lives and branching ratios, the $B(E2, 0^+_{g.s} \rightarrow 2^+_x)$ values were calculated and, using again the branching ratios, we estimated which percentage of the $B(E2, 0^+_{g.s} \rightarrow 2^+_x)$ excitation goes to the 2^+_1 state. Table 5.4 contains the 2^+ states of ^{142}Ce which feed the first 2^+ state located at 0.641 MeV. A feeding of 15.3 $\%$ was obtained for the 2^+_1 state in ^{142}Ce. A schematic picture of all 2^+ states included in table 5.4 is shown in Fig. 5.16. In table 5.5 the 2^+ states considered for ^{144}Nd are summarized. A total feeding of 10.5 $\%$ to the 2^+_1 state from the other 2^+ states is obtained for this nucleus. Additionally, shell model calculations using realistic effective interactions [111] were performed with the aim of quantifying this feeding for ^{136}Te. The effective charges were e_p = 1.7e and e_n = 0.7e. Table 5.6 contains the set of 2^+ states calculated for ^{136}Te, the energies and B(E2) (up and down) values are included in the table. A feeding of 14.1 $\%$ was obtained from the shell model calculations, in good agreement with the experimental information for ^{142}Ce and ^{144}Nd. Finally, a 15(5)$\%$ of feeding resulting from E2 excitations was adopted in the analysis. Therefore, of the 279(22) mb, $\sigma_{2^+_1}$ = 219(23) mb (= [279(22)-21(3)]$\times$0.85(5), 21(3) mb from the state at 4.2 MeV and 0.85(5) scaling due to unobserved feeding) correspond to the direct excitation of the 2^+_1 state. The exclusive cross sections for each state excited on the Au and C targets are summarized in table 5.7.

Table 5.4: Excited 2^+ states whose half-lives are known for ^{142}Ce in the energy range from 1.5 MeV up to the neutron separation energy, S_n=7168 keV [119]. The estimated total feeding to the first 2^+ state is labeled in red.

E_{level} (MeV)	J^π	$T_{1/2}$ (ps)	Branching Ratio $2^+_x \rightarrow 0^+_1$	B(E2) $\downarrow$ (e^2fm^4)	B(E2) $\uparrow$ (e^2fm^4)	Branching Ratio $2^+_x \rightarrow 2^+_1$	Effective B(E2) $\uparrow$ (e^2fm^4)
1.536	2^+	<0.83	0.00999	>0.792	>3.96	0.99	>3.92
2.005	2^+	0.045	0.28	108.5	542.5	0.7	379.8
2.365	2^+	0.016	0.235	111.96	560	0.743	416.1
2.543	2^+	0.21	0.45	11.35	56.75	0.30	17.0
2.697	2^+	0.08	Not known	-	-	-	-
2.853	2^+	0.076	0.36	14.15	70.75	0.64	45.3
3.154	2^+	0.11	0.29	4.6	23	0.14	3.22
						$\sum B_{eff}(E2) \uparrow$ = 865.3 e^2fm^4	
						$B(E2) \uparrow$ of 2^+_1 = 4790 e^2fm^4	
						$\%$ of feeding = 15.3	

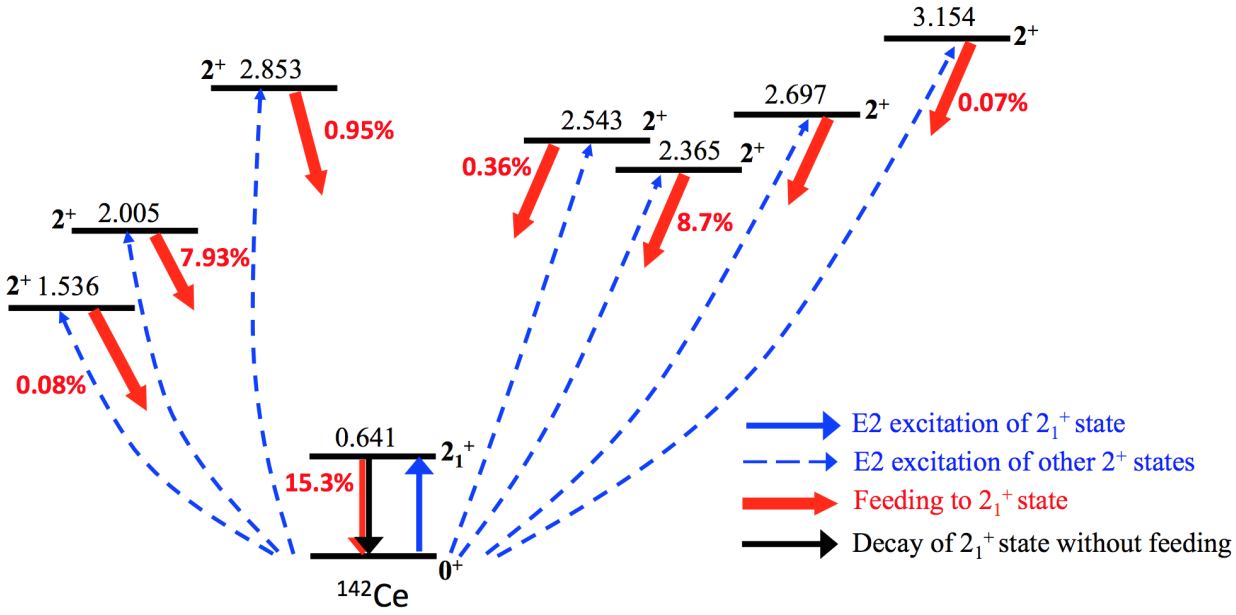

Figure 5.16: Schematic view of the 2^+ states considered in ^{142}Ce to estimate the feeding to the 2_1^+ state [119]. The energies are quoted in MeV. The percentage of each state that decays to the 2_1^+ state is labeled in red.

Table 5.5: Excited 2^+ states whose half-lives are known for ^{144}Nd in the energy range from 1.5 MeV up to the neutron separation energy S_n=7817 keV [119]. The estimated total feeding to the first 2^+ state is labeled in red.

E_{level} (MeV)	J^π	$T_{1/2}$ (ps)	Branching Ratio $2_x^+ \rightarrow 0_1^+$	B(E2) $\downarrow$ (e^2fm^4)	B(E2) $\uparrow$ (e^2fm^4)	Branching Ratio $2_x^+ \rightarrow 2_1^+$	Effective B(E2) $\uparrow$ (e^2fm^4)
1.560	2^+	0.56	0.086	9.41	47.05	0.914	42.8
2.073	2^+	0.059	0.298	74.69	373.5	0.70	261.5
2.369	2^+	0.039	0.192	37.2	186.0	0.81	160.66
2.528	2^+	0.040	0.49	66.5	332.5	0.51	169.6
2.593	2^+	0.19	0.03	0.76	3.79	0.83	3.15
2.693	2^+	>0.12	0.171	5.65	28.25	0.04	1.13
2.720	2^+	0.14	0.029	0.79	3.95	0.971	3.84
2.829	2^+	0.07	Not known	-	-	-	-
2.840	2^+	0.2	0.193	3.66	18.3	0.37	6.77
2.901	2^+	>0.06	0.089	<4.06	<20.3	0.13	<2.64
2.962	2^+	0.13	0.21	4	20	0.79	15.8
3.100	2^+	0.07	0.2	5.6	28	0.57	15.96
						$\sum B(E2) \uparrow$=683.85 e^2fm^4	
						$B(E2) \uparrow$ of 2_1^+=5800 e^2fm^4	
						% of feeding = 10.5	

Table 5.6: Set of 2^+ states for ^{136}Te calculated with shell model calculations employing realistic effective interactions [111].

E_{level} (MeV)	J_i^π	B($E2, 2_x^+ \rightarrow 0_1^+$) ($e^2fm^4$)	B($E2, 0_1^+ \rightarrow 2_x^+$) ($e^2fm^4$)	E_{level} (MeV)	J_i^π	B($E2, 2_x^+ \rightarrow 0_1^+$) ($e^2fm^4$)	B($E2, 0_1^+ \rightarrow 2_x^+$) ($e^2fm^4$)
0.674	2_1^+	410	2050	2.865	2_{10}^+	0.6	3
1.555	2_2^+	27.82	139.1	2.983	2_{11}^+	1.23	6.15
1.805	2_3^+	43.2	216	3.073	2_{12}^+	0.004	0.02
2.239	2_4^+	12.44	62.2	3.163	2_{13}^+	0.2	1
2.468	2_5^+	0.79	3.95	3.183	2_{14}^+	2.75	13.75
2.515	2_6^+	4.23	21.15	3.234	2_{15}^+	0.3	1.5
2.616	2_7^+	0.5	2.5	3.290	2_{16}^+	0.026	0.13
2.698	2_8^+	0.15	0.75	3.305	2_{17}^+	1.25	6.25
2.840	2_9^+	0.91	4.55				

Table 5.7: Exclusive cross sections for the different states observed with the Au and C targets.

E_{level} (MeV)	0.607	1.030	1.383	1.568	2.378	4.2
J_i^π	2_1^+	4_1^+	6_1^+	2_2^+		
σ_{Au} (mb)	219(23)	-	-	-	-	42(4)
σ_C (mb)	9.5(32)	5.6(13)	5.1(7)	0.7(5)	2.1(3)	-

5.1.6 Theoretical codes and optical potentials

To obtain the B(E2) value from the experimental absolute cross section, the use of a reaction code is necessary. At the incident beam energies and angular resolutions of the present experiment, the Coulomb and nuclear contributions can not be separated. Therefore, we need codes capable of considering both processes and the possible interferences between them. For that, the well known Coulomb potential and calculated optical potentials (real and imaginary part) are used in the calculations to take into account absorptions, the excitations due to the Coulomb and nuclear interactions and their possible interferences. In addition, not only the B(E2) values are obtained from the calculations, but also the differential inelastic cross sections, therefore, a comparison between the experimental points and the theoretical curves can be performed. There are three prominent reaction codes that can consider simultaneously the Coulomb and nuclear potentials: DWEIKO [120], ECIS97 [121] and FRESCO [122]. DWEIKO (*Distorted Wave EIKOnal Approximation*) is a computer program in which the excitation amplitudes for the Coulomb part are calculated assuming a straight-line trajectory for the projectile, while ECIS97 (*Equations Couplées en Itérations Séquentielles*) and FRESCO are non-relativistic coupled-

channel programs that use the Alder-Winther theory of Coulomb excitation [63]. ECIS has successfully reproduced many experimental angular distributions available [74, 123–126]. Unfortunately, for the case of our experiment, ECIS97 exhibits convergence problems. The matching radius parameter (which has to be large enough to ensure convergence) was varied from small to very large values, but the cross section did not converge. Therefore, ECIS97 could not be used in the present analysis, leaving only the options of DWEIKO, or FRESCO. Before using either DWEIKO, or FRESCO for our reaction, we tested the calculations of both codes for some of the experimental cases where high-resolution measurements were reported. The first test case was the ^{17}O+^{208}Pb reaction (at 84 MeV/u) measured by Barrette *et al.* [123]. The experimental results obtained for the excitations of the isoscalar giant quadrupole resonance (ISGQR) and the isovector giant resonance (IVGDR) in ^{208}Pb compared with ECIS calculations are shown in Fig. 5.17 a). A good agreement between the experimental points and the theoretical curves was observed. We repeated the calculations for the same excited states but using now DWEIKO and FRESCO. The same Woods-Saxon parameters for the optical potential, deformations lengths and reduced transitions probabilities as used in Ref. [123] were employed in the new calculations. Figures 5.17 b) and c) show the results obtained with DWEIKO and FRESCO, respectively. FRESCO exhibits results in excellent agreement with the results obtained using ECIS. Both the position of the maximum and the absorption at large scattering angles (small impact parameters) are well reproduced by FRESCO. Besides, for the case of the ISGQR, FRESCO also shows the strong interference (around 3°) between the Coulomb and nuclear interactions observed experimentally. In contrast, the calculations performed with DWEIKO do not show the absorption at the same position and as a consequence the differential cross sections drops at larger scattering angles. In addition, for the ISGQR, DWEIKO shows constructive interferences between the Coulomb and nuclear interactions while with FRESCO and ECIS the interference is destructive. The experimental points show that the interference has to be destructive because otherwise the position of the maximum would correspond to the maximum of the Coulomb part. Other published results obtained with ECIS have been studied with DWEIKO and FRESCO: ^{86}Kr+^{208}Pb (at 43 MeV/u) [127] and ^{32}Mg+^{208}Pb (at 195 MeV/u) [74]. In all studied cases, FRESCO provides results in perfect agreement with the ECIS calculations (and experiment), while DWEIKO does not seem to correctly treat the absorption at large angles and the Coulomb-nuclear interferences. Therefore, in the present work FRESCO will be used to convert the measured cross section into a B(E2) value and to obtain the differential cross section. A modified version of the FRESCO code provided by A. Moro was used. This modified version includes relativistic corrections to the kinematics but not to the dynamics. However, at the energy of the present experiment (139 MeV/u) these dynamical effects are much smaller than the kinematical ones and can be neglected [128]. A 5% error was assumed in the determination of the B(E2) due to the non-consideration of the dynamical effects.

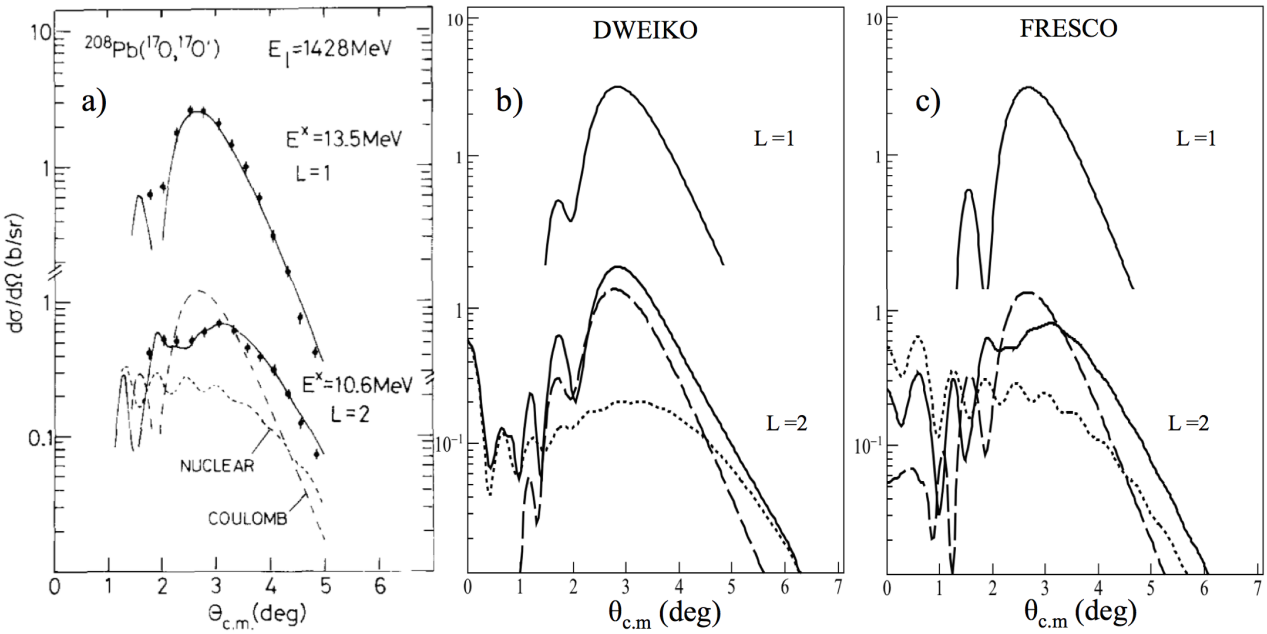

Figure 5.17: a) Experimental and calculated angular distributions for the ISGDR (upper part) and the ISGQR (lower part) in ^{208}Pb [123]. The calculations were performed using the ECIS code. For the ISGQR, the calculated Coulomb and nuclear contributions to the cross sections are also shown. b) Calculations for the same excitations using the DWEIKO program. c) Calculations using the FRESCO code.

The optical potentials used in the calculations were provided by T. Furumoto following the model presented in Ref. [129], where the optical potential is derived from the microscopic folding model with the complex G-matrix interaction, CEG07, and the global density based on the São Paulo parameterization. Figure 5.18 shows the calculated optical potentials for the ^{136}Te + ^{12}C (top part) and ^{136}Te + ^{197}Au (bottom part) reactions. The calculations were performed for the energies before, after and at mid-target to check if there are strong variations with the energy. Furthermore, to verify the effect of the potentials in the calculations performed with FRESCO, also optical potentials derived from t-$\rho\rho$ approximation [130] were used. A 5% variation was found between the cross sections obtained with the Furumoto model and the t-$\rho\rho$ approximation. Also, the potentials calculated according to the Furumoto model [129] were calculated using a more realistic theoretical density distribution obtained from the Hartree-Fock-Bogoliubov approach and the finite range density dependent Gogny force in the D1S parameterization [131]. The obtained cross sections changed by less than 2%. A 5% error was assumed due to the choice of the optical potential model.

5.1.7 Folding of the theoretical distributions

To compare the theoretical differential inelastic cross sections obtained with FRESCO to the experimental curves, the calculated distributions need to be folded with the experimental angular resolution. The folding is done with the following procedure (labeled as 2D): first, we

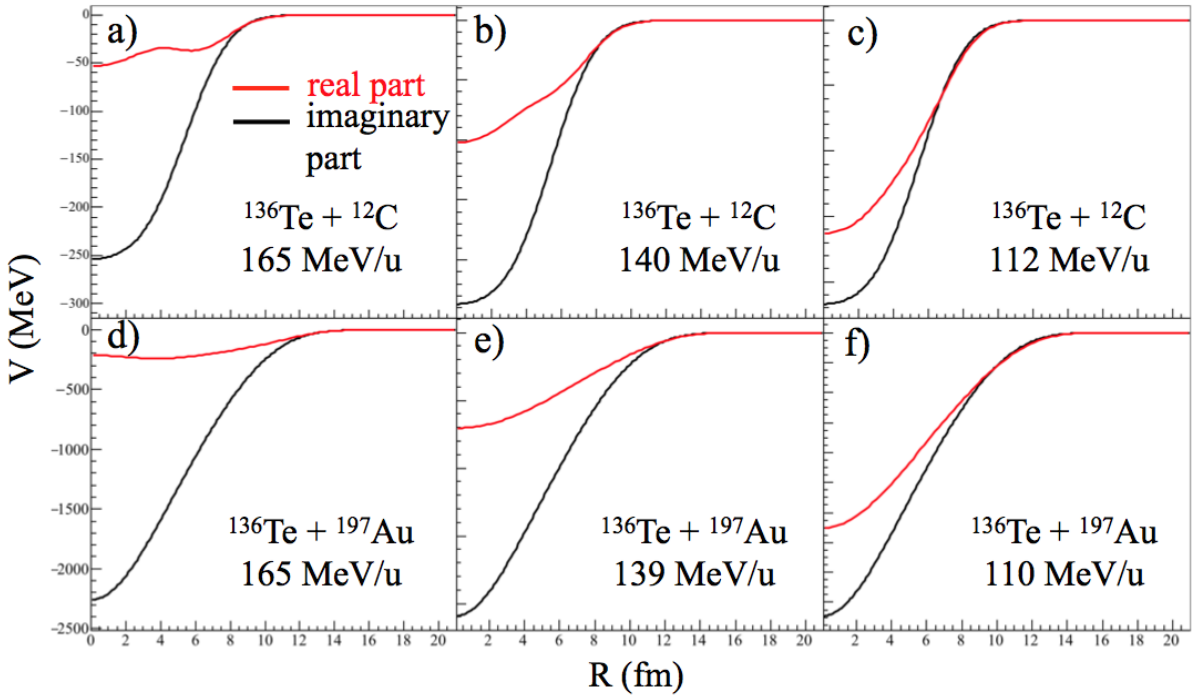

Figure 5.18: Optical potentials for the ^{136}Te + ^{12}C (top part) and ^{136}Te + ^{197}Au (bottom part) reactions. The red curves are the real part and the black curves correspond to the imaginary part. The optical potentials were calculated for the energies before (pictures a and d), after (pictures c and f) and at mid-target (pictures b and e).

choose randomly an angle, θ_1, from the theoretical distribution $d\sigma$ ($d\sigma = const * d\sigma/d\Omega * sin(\theta)$) obtained with FRESCO. In addition, an azimuthal angle, φ_1, is also randomly selected from a uniform distribution in the interval [0,2π]. These two angles (θ_1,φ_1) define the new direction of the ion after having been scattered by the target. This direction is defined with respect to the direction of the incident ion. Afterwards, a new random angle, θ_2, is chosen from the directly measured experimental angular distribution (or alternatively from a Gaussian distribution with the resolutions σ_{Au} or σ_C, depending on the target, and this Gaussian multiplied by $sin(\theta)$) and an azimuthal angle, φ_2, selected again from the uniform distribution between [0,2π]. This new pair of angles (θ_2,φ_2) defines the new direction of the ions caused by the angular straggling and the uncertainty in the position measurements. However, this direction is defined with respect to the initial direction of the real ion, so we need to define the (θ_2,φ_2) angles with respect to the direction given by the (θ_1,φ_1) angles. After this transformation of the coordinate system, the polar angle, θ_2, corresponds to the final angle that can be compared with the experimentally measured one. Figures 5.19 a) and b) show the effect of the folding for scattering angles of θ_1 from 0° up to 3° with a step of 0.5°. As is visible in this figure, after the folding some of the distribution is moved to lower angles and the rest towards higher angles. In addition, we verified that the folding procedure is independent on the order in which the angles are chosen. Figure 5.20 a) displays a theoretical $d\sigma$ distribution calculated with FRESCO and considering only the Coulomb interaction. This distribution has been folded in three different ways: in Fig. 5.20 b),

we assumed that first the scattering takes place and then the straggling, in Fig. 5.20 c) we considered that the straggling happens and is followed by scattering and, lastly, in Fig. 5.20 d) a more realistic sequence is considered: straggling-scattering-straggling, where the individual resolutions of the straggling have to satisfy, $\sigma^2_{Au,C} = \sigma^2_{stragg1} + \sigma^2_{stragg2}$. For the case of Fig. 5.20 d), the folding was performed with $\sigma_{stragg1} = \sigma_{stragg2} = 0.356°$ to verify $\sigma_{Au} = 0.504°$. As is visible in Fig. 5.20, the folding procedure is independent of the order in which the scattering and straggling processes are considered.

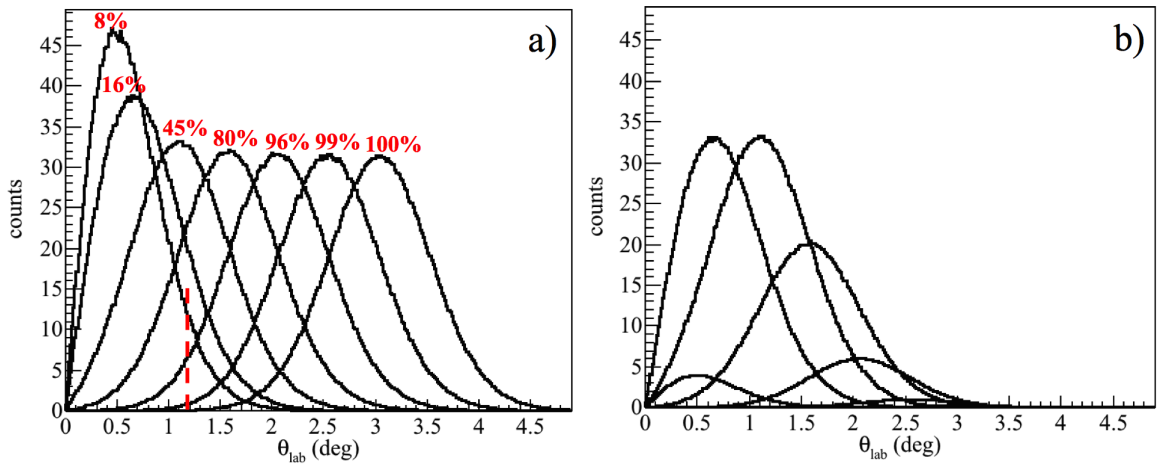

Figure 5.19: a) Effect of the folding for different individual scattering angles. The curves correspond to angles from 0° up to 3° with a step of 0.5°. The numbers in red represent the percentage of area outside of the maximum scattering angle determined using a minimum impact parameter corresponding to touching sphere +2 fm (1.178°). b) Same curves but now each curve is scaled proportional to the measured cross section for that angle (right of Fig. 5.13).

We also want to stress that a different folding procedure could be considered (labeled as 1D). With this procedure, firstly, a scattering angle, θ_1, is randomly chosen from the theoretical angular distribution, $d\sigma$, and then a second angle, θ_2, is randomly selected from a Gaussian function with the width corresponding to the one measured experimentally (σ_{Au}, or σ_C) and the peak centroid of this Gaussian distribution is the scattering angle, θ_1, determined in the first step. This angle, θ_2, is the final angle of the ion. Note that with this method, after the folding, part of the events are shifted to negative values of θ (for the case of θ_{scatt} = 0°, half of the statistics are moved towards negative angles and the other half towards positive angles). To solve this problem, there are two different solutions: recover the lost cross section towards negative angles with a global scaling of the total folded curve, or consider absolute values of θ_2 angles. The folded curves obtained with these two approaches are incorrect and we were not able to reproduce the experimental points, in particular for the case of the C target, where the effect of the folding is stronger because the theoretical distribution is concentrated at very low angles. The theoretical curves obtained applying the two folding procedures which has been discussed in detail above to the differential cross section calculated with FRESCO are

compared to the experimental data later in Fig. 5.24. Only good agreement is observed when the two-dimensional folding (2D) is applied to the theoretical curves.

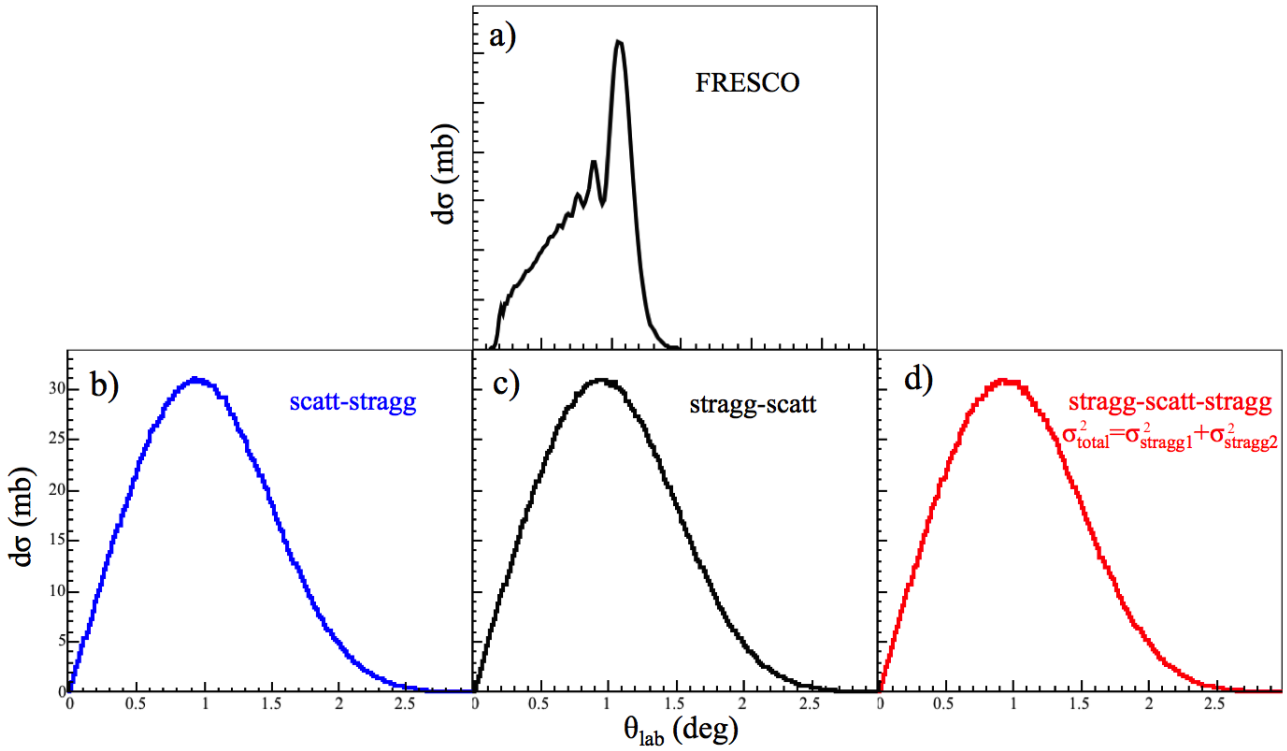

Figure 5.20: a) Angular distribution for the excitation of the 2_1^+ state in ^{136}Te calculated with FRESCO and considering only the Coulomb excitation. The calculation was performed for B(E2)=0.18 e^2b^2. b) Folding of the theoretical curve shown in a) considering that the scattering occurs first and then the straggling. c) Folding assuming that the straggling happens in the first place and afterwards the scattering d) Folding following the sequences straggling-scattering-straggling. The resolutions $\sigma_{stragg1}$ and $\sigma_{stragg2}$ are given by $\sigma^2_{total} = \sigma^2_{stragg1} + \sigma^2_{stragg2}$.

5.1.8 Determination of the deformation length δ_n and the B(E2) value and comparison between the theoretical and experimental differential cross sections

To obtain the B(E2) value for the first excited 2^+ state in ^{136}Te, we first need to determine the nuclear contributions to the total measured cross section for this state with the Au target. For that, the cross section obtained for the first excited 2^+ state with the C target was evaluated and converted to a δ_n value. The nuclear deformation, δ_n, was varied in the input of FRESCO and the cross section was calculated for each input. In table 5.8, the obtained cross sections as a function of the nuclear deformation are summarized for the energy at mid-target (140 MeV/u). Firstly, the FRESCO calculations were performed without considering the Coulomb interaction ($\delta_C = 0$). Afterwards the FRESCO calculations were done assuming that the Coulomb deformation is equal to the nuclear deformation ($\delta_C = \delta_N$) and lastly the calculations were carried out with a $\delta_C = 0.554$ fm which corresponds to a B(E2)=1800 e^2fm^4. As is shown in table 5.8 the

Coulomb effects with the C target are very small due to its low atomic number. For the analysis, the condition of $\delta_C = \delta_N$ was used to convert the cross section to δ_N since the feeding effects of other higher-lying states are considered to have the same Coulomb and nuclear deformation strength. The calculations were also performed for the energies before and after the target and assuming the condition of $\delta_C = \delta_N$. The obtained cross sections are summarized in table 5.9. The cross sections calculated for the three energies are plotted versus the nuclear deformation in Fig. 5.21. The experimental total cross section of σ = 23(3) mb for the 2_1^+ state measured with the C target was reproduced with a value of δ_N = 1.05(7) fm (table 5.10). This δ_N value includes information about the feeding to the 2_1^+ state originating from higher-lying states and can be interpreted as an effective value which takes into account the same kind of feeding (mainly nuclear feeding) with the Au target. The exclusive cross section of σ = 9.5(32) mb for the 2_1^+ state observed with the C target was reproduced with a value of δ_N = 0.68(10) (table 5.11). The calculated differential cross section with the C target is concentrated at very small scattering angles since the grazing angle is small. Figure 5.22 a) shows the angular distribution calculated with FRESCO for δ_N = 1.05(7) fm. To compare this calculation with the experimental points, we need to perform the folding of the theoretical distribution with the experimental angular resolution as explained in the previous section. Figure 5.22 b) displays the comparison between the experimental angular distribution and the folded theoretical calculation obtained with FRESCO, showing good agreement between the two distributions. After the folding, the theoretical calculation mainly reflects the experimental angular resolution since the scattering angles are very small. The folding of this curve is very sensitive to the method used since the theoretical curve is concentrated at small scattering angles. We also folded the theoretical curve with the 1D method described in the previous section. In that case, a clear disagreement between the folded curve and the experimental points is observed, as shown in Fig. 5.24.

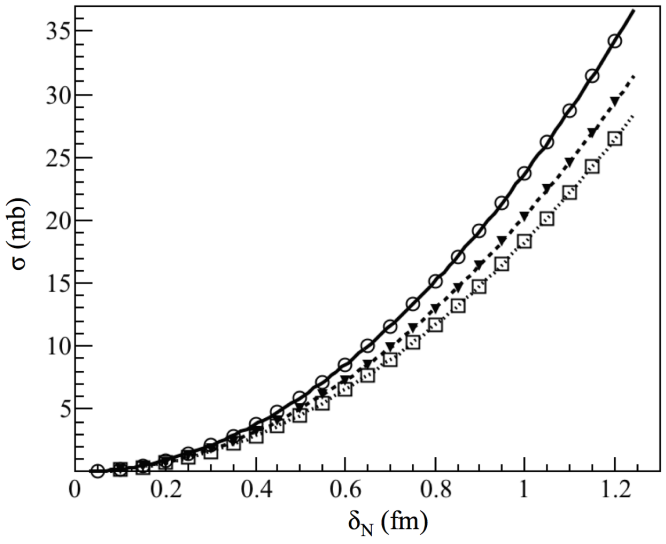

Figure 5.21: Cross section as a function of the nuclear deformation for the energies before (squares), at mid (triangles) and after (circles) target. The condition of $\delta_C = \delta_N$ was assumed in the FRESCO calculations.

Table 5.8: Results of FRESCO calculations where the nuclear deformation was varied and the total cross sections for the 2_1^+ state was calculated for the ^{136}Te+^{12}C reaction at 140 MeV/u. In the first column, the Coulomb interaction was not considered, in the second one the Coulomb deformation was assumed to be equal to the nuclear deformation and in the third column a Coulomb deformation δ_C = 0.554 fm was used which corresponds to B(E2)=1800 e^2fm^4.

E_{beam} = 140 MeV/u					
δ_C = 0		$\delta_C = \delta_N$		δ_C = 0.554 fm	
δ_N (fm)	σ (mb)	δ_N (fm)	σ (mb)	δ_N (fm)	σ (mb)
0.05	0.0466	0.05	0.0503	0.05	2.8115
0.10	0.1865	0.10	0.201	0.10	2.7222
0.15	0.4196	0.15	0.45303	0.15	2.7262
0.20	0.746	0.20	0.80546	0.20	2.8235
0.25	1.1658	0.25	1.2588	0.25	3.0143
0.30	1.6789	0.30	1.813	0.30	3.2987
0.35	2.2854	0.35	2.4685	0.35	3.6768
0.40	2.9853	0.40	3.2252	0.40	4.1487
0.45	3.779	0.45	4.083	0.45	4.7146
0.50	4.666	0.50	5.0432	0.50	5.3746
0.55	5.647	0.55	6.105	0.55	6.129
0.60	6.7218	0.60	7.269	0.60	6.9779
0.65	7.8907	0.65	8.5354	0.65	7.9214
0.70	9.1538	0.70	9.9046	0.70	8.96
0.75	10.51	0.75	11.377	0.75	10.094
0.80	11.963	0.80	12.953	0.80	11.323
0.85	13.509	0.85	14.633	0.85	12.647
0.90	15.151	0.90	16.418	0.90	14.068
0.95	16.887	0.95	18.308	0.95	15.585
1.00	18.719	1.00	20.303	1.00	17.198
1.05	20.647	1.05	22.404	1.05	18.909
1.10	22.671	1.10	24.612	1.10	20.717
1.15	24.792	1.15	26.928	1.15	22.622
1.20	27.09	1.20	29.352	1.20	24.626

Once an effective nuclear deformation value has been determined, we can now evaluate the exclusive cross section of σ = 219(23) mb for the 2_1^+ state observed with the Au target. The δ_N value was kept fixed and we varied the reduced quadrupole matrix element M(E2) until the measured cross section was obtained. The σ = 219(23) mb was reproduced with a matrix element of M(E2) = 44.17 efm^2. Using the definition, $B(\pi\lambda; i \rightarrow j) = \frac{1}{2I_i+1}M(E2)^2$, we get B(E2,$0 \rightarrow 2^+$) = M(E2)^2, giving, B(E2)=0.195(22) e^2b^2. In addition, we also obtained the B(E2) value when the nuclear deformation value of δ_N = 0.68(10) fm is considered to check the sensitivity of the B(E2) value to the nuclear deformation parameter. Assuming δ_N = 0.68(6) fm, a reduced matrix element of M(E2) = 45.1 efm^2 was obtained leading to B(E2)=0.203(23) e^2b^2. As we can see, the effect of considering an effective nuclear deformation, or an exclusive nuclear deformation value would lead to an increase of the B(E2) value by only 4%. Figures 5.23

a) and c) display the theoretical angular distributions obtained with FRESCO for the two nuclear deformations described above. The interferences between the Coulomb and nuclear part are destructive, shifting the position of the maximum of the total distribution to smaller angles. The nuclear deformation parameter determines the strength of the nuclear excitations, real part of the optical potentials, while the position of the absorption at large angles is due to the imaginary part of the optical potentials. The differences observed between both calculations disappear when we perform the folding of the theoretical curves. Figures 5.23 b) and d) show the comparison between the experimental points and the folded theoretical distributions for δ_N = 1.05 fm and δ_N = 0.68 fm, respectively. Both theoretical curves reproduce the experimental points well revealing that after the folding we are not sensitive to the value of nuclear deformation.

Table 5.9: Results of FRESCO calculations for the same case showed in the previous table but now for the energies before (165 MeV/u) and after (112 MeV/u) the target and assuming $\delta_N = \delta_C$.

E_{beam} = 165 MeV/u		E_{beam} = 112 MeV/u	
δ_C = δ_N		δ_C = δ_N	
δ_N (fm)	σ (mb)	δ_N (fm)	σ (mb)
0.05	0.0451	0.05	0.059
0.10	0.18073	0.10	0.236
0.15	0.40669	0.15	0.5314
0.20	0.7231	0.20	0.9448
0.25	1.1302	0.25	1.476
0.30	1.628	0.30	2.126
0.35	2.2166	0.35	2.894
0.40	2.896	0.40	3.7808
0.45	3.667	0.45	4.7858
0.50	4.53	0.50	5.9095
0.55	5.484	0.55	7.1519
0.60	6.531	0.60	8.5133
0.65	7.67	0.65	9.994
0.70	8.902	0.70	11.593
0.75	10.277	0.75	13.313
0.80	11.646	0.80	15.152
0.85	13.16	0.85	17.11
0.90	14.768	0.90	19.19
0.95	16.472	0.95	21.39
1.00	18.271	1.00	23.716
1.05	20.167	1.05	26.153
1.10	22.161	1.10	28.716
1.15	24.252	1.15	31.403
1.20	26.443	1.20	34.212

Table 5.10: δ_n values obtained with FRESCO to reproduce the inclusive cross section of σ = 23(3) mb measured for the 2_1^+ transition with the C target. The energies and potentials before, mid and after the target were used in the calculations. Finally, an average value was determined.

σ = 23(3) mb	E_{beam}=165 MeV/u	E_{beam}=140 MeV/u	E_{beam}=112 MeV/u
δ_N (fm)	1.12(7)	1.06(7)	0.98(6)
$\delta_{Average}$ (fm)	1.05(7)		

Table 5.11: δ_n values obtained with FRESCO to reproduce the exclusive cross section of σ = 9.5(32) mb measured for the 2_1^+ state with the C target. The energies and potentials before, mid and after the target were used in the calculations. Finally, an average value was determined

σ = 9.5(32) mb	E_{beam}=165 MeV/u	E_{beam}=140 MeV/u	E_{beam}=112 MeV/u
δ_N (fm)	0.72(12)	0.69(10)	0.63(10)
$\delta_{Average}$ (fm)	0.68(10)		

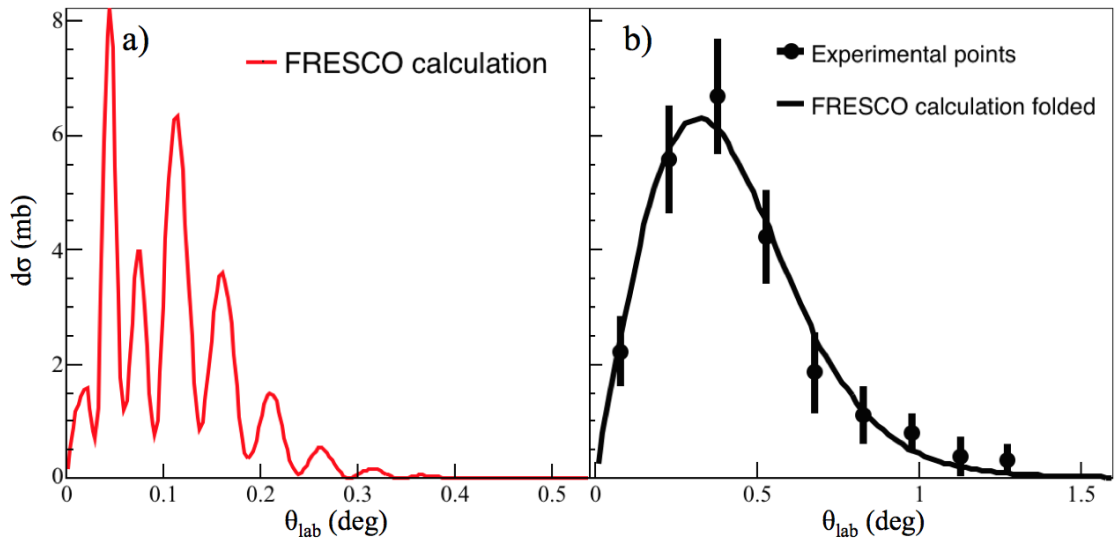

Figure 5.22: a) Angular distribution for the excitation of the 2_1^+ state in ^{136}Te on the C target calculated with FRESCO. b) Comparison between the experimental points of the angular distribution and the FRESCO calculation after folding for the C target. A value of δ_N = 1.05(7) fm was used in the calculation.

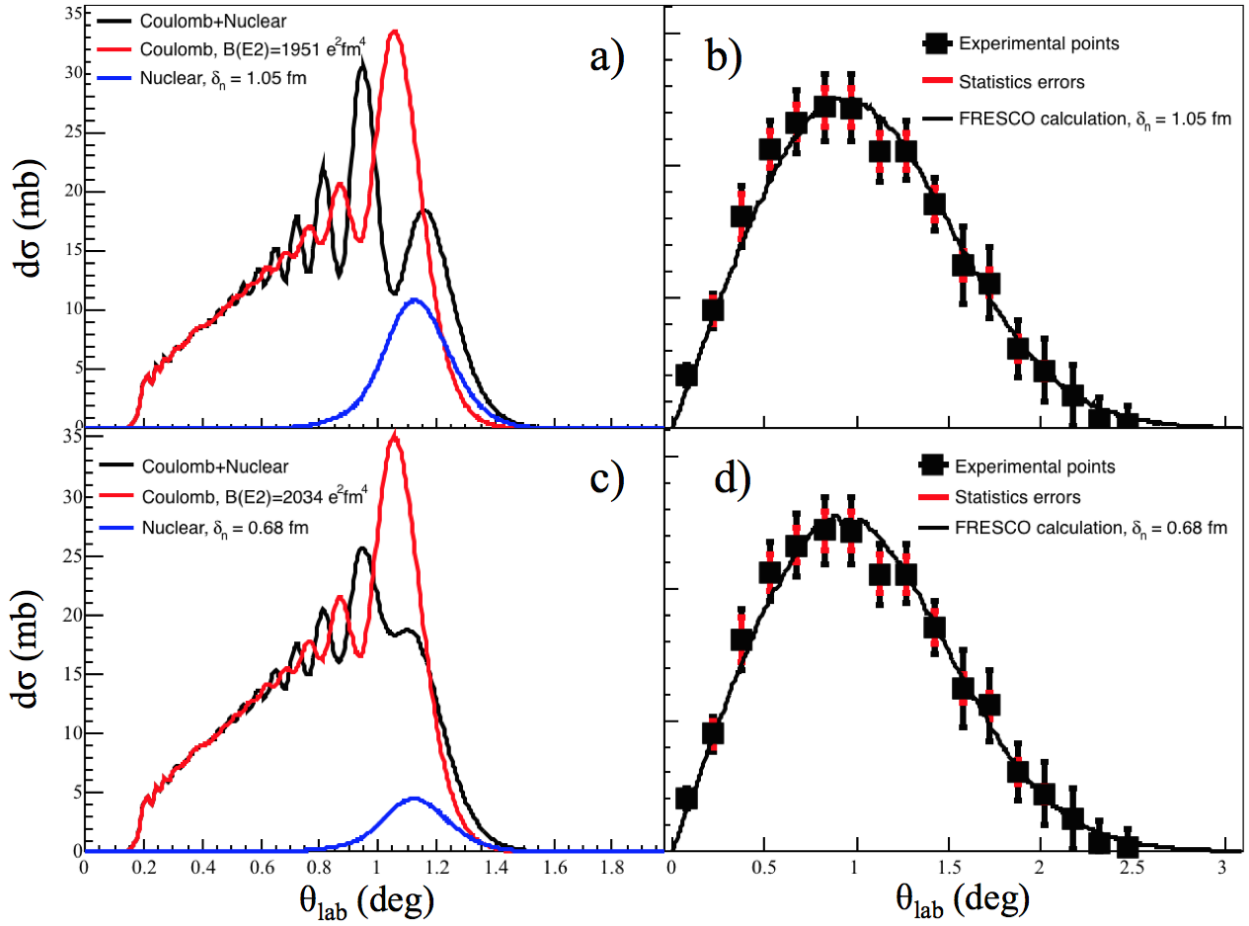

Figure 5.23: Angular distributions for the excitation of the 2_1^+ state in ^{136}Te on the Au target calculated with FRESCO for a) δ_N = 1.05 fm and B(E2) = 1951 e^2fm^4 and c) δ_N = 0.68 fm and B(E2) = 2034 e^2fm^4. The total distribution is shown by the black curve while the Coulomb and nuclear distributions are shown separately by the red and blue curves, respectively. The comparison between the experimental points and the folded angular distributions are shown in b) for δ_N = 1.05 fm and B(E2) = 1951 e^2fm^4 and in d) for δ_N = 0.68 fm and B(E2) = 2034 e^2fm^4. The experimental points show separately the total errors (black line) and the statistical errors (red line).

The obtained B(E2) value needs to be corrected and its error increased by some factors which have not been included so far. The first correction is due to the fact that we are not using a purely relativistic code to get the B(E2) values and therefore the cross sections obtained with FRESCO need to be corrected. Previously it was introduced that for the energy of the present experiment (139 MeV/u), the dynamical effects are small and an additional systematic uncertainty of 5% is considered in the determination of the B(E2). The second factor to consider is that, we are using a thick Au target (950 mg/cm^2). Inside the target, the ^{136}Te ions lost approximately 55 MeV/u. The cross section (and, therefore, the B(E2)) is not linear with these energy changes and these effects have to be taken into account if a fixed energy is used in the analysis. The calculated Coulomb cross sections for the energies at the entrance, the center and the exit of the target are: σ = 190 mb for 165 MeV/u, σ = 219 mb for 139 MeV/u and σ =

267 mb for 110 MeV/u. Therefore, to first order, the B(E2) value has to be scaled down by 2% [(267+190)/2+219]/(2×219] and an uncertainty of 100% was assumed for this factor. Finally, the third factor is an additional systematic uncertainty of 5% in the B(E2) due to the choice of the optical model potential. All these corrections and the final B(E2) value are summarized in table 5.12. Moreover, we have also repeated the B(E2) calculations considering a t-$\rho\rho$ potential and an optical potential using a more realistic theoretical density distribution obtained from the Hartree-Fock-Bogoliubov approach. The obtained B(E2) values with both potentials are also summarized in table 5.12. The left of Fig. 5.25 shows the comparison between the different FRESCO calculations and the experimental points. For the four studied cases (Furumoto potentials δ_N = 1.05 fm and δ_N = 0.68 fm, t-$\rho\rho$ potentials and optical potential using Hartree-Fock-Bogoliubov approach) a good agreement between the experimental points and the folded theoretical calculations is observed. The right of Fig. 5.25 displays the B(E2) values as a function of the maximum scattering angle up to which the cross section is integrated. A flat B(E2) behavior is observed for all the calculations. The B(E2) value obtained with the Furumoto potentials and δ_N = 1.05(7) fm was adopted as the final experimental value. The other values can be taken as reference and to illustrate the errors in the determination of the B(E2).

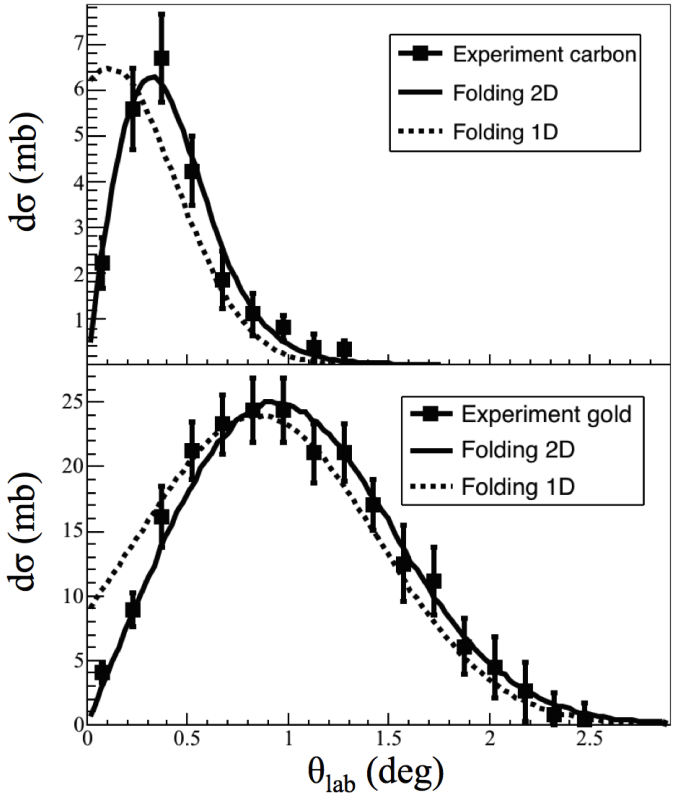

Figure 5.24: Experimental angular distributions for the excitation of the 2_1^+ state in ^{136}Te on the C target (top) and on the Au target (bottom) compared to the FRESCO calculations. The theoretical curves were obtained by applying the two folding procedures discussed in the text.

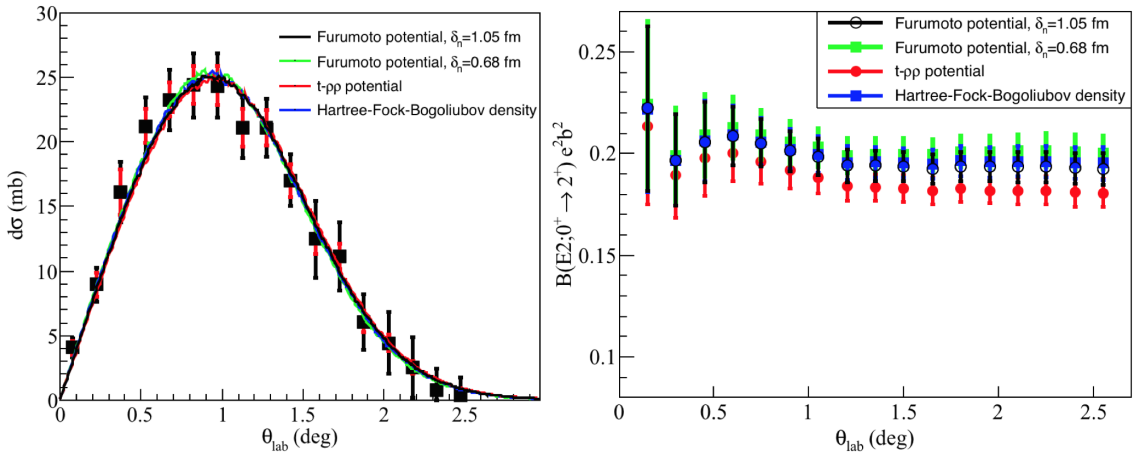

Figure 5.25: Left: Experimental angular distribution for the excitation of the 2_1^+ state in ^{136}Te on the Au target compared with the different folded differential cross sections calculated with FRESCO. Right: B(E2) values as a function of integrated maximum scattering angles. The B(E2) values have been already scaled with the corresponding factor due to energy changes inside the target.

Table 5.12: Summary of the obtained B(E2) values with the different optical models potentials. The final B(E2) values are quoted in red.

Furumoto potential	B(E2) (e^2b^2)	ΔB(E2) (e^2b^2)	error
FRESCO	0.195	0.022	Experimental σ
potentials error	0.195	0.024	5%
target thickness correction	0.191	0.024	2%
relativistic correction	0.191	0.026	5%
Final value	0.191	0.026	

HFB potential	B(E2) (e^2b^2)	ΔB(E2) (e^2b^2)	error
FRESCO	0.198	0.022	Experimental σ
potentials error	0.198	0.024	5%
target thickness correction	0.194	0.024	2%
relativistic correction	0.194	0.026	5%
Final value	0.194	0.026	

$t-\rho\rho$ potential	B(E2) (e^2b^2)	ΔB(E2) (e^2b^2)	error
FRESCO	0.183	0.021	Experimental σ
potentials error	0.183	0.023	5%
target thickness correction	0.179	0.023	2%
relativistic correction	0.179	0.025	5%
Final value	0.179	0.025	

5.1.9 B(E2) values from lifetime measurements

Instead of using the Coulomb excitation cross section, the reduced transition probability can also be obtained from the lifetime of the state through the following equation:

$$B(EL; I_i \rightarrow I_f) = \frac{\hbar}{\tau} \frac{L[(2L+1)!!]^2}{8\pi(L+1)} \left(\frac{\hbar c}{E_\gamma}\right)^{2L+1} \tag{5.2}$$

For the case of a $B(E2; 0 \rightarrow 2)$ it follows:

$$B(E2; 0 \rightarrow 2) = \frac{0.407}{E_\gamma^5(MeV) \cdot \tau(ps)} e^2 b^2 \tag{5.3}$$

The 2_1^+ state in ^{136}Te is known to have a lifetime of tens of picoseconds [47, 53] and as a result of this lifetime, the γ-ray emission takes place at a lower average recoil velocity as compared to the mid-target velocity, since the ions have already left the target. As a consequence, small shifts in energy are observed in the spectrum shown in the Fig. 5.3 a), where the velocity and angles used in the Doppler correction correspond to emission at mid-target. Through a comparison between the experimental spectrum and GEANT4 simulations assuming different lifetimes we can estimate the lifetime of the 2_1^+ state in ^{136}Te. Figures 5.26 a) and b) show the γ-ray spectrum for ^{136}Te on the Au target considering all γ-ray multiplicities. In Fig. 5.26 a) the spectrum was fitted with a two-exponential background and a DALI2 response function obtained with GEANT4 where a vanishing lifetime was considered for the 2_1^+ state in ^{136}Te. Clearly, a shift is observed between the DALI2 response function and the experimentally observed peak. In Fig. 5.26 b) the same spectrum is again fitted, but assuming a lifetime of τ=36 ps for the 2_1^+ state. This lifetime is the one for which we got the best χ^2 fit parameter. Now, a good agreement is achieved between the experimental spectrum and the fit. Figures 5.26 c) and d) show the γ-ray spectrum for ^{136}Te on the Au target considering only events with γ-ray multiplicity equal to 1. With this condition in principle we would be considering transitions directly to the ground state but this is not exactly the case because of the dependence of DALI2 efficiency on the γ energy. However, with this condition less feeding to the 2_1^+ state is expected. In Fig. 5.26 d) the fit which best reproduces the experimental spectrum corresponds to a lifetime of τ=33 ps. As expected, the lifetime is a little smaller because we have removed part of the delay due to lifetime of the feeding transitions. The lifetime of τ=33(15) ps was adopted as the determined experimental value, where the error in the value of lifetime was extracted from the χ^2 distribution.

Now, we can use the extracted lifetime of $\tau(2_1^+)$=33 ps obtained with the Au target to try to determine the lifetime of the 4_1^+ state observed with the C target. Figures 5.27 a) and b) show the γ-ray spectrum for ^{136}Te on the C target considering all γ-ray multiplicities. For Fig. 5.27 a), the lifetime of τ=33 ps was simulated for the 2_1^+ state while a vanishing lifetime was considered for the 4_1^+ state. Furthermore, the feeding from the 4_1^+ state to the 2_1^+ state was included in the fit. A clear discrepancy between the experimental spectrum and the fit is observed. In Fig. 5.27

b), a lifetime for the 4_1^+ state was also simulated, the lifetime $\tau(4_1^+)$=105 ps best reproduces the experimental spectrum. Now, trying to favor the sequence $4_1^+ \rightarrow 2_1^+ \rightarrow 0_1^+$, events with γ-ray multiplicity equal to 2 are studied. Figures 5.27 c) and d) show the γ-ray spectrum for ^{136}Te on the C target considering only events with γ-ray multiplicity equal to 2. The lifetime which best reproduces the spectrum is $\tau(4_1^+)$=98 ps, this value is, again, smaller than the value obtained with all γ-ray multiplicities. The lifetime of $\tau(4_1^+)$=98(50) ps was adopted as the experimental value. The extracted lifetime for the 4_1^+ state is an effective value as a result of the feeding of the higher-lying 6_1^+ state.

The obtained lifetimes, $\tau(2_1^+)$ and $\tau(4_1^+)$, and the B(E2) values deduced from these lifetimes are summarized in table 5.13. The quoted errors in the lifetimes were obtained based on the χ^2 distribution. To obtain the $B(E2; 4_1^+ \rightarrow 2_1^+)$ value the following expression was used:

$$B(E2; 4_1^+ \rightarrow 2_1^+) = \frac{0.0814}{E_\gamma^5(MeV) \cdot \tau(ps)} e^2 b^2 \tag{5.4}$$

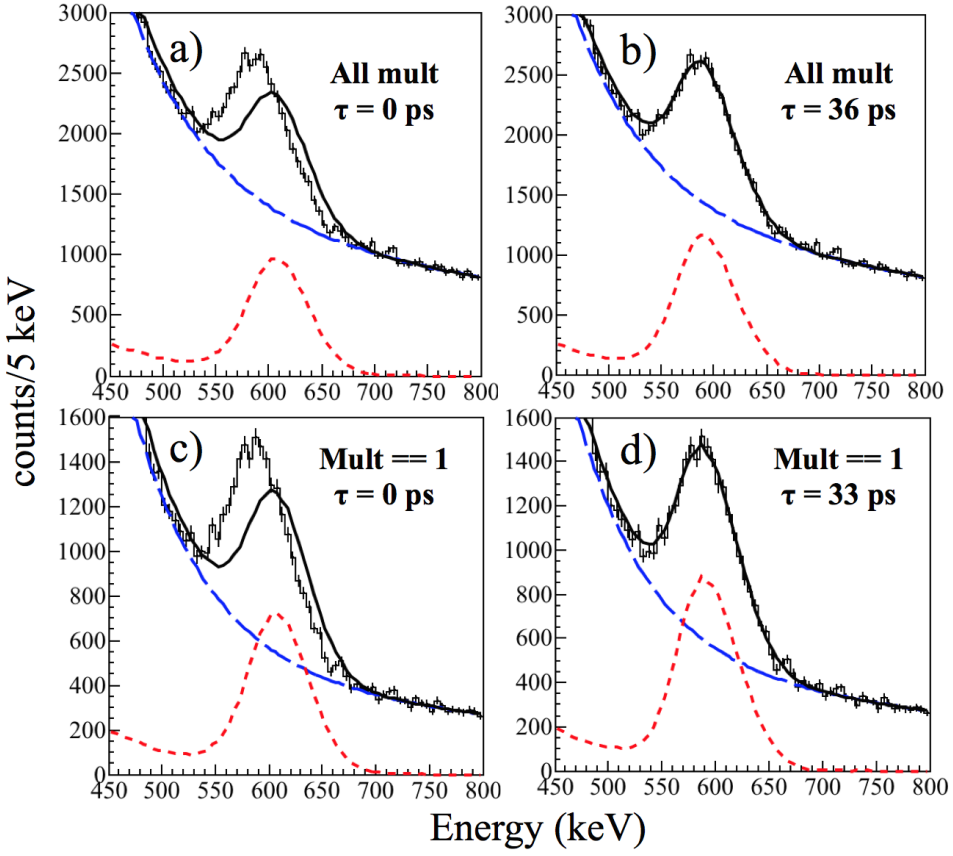

Figure 5.26: Comparison between the experimental spectrum for all γ-ray multiplicities measured with the Au target and GEANT4 simulations assuming a lifetime of a) $\tau(2_1^+)$=0 ps and b) $\tau(2_1^+)$=36 ps. Comparison considering events with γ-ray multiplicity equal to 1 and GEANT4 simulations assuming a lifetime of c) $\tau(2_1^+)$=0 ps and d) $\tau(2_1^+)$=33 ps.

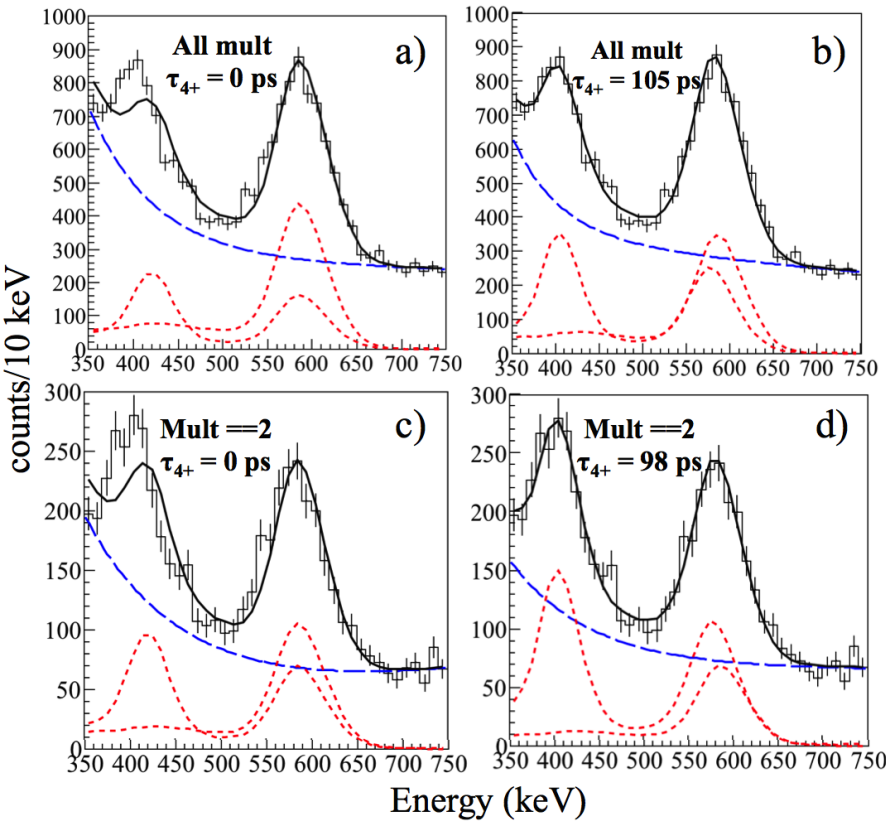

Figure 5.27: Comparison between the experimental spectrum for all γ-ray multiplicities measured with the C target and GEANT4 simulations assuming lifetimes of a) $\tau(2_1^+)$=33 ps and $\tau(4_1^+)$=0 ps and b) $\tau(2_1^+)$=33 ps and $\tau(4_1^+)$=105 ps. Comparison considering events with γ-ray multiplicity equal to 2 and GEANT4 simulations assuming a lifetime of c) $\tau(2_1^+)$=33 ps and $\tau(4_1^+)$=0 ps and d) $\tau(2_1^+)$=33 ps and $\tau(4_1^+)$=98 ps.

Table 5.13: Summary of ^{136}Te reduced transition probabilities obtained from the lifetimes.

State	E_{state} (MeV)	E_γ (MeV)	τ (ps)	B(E2) (e^2b^2)
2_1^+	0.606	0.606	33(15)	B(E2;$0_1^+ \rightarrow 2_1^+$) = 0.151(69)
4_1^+	1.030	0.423	98(50)	B(E2;$4_1^+ \rightarrow 2_1^+$) = 0.061(31)

5.1.10 Limit for the B(E2) value of the 2_{ms}^+ mixed-symmetry state

Since the anomalously small B(E2;$0_1^+ \rightarrow 2_1^+$) value of ^{136}Te was observed for the first time by Radford *et al.* [45], numerous theoretical calculations have tried to find the origin of this anomaly. All calculations agree to attribute this low B(E2) value as a consequence of a strong proton-neutron asymmetry in the wave function of the 2_1^+ state in ^{136}Te, with the wave function dominated by two-neutron excitations. One possible approach to probe the proton-neutron asymmetry in the wave function is to study the decay properties of the isovector analogue of

the 2_1^+ state, the one-phonon state with mixed proton-neutron symmetry, 2_{ms}^+. This so-called mixed-symmetry state decays via a strong M1 transition to the first excited 2^+ state and a weak E2 transition to the ground state. Studying the $2_{ms}^+ \rightarrow 2_1^+$ M1 transition, information about the proton-neutron balance of the wave functions can be obtained. This mechanism was already studied in the neighboring isotope ^{132}Te [47], concluding that in this nucleus the wave function of the 2_1^+ state shows a balanced proton-neutron composition.

Theoretical calculations predict a 2_{ms}^+ state at different excitation energies: Shimizu *et al.* [50] calculated the 2_{ms}^+ state around 1.500 MeV and with a B(E2;$0_1^+ \rightarrow 2_{ms}^+$) = 0.03 e^2b^2, Covello *et al.* [49] gave values of 1.805 MeV and B(E2;$0_1^+ \rightarrow 2_{ms}^+$) = 0.022 e^2b^2 and, finally, Severyukhin *et al.* [52] predicted the 2_{ms}^+ state at 2.010 MeV and with a B(E2;$0_1^+ \rightarrow 2_{ms}^+$) = 0.074 e^2b^2. In the spectrum shown in Fig. 5.3 a) obtained with the Au target, there is no evidence of any transition in the energy range from 800 to 2000 keV so we can not determine experimentally the B(E2;$0_1^+ \rightarrow 2_{ms}^+$) value. An upper limit for the B(E2;$0_1^+ \rightarrow 2_{ms}^+$) value can be established considering the possible indication for such a transition with the level of background observed in the spectrum displayed in Fig. 5.3 a) and the experimental sensitivity. Figures 5.28 a) and b) show the Doppler corrected γ-ray spectrum obtained with the Au target. Besides the $2_1^+ \rightarrow 0_1^+$ transition, γ rays with energies of 900 keV (Fig. 5.28 a)) and 1800 keV (Fig. 5.28 b)) were included in the fit assuming yields of 10% and 16% relative to the 2_1^+ transition, respectively. These values were considered as the lower observational limits. Figure 5.28 c) displays the relative deviations between the experimental spectrum and the fit when only the 2_1^+ state is considered for the DALI2 response, the quality of the fit is shown to be excellent. Figures 5.28 d) and e) show the same relative deviations, but when γ rays with energies of 900 keV and 1800 keV, respectively, are included in the fit showing that, with the quoted intensities, such transitions should have been observed. The upper limit for the B(E2;$0_1^+ \rightarrow 2_{ms}^+$) was obtained relative to the B(E2;$0_1^+ \rightarrow 2_1^+$)=0.191 e^2b^2 value and using the relative yields quoted above. In table 5.14, the obtained upper limits for both energies as a function of the unknown $2_{ms}^+ \rightarrow 2_1^+ / 2_{ms}^+ \rightarrow 0_1^+$ branching ratio (BR) are summarized.

Table 5.14: Upper limits for the B(E2;$0_1^+ \rightarrow 2_{ms}^+$) value as a function of the branching ratio (BR) between the $2_{ms}^+ \rightarrow 2_1^+$ and $2_{ms}^+ \rightarrow 0_1^+$ transitions.

E_{state} 2_{ms}^+ (MeV)	E_γ $2_{ms}^+ \rightarrow 2_1^+$ (MeV)	B(E2;$0_1^+ \rightarrow 2_{ms}^+$) ($e^2b^2$)
1.500	0.900	$< \frac{(BR+1)}{BR} \cdot$ 0.019
2.400	1.800	$< \frac{(BR+1)}{BR} \cdot$ 0.031

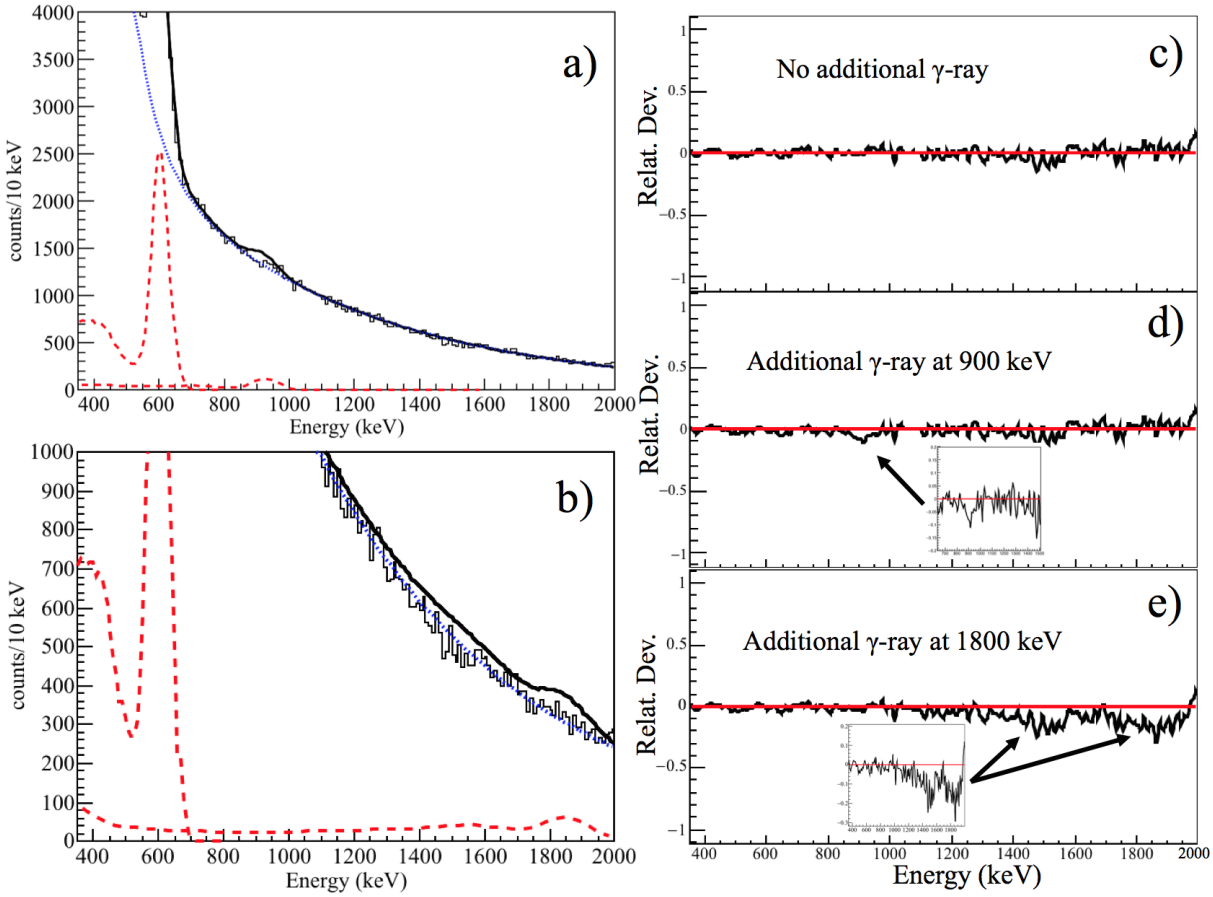

Figure 5.28: Doppler-corrected γ-ray spectrum for ^{136}Te from inelastic scattering on the Au target and assuming additional simulated lines for γ rays with energies of a) 900 keV and b) 1800 keV. The relative deviations between the experimental spectrum and the fit are shown in c) when no additional lines are considered, in d) when a γ ray of 900 keV is also included in the fit and in e) when the energy of the additional γ ray is 1800 keV. Parts d) and e) are expanded about the region of interest.

5.1.11 Comparison between the experimental B(E2) values and theoretical calculations

In this section, we will compare the experimental B(E2) values of the 2_1^+ and 4_1^+ states and the upper limit for the B(E2;$0_1^+ \rightarrow 2_{ms}^+$) to the possible 2_{ms}^+ state obtained in this work to already published experimental data and to different theoretical calculations. In total, there are three different experimental measurements of the B(E2) value for the 2_1^+ state of ^{136}Te. Firstly, Radford *et al.* [45] measured the B(E2) values for the first 2^+ states of neutron-rich ^{132,134,136}Te using the Coulomb excitation technique at low beam energies at the HRIBF facility. For ^{136}Te, they deduced a B(E2;$0_1^+ \rightarrow 2_1^+$) = 0.103(15) e^2b^2. Afterwards, Danchev *et al.* [47] corrected this value due to an erroneous target thickness. As a consequence, the value was corrected to B(E2;$0_1^+ \rightarrow 2_1^+$) = 0.122(18) e^2b^2. In 2008, Fraile *et al.* [46] reported a B(E2;$0_1^+ \rightarrow 2_1^+$) = 0.122(24) for the 2_1^+ state of ^{136}Te using the fast timing technique at ISOLDE. Very recently,

Allmond *et al.* [53] performed another Coulomb excitation experiment at HRIBF [45] but now using a titanium target instead of a carbon target in order to increase the cross section of the excitation to the 2_1^+ state. The quoted new value was B(E2;$0_1^+ \rightarrow 2_1^+$) = 0.181(15) e^2b^2. They also obtained a B(E2) value for the $4_1^+ \rightarrow 2_1^+$ transition and an upper limit for the excitation of the 2_2^+ state. The reported values were B(E2;$4_1^+ \rightarrow 2_1^+$) = 0.060(9) e^2b^2 and B(E2;$0_1^+ \rightarrow 2_2^+$) $<$ 0.02 e^2b^2.

From the theoretical point of view, many calculations have tried to reproduce the low experimental B(E2) value for the 2_1^+ state of ^{136}Te. In 2002, Terasaki and collaborators [51] used a separable quadrupole-plus-pairing Hamiltonian and the quasiparticle random phase approximation (QRPA) to calculate B(E2) values, their calculated value was B(E2;$0_1^+ \rightarrow 2_1^+$) = 0.09 e^2b^2. Later, in 2004, Shimizu *et al.* [50] performed shell model calculations using the single-particle space and Hamiltonian which have been used successfully for a systematic description of the spherical-deformed shape phase transition in Ba isotopes. They reported a value of B(E2;$0_1^+ \rightarrow 2_1^+$) = 0.15 e^2b^2 for ^{136}Te. Moreover, they also calculated the energy and B(E2) of the 2_2^+ mixed-simmetry state in ^{136}Te, E = 1.5 MeV and B(E2;$0_1^+ \rightarrow 2_2^+$) = 0.03 e^2b^2. Afterwards, Severyukhin *et al.* [52] performed calculations within the finite-rank separable approximation, which enables one to perform QRPA calculations in very large two-quasiparticle configurational spaces. The theoretical predictions of the reduced transition probabilities for the 2_1^+ and 2_2^+ states in ^{136}Te were B(E2;$0_1^+ \rightarrow 2_1^+$) = 0.112 e^2b^2 and B(E2;$0_1^+ \rightarrow 2_2^+$) = 0.074 e^2b^2, respectively. In Ref. [53], the authors showed shell model calculations using realistic effective interactions [49]. We have repeated these shell model calculations using the same interaction but with the ANTOINE code [132]. These shell model calculations consider ^{132}Sn as a doubly-magic core and let the valence protons occupy the levels 0g$_{7/2}$, 1d$_{5/2}$, 1d$_{3/2}$, 2s$_{1/2}$ and 0h$_{11/2}$ of the 50-82 shell, while for the valence neutrons the available levels are 0h$_{9/2}$, 1f$_{7/2}$, 1f$_{5/2}$, 2p$_{3/2}$, 2p$_{1/2}$ and 0i$_{13/2}$ of the 82-126 shell. The calculations have been performed using an effective neutron charge of e_n = 0.7e and an effective proton charge of e_p = 1.7e. With this approach, the B(E2) for the first excited 2^+ state in ^{136}Te is B(E2;$0_1^+ \rightarrow 2_1^+$) = 0.205 e^2b^2. We also calculated the energies, wave function compositions and B(E2) values for the second and the third 2^+ states and we found that with these shell model calculations the 2_3^+ state is the mixed-symmetry state. The energy and B(E2) calculated for the 2_2^+ were 1.55 MeV and B(E2;$0_1^+ \rightarrow 2_2^+$) = 0.014 e^2b^2, respectively, while for the 2_3^+ they are 1.805 MeV and B(E2;$0_1^+ \rightarrow 2_3^+$) = 0.022 e^2b^2. Very recently, Naïdja *et al.* [133] investigated the collectivity in the nuclei beyond ^{132}Sn using an effective interaction based on the realistic effective field theory potential, N3LO. The calculated B(E2) value in this work was B(E2;$0_1^+ \rightarrow 2_1^+$) = 0.205 e^2b^2.

All the experimental B(E2;$0_1^+ \rightarrow 2_1^+$) values in ^{136}Te discussed above together with the different theoretical calculations are plotted in Fig. 5.29. In addition, the experimental B(E2) values [47] and the theoretical calculations for the ^{132,134}Te isotopes are also included in the figure. Our

experimentally derived B(E2)↑ value is in good agreement with the value B(E2)=0.181(15) e^2b^2 obtained recently in Ref. [53], but it deviates considerably from the value of B(E2)=0.122(18) e^2b^2 reported in Ref. [47] and from the value of B(E2)=0.122(24) e^2b^2 reported in Ref. [46]. Regarding the theoretical calculations, the shell model calculations [49, 50, 133] are consistent with our B(E2), while the remaining calculations [51, 52] are far from reproducing our experimental B(E2). In table 5.15 all the experimental and theoretical B(E2) values reported so far are summarized. Our result confirms a higher proton content in the wave-function of the 2_1^+ state than previously suggested.

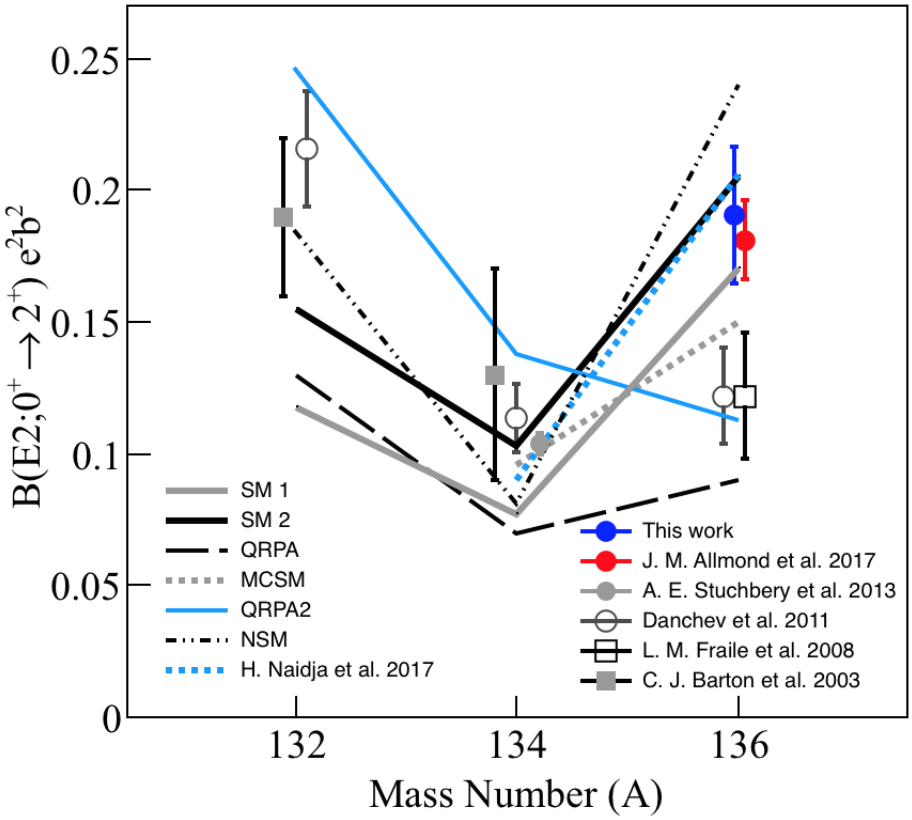

Figure 5.29: Experimental B(E2;$0_1^+ \rightarrow 2_1^+$) values for the ^{132,134,136}Te isotopes from this work (blue point) and previous values from the literature [46, 47, 53] compared to different theoretical calculations [49–52, 133]. The labels of each theoretical calculation are explained in table 5.15.

5.1.12 Spin of the new state at 4.2 MeV

The angular distribution of scattered ions can be used to determine the unknown spin and parity of new excited states. This is possible for the state observed at 4.2 MeV in ^{136}Te scattered on the Au target. This state has two branches decaying with the same intensity to the 2_1^+ and ground states. At intermediate/relativistic energies, the Coulomb excitation is dominated by single-step excitations while multistep excitations play only a minor role. Therefore, the observation of this state can only be attributed to E1, E2 and E3 excitations, limiting the possible

Table 5.15: Summary of experimental and theoretical energies and B(E2) values for the 2_1^+, 4_1^+ and 2_x^+ states in ^{136}Te.

Experimental			Theoretical			
Ref.	state	B(E2;$0_1^+ \rightarrow 2_1^+$) (e^2b^2)	Ref.	state	E (MeV)	B(E2;$0_1^+ \rightarrow 2_1^+$) (e^2b^2)
Danchev [47]	2_1^+	0.122(18)	Terasaki (QRPA) [51]	2_1^+	-	0.09
Fraile [46]	2_1^+	0.122(24)	Shimizu (MCSM) [50]	2_1^+	0.650	0.15
Allmond [53]	2_1^+	0.181(15)	Severyukhin (QRPA2) [52]	2_1^+	0.920	0.112
This work [a]	2_1^+	0.191(26)	Realistic SM (SM2) [49]	2_1^+	0.674	0.205
			Naïdja [133]	2_1^+	0.626	0.205
			SM1 [53]	2_1^+	-	0.170
			NSM [53]	2_1^+	0.610	0.240
Ref.	state	B(E2;$4_1^+ \rightarrow 2_1^+$) (e^2b^2)	Ref.	state	E (MeV)	B(E2;$4_1^+ \rightarrow 2_1^+$) (e^2b^2)
Allmond [53]	4_1^+	0.060(9)	Realistic SM [49]	4_1^+	1.083	0.052
This work [b]	4_1^+	0.061(31)				
Ref.	state	B(E2;$4_1^+ \rightarrow 2_x^+$) (e^2b^2)	Ref.	state	E (MeV)	B(E2;$0_1^+ \rightarrow 2_x^+$) (e^2b^2)
Allmond [53]	2_2^+	< 0.02	Shimizu [50]	2_2^+	1.500	0.03
This work [c]	2_x^+ (1.5 MeV)	< 0.019	Severyukhin [52]	2_2^+	2.010	0.074
	2_x^+ (2.4 MeV)	< 0.031	Realistic SM [49]	2_2^+	1.550	0.014
				2_3^+	1.800	0.022

[a] from the cross section
[b] from the effective lifetime
[c] upper limits

spin and parity values for the new state to 1^-, 2^+ and 3^-. The same approach used before to describe the angular distributions of the 2_1^+ state on the Au and C targets will be used now to deduce the spin of the state at 4.2 MeV. For the case of the 2_1^+ state, the nuclear contributions (δ_N) were determined using the C target. Unfortunately, for this new state we could not extract the nuclear contributions from the C target, since, as it was explained previously, the spectrum measured with the C target is contaminated at high energies (Fig. 5.15). However, from the experimental exclusive cross section to the 2_1^+ state on the C target (σ = 9.5(32) mb) and the 50% branching ratio of the state at 4.2 MeV feeding the 2_1^+, we can estimate an upper limit for the nuclear deformation of the state at 4.2 MeV. Considering that the cross section, σ = 9.5(32) mb, to the 2_1^+ state is fully due to the feeding from the state at 4.2 MeV, we obtain a cross section of σ = 19 mb to this state on the C target which can be used to determine an upper limit for its nuclear deformation length value. In contrast, the other extreme case is given by δ_{nuc}=0 fm.

Calculations were performed with FRESCO for multipolarities E1, E2 and E3 and considering an excitation energy of 4.2 MeV for the state. Then, the matrix elements M(E1), M(E2) and M(E3) and the nuclear deformation length δ_N were varied (always satisfying the condition mentioned above) to reproduce the measured cross section of $\sigma = 42(4)$ mb for the state at 4.2 MeV on the Au target. For E1 excitations, the nuclear contributions are negligible, for E2 excitations the nuclear part plays a minor role (as it was shown for the case of the 2_1^+ state)

and, after folding, the shape of the theoretical distribution is independent of the δ_{nuc} value, while for E3 excitations the Coulomb and nuclear excitations can have comparable strengths and the interferences between both interactions can caused small shifts in the shape of the angular distribution. Figure 5.30 a) shows the theoretical angular distributions obtained for each multipolarity. For the case of E1 and E2 excitations (whose shapes of the theoretical distributions and reduced transition probabilities are independent on δ_N) the cross section of $\sigma = 42(4)$ mb on the Au target was reproduced with transition probabilities values of B(E1;$0 \rightarrow 1^-$) = 0.150(15) e^2fm^2 and B(E2;$0 \rightarrow 2^+$) = 0.368(32) e^2b^2, respectively. For E3 excitations, the cross section of σ = 19 mb on the C target was reproduced with FRESCO using a value of δ_{nuc}=1.1 fm. In the limit δ_{nuc}=0.0-1.1 fm, the reduced transition probability calculated to reproduce the cross section of $\sigma = 42(4)$ mb on the Au target ranged between B(E3;$0 \rightarrow 3^-$) = 0.265-0.59 e^2b^3. Figure 5.30 b) shows the unfolded theoretical calculations performed with FRESCO for three studied cases for an E3 excitation ($\delta_{E3\,N}$ = 0, 0.685 and 1.1 fm).

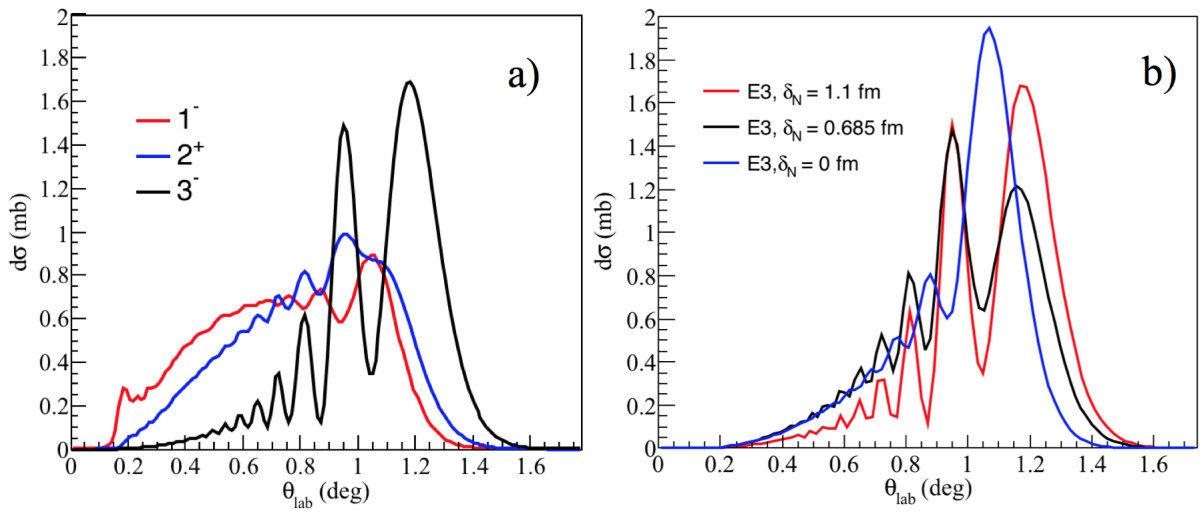

Figure 5.30: a) Theoretical angular distributions for E1, E2 and E3 multipolarities obtained with FRESCO without folding. b) Theoretical angular distributions only for E3 excitations and considering different nuclear deformation lengths, δ_N, and reduced transition probabilities, B(E3) (see the text for more details).

Figure 5.31 shows a comparison between the experimental angular distribution for the state at 4.2 MeV and the folded theoretical calculations determined with FRESCO for the cases listed above. Clearly, the theoretical distributions for E1 and E2 multipolarities can not describe the experimental points. For the case of E3 excitations, the calculated distributions in the range δ_N=0.0-0.9 fm reproduce perfectly the experimental points. However, for δ_N=1.1 fm, the total cross section starts to be dominated by nuclear excitations and a shift is observed in the theoretical distribution which worsens the agreement between the experimental and theoretical distributions. Furthermore, the δ_N=1.1 fm value was obtained assuming no direct excitation of the 2^+_1 state on the C target, which is unphysical and, therefore, can be discarded. Based on the comparison displayed in Fig. 5.31, we assign the spin and parity of 3^- to the state at 4.2 MeV.

The range of the reduced transition probability was obtained considering that the cross section to the 4.2 MeV state on the C target can not be much higher than the cross section to the 2_1^+ state [134]. With this assumption, a B(E3;$0 \rightarrow 3^-$) = 0.42-0.59 e^2b^3 range was determined.

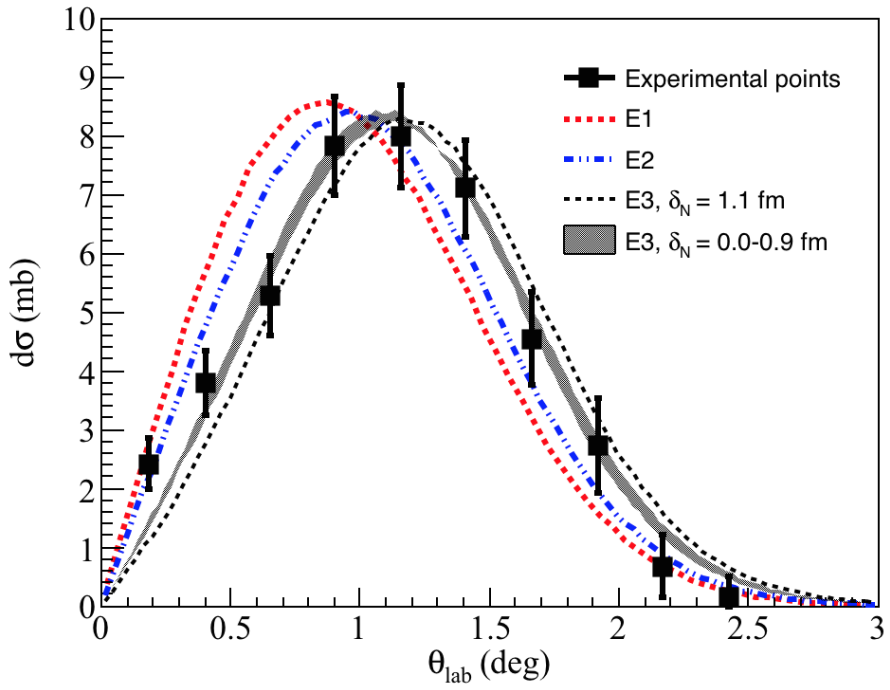

Figure 5.31: Comparison between the experimental angular distribution measured in coincidence with the state at 4.2 MeV and theoretical calculations performed with FRESCO assuming different multipolarities and folded with the experimental resolution. For E3 excitations, the gray area corresponds to the δ_N=0.0-0.9 fm range while the black dashed line corresponds to δ_N =1.1 fm.

To obtain information about the possible origin of this new state, Hartree-Fock-Bogoliubov mean-field calculations will be performed after the presentation of this thesis.

5.2 Inclusive cross sections

In this section, we will describe in detail the different steps followed in the analysis to obtain the inclusive cross sections for the multiple knockout of neutrons and protons from different projectiles at energies around 165 MeV/u. The experimental cross sections will be compared to predictions from state-of-the-art calculations based on the Monte Carlo description of the cascade and evaporation processes obtained with the INCL-ABLA reaction code. Finally, from the comparison between the experimental and theoretical cross sections, nuclear structure information about the different projectiles will be revealed.

5.2.1 Experimental conditions and PID plots

To increase the yields of ^{134}Sn and ^{136}Sb compared to the first setting which centered on the ^{136}Te ions, the slits and $B\rho$ values of both spectrometers were modified. As we moved towards more exotic regions, we could increase the intensity of the ^{238}U primary beam from 2.5 pnA (^{136}Te setting) to 15 pnA. Also the downscale factor for the F7 trigger was changed from 1/60 to 1/40 since the beam intensity was lower. The same C target (535 mg/cm^2) employed in the Coulomb excitation experiment to extract the nuclear contributions to the total cross section was used now to induce knockout reactions. The total time of data acquisition was around 22 hours.

In table 5.16, the number of ions detected for each isotope are summarized. With this setting, ^{135}Sb beam is the most intense of the cocktail RIB with the ^{136}Te and ^{134}Sn ions having similar intensities. This is reflected in the particle identification plot for the BigRIPS spectrometer shown in Fig. 5.32 a), where ^{135}Sb ions now dominate. Figure 5.32 b) displays the PID for the ZeroDegree spectrometer when we gate on ^{134}Sn in BigRIPS, where many by-products are observed. The ^{133}Sn ions are highlighted and will be studied in next section.

Table 5.16: Total number of ions detected in BigRIPS during the 22 hours of the measurement focussed on ^{134}Sn and ^{135}Sb.

Number of ions in BigRIPS C target			
^{135}Sb	$3.53{\cdot}10^8$	^{133}Sn	$1.69{\cdot}10^7$
^{136}Te	$9.64{\cdot}10^7$	^{136}Sb	$1.13{\cdot}10^7$
^{134}Sn	$8.56{\cdot}10^7$	^{137}Te	$8.89{\cdot}10^6$
^{134}Sb	$5.04{\cdot}10^7$	^{135}Sn	$2.13{\cdot}10^6$

5.2.2 Determination of inclusive cross sections

The experimental multi-proton and multi-neutron removal cross sections were derived from the three different settings run with the C target. The first of them with the BigRIPS and ZeroDegree spectrometers centered on ^{136}Te (Fig. 5.1 c)) and the other two with the BigRIPS and ZeroDegree settings tuned to more exotic regions (Fig. 5.32 a)). The cross sections were measured for ^{137}I, ^{137}Te, ^{136}Te, ^{136}Sb, ^{135}Te, ^{135}Sb, ^{134}Sb, ^{134}Sn and ^{133}Sn projectiles. To illustrate the different steps followed in the analysis, we will take as an example the case of the ^{135}Sb projectile since it was produced with the highest intensity. Figure 5.33 a) shows the particle identification plot for the ZeroDegree spectrometer when we gate on ^{135}Sb in BigRIPS, where many by-products are observed. In the figure are highlighted the x-neutron removal channels (red dashed line), the one-proton and x-neutron removal channels (purple dashed line), and

the two-proton and x-neutron removal channels (green dashed channel). Figure 5.33 b) displays the A/Q ratio for the Sb isotopes (the condition 50.5<Z<51.5 was applied to the atomic number) of the PID shown on the left. A good A/Q resolution is achieved which allows us to determine cross sections for the different reaction channels. Again, a fraction of the ions are also observed in the hydrogen and helium-like charge states.

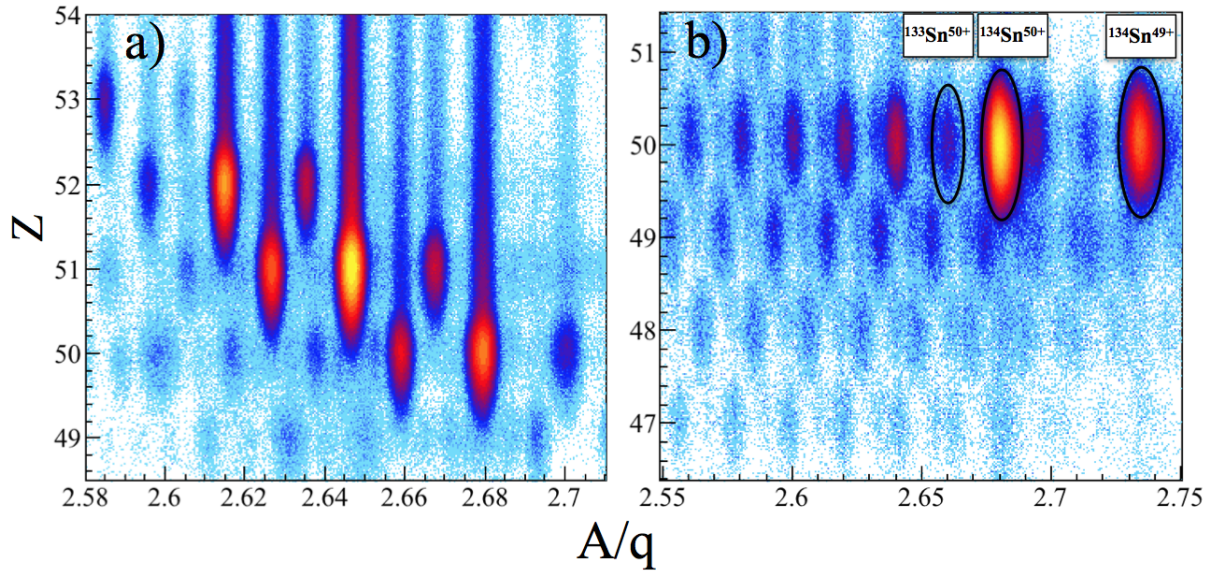

Figure 5.32: a) Particle identification plot for the BigRIPS spectrometer. b) Identification plot for the ZeroDegree spectrometer requiring the identification of ^{134}Sn ions in BigRIPS.

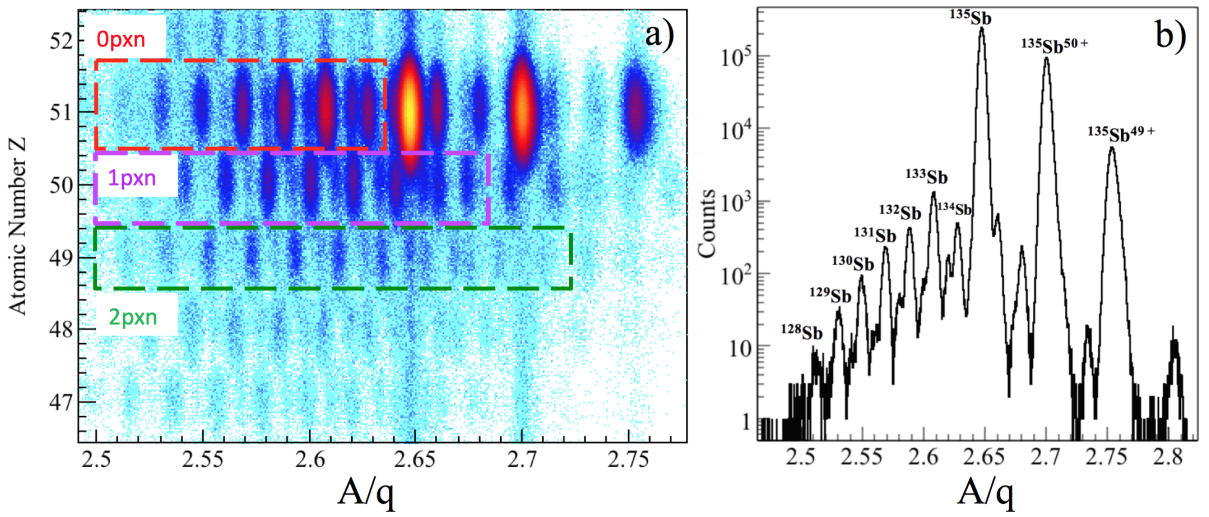

Figure 5.33: a) Particle identification plot for the ZeroDegree spectrometer requiring the identification of ^{135}Sb ions in BigRIPS obtained with the C target. The Sb isotopes produced in the multi-neutron removal channel are highlighted by the red dashed line, the one-proton and x-neutron removal channels are highlighted by the purple dashed line, and the two-proton and x-neutron removal channels are highlighted by the green dashed line. b) A/Q identification of the Sb isotopes produced from the multi-neutron removal of the incoming ^{135} Sb.

If we consider the case of the one-neutron knockout from the ^{135}Sb projectile, the cross section for this reaction is given by:

$$\sigma = \frac{N(^{134}Sb)}{n \cdot I(^{135}Sb)} \tag{5.5}$$

where $N(^{134}Sb)$ is the number of ^{134}Sb ions produced in the C target, $I(^{135}Sb)$ is the number of ^{135}Sb ions impinged on the C target and n is the number of C atoms per cm^2 in the target given by $n = \frac{\rho_{target} L_{target} N_A}{M_{target}}$. In order to obtain the cross sections we need to count the number of incoming and outgoing ions in the target. For that we have to apply several conditions based on the trigger pattern. Figure 5.34 shows the trigger distribution of the experiment. The trigger = 1 is the F7 downscaled trigger (DS F7). It corresponds to the beam rate at the F7 focal plane and is downscaled by a factor 40 (for the most exotic run). The trigger = 3 is the DS F7 trigger in coincidence with a signal in the F11 focal plane. The trigger = 6 means the F7 (not downscaled) and F11 focal planes have signals in coincidence with a signal in DALI2. Lastly, the trigger = 7 is the same trigger as 6, but with F7 downscaled (DS F7xF11xDALI2). To obtain the number of incoming and outgoing ions an OR condition on all triggers in which the DS F7 trigger was active has to be applied (trigger =1 or 3 or 7). In eq. 5.5, $I(^{135}Sb)$ is the number of ^{135}Sb ions impinging on the target and $N(^{134}Sb)$ is the number of ^{134}Sb ions produced in the target. However, the identification of the incoming ions ends in the F7 focal plane while the identification of the outgoing ions finishes at the F11 focal plane. There are several layers of material between the F7 focal plane and the target, and between the target and the F11 focal plane. Therefore, we need to introduce some factors into eq. 5.5 to take this into account. Figure 5.35 shows the different possible losses along the beam line from the ion identification in the F7 MUSIC detector until the end of the ZeroDegree line. To obtain the cross section we will use the number of ions identified in the ZeroDegree spectrometer since we will not need to consider corrections due the charge states distribution. The relation between the number of ions in eq. 5.5 and the number of ions in ZD is given by:

$$I(^{135}Sb) = \frac{N_{ZD}(^{135}Sb)}{\epsilon_{ZD} \cdot \frac{\epsilon_{loss}}{2} \cdot T(^{135}Sb)} \tag{5.6}$$

$$N(^{134}Sb) = \frac{N_{ZD}(^{134}Sb)}{\epsilon_{ZD} \cdot \frac{\epsilon_{loss}}{2} \cdot T(^{134}Sb)} \cdot \chi \tag{5.7}$$

where now $N_{ZD}(^{135}Sb)$ is the number of ^{135}Sb ions detected in ZeroDegree, $N_{ZD}(^{134}Sb)$ is the number of ^{134}Sb ions measured in ZeroDegree, $T(^{135}Sb)$ and $T(^{134}Sb)$ are the ZeroDegree transmissions for the ^{135}Sb and ^{134}Sb ions, respectively, i.e. losses due to the acceptance of the ZeroDegree spectrometer, ϵ_{loss} takes into account the reaction losses in the C target and ϵ_{ZD} takes into account the efficiency of the ZeroDegree line (from behind the target up to the F11 MUSIC), i.e reaction losses in PPAC/plastics/MUSIC, as well as the PID reconstruction efficiency. The correction factor due to target losses is divided by 2 since we assume that, on average, the reaction occurs at mid-target. The χ factor in eq. 5.7 takes into account the ratio

of ^{134}Sb produced in the target-to-target+material (where "+material" refers to the remaining material layers between F7 and F8). In the χ factor we do not have to consider the rest of materials from F8 to F11 because any ^{134}Sb produced along this section will have an incorrect A/Q and, as a consequence, it will not be identified as ^{134}Sb in ZeroDegree. However, we can not distinguish the ^{134}Sb produced in the target from the ^{134}Sb produced in any material between F7 MUSIC and the target since this region is not used for the particle identification in ZeroDegree. For the projectile, ^{135}Sb, we do not have to consider any χ factor since it is not possible to produce more ^{135}Sb along the beam line. Replacing in eq. 5.5 the definitions 5.6 and 5.7 we obtain:

$$\sigma = \frac{N_{ZD}(^{134}Sb)}{n \cdot N_{ZD}(^{135}Sb) \cdot T^*} \cdot \chi \tag{5.8}$$

where we have defined a relative transmission, $T^* = T(^{134}Sb)/T(^{135}Sb)$. Now, the cross section can be obtained by normalizing to the particles detected in the ZeroDegree spectrometer, where one assumes that the reaction losses are the same for secondary beam and reaction products. However, normalizing to the particles detected in ZeroDegree, as already mentioned, we have to consider that a reaction can also take place in any of the materials situated between F7 (where the BigRIPS PID finishes) and F8 (where the ZeroDegree PID starts) focal planes. This contribution can not be obtained directly from the experiment since we can not separate the contribution between F7 and F8 from the rest of the beam line. To know the ratio of knockout products produced in the target-to-target+materials (χ factor) we use the LISE^{++} code [107]. Before obtaining the former ratio from LISE^{++}, we verify that the numbers calculated with LISE^{++} are in good agreement with other experimental observations.

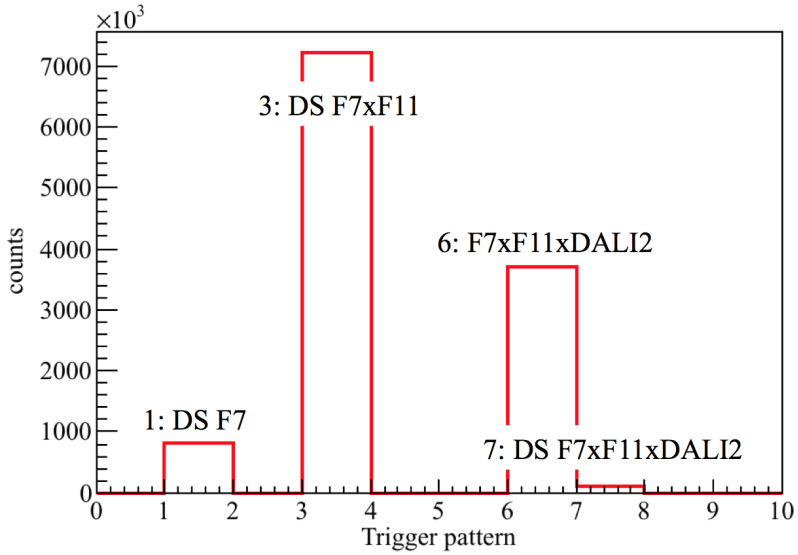

Figure 5.34: Trigger pattern: trigger = 1 means DS F7 was active, but the beam did not reach the F11 focal plane, trigger = 3 means DS F7 was active and the beam arrived at the F11 focal plane, trigger = 6 means F7 was active (no DS), the beam arrived at F11 and there was a signal in DALI2, and, lastly, trigger = 7 means DS F7 was active, the beam arrived at F11 and there was a signal in DALI2.

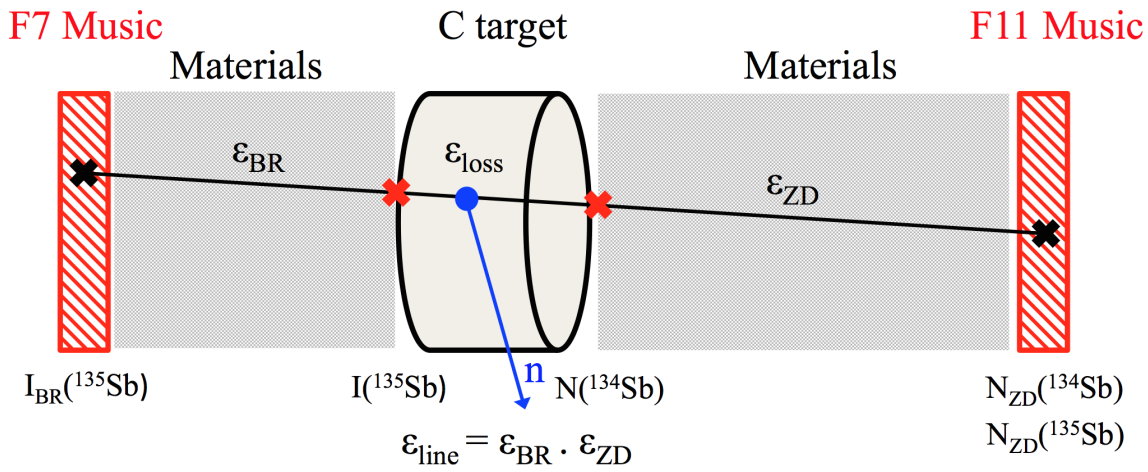

Figure 5.35: Scheme of the one-neutron knockout from the ^{135}Sb beam indicating the different losses along the line. See the text for more details.

Before placing the target in the F8 position, a run without target was performed with the aim of quantifying the losses along the line between the identification at F7 and the arrival at F11. This setting with empty target was centered for the ^{136}Te beam both in the BigRIPS and the ZeroDegree spectrometers. For an isotope centered in BigRIPS, the number of particles identified in ZeroDegree should be the same as the number of particles identified in BigRIPS if the efficiency of the detectors along the line would be 100%. However the efficiency is not 100% and, furthermore, there are reaction losses in the interaction of the ions with the material situated along the beam line. In addition, as our primary beam consists of heavy ions, in the interaction with the material, these ions can pick up electrons from the material and as a result of their change of mass-to-charge ratio, A/Q, they become uncentered. Thus, for the case of ^{136}Te without target, the relation between the number of ions in BigRIPS and ZeroDegree is given by:

$$N_{BR}(^{136}Te) = \frac{N_{ZD}(^{136}Te^{52+})}{\epsilon_{line} * T(^{136}Te^{52+})} + \frac{N_{ZD}(^{136}Te^{51+})}{\epsilon_{line} * T(^{136}Te^{51+})} + \frac{N_{ZD}(^{136}Te^{50+})}{\epsilon_{line} * T(^{136}Te^{50+})} \quad (5.9)$$

where $N_{ZD}(^{136}Te^{52+})$, $N_{ZD}(^{136}Te^{51+})$ and $N_{ZD}(^{136}Te^{50+})$ are the number of fully stripped, hydrogen-like and helium-like ^{136}Te ions measured in ZeroDegree, respectively, T is the transmission for each charge state and ϵ_{line} takes into account the efficiency and losses from the F7 to the F11 focal plane ($\epsilon_{line} = \epsilon_{BR} \cdot \epsilon_{ZD}$). To obtain the ϵ_{line} and T factors we use the horizontal x distribution of each nucleus in the F5 focal plane determined with the PPAC detectors. We use the F5 plane since it is situated in the BigRIPS spectrometer and it is momentum dispersive (see Fig. 3.5). The F5X distributions of ^{136}Te (top) an ^{135}Sb (bottom) are shown in Fig. 5.36, where we have compared the distribution only with a gate on BigRIPS (black curve) to the distributions with a selection also in the ZeroDegree spectrometer for the different charge states (red curves). In blue, the ϵ scale factor is quoted which has been applied to the curve gated

only on BigRIPS in order to reproduce the curve with the ZeroDegree gate on the side where the distribution is not cut. Then the transmission, T (black numbers), is calculated as the ratio between the areas of the two curves, the one with ZeroDegree gate and the scaled one only with gate on BigRIPS. The ϵ_{line} factor is obtained as the sum of the three scale factors of each charge state. The ϵ_{line} factor is quoted in blue on the right hand side, being $\epsilon_{line} = 0.946(14)$ and $\epsilon_{line} = 0.947(14)$ for ^{136}Te and ^{135}Sb, respectively. Since both nuclei have very similar atomic number and mass, the losses in the materials and the ZeroDegree efficiency are very similar for both isotopes. With LISE^{++}, we can calculate the different reaction losses from when the ion is identified in F7 until it arrives at F11. We obtain a value of 0.964 for the reaction losses in the beam detectors for both ^{136}Te and ^{135}Sb. Comparing these losses to the ϵ_{line} factors quoted in blue on the right side of the Fig. 5.36, the PID efficiency should be around 98% ($\epsilon_{line} = \epsilon_{losses\ line} \cdot \epsilon_{eff\ line}$). This efficiency is consistent with the experimental observations.

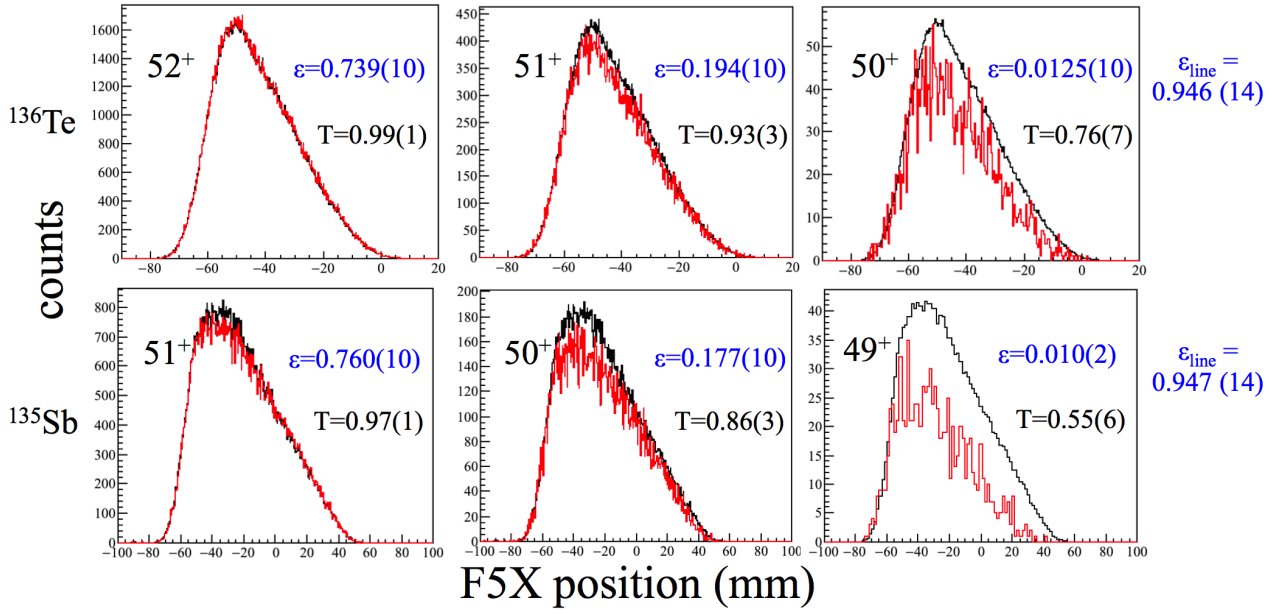

Figure 5.36: Determination of the transmission through ZeroDegree and losses along the beam line for the cases of ^{136}Te (top) and ^{135}Sb (bottom). The black curve is the F5X distribution gated only on BigRIPS while the red ones are also gated on ZeroDegree for the different charge states. The transmissions of each charge state are quoted in black and the ϵ factors in blue. All F5X distributions are obtained without target.

Once the target is placed in the F8 focal plane, the number of ions in BigRIPS can be expressed as:

$$N_{BR}(^{136}Te) = \frac{N_{ZD}(^{136}Te^{52+})}{\epsilon_{line}\epsilon_{loss} * T(^{136}Te^{52+})} + \frac{N_{ZD}(^{136}Te^{51+})}{\epsilon_{line}\epsilon_{loss} * T(^{136}Te^{51+})} + \frac{N_{ZD}(^{136}Te^{50+})}{\epsilon_{line}\epsilon_{loss} * T(^{136}Te^{50+})} \tag{5.10}$$

where ϵ_{loss} are the losses in the C target. Figure 5.37 shows the F5X distributions of ^{136}Te (top) and ^{135}Sb (bottom) measured with the C target and, again, we compare the F5X distribution gated only in BigRIPS to the distributions gated on the different charge states in ZeroDegree.

Now, the sum of the scaling factors is $\epsilon_{line}\epsilon_{loss}$, getting $\epsilon_{line}\epsilon_{loss} = 0.881(15)$ and $\epsilon_{line}\epsilon_{loss} = 0.884(14)$ for the ^{136}Te and ^{135}Sb, respectively. Using the ϵ_{line} factors derived above from the empty target run, we can experimentally determine the losses in the C target for ^{136}Te and ^{135}Sb, obtaining ϵ_{loss}=0.931(21) and ϵ_{loss}=0.933(20), respectively. From LISE^{++} we obtain that the losses in the C target are $\epsilon_{loss\ LISE^{++}}$=0.9307 (^{136}Te) and $\epsilon_{loss\ LISE^{++}}$=0.9309 (^{135}Sb). The losses calculated with LISE^{++} are in excellent agreement with the experimental ones and therefore, we can rely on LISE^{++} to calculate the ratio of knockout products produced in the target-to-target+materials. Of all the reactions between F7 and F8, χ=83(7)% take place in the C target (see Fig. 5.38 for more details). Thus the inclusive cross sections are finally given by:

$$\sigma = \frac{N_{ZD}(^{134}Sb)}{n \cdot N_{ZD}(^{135}Sb) \cdot T^*} \times 0.83(7) \tag{5.11}$$

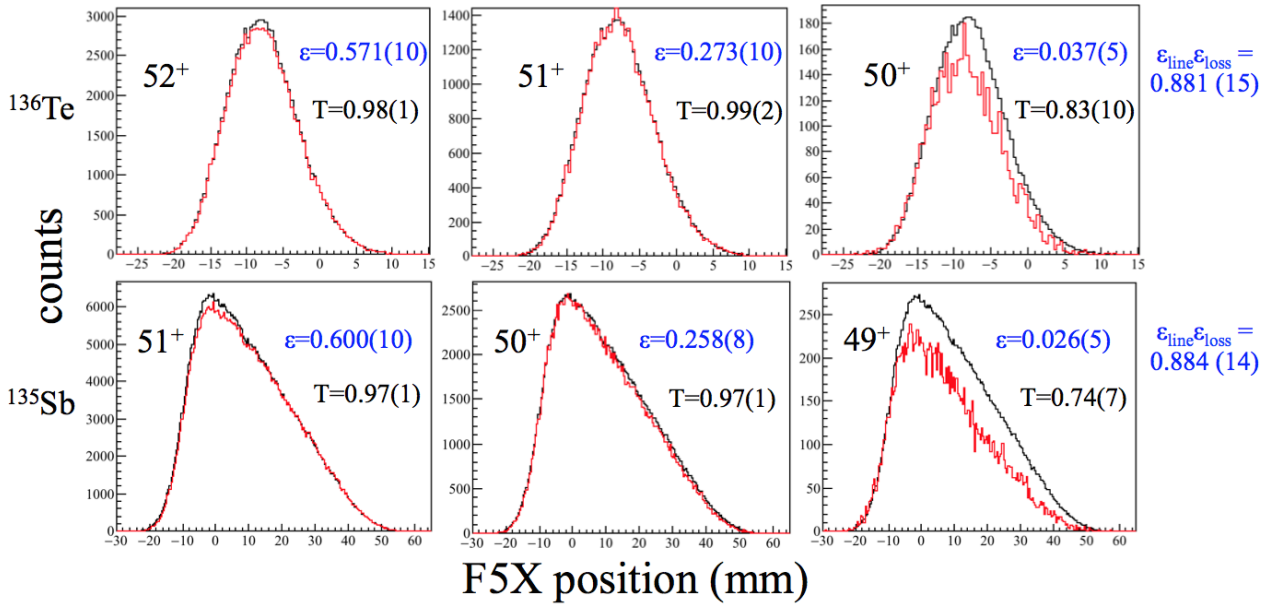

Figure 5.37: Determination of the transmission through ZeroDegree, losses along the beam line and losses in the C target for the cases of ^{136}Te (top) and ^{135}Sb (bottom). The black curve is the F5X distribution gated only on BigRIPS while the red ones are also gated on ZeroDegree for the different charge states. The transmissions of each charge state are quoted in black and the ϵ factors in blue. All F5X distributions are obtained with the C target.

The only factor which has not been explained so far is the relative transmission, T^*. To determine this factor, again we compare the F5X distributions of the knockout products to the F5X distribution of the mother nucleus detected in ZeroDegree. As the factor, T^*, is relative, we can consider only the fully-stripped ions and impose conditions, such as no charge state change between the secondary target and the F11 focal plane in order to obtain cleaner F5X distributions (doing this we are assuming that the charge state distributions are more, or less the same for the different isotopes). Furthermore, since we are only interested in the relative shape of the

F5X distributions, to obtain the T^* factors we can also consider the trigger = 6 (F7xF11xDALI2) and thus increase statistics. Figure 5.39 shows the F5X distributions of the knockout products from the ^{135}Sb projectile compared to the F5X distribution of the mother nucleus in ZeroDegree (^{135}Sb), where the F5X distribution of the mother nucleus has been scaled to reproduce the distributions of the products on the side where they are not cut. With this scaling factor and the number of ions in the two F5X distributions we get T^*. The relative transmissions, T^*, between the products and the mother nucleus are quoted in black. As is shown in Fig. 5.39, as more neutrons are removed, the relative transmission, T^*, is lower since the A/Q ratio diverges more strongly from the centered value, meaning the transmissions get smaller.

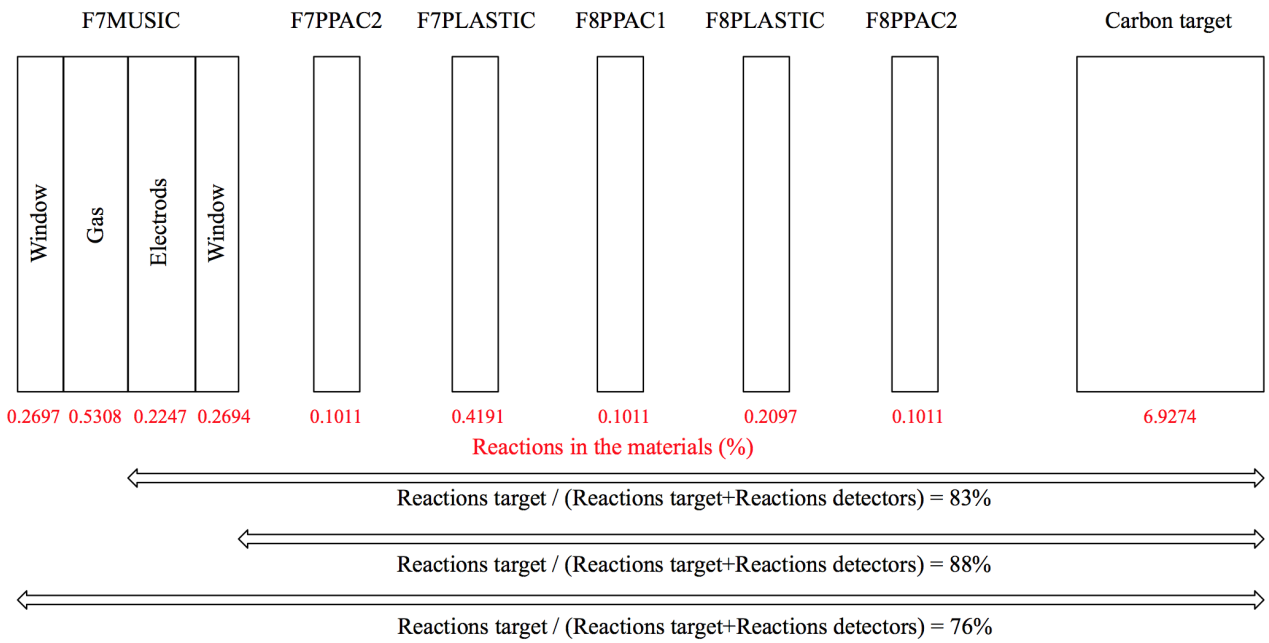

Figure 5.38: Reactions in the different materials situated between the F7 and F8 focal planes calculated with LISE^{++}. The reactions in each material are quoted in red. Of all the reactions between F7 and F8, a 83(7)% take place in the C target, where the error has been estimated considering more, or fewer layers of the F7 MUSIC.

The same procedure discussed above for the case of ^{135}Sb was also applied to all other projectiles and knockout products, where the inclusive cross sections were obtained from the following general expression:

$$\sigma = \frac{N_{ZD}(product)}{n \cdot N_{ZD}(mother) \cdot T^*} \times 0.83 \tag{5.12}$$

with n = 2.67976*10^{22} cm^{-2}. In tables 5.17 and 5.18 the number of product and mother ions in ZeroDegree, the relative transmissions, T^*, and the inclusive cross sections are summarized.

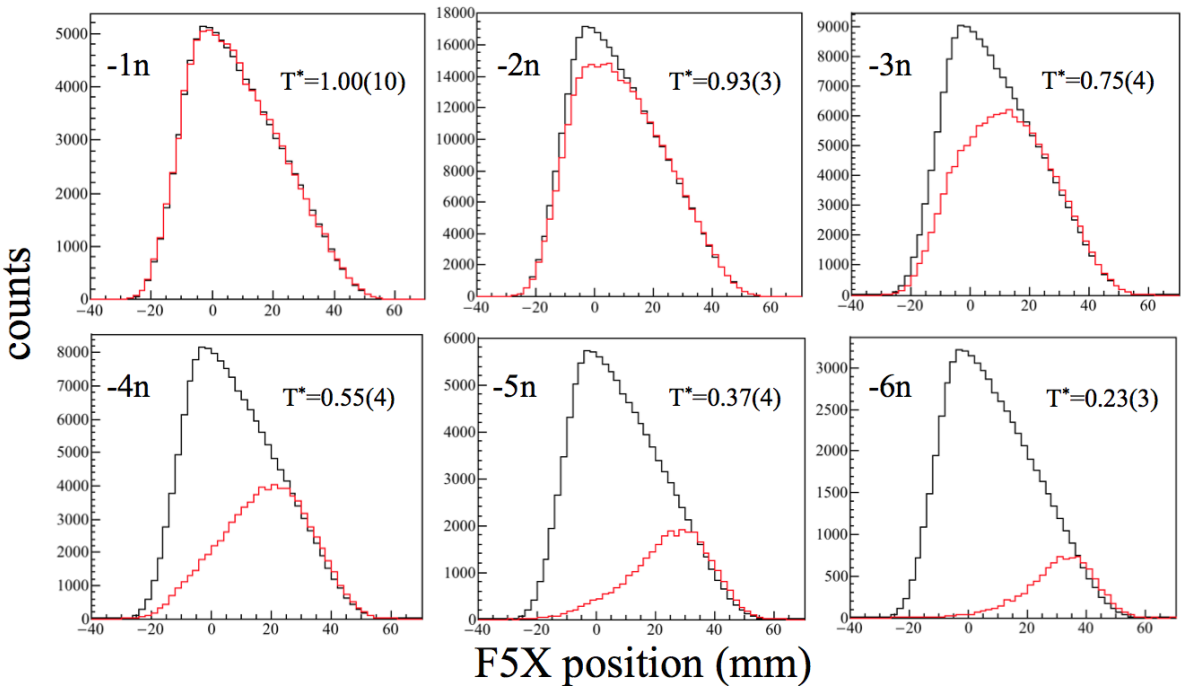

Figure 5.39: Determination of the relative transmission, T^*, through ZeroDegree for the case of the x-neutron knockout from the ^{135}Sb projectile. The red curves are the F5X distributions of the products while the black one is the F5X distribution of the mother nucleus gated on ZeroDegree. The relative transmissions between the knockout products and the mother nucleus are quoted in black. All F5X distributions are obtained with the C target.

5.2.3 INCL/ABLA07 calculations

The nuclear reactions in which a projectile with kinetic energy $>$150MeV/u interacts with a target are usually described by means of models consisting of an intranuclear-cascade (INC) stage followed by a statistical de-excitation stage. The interest in these models has grown over the years since they are able to accurately predict a large number of experimental observables. The main applications of these codes are related to the work on spallation reactions to incinerate nuclear waste, neutron spallation sources, radioprotection of astronauts against cosmic rays in space missions, the development of cancer hadrontherapy and cross section predictions for radioactive beam facilities [135, 136].

The INCL models [137, 138] assume that in the initial state all the nucleons are prepared in phase space. The positions and momenta of the target nucleons are randomly assigned from Woods-Saxon and Fermi sphere distributions. The nucleons are moving in a constant potential well under the nuclear mean field. The incident nucleons are traveling along straight-line trajectories with randomly assigned energy and impact parameters. Then, the nuclear collision is treated as an avalanche of binary collisions within the target nucleus leading to two types of nucleons: *spectators*, nucleons which will never interact with the target nucleus and *participants*,

Table 5.17: Inclusive cross sections from ^{136}Te, ^{135}Sb and ^{134}Sn projectiles.

Projectile	Number of ZeroDegree nuclei	Channel	Product	Number of ZeroDegree nuclei	$T^*(\%)$	Inclusive cross section (mb)
^{136}Te	483874	-1n	^{135}Te	1539	98(5)	100(11)
		-2n	^{134}Te	1903	91(6)	134(15)
		-3n	^{133}Te	943	75(5)	80(10)
		-4n	^{132}Te	513	60(5)	55(7)
		-5n	^{131}Te	236	43(6)	35(6)
		-6n	^{130}Te	91	22(3)	26(5)
		-1p	^{135}Sb	162	91(8)	11(2)
		-1p1n	^{134}Sb	164	95(9)	11(2)
		-1p2n	^{133}Sb	432	97(9)	28(4)
		-1p3n	^{132}Sb	369	95(8)	25(3)
		-1p4n	^{131}Sb	341	92(9)	24(3)
^{135}Sb	4435409	-1n	^{134}Sb	8763	100(10)	61(8)
		-2n	^{133}Sb	23523	93(3)	176(16)
		-3n	^{132}Sb	8113	75(4)	75(7)
		-4n	^{131}Sb	4297	55(4)	54(6)
		-5n	^{130}Sb	1538	37(4)	29(4)
		-6n	^{129}Sb	478	23(3)	14(3)
		-1p	^{134}Sn	347	94(6)	2.6(3)
		-1p1n	^{133}Sn	2196	94(13)	16(3)
		-1p2n	^{132}Sn	5820	97(8)	42(5)
		-1p3n	^{131}Sn	3429	96(11)	25(4)
		-1p4n	^{130}Sn	3026	88(9)	24(3)
		-1p5n	^{129}Sn	2244	93(14)	17(3)
^{134}Sn	1040087	-1n	^{133}Sn	2150	92(10)	69(10)
		-2n	^{132}Sn	5488	89(3)	184(17)
		-3n	^{131}Sn	2137	80(4)	79(8)
		-4n	^{130}Sn	1335	65(3)	62(6)
		-5n	^{129}Sn	780	47(4)	49(7)
		-6n	^{128}Sn	392	30(2)	39(5)
		-1p	^{133}In	362	83(8)	13(2)
		-1p1n	^{132}In	-	-	-
		-1p2n	^{131}In	726	85(9)	25(4)
		-1p3n	^{130}In	617	102(2)	18(3)
		-1p4n	^{129}In	708	85(8)	25(3)
		-1p5n	^{128}In	531	71(6)	22(3)

Table 5.18: Inclusive cross sections from ^{134}Sb, ^{133}Sn, ^{137}Te, ^{136}Sb, ^{135}Te and ^{137}I projectiles.

Projectile	Number of ZeroDegree nuclei	Channel	Product	Number of ZeroDegree nuclei	$T^*(\%)$	Inclusive cross section (mb)
^{134}Sb	622338	-1n	^{133}Sb	3146	95(7)	169(19)
		-2n	^{132}Sb	1959	95(7)	102(12)
		-3n	^{131}Sb	1310	83(6)	78(9)
		-4n	^{130}Sb	737	64(5)	57(7)
		-5n	^{129}Sb	304	45(5)	34(5)
^{133}Sn	203416	-1n	^{132}Sn	1145	95(7)	183(21)
		-2n	^{131}Sn	656	94(7)	106(13)
		-3n	^{130}Sn	561	87(7)	98(12)
		-4n	^{129}Sn	302	74(9)	62(10)
		-5n	^{128}Sn	212	57(8)	57(10)
		-6n	^{127}Sn	111	39(5)	43(8)
^{137}Te	81357	-1n	^{136}Te	283	95(9)	114(16)
		-2n	^{135}Te	171	72(8)	90(14)
		-3n	^{134}Te	49	41(5)	45(10)
^{136}Sb	108408	-1n	^{135}Sb	631	100(13)	180(29)
		-2n	^{134}Sb	352	79(8)	127(18)
		-3n	^{133}Sb	162	59(6)	79(13)
^{135}Te	34478	-1n	^{134}Te	199	96(8)	186(26)
		-2n	^{133}Te	115	92(12)	111(21)
^{137}I	62513	-1n	^{136}I	243	99(8)	122(17)
		-2n	^{135}I	288	95(5)	150(18)

which are defined as particles that have collided with at least one other participant. At the end of the intranuclear cascade, an excited remnant is left. This remnant nucleus relaxes emitting low-energy particles, or, when possible, by fissioning. The time scale for the de-excitation process is much longer than that for the intranuclear cascade. Figure 5.40 displays a schematic view of both stages.

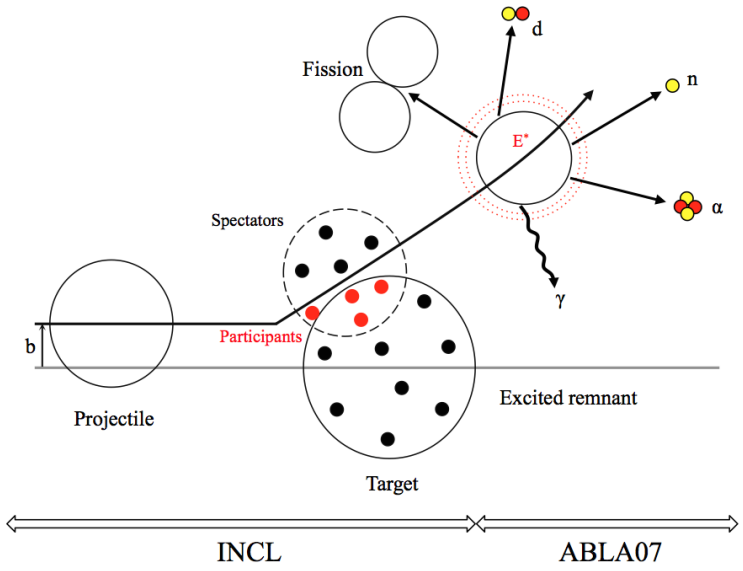

Figure 5.40: Scheme of a nucleus-nucleus collision in INCL++/ABLA07.

The Liège INCL++ [139] code was used for the first stage while the de-excitation stage, was treated with the ABLA07 model [140]. This combination of these models has been very successful in describing a great number of observables in nuclear reactions at incident energies between 60-3000 MeV/u. Recently, numerous improvements have been introduced in the Liège INCL++ model, highlighting the use of shell model calculations to introduce some structural effects in the initial condition of the nuclear surface [141], or Hartree-Fock-Bogoliubov calculations with the Skyrme interaction to obtain a more realistic description of the radial-density distributions of protons and neutrons [142]. With these improvements a better description of the one-nucleon removal and total reaction cross sections was achieved.

5.2.4 Experimental vs theoretical cross sections

Figure 5.41 displays the experimental results for the xn-neutron removal cross sections from the different projectiles. The experimental removal cross sections from a ^{112}Sn projectile published in Ref. [143] have also been included in the figure for comparison. The experimental results have been compared to calculations performed with the standard version of the INCL code (blue dashed line) and with a modified version [142] (black line), in which Hartree-Fock-Bogoliubov calculations with the Skyrme interaction are used to obtain a more realistic description of the radial-density distribution of protons and neutrons and, thus, to get a better description of the

available experimental data [144]. Figure 5.42 shows the experimental results for the 1pxn neutron removal cross sections compared to the same type of theoretical calculations. In general, the agreement between the experimental and INCL cross sections is excellent and the modified INCL version reproduces the experimental values slightly more consistently than the standard version. However, two anomalies are observed in the data. The first anomaly is observed for the neutron removal cross sections from the N=84 isotones, where the 2n removal cross sections are higher than those for 1n removal. To explain this phenomenon, we have to take a look at the neutron separation energies of the different xn channels. Figure 5.43 displays the neutron-separation energies for the xn channels from the ^{134}Sn (case with anomaly) and ^{133}Sn (case without anomaly) projectiles. In the case of the ^{133}Sn projectile, the neutron separation energies are similar for all xn channels and the only effect observed is the staggering in S_n due to the odd-even pairing. However, in the case of the xn channels from the ^{134}Sn projectile, the one neutron removal channel (^{133}Sn) presents a very low neutron separation energy ($S_n = 2.402(4)MeV$) meaning it is easier to evaporate a neutron from the ^{133}Sn nucleus. As a result of this neutron evaporation, the final nucleus is identified as ^{132}Sn in the ZeroDegree spectrometer and thus the measured cross section for the two-neutron removal channel is larger than the cross section for the one-neutron removal channel (see Fig. 5.41). In the case of the one neutron removal from ^{134}Sn, ^{133}Sn can be populated from ^{134}Sn only by removing one neutron from the $f_{7/2}$ orbital (assuming spectroscopic factor, C^2S=2, for this orbital and no γ-ray vs neutron competition in the decay) while neutron removal from the $h_{11/2}$, or other orbitals below the N=82 gap leads to the population of unbound states. The INCL model is not able to reproduce this anomaly because it does not consider any information on the orbital/state density which is critical in the case of ^{133}Sn since only one orbital is accessible, while INCL integrates a continuous excitation function up to $S_n = 2.402(4)MeV$ to get the cross section. The second anomaly concerns the 1p0n removal channel from the three N=84 isotones. As is visible in Fig. 5.42, the cross sections for this channel are very low and the INCL model overestimate the experimental cross sections. However, it is well known that the INCL calculation overestimates the removal cross sections for the more bound nucleon species (see for example Ref. [143] or Ref. [142]) and, until now, there was no explanation for this phenomenon.

5.3 Neutron unbound states in ^{133}Sn

In this section, we will show the experimental results obtained for the nucleus ^{133}Sn. This nucleus was studied via the one-neutron knockout reaction from ^{134}Sn to ^{133}Sn. Besides the known γ-ray transitions emitted from the neutron single-particle states, additional γ strength was observed above the neutron separation energy. The origin of this new γ-ray strength above the neutron threshold will be revealed through realistic shell model calculations and the eikonal reaction theory. Also the γ-ray branching ratio for states situated above the neutron-separation energy will be determined. The obtained results were recently published in Ref. [110].

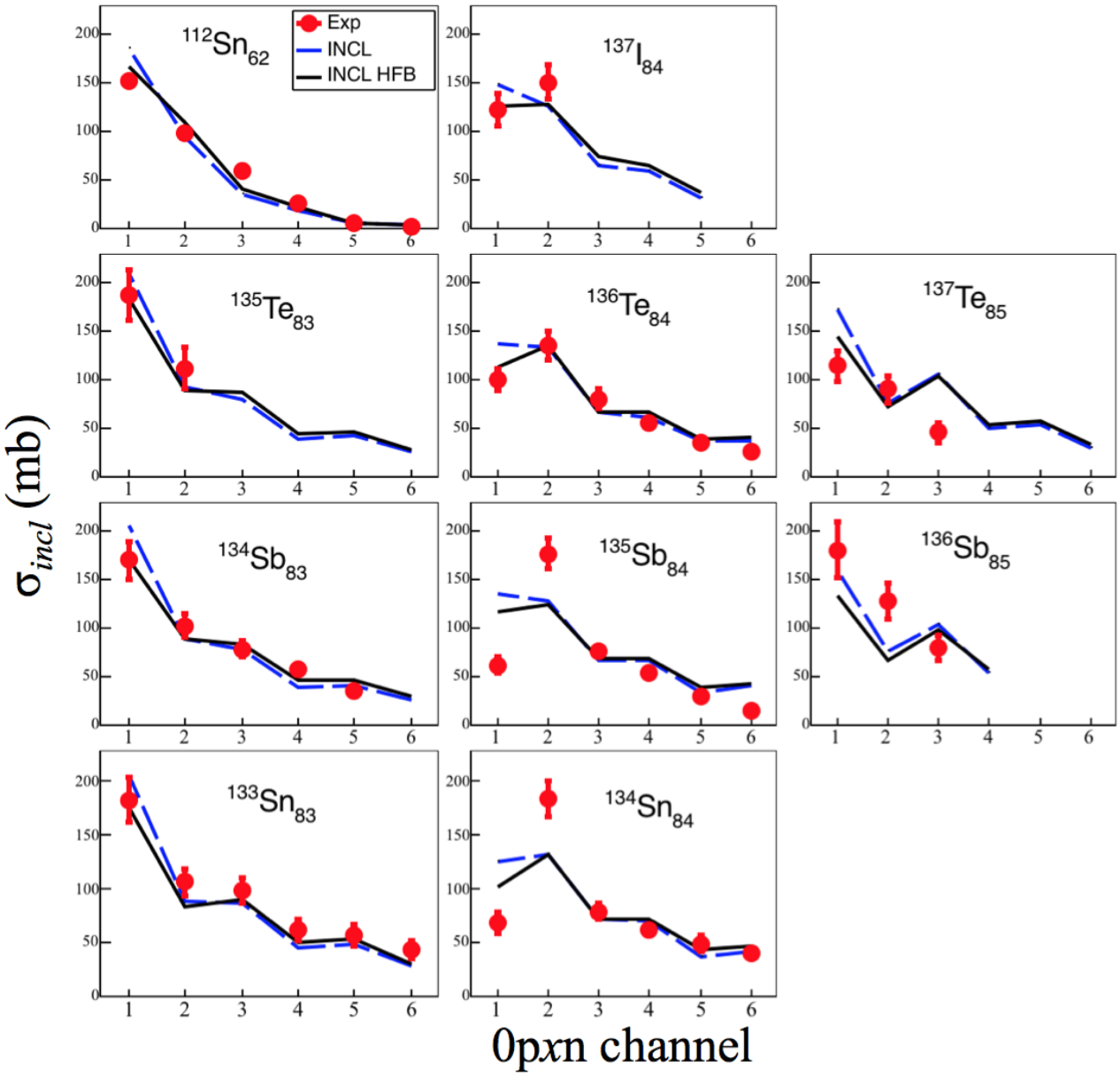

Figure 5.41: Comparison between experimental inclusive xn neutron removal cross sections (red points) and the results of the INCL using the standard version (blue-dashed line) and the modified version where a more realistic description of the radial-density distributions of protons and neutrons is considered (black line).

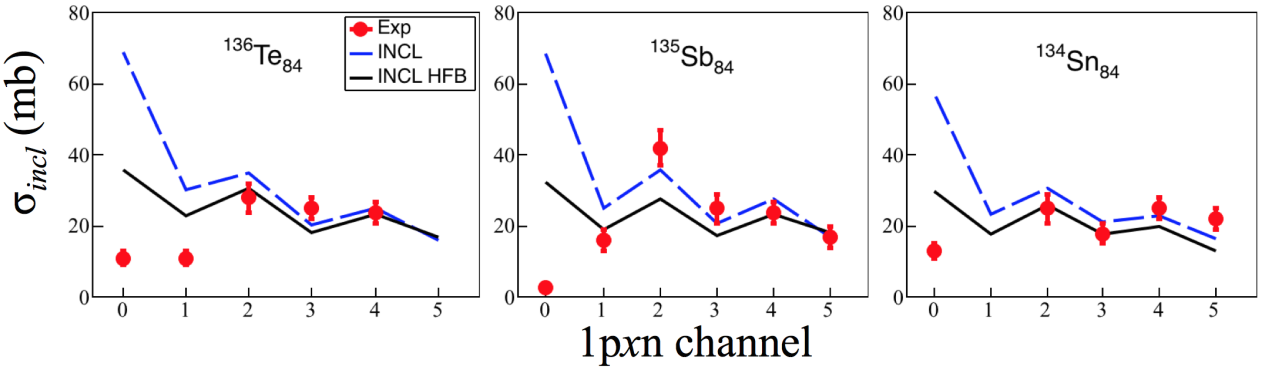

Figure 5.42: Comparison between experimental inclusive 1pxn neutron removal cross sections (red points) and the results of the INCL using the standard version (blue-dashed line) and the modified version where a more realistic description of the radial-density distributions of protons and neutrons is considered (black line).

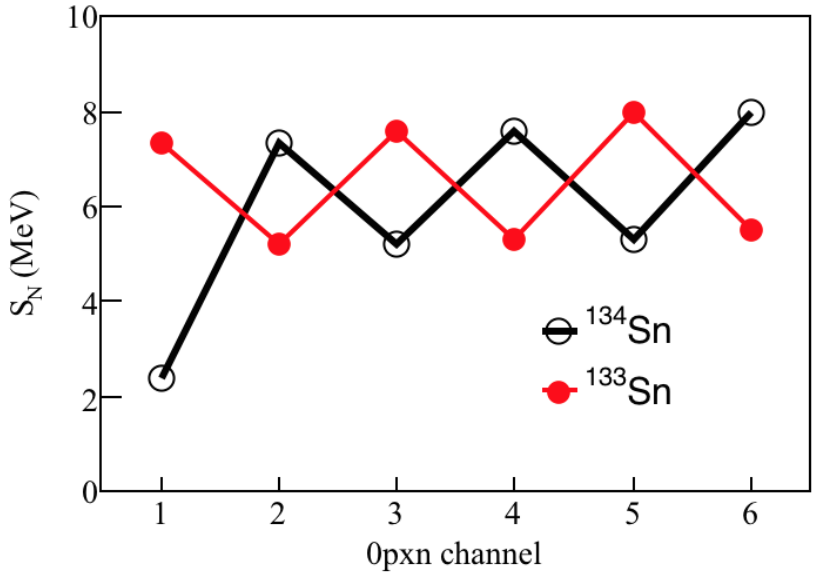

Figure 5.43: Experimental neutron separation energy (S_n) for the different xn channels from the ^{134}Sn (black line) and ^{133}Sn (red line) projectiles. The values are taken from Ref. [119].

5.3.1 γ-ray spectrum

For this part of the experiment we employed the full array of the DALI2 spectrometer. With 186 NaI(Tl) detectors, we covered polar angles from 20° to 150°. Furthermore, as the background produced in knockout reactions is low compared to Coulomb excitation experiments, the addback algorithm, explained in subsection 4.2.4, was applied and the energies of γ rays with multiplicity greater than one and that are detected in neighboring detectors, up to 15 cm, were summed and considered as a single γ-ray event. The ^{134}Sn ions impinged with a kinetic energy of 165 MeV/u on the C target, the mid-target velocity was equal to β=0.497. This velocity was used to perform the Doppler correction of the γ-ray spectrum. Figure 5.44 shows the Doppler-corrected γ-ray spectrum up to 2.5 MeV measured in coincidence with ^{134}Sn ions detected in BigRIPS and ^{133}Sn nuclei detected in the ZeroDegree spectrometer. The Doppler-corrected spectrum was fitted with two exponential functions and a step function to reproduce the background, and the DALI2 response functions. Four γ-ray transitions are observed in the spectrum displayed in Fig. 5.44. ^{133}Sn, which consists of a single neutron coupled to the doubly-magic nucleus ^{132}Sn, provides information about the position of the neutron single-particle orbitals belonging to the N = 82-126 major shell. The lowest-energy neutron single-particle states situated above the N = 82 shell closure are the $1f_{7/2}$, $2p_{3/2}$, $2p_{1/2}$, $0h_{9/2}$, $1f_{5/2}$ and $0i_{13/2}$ orbitals. Before this work, candidates for all of these states have been identified in ^{133}Sn [31–33]. The three γ rays observed at 854, 1561 and 2002 keV in the spectrum shown in Fig. 5.44 correspond to the γ-ray decays of the $2p_{3/2}$, $0h_{9/2}$ and $1f_{5/2}$ neutron single-particle states to the $1f_{7/2}$ ground state. Regarding the γ ray situated at 513 keV, it corresponds to the decay of the $2p_{1/2}$ state located at 1367 keV to the $2p_{3/2}$ states placed at 854 keV. No more γ rays are observed in the energy range of 0-2800 keV, so the position of the $0i_{13/2}$ orbital remains an open question. In Fig. 5.44 we have included the configurations depopulated by the four γ-ray transitions, where a single neutron is situated above the shell gap N=82.

Figure 5.45 displays the Doppler-corrected γ-energy spectrum of ^{133}Sn in the energy range from 0 to 8 MeV, where clearly additional new γ-ray strength is observed above the neutron-separation energy. In particular, a strong transition is observed at 3570(50) keV. This γ-ray strength, situated above the neutron-separation energy, can only be produced by the knockout of a neutron from the N=82 core of the ^{134}Sn projectile. Thus, the transition observed at 3570(50) keV could correspond to the γ-ray decay of the $0h_{11/2}$ neutron-hole state, the knockout from this orbital is expected to have the highest cross section since it is occupied by twelve neutrons and is situated close to the Fermi level. In fact, Hoff *et al.* [31] observed a peak at 1.26 MeV in the delayed neutron spectrum and concluded that this neutron transition was quite likely due to the decay of the $0h_{11/2}$ neutron-hole state. Adding the neutron-separation energy, S_n, to the 1.26 MeV places this state at an excitation energy of 3.66 MeV, i.e, close to the energy of the γ ray observed in the present work. The remaining γ-ray strength observed between 4-5.5 MeV could be caused by neutron removal from other orbitals in the N=50-82 shell (in partic-

ular from the $1d_{5/2}$ and $0g_{7/2}$ orbitals), which occurs with lower cross section because these orbitals are more deeply bound and occupied by less neutrons. The neutron knockout from the $0h_{11/2}$ orbital which is proposed to be responsible for the transition observed at 3570(50) keV is schematically illustrated in the inset of Fig. 5.45.

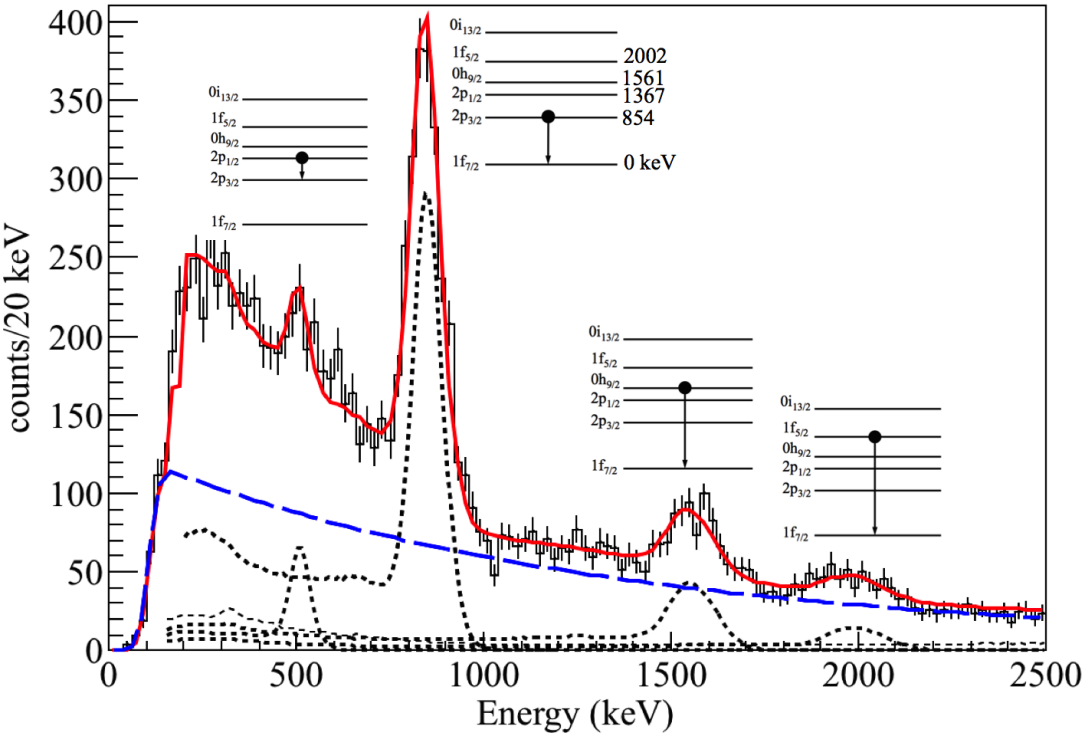

Figure 5.44: Doppler-corrected γ-ray spectrum for γ-ray events with multiplicity M_γ=1 and after applying addback of ^{133}Sn produced via one-neutron knockout from ^{134}Sn. The neutron configurations depopulated by each γ-ray transition are situated next to each peak.

The next question to be answered is why these states, which are situated well above the neutron-separation energy, decay via the emission of γ radiation and not completely by the emission of a neutron, a faster process. To give an answer to this question, the reaction process that populates the excited states situated above the neutron-separation energy has to be considered. This is done in Fig. 5.46 for the case in which the neutron is removed from the $0h_{11/2}$ orbital. First, in the part a) we have illustrated the neutron configuration of the ground state of the ^{134}Sn projectile, a nucleus with two neutrons outside the N=82 shell closure. In subsection 5.3.2, we have performed shell model calculations in order to predict the composition of the wave function for the ground state of ^{134}Sn, but for the current discussion we consider that the two neutrons are 100% situated in the $1f_{7/2}$ orbital. Then, in Fig. 5.46 b), a neutron is removed from the $0h_{11/2}$ orbital of the ^{134}Sn projectile leading to a hole in this orbital for the ^{133}Sn nucleus. Since this state is situated above the neutron-separation energy it is expected to decay via the emission of a neutron and populate states of ^{132}Sn. The ^{132}Sn doubly-magic nucleus has its first excited state, 2^+_1, at an excitation energy of 4.041 MeV. Therefore, the neutron situated in the $0h_{11/2}$ orbital can only populate the ground state of ^{132}Sn. The angular

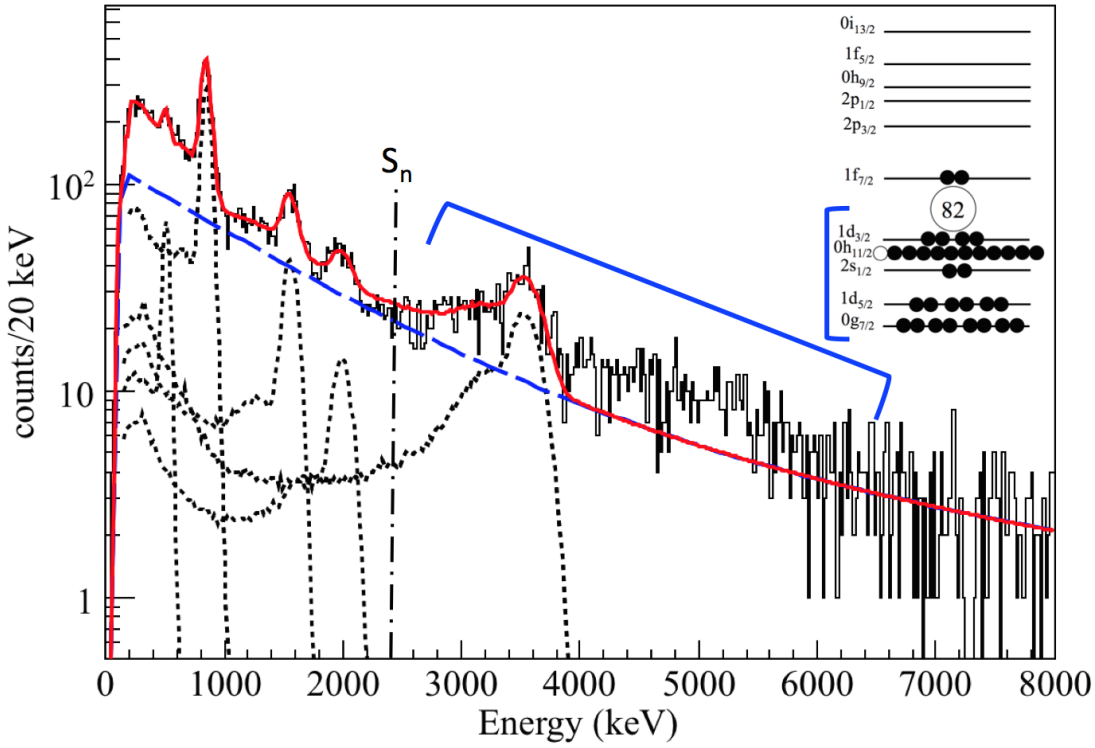

Figure 5.45: Doppler-corrected γ-ray spectrum for γ-ray events with multiplicity M_γ=1 and after applying addback of ^{133}Sn produced via one-neutron knockout from ^{134}Sn. The γ-ray strength observed above the neutron-separation energy (highlighted by the blue line) is produced by the removal of a neutron from the N=82 core, as illustrated in the inset of the figure.

momentum of the emitted neutron would be l=5 and its energy, E_n=1.2 MeV. The previously described process is schematically illustrated in Fig. 5.46 d), where the ^{132}Sn has two neutrons in the $1f_{7/2}$ orbital and two neutron-holes in the $0h_{11/2}$ orbital. The contribution of this 2p-2h configuration to the ground state of ^{132}Sn is expected to be very low, therefore, the overlap between the wave-functions of the parent and daughter states is very small. According to Fermi's Golden Rule [145], the transition rate (transition probability per unit time) from the initial state, i, to a final state, f, is given by:

$$\Gamma_{i\to f} = \frac{2\pi}{\hbar}\left|V_{fi}\right|^2 \rho \tag{5.13}$$

where ρ is the density of final states and V_{fi} is the transition matrix element defined as $V_{fi} = \int \Psi_f^* V_{int} \Psi_i dV$. The factor, V_{int}, takes into account the strength of the interaction and $\Psi_{i,f}$ are the wave functions of the initial and finals states. In our case, the small overlap between the $\Psi_{i,f}$ functions is responsible for the γ-ray emission competition with neutron decay despite the fact that neutron emission is orders of magnitude faster than the γ-ray emission. This competition between the γ and neutron emission in the decay of unbound states situated above the neutron separation energy has already been reported for several cases [146–149]. Instead of emitting a neutron, the hole in the $0h_{11/2}$ orbital can be filled with one neutron occupying the $1f_{7/2}$

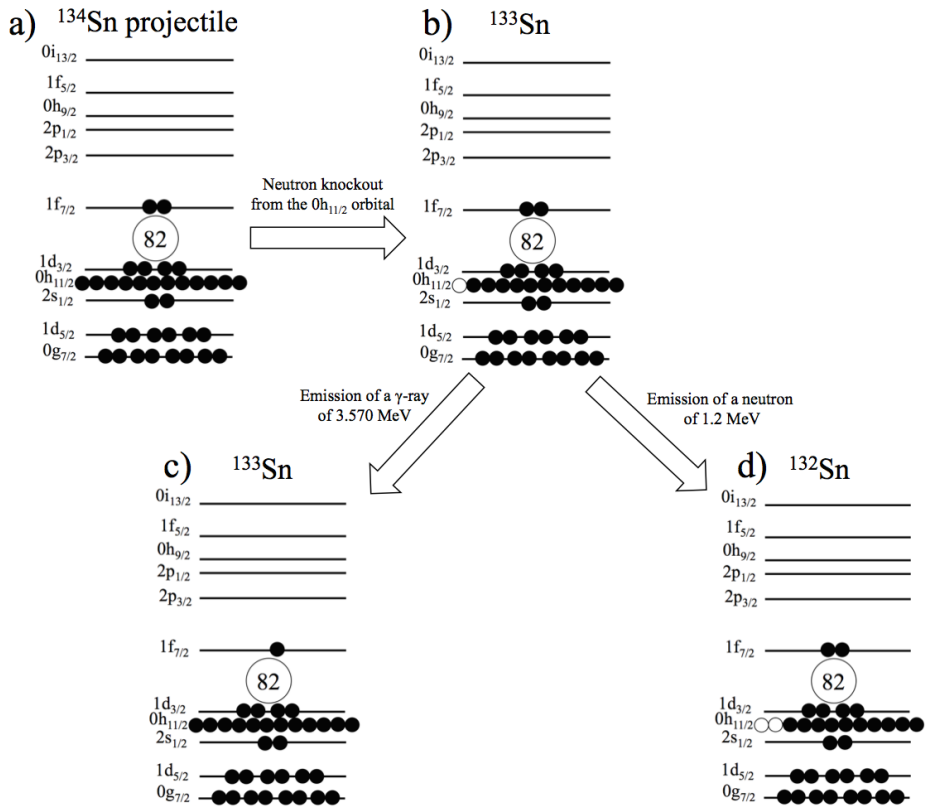

Figure 5.46: Schematic of the neutron orbital occupancies a) for the ground state configuration of the ^{134}Sn projectile, b) after the knockout of a neutron from the $0h_{11/2}$ orbital, c) after γ decay that populates the ground state of ^{133}Sn and d) after neutron emission that populates the ground state of ^{132}Sn with a 2p-2h configuration.

orbital with the simultaneous emission of a γ ray with an energy of 3570 keV. This process is illustrated in the Fig. 5.46 c) and leads to the ground state of ^{133}Sn. This discussion about the knockout from the $0h_{11/2}$ orbital and the competition between the γ-ray/neutron emission is also valid for any orbital located in the N=50-82 shell. In order to obtain a better understanding about the reaction process that leads to the spectrum shown in Fig. 5.45, we need to know the composition of the wave function for the ground state of ^{134}Sn. This allows exact knowledge of the occupation probability distributions for the different orbitals. We also have to know the cross sections for the one-neutron knockout from each orbital. These cross section were calculated using the eikonal reaction theory.

5.3.2 Shell model calculations

Since the neutron can be removed from any orbital which is occupied in the ground state of ^{134}Sn, we need to know its wave function composition. For that, we performed shell model calculations using realistic effective interactions [150]. In these calculations, the five orbitals $0g_{7/2}$, $1d_{5/2}$, $1d_{3/2}$, $0h_{11/2}$ and $2s_{1/2}$ of the 50-82 shell were considered for the valence space of the protons while the valence neutrons have available the six orbits $1f_{7/2}$, $2p_{3/2}$, $2p_{1/2}$, $0h_{9/2}$,

$1f_{5/2}$ and $0i_{13/2}$ of the 82-126 shell. The single particle energies were taken from the experimental spectra of ^{133}Sb (for protons) and ^{133}Sn (for neutrons), with the exception of the proton $2s_{1/2}$ and the neutron $0i_{13/2}$ energies which were taken from Refs. [151] and [152], respectively. Table 5.19 contains the composition of the wavefunction for the ground state of ^{134}Sn. Since the spin of the ground state is 0^+, the two neutrons have to be placed in the same orbital and couple to spin 0. The most probable configuration (80%) is that the two neutrons are situated in the $1f_{7/2}$ orbital (Fig. 5.46 a)). The neutron knockout from this orbital would lead to the ground state of ^{133}Sn and, therefore, no γ ray would be emitted. For the other orbitals located in the N=82-126 shell, the probabilities range from 1.55% to 5.7%. The one-neutron removal from any of the $2p_{3/2}$, $2p_{1/2}$, $0h_{9/2}$ and$1f_{5/2}$ orbitals produces the emission of γ rays with the energies observed in the spectrum shown in Fig. 5.44. Regarding the $0i_{13/2}$ orbital, the probability that the two neutrons are in this orbital is 3.2%. Nevertheless, in the present experiment no γ ray was observed in the expected energy range.

Table 5.19: Probability of occupation for the valence-neutrons pair in the ground state of ^{134}Sn.

Ground state 0_1^+	$1f_{7/2}$	$2p_{3/2}$	$2p_{1/2}$	$0h_{9/2}$	$1f_{5/2}$	$0i_{13/2}$
Probability (%)	80.30	5.19	1.55	5.67	4.07	3.19

5.3.3 Eikonal reaction calculations

The one-neutron removal cross sections were calculated using the eikonal reaction theory [76, 77], in which the projectile is considered to follow straight-line trajectories at constant velocity. The cross section for the knockout of a nucleon from an orbital with quantum numbers n, l,j of the projectile and the population of a final state of the residual nucleus is given by:

$$\sigma(c) = \sum C^2S(c, nlj)\sigma_{sp}(S_n, nlj) \tag{5.14}$$

with C^2S being the spectroscopic factors and σ_{sp} the single-particle removal cross sections. Two different processes contribute to the single-particle knockout cross section: $\sigma_{sp} = \sigma_{sp}^{str} + \sigma_{sp}^{diff}$. The first term, σ_{sp}^{str}, is the cross section for all processes where the removed nucleon excites the target and then is absorbed, called stripping, or inelastic breakup. The second term, σ_{sp}^{str}, is the cross section for the elastic breakup of the projectile nucleus, in which the target is in its ground state, called diffractive dissociation.

We have employed eikonal theory to calculate the one-neutron knockout from ^{133}Sn and ^{134}Sn projectiles [153], both cases studied in our experiment. From the reaction point of view, a projectile+target optical potential was needed. The neutron and proton densities were calcu-

lated with the Hartree-Fock approach and the SKX Skyrme interaction. From the structure point of view, the radial overlaps, $\langle A(E^*, j^\pi)|(A-1)(g.s)\rangle$, and the spectroscopic factors were needed. The radial forms of these overlaps were computed in Woods-Saxon wells with geometries constrained by the Hartree-Fock orbital properties. Regarding the excitations energy, E^*, the known single-particle energies from the ^{133}Sn spectrum were considered, while for the neutron-hole states these energies were computed based on a spherical Hartree-Fock calculation. Tables 5.21 and 5.20 show the calculated cross sections for the one-neutron knockout from ^{134}Sn and ^{133}Sn projectiles, respectively. For the case of the one-neutron removal from the ^{134}Sn projectile, the cross section is σ_{1n}=172 mb, where 20 mb are due to the knockout from the neutron valence space and 152 mb are due to the neutron removal from the N=50-82 shell. For the case of the one-neutron removal from the ^{133}Sn projectile, the cross section is σ_{1n}=200 mb, where 14 mb are due to the knockout from the neutron valence space and 186 mb are due to the neutron removal from the N=50-82 shell. The theoretical cross sections include a small center of mass correction, which is given by $(A/(A-1))^4$.

Table 5.20: One neutron removal cross section from a ^{134}Sn projectile calculated with the eikonal reaction theory [153].

	n	l	2j	e_{sp}(^{134}Sn) (MeV)	E*(^{133}Sn) (MeV)	S_n (MeV)	Occ	σ_{sp} (mb)	σ_{th} (mb)	σ_{tot} (mb)	
	1	g	7	-9.388	7.141	10.77	8	2.738	2.821	22.569	
	2	d	5	-9.652	7.405	11.034	6	5.363	5.526	33.157	
Unbound N<82	2	d	3	-7.837	5.59	9.219	4	6.338	6.530	26.122	σ_{core}=152 mb
	3	s	1	-7.977	5.73	9.359	2	7.037	7.251	14.503	
	1	h	11	-7.073	4.826	8.455	12	4.525	4.662	55.945	
	2	f	7	-2.247	0	3.629	1.606	10.267	10.580	16.991	
	3	p	3	-3.101	0.854	4.483	0.104	11.075	11.412	1.187	
Bound N>82	3	p	1	-3.614	1.367	4.996	0.031	9.578	9.869	0.306	σ_{val}=20 mb
	1	h	9	-3.808	1.561	5.19	0.1134	3.918	4.037	0.458	
	2	f	5	-4.249	2.002	5.631	0.0814	7.632	7.864	0.640	
							n=34				σ_{tot}=172 mb

Table 5.21: One neutron removal cross section from a ^{133}Sn projectile calculated with the eikonal reaction theory [153].

	n	l	2j	e_{sp}(^{133}Sn) (MeV)	E*(^{132}Sn) (MeV)	S_n (MeV)	Occ	σ_{sp} (mb)	σ_{th} (mb)	σ_{tot} (mb)	
	1	g	7	-9.387	7.129	9.531	8	3.309	3.408	27.266	
	2	d	5	-9.69	7.432	9.834	6	6.577	6.774	40.646	
Bound N<82	2	d	3	-7.853	5.595	7.997	4	7.875	8.111	32.445	σ_{core}=186 mb
	3	s	1	-7.972	5.714	8.116	2	8.962	9.231	18.462	
	1	h	11	-7.043	4.785	7.187	12	5.453	5.617	67.399	
Bound N>82	2	f	7	-2.258	0	2.402	1	13.959	14.378	14.378	σ_{val}=14 mb
							n=33				σ_{tot}=200 mb

5.3.4 Inclusive cross sections and determination of the γ vs neutron branching ratio

The theoretical cross sections obtained with the eikonal reaction theory in the previous subsection have been compared to the experimental values. Details about the determination of the experimental nucleon removal cross sections have been presented in section 5.2. Here, we compare the neutron removal from ^{133}Sn and ^{134}Sn projectiles. Figure 5.47 shows the neutron removal (1n, 2n, 3n, 4n and 5n knockout) cross sections from the ^{133}Sn (black line) and ^{134}Sn (red line) beams. The experimental cross sections for the knockout of 3, 4 and 5 neutrons are very similar for both projectiles. However, for the knockout of 1 and 2 neutrons the experimental values are very different for both cases. To understand these differences, we will discuss the inclusive cross sections for the one-neutron knockout from the ^{133}Sn and ^{134}Sn projectiles. For the ^{133}Sn projectile, since the neutron separation energy of ^{132}Sn (one-neutron knockout channel) is quite high (S_n = 7.343(7) MeV), the one-neutron knockout from the neutron valence and core spaces of ^{133}Sn populates bound states in ^{132}Sn. The experimental cross section for the one-neutron knockout from ^{133}Sn is σ_{1n}^{exp} = 183(21) mb. This experimental value is in good agreement with the eikonal theoretical value of σ_{1n}^{theo} = 200 mb, revealing that the eikonal theory employed in the calculations correctly quantifies the nucleon removal cross sections in this region of the nuclear chart. For the case of the one-neutron removal from the ^{134}Sn beam, the situation is completely different, since the neutron separation energy of ^{133}Sn (one-neutron knockout channel) is quite low (S_n = 2.402(4) MeV), so that the one-neutron removal from the neutron valence space (N>82) of ^{134}Sn populates bound states in ^{133}Sn, but the one-neutron knockout from the core (N<82) of ^{134}Sn leads to unbound states in ^{133}Sn which can decay via γ-ray or neutron emission. If these unbound states decay via neutron emission they populate bound states in ^{132}Sn and we will detect ^{132}Sn in the ZeroDegree spectrometer. As a consequence, the cross section for the two-neutron knockout channel from the ^{134}Sn beam is higher than the cross section for the one-neutron removal. This effect is clearly visible in Fig. 5.47 (red line). Therefore the experimental one-neutron knockout cross section of σ_{1n}^{exp} = 69(10) mb from the ^{134}Sn beam includes three different contributions: 1) cross section to the ground state of ^{133}Sn, 2) exclusive cross section to bound excited states in ^{133}Sn and 3) exclusive cross section to unbound excited states in ^{133}Sn which decay via γ-ray emission (in any other case the ion would not be identified as ^{133}Sn in the ZeroDegree spectrometer). Subtracting the cross section calculated for the neutron knockout from the neutron valence space in ^{134}Sn, σ_{1n}^{val} = 20 mb (see table 5.21), from the experimental one-neutron knockout cross section value of σ_{1n}^{exp} = 69(10) mb, we obtain $\sim$ 49 mb which corresponds to the γ-ray decay of unbound states in ^{133}Sn. The calculated cross section for the neutron knockout from the core in ^{134}Sn is σ_{1n}^{core} = 152 mb (see table 5.21) and we are measuring $\sim$ 49 mb, so 25-39% of the decay of neutron unbound states in ^{133}Sn proceeds via the emission of γ rays.

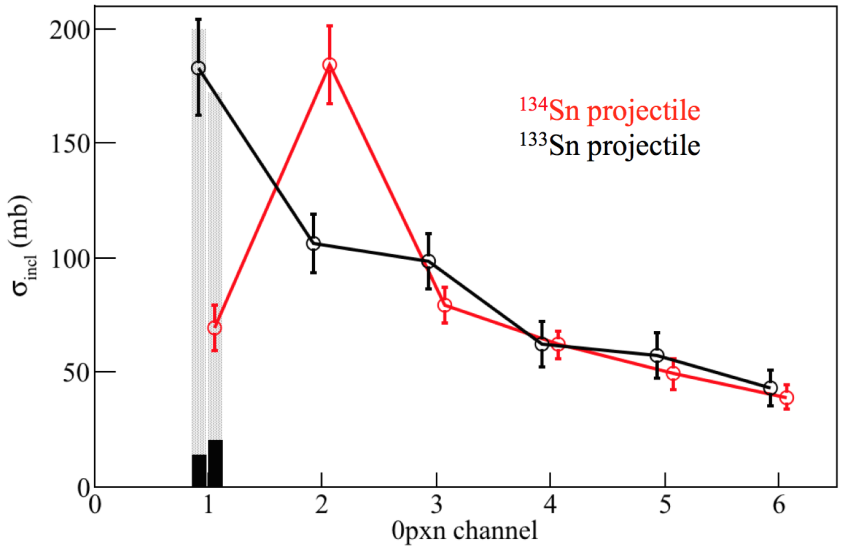

Figure 5.47: Experimental neutron removal cross sections from ^{133}Sn (black line) and ^{134}Sn (red line) projectiles. The vertical bars represent the eikonal calculations for the one-neutron knockout from both projectiles. The black bars indicate the neutron knockout from the neutron valence space (N>82) and the gray bars show the cross sections from the neutron core (N≤82).

5.3.5 Lifetime of the 2p$_{3/2}$ state

The same procedure previously explained to obtain the lifetime of the 2_1^+ and 4_1^+ states in ^{136}Te (see subsection 5.1.9) was used to determine the lifetime of the 2p$_{3/2}$ neutron-single particle state in ^{133}Sn. Since, for this part of the experiment the full DALI2 array was available, we could study separately the shift in energy for the backward and forward DALI2 detectors. Again, the velocity (β = 0.497) and the angles at mid-target were used to perform the Doppler correction of the γ-ray spectrum. Figures 5.48 a) and b) show separately the DALI2 response for the backward ($\theta > 67°$) and for the forward ($\theta < 67°$) crystals, respectively. In both spectra, we have included the simulated DALI2 responses assuming vanishing lifetime (τ=0 ps) and in both cases a shift in energy is observed between the experimental line and the GEANT4 simulations. The lifetime with which we got the best fit for both spectra was τ=30(15) ps. The GEANT4 simulations considering a lifetime of τ=30 ps for the the 2p$_{3/2}$ neutron single-particle state are shown in red. With this lifetime, a reduced transition probability B(E2;$2p_{3/2} \rightarrow 1f_{7/2}$) = 1.6(8) W.u was derived. This value is in good agreement with the strength of the $2d_{5/2} \rightarrow 1g_{9/2}$ (B(E2) = 2.5(7) W.u) and $3s_{1/2} \rightarrow 2d_{5/2}$ (B(E2) = 2.13(8) W.u) transitions in ^{209}Pb, which have the same neutron single-particle character with respect to the N=126 neutron shell. In addition, we performed realistic shell model calculations in order to obtain the strength for the $2p_{3/2} \rightarrow 1f_{7/2}$ transition in ^{133}Sn. A value of B(E2;$2p_{3/2} \rightarrow 1f_{7/2}$) = 2.5 W.u was calculated. It is worth noting that the experimental B(E2;$2p_{3/2} \rightarrow 1f_{7/2}$) value in ^{133}Sn is consistent with the effective charge usually used for neutrons above the 82 shell closure, 0.7 e.

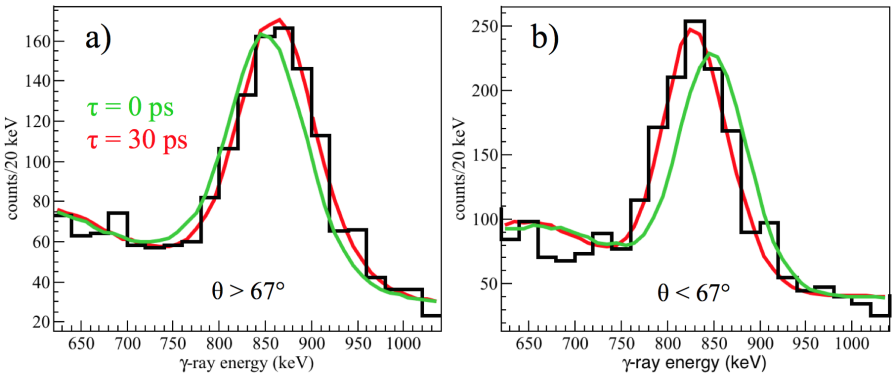

Figure 5.48: a) Comparison between the experimental shape of the 854-keV line for events with γ-ray multiplicitiy, M_γ=1 and polar angles $\theta > 67°$ and GEANT4 simulations assuming a lifetime of τ=0 ps (green curve) and τ=30 ps (red curve). b) Same comparison but now for the DALI2 detectors with polar angles $\theta < 67°$.

Chapter 6

Conclusions and Future Perspectives

In this work, the in-beam γ-ray spectroscopy at intermediate energies of different isotopes in the ^{132}Sn region has been discussed. The experiment was conducted at the RIBF, Japan. The radioactive beam was produced by the in-flight abrasion fission of a ^{238}U primary beam at 345 MeV/u on a ^{9}Be target. The first stage of the BigRIPS spectrometer was used to separate and select the isotopes of interest and the second stage was used to identify the secondary beam through the TOF-$B\rho$-ΔE method. After the identification, the radioactive beam was delivered to the F8 focal plane where we installed two different reactions targets (Au and C) to induce different reactions. The DALI2 spectrometer, which is an array formed by 186 NaI(Tl) detectors, surrounded the reaction target. This array was used to detect the γ rays emitted in the decay of excited states from different reaction products. Finally, the fragments were delivered to the ZeroDegree spectrometer where they were identified using the same method as in BigRIPS. We have described the different steps followed in the analysis of the data in order to improve the quality of the particle identification in BigRIPS and ZeroDegree. A complete characterization of the DALI2 spectrometer, aided by GEANT4 simulations, was performed, allowing us to estimate lifetimes of different excited states from the energy shifts of their γ-ray energies in the Doppler-corrected spectrum with respect to their nominal values. Finally, a procedure to determine inclusive cross sections from the different projectiles was presented. The main results of this thesis are:

- A value of B($E2$)=0.191(26) e^{2}b^2 was derived for the 2_1^+ state of ^{136}Te from the experimental exclusive inelastic scattering cross section on the Au target considering, simultaneously, the Coulomb and nuclear contributions. Our B($E2$) value is in good agreement with a recent measurement reported in Ref. [53] and different shell model calculations, but is at variance with two other previous results from literature [46, 47] and QRPA calculations. The present result suggests a higher proton content in the wave function of the 2_1^+ state in ^{136}Te than previously suggested.

- A competition between γ-ray and neutron emission has been observed in the decay of unbound neutron-hole states in ^{133}Sn. In particular, a strong γ-ray transition at 3570(50)

keV is observed in the Doppler-corrected γ-ray spectrum. The γ-ray decay of the unbound neutron states is explained through a nuclear structure effect which hinders the neutron emission and allows γ-ray decay to compete in the decay of these unbound states. These results raise the question whether the nuclear structure effect observed in ^{133}Sn is present also in other nuclei in the ^{132}Sn region, in particular in nuclei with Z$<$50 and N$>$82, a region in which β decay populates similar neutron core-excited states. Furthermore, this region is very important for the description of the r-process and the competition between the γ-ray/neutron decay of unbound states could have an important impact on nucleosynthesis calculations.

- A systematic scheme of multi-nucleon knockout cross sections from different Sn, Sb and Te isotopes has been established. The experimental cross sections have been compared to calculations performed with the Liège intranuclear cascade model, INCL. A good agreement is observed between the experimental and theoretical values, in particular when the most recent version of the code is used. However, the experimental cross sections for the one- and two-neutron knock-out from ^{134}Sn and ^{135}Sb projectiles are in clear disagreement with the theoretical predictions, as are the ones for the one-proton knockout from all N=84 isotones.

- The resolutions achieved in the BigRIPS and ZeroDegree spectrometers allowed us to study the in-beam γ-ray decay of excited states from several N=82-84 isotopes populated via nucleon knockout reactions from the different projectiles.

Possible continuations of the studies presented in this thesis are:

- To study the γ-ray spectrum of ^{133}Sn populated via the one-neutron knockout from ^{134}Sn with higher statistics which will allow to resolve the γ-ray strength observed around 4-5 MeV and determine the position of the remaining neutron-holes states. With higher statistics and an adequate target it will be possible to determine longitudinal momentum distributions which will allow us to determine the orbital angular momentum of the new neutron unbound states. These possible studies were presented as a proposal to the 17th PAC meeting for Nuclear-Physics Experiments at RIBF and accepted. The experiment (NP1612-RIBF149) is scheduled for the end of 2018.

- A study of the neutron vs γ-ray competition in the decay of unbound states in exotic nuclei situated in the south-east region of ^{132}Sn using techniques such as delayed neutron spectroscopy and total absorption γ-ray spectroscopy (TAS).

- The anomaly in the B(E2) of the 2_1^+ state in ^{136}Te is still an open issue, given the disagreement between the available experimental data. Therefore, a new experimental measurement of this value is necessary in order to confirm which of the two sets of data points is correct.

- As was shown in Fig. 5.4, a state at 4.2 MeV was strongly populated in the Coulomb excitation of ^{136}Te. The analysis of the differential cross section suggests that the spin of this state is likely 3^-. A more detailed study of this state with more statistics and better angular resolution, and a search for the same type of excitation in other isotopes close to ^{136}Te was proposed to the 18^{th} PAC meeting for Nuclear-Physics Experiments at RIBF and accepted. The experiment (NP1712-RIBF162) is scheduled for the end of 2018.

- A future work will be to compare the results on the inclusive multi-nucleon removal cross sections to the eikonal theory calculations. This comparison will raise the question whether it is necessary to apply the quenching factors, R_s, to the theoretical cross sections. Furthermore, another good experimental case to answer this question is the exclusive cross sections for the one-nucleon knockout from the doubly-magic nucleus, ^{132}Sn (very pure initial and final states). The comparison between the theoretical exclusive cross sections obtained from eikonal theory and the experimental ones will reveal the need, or not, to apply such quenching factors.

- The γ-ray spectra of the remaining by-products populated via knockout reactions are shown in appendix A. For some of the isotopes, the density of states populated through the knockout reaction is very high and the moderate energy resolution of DALI2 is not sufficient to resolve the individual γ-ray transitions. The use of high-resolution γ-ray detector arrays, such as AGATA [154] and GRETA [155], will allow us to perform in-beam γ-ray spectroscopy of nuclei with a high density of states and to use γ-γ coincidences in order to elucidate the level scheme. Figure 6.1 shows a comparison between the experimental γ-ray spectrum for the ^{12}C(^{136}Te,^{135}Te+γ)X reaction measured with DALI2 and a simulated spectrum of the same reaction for GRETA [118].

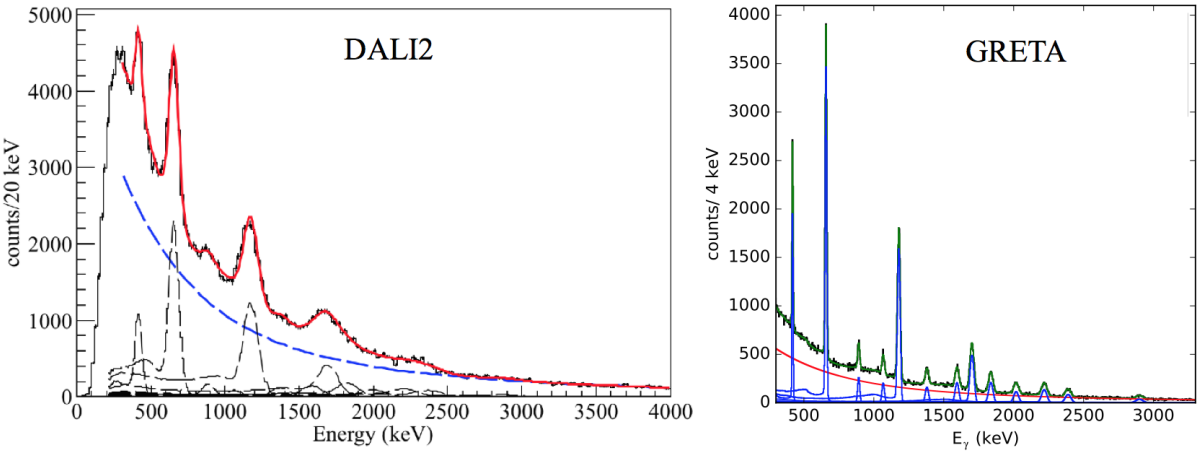

Figure 6.1: Left: experimental Doppler-corrected γ-ray spectrum for the ^{12}C(^{136}Te,^{135}Te+γ)X reaction obtained with DALI2. Right: simulated Doppler-corrected γ-ray spectrum for the same reaction and the same γ-ray emissions obtained for the GRETA array.

Chapter 7

Introducción y resumen en castellano

7.1 Introducción

Los núcleos atómicos son los principales constituyentes de la mayor parte de materia conocida en nuestro universo, de modo que entender sus propiedades y comprender sus modos de interacción resulta de vital importancia para el ámbito científico. Cada núcleo es un sistema cuántico compuesto por un número finito de fermiones conocidos con el nombre de nucleones, distinguiéndose dos tipos distintos de estos últimos: protones y neutrones. Los protones son las partículas que otorgan carga eléctrica al núcleo, siendo la carga individual de cada protón $+e$, mientras que los neutrones, como su propio nombre indica, son partículas con carga total cero. Dado que los protones que conforman el núcleo tienen cargas del mismo signo, el núcleo debería ser un sistema no ligado si únicamente la interacción electromagnética estuviera presente en estos medios; sin embargo, existe otra interacción en el núcleo que es capaz de apantallar, vencer esta repulsión electromagnética y hacer que los protones y neutrones que conforman el núcleo se mantengan unidos: la interacción fuerte.

Desde el descubrimiento del núcleo atómico por E. Rutherford [1] en 1911, una gran cantidad de descubrimientos y avances científicos han sido llevados a cabo en el campo de la física nuclear. Entre todo ellos resaltan los trabajos llevados a cabo por M. Goeppert-Mayer [5, 6] y O. Haxel, J. Jensen y H. Suess [7], quienes observaron que había ciertas combinaciones de números de protones y neutrones que otorgaban propiedades especiales a los núcleos que poseían dichas combinaciones. Estos números son el 2, 8, 20, 28, 50, 82 y 126 y fueron designados con el nombre de “números mágicos”. Durante varios años, las investigaciones en el campo de la física nuclear estuvieron limitadas a núcleos situados en el valle de la estabilidad y sus proximidades. Sin embargo, en las últimas tres décadas y con la aparición de instalaciones radioactivas capaces de producir núcleos alejados de la estabilidad, nuestro conocimiento sobre el núcleo atómico ha sido extendido y en algunas ocasiones incluso corregido cuando nos alejamos del valle de la estabilidad. Estos núcleos alejados del valle de la estabilidad se conocen con el nombre de “núcleos exóticos” y están caracterizados por tener relaciones N/Z muy

diferentes a las que poseen los núcleos estables.

El presente trabajo está centrado en la región situada alrededor del núcleo doblemente mágico, Z=50 y N=82, ^{132}Sn. Esta región de la carta nuclear es de gran importancia para investigaciones en estructura nuclear, ya que actualmente es la región más pesada alrededor de un núcleo doblemente mágico accesible experimentalmente. La Fig. 7.1 muestra la región alrededor del núcleo doblemente mágico ^{132}Sn y la información experimental disponible hasta el momento de escritura de esta tesis. Como es visible en esta imagen, muchos de los núcleos situados en esta región han sido recientemente sintetizados por primera vez [18], una gran cantidad de información experimental ha sido obtenida recientemente dentro de la campaña EURICA [19, 22–29] llevada a cabo en la instalación radioactiva RIBF (RIKEN), mientras que para otro gran número de núcleos todavía no disponemos de información espectroscópica.

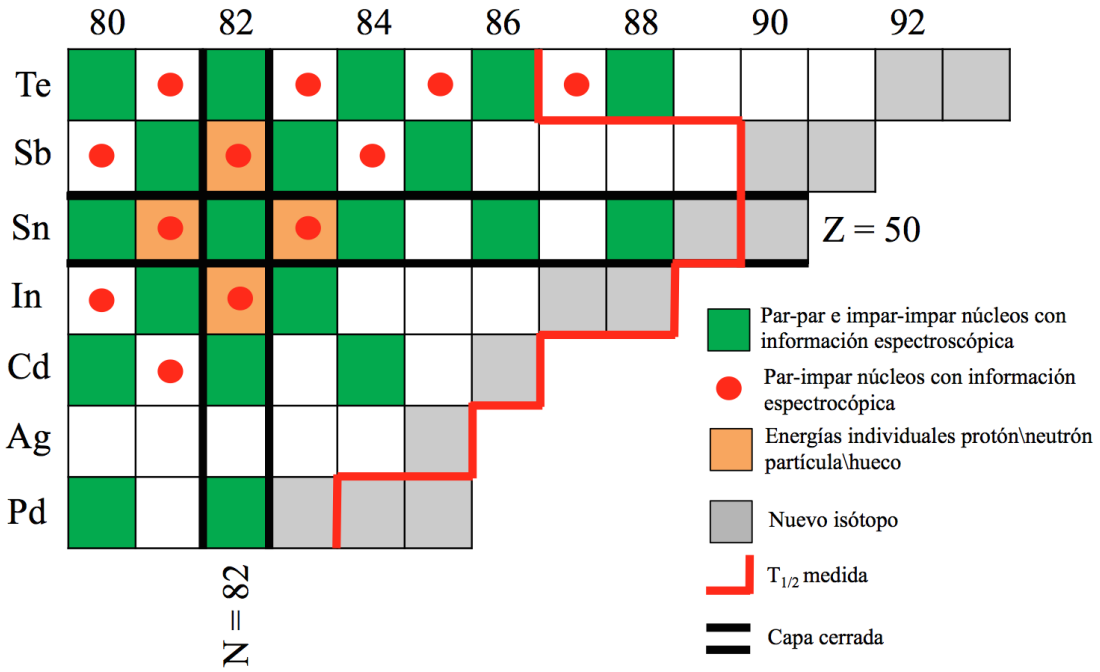

Figure 7.1: Imagen esquemática de la región alrededor del núcleo doblemente mágico ^{132}Sn mostrando la información experimental disponible hasta la fecha de este trabajo.

Para los núcleos que poseen tanto un número par de protones como de neutrones, los principales observables experimentales son la energía de excitación del primer estado excitado 2_1^+, $E(2_1^+)$, la relación $R_{42} = E(4_1^+)/E(2_1^+)$ y la probabilidad de transición reducida B$(E2; 0_1^+ \rightarrow 2_1^+)$, abreviada B$(E2)$, los cuales revelan información sobre el grado y tipo de colectividad presente en el núcleo. En general, estos observables están bien reproducidos por relaciones empíricas o cálculos teóricos más complejos, como puede ser el modelo de capas. Sin embargo, en la región alrededor del núcleo ^{132}Sn, dos anomalías han sido observadas en relación a estos observables para los núcleos par-par. La Fig. 7.2 muestra las energías del primer estado excitado 2^+ (izquierda) así como las probabilidades de transición reducida B(E2) (derecha) para

diferentes isótopos situados en las inmediaciones del ^{132}Sn. Como es de esperar, la energía del estado 2_1^+ aumenta a medida que nos acercamos al cierre de capas N=82 y, una vez superado el cierre de capa, de nuevo comienza a decaer; mientras que la B(E2) sigue el comportamiento opuesto, disminuye hasta N=82 y posteriormente comienza a aumentar de nuevo. Sin embargo, en esta imagen son visibles dos anomalías que no siguen los comportamientos esperados con respecto a la energía y la probabilidad de transición reducida. La primera anomalía es visible en el canal isotópico de los cadmios, donde las energías de los estados 2_1^+ son prácticamente constantes para todos los isótopos del cadmio situados a la izquierda del cierre N=82. La segunda anomalía concierne al valor de la probabilidad de transición reducida B($E2$) para el núcleo ^{136}Te, cuyo valor es realmente bajo y similar a la B(E2) del isótopo de Te con N=82 (^{134}Te).

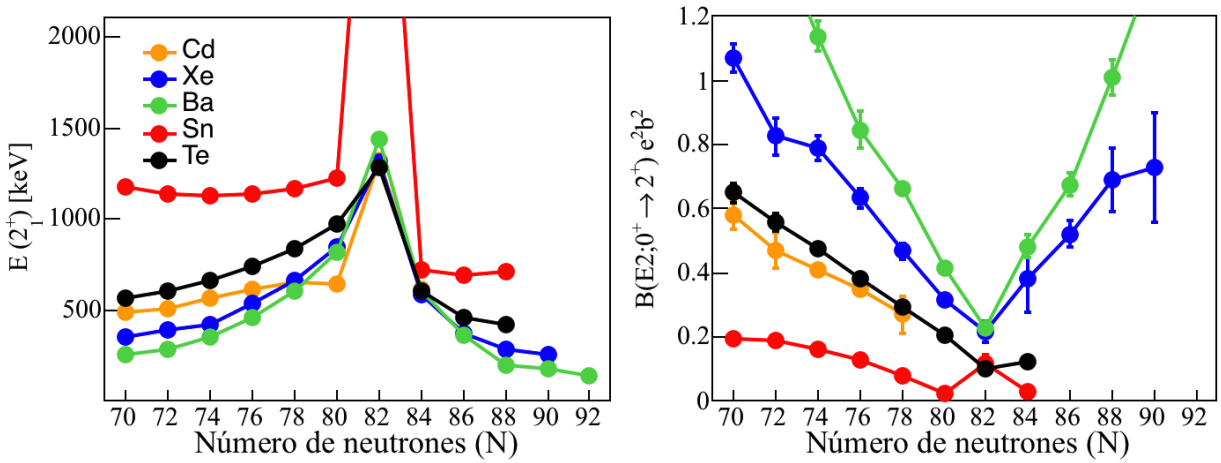

Figure 7.2: Valores experimentales de la energía de excitación del primer estado excitado 2^+ (izquierda) y $B(E2;0_1^+ \rightarrow 2_1^+)$ (derecha) para núcleos con un número par de protones y neutrones en la región alrededor del ^{132}Sn: Cd (naranja), Xe (azul), Ba (verde), Sn (rojo) y Te (negro).

Mientras que la anomalía observada en las energías del estado 2_1^+ en los isótopos del Cd fue explicada con ayuda de modernos cálculos de más allá de campo medio empleando la fuerza de Gogny [44] y revelando un comportamiento especial en esta cadena isotópica, la cual favorece deformaciones proladas cerca del cierre de capas N=82, la anomalía observada en el núcleo ^{136}Te fue explicada en términos de la composición de onda del estado 2_1^+, la cual está dominada por excitaciones de los dos neutrones situados por encima del cierre de capas N=82 y conduciendo, por lo tanto, a un valor de B(E2) más reducido. El presente trabajo se centra en la anomalía observada para la B(E2) del núcleo ^{136}Te. Para ello, en 2015 se llevó a cabo un experimento en la instalación radioactiva RIBF (RIKEN) con los siguientes objetivos:

- Determinación de la probabilidad de transición reducida B($E2;0_1^+ \rightarrow 2_1^+$) del isótopo ^{136}Te a partir de la técnica de excitación Coulombiana a energías intermedias. Además, durante el transcurso de esta tesis, un nuevo valor más grande fue reportado para la B(E2) en ^{136}Te [53] con el cual la anomalía sería mucho menor. Por lo tanto, se ha establecido

una ambigüedad en torno al valor de la B(E2) en ^{136}Te y una nueva medida es aun más necesaria.

- Estudio de la excitación y el decaimiento de un posible estado mezcla-simetría 2^+ en ^{136}Te. Con el estudio de este estado obtendremos información sobre la composición de onda del estado 2^+_1, lo cual nos permitirá verificar si su función de onda está muy dominada por la excitación de los neutrones de valencia como indican los cálculos teóricos.

- Desarrollo de un modelo de análisis para la determinación de la B(E2) a partir de la técnica de excitación Coulombiana a energías intermedias. De modo que una gran cantidad de estadística es necesaria para obtener información sobre las distintas contribuciones en la sección eficaz y las incertidumbres inherentes al análisis.

- Extensión de la información experimental disponible para varios de los N=82-84, Z$\geq$50 isótopos que forman parte del haz secundario generado para el estudio del núcleo ^{136}Te.

7.2 Resumen de los resultados y conclusiones

El experimento fue llevado a cabo en la instalación radioactiva RIBF, RIKEN, Japón, y tuvo lugar en Abril de 2015 con una duración de 2.5 días. En esta instalación, el haz secundario es generado a partir de la fragmentación/fisión de un haz primario más pesado. En el presente caso, el haz secundario fue generado a partir de un haz primario de ^{238}U acelerado hasta energías de 345 MeV/u. La intensidad media del haz primario varió desde 2.5 (parte de excitación Coulombiana) hasta 15 pnA (parte de reacciones de pérdida de nucleones). El haz de ^{238}U incidió sobre un blanco de 4 mm de ^{9}Be y una gran cantidad de elementos secundarios fueron generados. Estos elemento secundarios fueron entregados al espectrómetro BigRIPS [88–90], el cual tiene una estructura en dos etapas. La primera etapa actúa como separador para seleccionar el núcleo exótico que queremos estudiar. La separación es llevada a cabo con el método Bρ-ΔE-Bρ, basado en una selección magnética (dependiente de la relación A/Q) y en una selección energética (dependiente del número atómico Z). La segunda etapa del espectrómetro BigRIPS es utilizada para realizar la identificación del haz secundario. Esta identificación se realiza con el método TOF-Bρ-ΔE, donde el tiempo de vuelo (TOF) es determinado con dos plásticos centelleadores, la rigidez magnética (Bρ) se obtiene con detectores sensibles a la posición conocidos con el nombre de PPACs y la pérdida de energía (ΔE) es medida con una cámara de ionización llamada MUSIC. Con la medida de estas tres cantidades, podemos determinar la relación masa carga, A/Q, y el número atómico, Z, de cada núcleo. Además, esta identificación es desarrollada evento por evento. Una vez realizada la identificación, el haz secundario fue entregado al plano focal F8 donde se encontró instalado el blanco de reacción con el cual se indujeron las reacciones de interés. Dos diferentes blancos de reacción fueron usados en el presente experimento: un blanco de oro (948.34 mg/cm^2), empleado para inducir la excitación Coulombiana debido a su alto número atómico (Z=79),

y un blanco de carbono (534.44 mg/cm^2), utilizado para obtener las contribuciones nucleares presentes en la excitación del haz secundario con el blanco de oro y para inducir reacciones de pérdida de nucleones que nos permitan estudiar diferentes isótopos. Rodeando a estos blancos de reacción se encontraba instalado el espectrómetro DALI2 [103], el cual fue utilizado para medir los rayos γ emitidos en el decaimiento de estados excitados de los diferentes isótopos. Este espectrómetro γ consta de 186 detectores centelleadores de yoduro de sodio y cubre ángulos polares desde 20° hasta 150°. DALI2 está caracterizado por tener una eficiencia en fotopico bastante elevada y una resolución energética moderada (para el caso de rayos γ con una energía de 0.5 MeV emitidos desde iones moviéndose a una velocidad de β=0.5, la eficiencia en fotopico es de aproximadamente el 30% mientras que la resolución energética es del 6%). Para aumentar la eficiencia en fotopico, el algoritmo de addback fue aplicado a los datos. Este algoritmo trata de recuperar la energía original del rayo γ que ha sido distribuida sobre distintos detectores a través de procesos Compton. Por último, los productos de reacción originados en la interacción del haz secundario con el blanco de reacción son entregados al espectrómetro ZeroDegree [90] donde se procederá a su identificación. Esta identificación es realizada de nuevo con el método TOF-Bρ-ΔE. La Fig. 7.3 a) muestra la identificación del haz secundario obtenida con el espectrómetro BigRIPS para la parte del experimento en la cual queríamos determinar las contribuciones nucleares y empleamos para ello el blanco de C. Todos los distintos núcleos que componen el haz secundario están claramente separados, siendo el isótopo con más estadística el ^{136}Te. La Fig. 7.3 b) muestra la identificación en ZeroDegree de los productos formados en la interacción del ^{136}Te con el blanco de C. En dicha imagen, una gran cantidad de fragmentos provenientes de las reacciones de substracción de nucleones son observados. Además, en ZeroDegree, los diferentes isótopos son observados en tres diferentes estados de carga (especialmente visibles para el ^{136}Te), debido a que en la interacción con el blanco y los materiales que forman la línea de ZeroDegree, los distintos isótopos pueden capturan electrones y, como consecuencia, cambiar su relación A/Q. La resolución en ZeroDegree es lo suficientemente buena para distinguir de manera inequívoca los distintos productos y estados de carga.

7.2.1 Excitación Coulombiana a energías intermedias del núcleo ^{136}Te

El objetivo de esta parte del experimento fue llevar a cabo la excitación Coulombiana del núcleo ^{136}Te para determinar la B(E2) del primer estado excitado 2^+ y para estudiar la excitación y el decaimiento de un posible estado mezcla-simetría 2^+. Por lo tanto, tanto BigRIPS como ZeroDegree estuvieron optimizados para la transmisión de este núcleo. La energía del haz secundario de ^{136}Te antes del blanco de reacción fue de 165 MeV/u. Como ha sido comentado anteriormente, dos diferentes blancos de reacción fueron empleados: un blanco de oro para inducir la excitación Coulombiana y un blanco de carbono para obtener las contribuciones nucleares presentes en la excitación con el blanco de oro. La Fig. 7.4 muestra los espectros γ corregidos Doppler para la excitación del núcleo ^{136}Te con los blancos de a) oro y b) car-

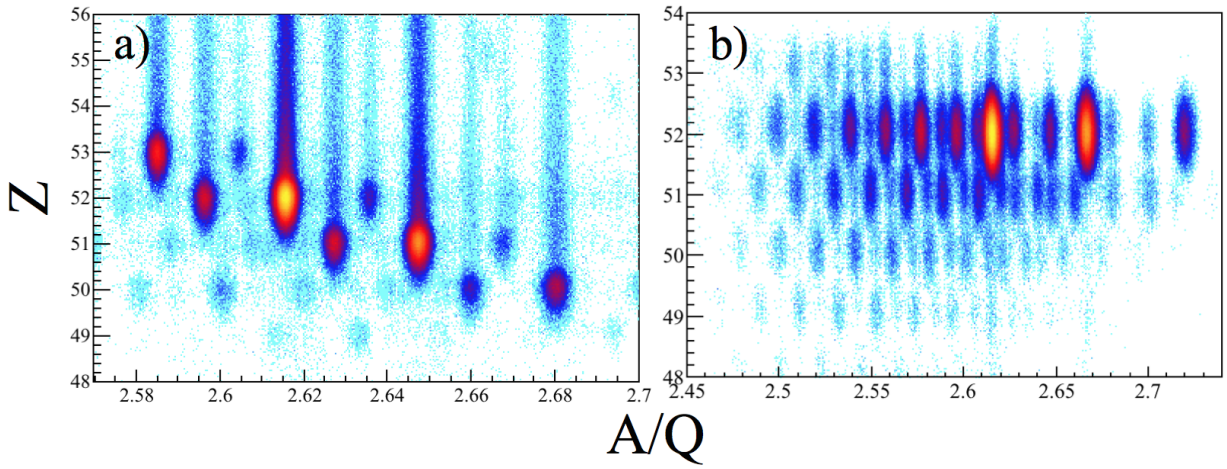

Figure 7.3: a) Identificación del haz secundario llevada a cabo con el espectrómetro BigRIPS antes de incidir sobre el blanco de reacción de C. b) Identificación obtenida con el espectrómetro ZeroDegree de los fragmentos provenientes de la interacción del ^{136}Te con el blanco de C.

bono. Estos espectros fueron corregidos Doppler con la β a mitad de blanco (β=0.4912 para el blanco de Au y β=0.4924 para el blanco de C). Con respecto al espectro obtenido con el blanco de Au (Fig. 7.4 a)), únicamente un rayo γ situado en torno a 600 keV es observado en el rango de energías hasta 2 MeV. Esta transición corresponde al decaimiento del estado 2_1^+ al estado fundamental, cuya energía nominal es 607 keV. Dicha transición se encuentra algo desplazada en energía con respecto a su valor nominal debido a la vida media de este estado [46, 47, 53]. Como consecuencia de esta vida media, el decaimiento medio de dicho estado ocurre prácticamente fuera del blanco de reacción y la β y ángulos utilizados para la corrección Doppler no son los óptimos para el estado 2_1^+. Con la ayuda de simulaciones GEANT4 [105] podemos determinar la vida media de este estado, obteniéndose un valor de $\tau_{2_1^+}$ = 33(15) ps. Con respecto al estado mezcla-simetría 2^+, su excitación no es visible en el espectro obtenido con el blanco de Au y únicamente se puede determinar un límite superior para su probabilidad de transición reducida. Dicho límite será mostrado más adelante en la tabla 7.4. Cuando el espectro γ corregido Doppler obtenido para el ^{136}Te con el blanco de Au es sorteado en un rango más grande de energías, dos transiciones γ adicionales con energías 3.6(1) y 4.2(1) MeV son observadas. Estas dos transiciones son observadas por primera vez y, a partir de un análisis de las diferentes multiplicidades γ, obtenemos que ambas proceden del decaimiento de un estado situado a 4.2 MeV con dos diferentes ramas con la misma intensidad: la primera rama decayendo al estado fundamental (rayo γ a 4.2 MeV) y la segunda decayendo al estado 2_1^+ (rayo γ a 3.6 MeV). Con respecto al espectro γ corregido Doppler obtenido con el blanco de C (Fig. 7.4 b)), además de la transición $2_1^+ \rightarrow 0_1^+$ situada en torno a 600 keV, cuatro transiciones adicionales son visibles a 330, 400, 810 y 960 keV. Las primeras dos transiciones corresponden a los decaimiento $6_1^+ \rightarrow 4_1^+$ (353 keV) y $4_1^+ \rightarrow 2_1^+$ (423 keV), respectivamente [113, 114]. De nuevo, las transiciones en el espectro mostrado en la Fig. 7.4 b)

están desplazadas en energías con respecto a su valor nominal debido a su vida media. Para el caso del decaimiento $4_1^+ \rightarrow 2_1^+$, la estadística fue suficiente para obtener la vida media efectiva del estado 4_1^+ (decimos efectiva porque lleva incluido la alimentación desde la transición $6_1^+ \rightarrow 4_1^+$) empleando el mismo método al aplicado para determinar la vida media del estado 2_1^+, obteniéndose una vida media de $\tau_{4_1^+}$ = 98(50) ps. Con respecto a la transición situada a 960 keV, en Ref. [115] un rayo γ a 962 keV fue observado por primera vez y asignado como la transición $2_2^+ \rightarrow 2_1^+$ desde un estado 2_2^+ situado a 1568 keV. De modo que nuestra emisión γ a 960 keV se corresponde con esta transición. Por último, no hay ninguna evidencia en la literatura de la transición observada a 810 keV y, por lo tanto, concluimos que esta ha sido observada por primera vez en el presente experimento. A partir de un análisis de coincidencias γ-γ, esta transición corresponde al decaimiento de un estado situado a 2378 keV el cual tiene una rama al estado 2_2^+ via la emisión de un rayo γ con una energía de 810 keV.

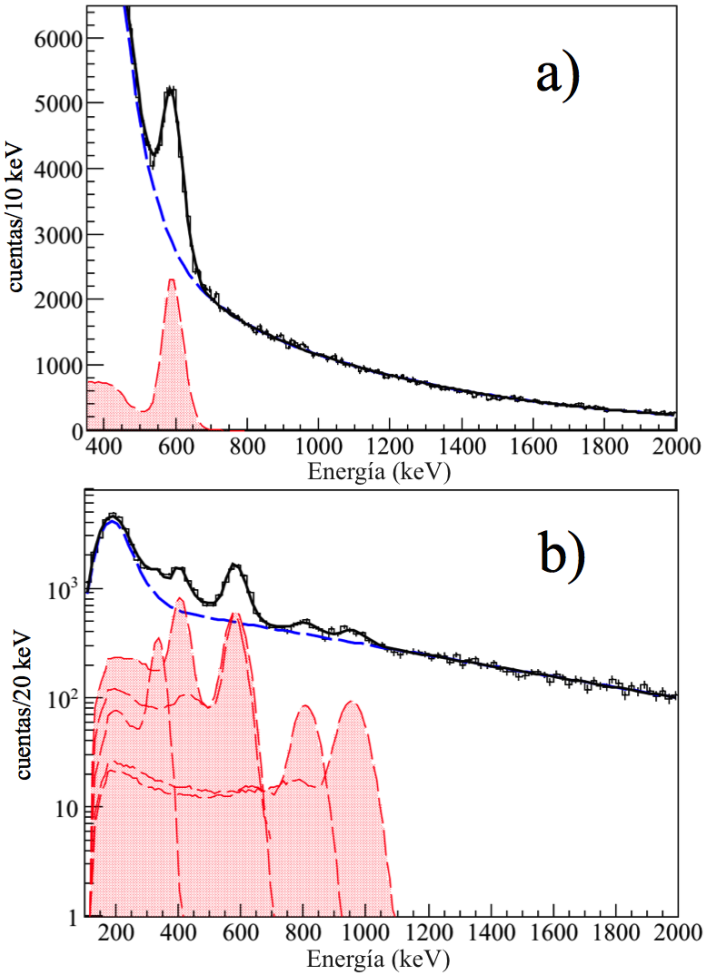

Figure 7.4: Espectro γ corregido Doppler para el núcleo ^{136}Te después de experimentar dispersión inelástica con los blancos de a) oro y b) carbono. Cada espectro ha sido fiteado con dos exponenciales (línea discontinua azul) para reproducir el fondo y con las funciones respuesta de DALI2 para cada transición obtenidas con GEANT4 (curvas rojas). La suma de ambas componentes es representada por la línea negra.

Para obtener las secciones eficaces exclusivas de cada transición, primero es necesario determinar la sección eficaz diferencial en función del ángulo de dispersión y, posteriormente, integrarla para obtener la sección eficaz total. El ángulo de dispersión fue calculado con la ayuda de dos detectores PPACs situados antes del blanco de reacción para calcular el ángulo de entrada del proyectil en el blanco y, una tercera PPAC situada después del blanco de reacción, para calcular el ángulo de salida del fragmento. A partir de de las posiciones de entrada y de salida resulta trivial calcular el ángulo de dispersión que experimentan los iones al interaccionar con el blanco. La resolución de la distribución de ángulo de dispersión sin blanco de reacción fue de σ = 4.8 mrad. Esta resolución refleja la incertidumbre en los PPACs a la hora de determinar las posiciones de entrada y salida en el blanco. Una vez instalados los blancos de Au y C en el plano focal F8, las resoluciones de las distribuciones del ángulo de dispersión fueron de σ = 8.8 mrad y σ = 5.4 mrad, respectivamente. Ahora, además de la incertidumbre en la posición, estas distribuciones incluyen el efecto de "straggling" angular causado por las múltiples dispersiones que los iones sufren en el interior del blanco. A partir de la distribución angular inelástica de los iones como función del ángulo de dispersión es posible determinar la sección eficaz diferencial usando para ello la siguiente ecuación:

$$\frac{d\sigma}{d\Omega}(bin) = \frac{N_\gamma(bin)}{T(bin) \cdot N_{ions\ BR} \cdot d\Omega(bin) \cdot N_{target} \cdot \epsilon_{\gamma\ losses}} \tag{7.1}$$

donde $N_\gamma(bin)$ es el número de emisiones γ para cada rango angular, $T(bin)$ es la transmisión angular en ZeroDegree incluyendo pérdidas en la línea debido a reacciones con sus materiales y distribución de estados de carga, $N_{ions\ BR}$ es el número de iones en BigRIPS, $d\Omega$ es el ángulo sólido por cada rango angular, N_{target} es el número de átomos en el blanco por cm^2 y $\epsilon_{\gamma\ losses}$ es un factor de corrección que tiene un cuenta un problema que surgió con la electrónica de adquisición durante el experimento. A partir de esta sección eficaz diferencial, la sección eficaz total es calculada como σ_{total}=$\sum_{bin=1}^{n} d\sigma(bin)$, donde n es el número total de cortes angulares. Para las transiciones γ sin suficiente estadística para determinar la sección eficaz diferencial, su sección eficaz total puede ser calculada a partir de la relación entre su intensidad total en el espectro Doppler y la intensidad de cualquier transición con suficiente estadística para obtener su sección eficaz diferencial. La tabla 7.1 contiene las secciones eficaces totales para las diferentes transiciones observadas con los dos blancos.

Table 7.1: Secciones eficaces totales para las diferentes transiciones γ medidas con los blanco de Au y C.

E_γ (MeV)	0.353	0.423	0.607	0.810	0.962	3.6	4.2
σ_{Au} (mb)	-	-	279(22)	-	-	21(3)	21(3)
σ_C (mb)	5.1(7)	10.7(11)	23(3)	2.1(3)	2.8(4)	-	-

Para obtener las secciones exclusivas de cada estado es necesario substraer la alimentación entre los distintos niveles. Para el caso del blanco de C, esta alimentación es observada experimentalmente en el espectro Doppler y puede ser substraída haciendo uso del esquema de niveles. Para el blanco de Au, la transición γ a 3.6 MeV se encuentra en coincidencia con el estado 2_1^+ y, por lo tanto, su sección eficaz tiene que ser substraída de la sección eficaz del estado 2_1^+. Además, para el blanco de Au también hay alimentación no observable y cuya intensidad está distribuida sobre los diferentes estados 2^+ situados por encima del primer 2_1^+. Esta alimentación fue obtenida a partir de una comparativa con la información experimental disponible en los núcleos con N= 84, ^{142}Ce y ^{144}Nd y con cálculos de modelo de capas para el núcleo ^{136}Te, obteniéndose finalmente una alimentación del 15(5)%. La tabla 7.2 contiene las secciones eficaces exclusivas para los diferentes estados observados con ambos blancos.

Table 7.2: Secciones eficaces exclusivas para los diferentes estados observados con los blancos de Au y C.

E_{nivel} (MeV)	0.607	1.030	1.383	1.568	2.378	4.2
J_i^π	2_1^+	4_1^+	6_1^+	2_2^+		
σ_{Au} (mb)	219(23)	-	-	-	-	42(4)
σ_C (mb)	9.5(32)	5.6(13)	5.1(7)	0.7(5)	2.1(3)	-

Para obtener el valor de B(E2) del estado 2_1^+ en ^{136}Te, es necesario el uso de un código de reacciones que tenga en cuenta tanto la contribución Coulombiana como la excitación nuclear en la sección eficaz, ya que a las energías del presente experimento y con las resoluciones angulares comentadas anteriormente resulta imposible poder separar una componente de otra. El código utilizado para el tratamiento simultáneo de la parte Coulombiana y nuclear fue FRESCO [122]. Los potenciales ópticos necesarios para los cálculos desarrollados con FRESCO fueron proporcionados por T. Furumoto siguiendo el modelo mostrado en Ref. [129]. En primer lugar, la sección eficaz del estado 2_1^+ medida con el blanco de C fue convertida con la ayuda de FRESCO en un valor de deformación nuclear que tuviera en cuenta las excitaciones nucleares, correspondiéndose la sección eficaz de $\sigma^C_{2_1^+}$ = 23(3) mb a una deformación nuclear de δ_N = 1.05(7) fm. Posteriormente, este valor de deformación nuclear fue utilizado con el blanco de Au y la probabilidad de transición reducida B(E2) fue modificada en FRESCO hasta reproducir la sección eficaz de $\sigma^{Au}_{2_1^+}$ = 219(23) mb medida con el blanco de Au. El valor de B(E2) con el que reproducimos esta sección eficaz fue B($E2; 0_1^+ \rightarrow 2_1^+$) = 0.195(22) e^2b^2. A la izquierda de la Fig. 7.5 se muestra una comparativa de la distribución inelástica del estado 2_1^+ en ^{136}Te obtenida con el blanco de Au comparada con distintos cálculos teóricos obtenidos con FRESCO y convolucionados dichos cálculos con la resolución experimental. Los distintos cálculos se corresponden a diferentes valores de deformación nuclear o potenciales ópticos derivados con otros métodos distintos a los estándares usados por T. Furumoto [129]. Todos

los cálculos reproducen perfectamente los puntos experimentales y validan la utilización de FRESCO para el análisis de experimentos a energías intermedias. A la derecha de la Fig. 7.5 se muestra el valor de B(E2) como función del máximo ángulo de dispersión integrado, observándose un comportamiento plano de la B(E2) como función de dicho ángulo y revelando dicho comportamiento, por lo tanto, una perfecta reproducción de la curva experimental para todos los ángulos de dispersión. Finalmente, al valor de B($E2; 0_1^+ \rightarrow 2_1^+$) = 0.195(22) e^2b^2 obtenido con FRESCO tenemos que aplicarle ciertas correcciones e incrementar su error para tener en cuenta el error debido a los potenciales ópticos, el efecto de no utilizar un código de reacciones que considere los efectos relativistas dinámicos y el hecho de utilizar un blanco de gran grosor. La tabla 7.3 muestra el valor final de B(E2) obtenido después de aplicar las diferentes correcciones.

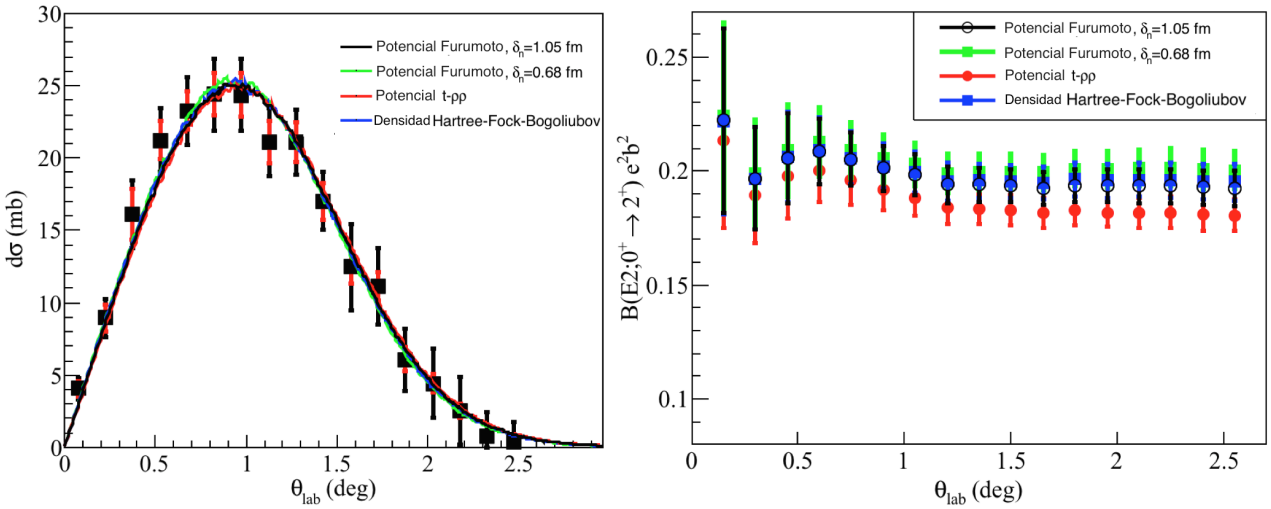

Figure 7.5: Izquierda: distribución angular experimental para la excitación del estado 2_1^+ en ^{136}Te en el blanco de Au comparada con diferentes cálculos teóricos obtenidos con FRESCO y convolucionados con la resolución experimental. Derecha: valores de B(E2) como función del máximo ángulo de dispersión integrado. El valor de B(E2) ha sido escalado con los diferentes factores de corrección explicados en el texto.

Table 7.3: Valor de B(E2) obtenido después de aplicar las diferentes correcciones explicadas en el texto.

Potencial Furumoto	B(E2) (e^2b^2)	ΔB(E2) (e^2b^2)	error
FRESCO	0.195	0.022	Experimental σ
error potencial	0.195	0.024	5%
corrección grosor blanco	0.191	0.024	2%
corrección relativista	0.191	0.026	5%
Valor final	0.191	0.026	

Table 7.4: Límite superior para el valor B(E2;$0^+_1 \rightarrow 2^+_{ms}$) como función de la relación de ramificación (BR) entre las transiciones $2^+_{ms} \rightarrow 2^+_1$ y $2^+_{ms} \rightarrow 0^+_1$.

E$_{estado}$ 2^+_{ms} (MeV)	E$_\gamma$ $2^+_{ms} \rightarrow 2^+_1$ (MeV)	B(E2;$0^+_1 \rightarrow 2^+_{ms}$) ($e^2b^2$)
1.500	0.900	$< \frac{(BR+1)}{BR} \cdot$ 0.019
2.400	1.800	$< \frac{(BR+1)}{BR} \cdot$ 0.031

El valor de B(E2) experimental obtenido en este trabajo ha sido comparado con los distintos valores experimentales y teóricos disponibles en la literatura. Desde el punto de vista experimental, tres valores han sido previamente reportados para la B(E2) del estado excitado 2^+_1 en ^{136}Te. Primero, Danchev *et al.* [47] dieron un valor de B(E2;$0^+_1 \rightarrow 2^+_1$) = 0.122(18) e^2b^2 obtenido en un experimento de excitación Coulombiana a bajas energías. Posteriormente, Fraile *et al.* [46] publicaron un valor de B(E2;$0^+_1 \rightarrow 2^+_1$) = 0.122(24) utilizando la técnica de "fast timing". Por último, muy recientemente, Allmond *et al.* [53] obtuvieron un nuevo valor de B(E2;$0^+_1 \rightarrow 2^+_1$) = 0.181(15) e^2b^2 medido en un experimento usando de nuevo la técnica de excitación Coulombiana a bajas energías. Nuestro valor está en perfecto acuerdo con la B(E2) reportada recientemente por Allmond *et al.*, pero se desvía considerablemente de los otros dos valores experimentales determinados por Danchev *et al.* y Fraile *et al.*. Desde el punto de vista teórico, diferentes cálculos trataron de reproducir el bajo valor experimental de B(E2). En 2002, Terasaki *et al.* [51] calcularon un valor de B(E2;$0^+_1 \rightarrow 2^+_1$) = 0.09 e^2b^2 a partir de cálculos QRPA. Más tarde, en 2002, Shimizu *et al.* [50] obtuvieron un valor de B(E2;$0^+_1 \rightarrow 2^+_1$) = 0.15 e^2b^2 utilizando cálculos de modelos de capas. Posteriormente, Severyukhin *et al.* [52] ofrecieron un valor de B(E2;$0^+_1 \rightarrow 2^+_1$) = 0.112 e^2b^2 usando de nuevo cálculos QRPA. Por último, dos nuevos valores han sido calculados desde el modelo de capas. Un valor de B(E2;$0^+_1 \rightarrow 2^+_1$) = 0.205 e^2b^2 ha sido reportado desde modelos realistas de capas basados en Ref. [49], mientras que muy recientemente Naïdja *et al.* [133] publicaron un valor B(E2;$0^+_1 \rightarrow 2^+_1$) = 0.205 e^2b^2. La Fig. 7.6 muestra una comparativa entre los distintos valores experimentales para la B(E2) del primer estado excitado 2^+_1 en ^{136}Te y los cálculos teóricos comentados anteriormente. La misma información para los isótopos ^{132,134}Te ha sido incluida en la imagen. Nuestro valor está en perfecto acuerdo con los valores teóricos obtenidos desde los diferentes modelos de capas, revelando que la función de onda del estado 2^+_1 en ^{136}Te está dominada por la excitación de los dos neutrones de valencia situados por encima del cierre de capas N=82 pero no tan fuertemente como previamente había sido sugerido.

7.2.2 Secciones eficaces inclusivas

Una vez que obtuvimos la suficiente estadística para llevar a cabo un estudio metodológico de las distintas incertidumbres presentes en el análisis de experimentos de excitación Coulom-

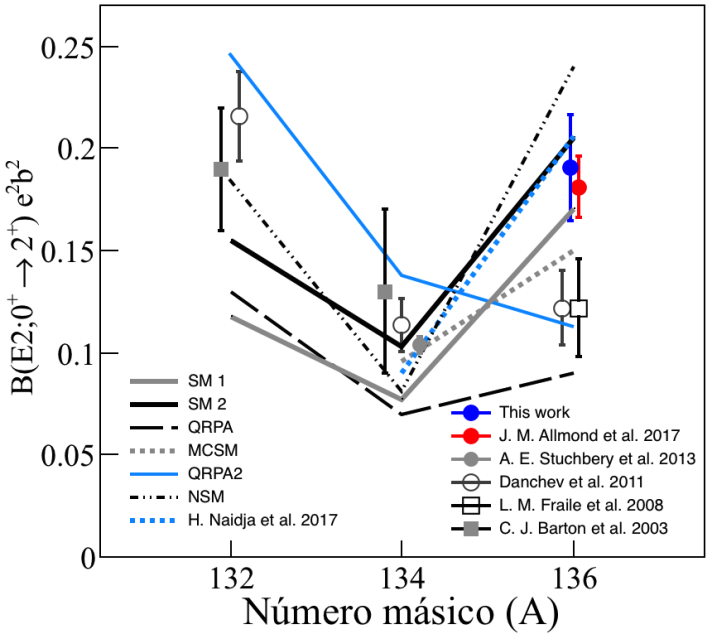

Figure 7.6: Valores experimentales de B(E2;$0_1^+ \rightarrow 2_1^+$) para los isótopos ^{132,134,136}Te obtenidos en este trabajo (punto azul) y valores previos [46,47,53] comparados con los distintos cálculos teóricos comentados en el texto [49–52,133].

biana a energías intermedias, la configuración de BigRIPS y ZeroDegree fue optimizada para la transmisión de especies más exóticas con el objetivo de inducir reacciones de pérdida de nucleones usando el blanco de C. En esta sección se muestran las secciones eficaces experimentales para la substracción de uno o mas protones/neutrones desde diferentes proyectiles en su interacción con el blanco de C. Las secciones eficaces han sido derivadas desde tres configuraciones distintas de BigRIPS y ZeroDegree y a partir de los proyectiles ^{137}I, ^{137}Te, ^{136}Te, ^{136}Sb, ^{135}Te, ^{135}Sb, ^{134}Sb, ^{134}Sn y ^{133}Sn. Las secciones eficaces son obtenidas a través de la siguiente expresión:

$$\sigma = \frac{N_{ZD}(product)}{n \cdot N_{ZD}(mother) \cdot T^*} \times 0.83 \tag{7.2}$$

donde $N_{ZD}(product)$ es el número de iones del canal de reacción de interés medido en ZeroDegree, $N_{ZD}(mother)$ es el número de iones del proyectil medido también en ZeroDegree, n es el número de átomos en el blanco de C por cm^2, T^* es la transmisión relativa a lo largo de la línea de ZeroDegree entre el producto de reacción y el proyectil y el factor 0.83 tiene en cuanta la relación entre las reacciones originadas en el blanco de C y las reacciones producidas en el resto de la línea desde que el proyectil es identificado hasta que alcanza el blanco. En las tablas 7.5 y 7.6 se encuentran los valores experimentales de las secciones eficaces inclusivas.

Estos valores experimentales han sido comparados con cálculos obtenidos con el código INCL/ABLA07, donde el modelo INCL [139] considera la reacción como una avalancha binaria de colisiones, distinguiéndose dos tipos de nucleones: espectadores y participantes. Los

espectadores son nucleones que nunca interactúan con el blanco, mientras que los participantes son definidos como las partículas que interactúan con al menos otro participante. Al final de la cascada, el núcleo se encuentra con una ganancia en energía de excitación y se desexcita a través de la emisión de partículas según el modelo ABLA07 [140]. Las Figs. 7.7 y 7.8 muestran las secciones eficaces experimentales comparadas con los cálculos teóricos obtenidos desde el código INCL/ABLA07. Dos tipos diferentes de cálculos han sido llevados a cabo. El primero de ellos usando la version estándar de INCL [137,138] (línea azul discontinua) y el segundo utilizando una versión modificada en la cual una descripción más realista de la densidad radial de la distribución de protones y neutrones es obtenida a través de cálculos Hartree-Fock-Bogoliubov usando la interacción de Skyrme [142] (línea negra). En general, el acuerdo entre los valores experimentales y la secciones eficaces calculadas con INCL es realmente bueno; además, la versión modificada de INCL reproduce mejor los datos experimentales. Sin embargo, dos anomalías son observadas en los datos. La primera anomalía concierne a las secciones eficaces para la pérdida de 1 y 2 neutrones desde los isótonos N=84, donde la sección eficaz para la substracción de 2 neutrones es mayor que la de 1 neutrón. Este fenómeno es debido a un efecto de la energías de separación de neutrón (S_n), la cual es realmente baja para el canal 1n y prácticamente constante para el resto de canales producidos desde los isótonos N=84. De modo que resulta más fácil evaporar un neutrón debido a la energía comunicada al proyectil en su interacción con el blanco. Como consecuencia de esta evaporación, el núcleo final es identificado en ZeroDegree como el canal -2n y, por lo tanto, la sección eficaz para la substracción de dos neutrones es mayor que la sección eficaz para la pérdida de 1 neutrón. La razón por la que INCL no es capaz de reproducir esta anomalía es debido a que INCL no posee información sobre el orbital del que se ha producido la eliminación del nucleón y para los canales poblados con una baja energía de separación esta información es vital, ya que únicamente la substracción desde unos pocos orbitales contribuyen a la sección eficaz del canal 1n, mientras que la pérdida de nucleones desde orbitales más profundos puebla estados no-ligados que contribuyen a la sección eficaz del canal 2n. La segunda anomalía es observada para el canal de substracción de un protón (ver Fig. 7.8), para el cual la sección eficaz es bastante pequeña y los cálculos de INCL sobreestiman los valores experimentales. Sin embargo, el hecho de que INCL sobreestime las secciones eficaces para la pérdida de un protón (neutrón) desde núcleos ricos en neutrones (protones) es bien conocido [142,143] y hasta ahora no se ha encontrado una explicación para tal fenómeno.

Table 7.5: Secciones eficaces inclusivas derivadas desde los proyectiles ^{136}Te, ^{135}Sb y ^{134}Sn.

Proyectil	Número de núcleos en ZeroDegree	Canal	Producto	Número de núcleos en ZeroDegree	$T^*(\%)$	Sección eficaz inclusiva (mb)
^{136}Te	483874	-1n	^{135}Te	1539	98(5)	100(11)
		-2n	^{134}Te	1903	91(6)	134(15)
		-3n	^{133}Te	943	75(5)	80(10)
		-4n	^{132}Te	513	60(5)	55(7)
		-5n	^{131}Te	236	43(6)	35(6)
		-6n	^{130}Te	91	22(3)	26(5)
		-1p	^{135}Sb	162	91(8)	11(2)
		-1p1n	^{134}Sb	164	95(9)	11(2)
		-1p2n	^{133}Sb	432	97(9)	28(4)
		-1p3n	^{132}Sb	369	95(8)	25(3)
		-1p4n	^{131}Sb	341	92(9)	24(3)
^{135}Sb	4435409	-1n	^{134}Sb	8763	100(10)	61(8)
		-2n	^{133}Sb	23523	93(3)	176(16)
		-3n	^{132}Sb	8113	75(4)	75(7)
		-4n	^{131}Sb	4297	55(4)	54(6)
		-5n	^{130}Sb	1538	37(4)	29(4)
		-6n	^{129}Sb	478	23(3)	14(3)
		-1p	^{134}Sn	347	94(6)	2.6(3)
		-1p1n	^{133}Sn	2196	94(13)	16(3)
		-1p2n	^{132}Sn	5820	97(8)	42(5)
		-1p3n	^{131}Sn	3429	96(11)	25(4)
		-1p4n	^{130}Sn	3026	88(9)	24(3)
		-1p5n	^{129}Sn	2244	93(14)	17(3)
^{134}Sn	1040087	-1n	^{133}Sn	2150	92(10)	69(10)
		-2n	^{132}Sn	5488	89(3)	184(17)
		-3n	^{131}Sn	2137	80(4)	79(8)
		-4n	^{130}Sn	1335	65(3)	62(6)
		-5n	^{129}Sn	780	47(4)	49(7)
		-6n	^{128}Sn	392	30(2)	39(5)
		-1p	^{133}In	362	83(8)	13(2)
		-1p1n	^{132}In	-	-	-
		-1p2n	^{131}In	726	85(9)	25(4)
		-1p3n	^{130}In	617	102(2)	18(3)
		-1p4n	^{129}In	708	85(8)	25(3)
		-1p5n	^{128}In	531	71(6)	22(3)

Table 7.6: Secciones eficaces inclusivas derivadas desde los proyectiles ^{134}Sb, ^{133}Sn, ^{137}Te, ^{136}Sb, ^{135}Te y ^{137}I.

Proyectil	Número de núcleos en ZeroDegree	Canal	Producto	Número de núcleos en ZeroDegree	$T^*(\%)$	Sección eficaz inclusiva (mb)
^{134}Sb	622338	-1n	^{133}Sb	3146	95(7)	169(19)
		-2n	^{132}Sb	1959	95(7)	102(12)
		-3n	^{131}Sb	1310	83(6)	78(9)
		-4n	^{130}Sb	737	64(5)	57(7)
		-5n	^{129}Sb	304	45(5)	34(5)
^{133}Sn	203416	-1n	^{132}Sn	1145	95(7)	183(21)
		-2n	^{131}Sn	656	94(7)	106(13)
		-3n	^{130}Sn	561	87(7)	98(12)
		-4n	^{129}Sn	302	74(9)	62(10)
		-5n	^{128}Sn	212	57(8)	57(10)
		-6n	^{127}Sn	111	39(5)	43(8)
^{137}Te	81357	-1n	^{136}Te	283	95(9)	114(16)
		-2n	^{135}Te	171	72(8)	90(14)
		-3n	^{134}Te	49	41(5)	45(10)
^{136}Sb	108408	-1n	^{135}Sb	631	100(13)	180(29)
		-2n	^{134}Sb	352	79(8)	127(18)
		-3n	^{133}Sb	162	59(6)	79(13)
^{135}Te	34478	-1n	^{134}Te	199	96(8)	186(26)
		-2n	^{133}Te	115	92(12)	111(21)
^{137}I	62513	-1n	^{136}I	243	99(8)	122(17)
		-2n	^{135}I	288	95(5)	150(18)

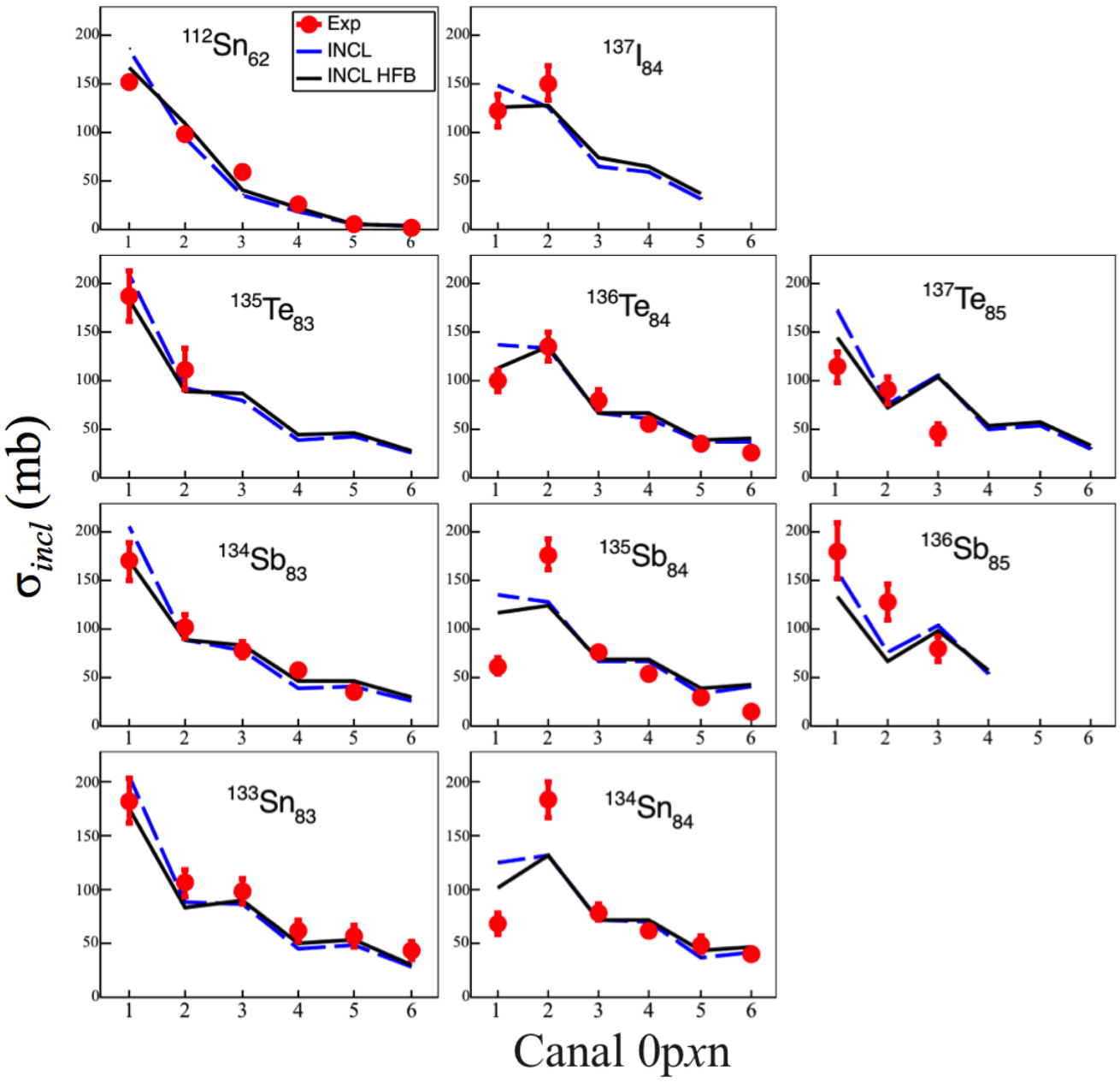

Figure 7.7: Comparativa entre las secciones eficaces inclusivas experimentales para la substracción de uno o más neutrones (puntos rojos) y los resultados obtenidos con la versión estándar de INCL (línea discontinua azul) y con una versión modificada donde una distribución más realista de la densidad radial de los protones y neutrones que forman el núcleo es usada (línea negra).

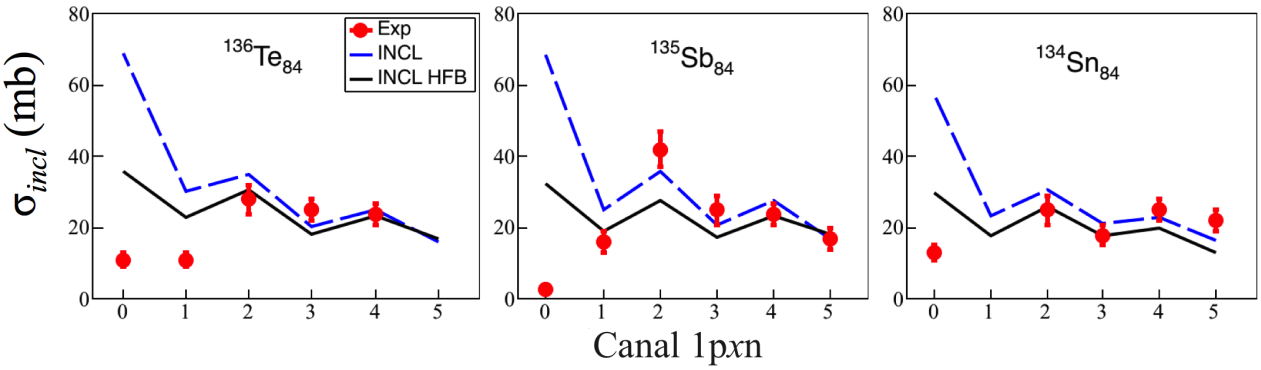

Figure 7.8: Comparativa entre las secciones eficaces inclusivas experimentales para la substracción de un protón y uno o más neutrones (puntos rojos) y los resultados obtenidos con la versión estándar de INCL (línea discontinua azul) y con la versión modificada (línea negra).

7.2.3 Decaimiento γ de estados no-ligados de neutrones en ^{133}Sn

Una de las reacciones estudiadas fue la extracción de un neutrón desde el haz secundario de ^{134}Sn produciendo ^{133}Sn. El núcleo ^{133}Sn está caracterizado por tener únicamente un neutrón por encima del cierre de capas N=82, de modo que sus estados excitados más bajos en energía proporcionan información sobre la posición de los estados de partícula independiente de neutrones situados en la región del espacio N=82-126. La Fig. 7.9 muestra el espectro γ corregido Doppler para la reacción mencionada anteriormente. Sobre dicho espectro se ha aplicado la condición de registrar únicamente eventos con multiplicidad M_γ=1. Ademas, el algoritmo de addback fue aplicado a los datos con vistas a aumentar la eficiencia γ en la región de altas energías. Las rayos γ observados por debajo de la energía de separación de neutrones (S_n = 2.402(4) MeV) corresponden al decaimiento de los ya conocidos estados de partícula independiente de neutrones [31–34]. Más en concreto, la transición situada en torno a 854 keV corresponde al decaimiento del estado de partícula independiente de neutrones $2p_{3/2}$ al estado fundamental $1f_{7/2}$. La energía de esta transición esta desplazada con respecto a su valor nominal debido a la vida media del estado. El mismo método utilizado anteriormente para derivar la vida media de los estados 2_1^+ y 4_1^+ en ^{136}Te es usado ahora para determinar la vida media del estado $2p_{3/2}$, obteniéndose un valor de τ = 30(15) ps, el cual corresponde a una probabilidad de transición reducida B($E2; 2p_{3/2} \rightarrow 1f_{7/2}$) = 1.6(8) W.u. Volviendo al espectro de la Fig. 7.9, las transiciones visibles a 1561 y 2002 keV corresponden al decaimiento γ de los estados $0h_{9/2}$ y $1f_{5/2}$ al estado fundamental $1f_{7/2}$. Con respecto al rayo γ observado a 513 keV, dicha transición corresponde al decaimiento del estado de partícula independiente de neutrones $2p_{1/2}$, situado a 1367 keV, al primer estado excitado $2p_{3/2}$, localizado a 854 keV, con la consiguiente emisión de un rayo γ con una energía de 513 keV. Por encima de la energía de separación de neutrones, es visible adicional intensidad γ, en particular una fuerte transición es observada a 3570(50) keV. Esta emisión γ situada por encima de S_n puede ser producida únicamente por el decaimiento de estados excitados poblados en la substracción de un neutrón

desde el núcleo de neutrones N=82 del proyectil ^{134}Sn. De modo que el rayo γ observado a 3570(50) keV es probablemente provocado por el decaimiento γ del estado neutrón-hueco producido en el orbital $0h_{11/2}$, debido a que la probabilidad de substraer un neutrón desde este orbital es más alta, ya que está ocupado por 12 neutrones y situado cerca del nivel de Fermi. Mientras que el resto de intensidad γ situada en el rango entre 4-6 MeV podría ser producida por la extracción de un neutrón desde los otros orbitales pertenecientes a la capa N =50-82 (en particular con más probabilidad desde los orbitales $1d_{5/2}$ y $0g_{7/2}$).

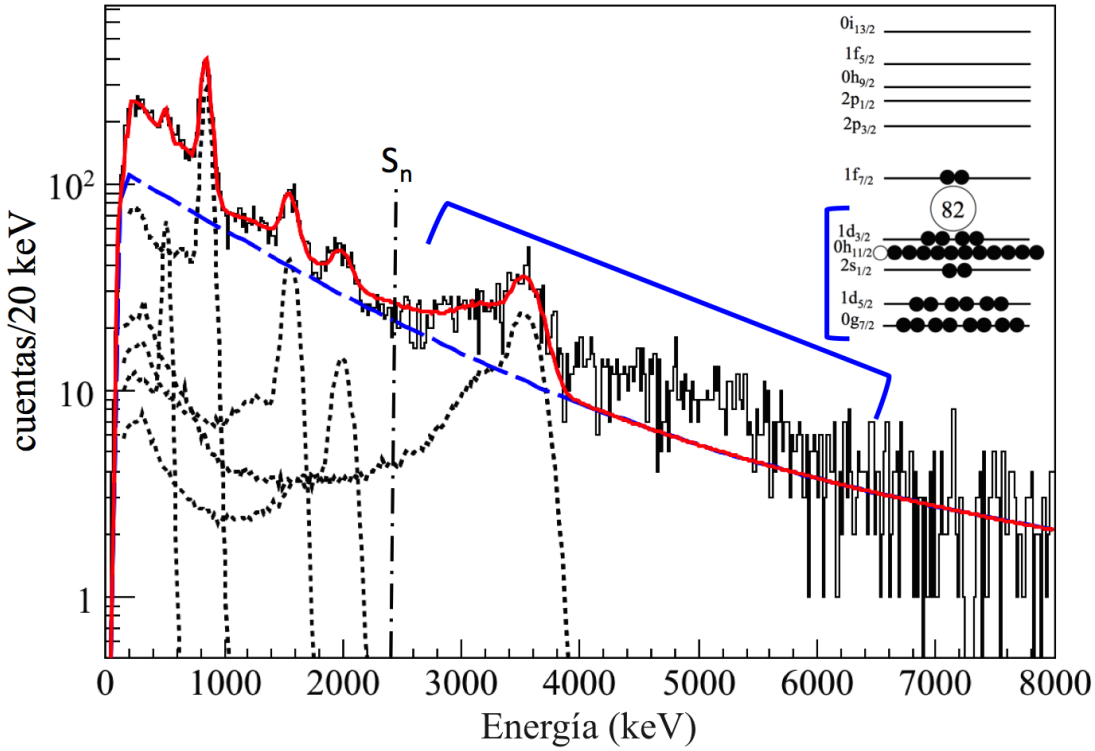

Figure 7.9: Espectro γ corregido Doppler para eventos con multiplicidad M$_\gamma$=1 y después de aplicar addback para el núcleo ^{133}Sn poblado a través de la extracción de un neutrón del proyectil ^{134}Sn. Las transiciones γ situadas por encima de la energía de separación de neutrón (remarcadas por la línea azul) provienen del decaimiento de estados poblados por la eliminación de un neutrón perteneciente a las capas situadas por debajo de N=82, siendo más probable la substracción desde el orbital $0h_{11/2}$, cuya configuración es ilustrada en el interior de la figura.

Para entender por qué estos estados situados bastante por encima de la energía de separación de un neutrón decaen vía la emisión de rayos γ y no completamente por la emisión de neutrones, necesita ser considerado el proceso de reacción que puebla estos estados excitados. Para ello, consideramos el caso en que el neutrón es substraído desde el orbital $0h_{11/2}$ situado en el espacio N = 50-82 perteneciente al proyectil ^{134}Sn. Una vez substraído este neutrón, la configuración poblada corresponde a un hueco en el orbital $0h_{11/2}$ del núcleo ^{133}Sn. Debido a que este estado se encuentra situado por encima de la energía de separación de un neutrón, se espera que decaiga completamente por la emisión de un neutrón poblando el

núcleo doblemente mágico ^{132}Sn. El núcleo ^{132}Sn, al ser doblemente mágico, tiene su primer estado excitado 2_1^+ situado a una energía de excitación muy elevada (4.041 MeV), de modo que la emisión del neutrón situado en el orbital $0h_{11/2}$ del núcleo ^{133}Sn puede poblar únicamente el estado fundamental del núcleo ^{132}Sn a través de la emisión de un neutrón con momento angular l=5 y energía E_n = 1.2 MeV, ya que la población del resto de estados excitados no es energéticamente posible. Todo este proceso conduciría al estado fundamental del ^{132}Sn con dos neutrones en el orbital $1f_{7/2}$, situado por encima del cierre de capas N=82, y dos huecos en el orbital $0h_{11/2}$, situado en el espacio N = 50-82. Esta configuración 2p-2h del estado fundamental de ^{132}Sn es muy pequeña y prácticamente despreciable y, como consecuencia, la superposición entre la función de onda de los estados del núcleo padre e hijo es realmente pequeña. Según la regla de oro de Fermi [145], es esta pequeña superposición la responsable de que la emisión γ pueda competir con la emisión de un neutrón para el decaimiento de estados situados por encima de S_n en ^{133}Sn. De modo que, en lugar de emitir un neutrón, el hueco situado en el orbital $0h_{11/2}$ del núcleo ^{133}Sn es completado con un neutrón situado en el orbital $1f_{7/2}$ y la consiguiente emisión de radiación γ. El argumento explicado anteriormente para el orbital $0h_{11/2}$ es válido para el resto de orbitales situados en la región del espacio N = 50-82.

Para poder cuantificar la competitividad γ/neutrón para el decaimiento de estados no-ligados de neutrón situados por encima de S_n en ^{133}Sn, en primer lugar necesitamos conocer la composición de la función de onda del estado fundamental del proyectil ^{134}Sn. Para ello, se han llevado a cabo cálculos de modelos de capas [150], obteniéndose los porcentajes mostrados en la tabla 7.7, donde los dos neutrones tienen que estar situados en el mismo orbital para poder acoplarse al estado fundamental 0^+ del ^{134}Sn. Una vez conocida la composición de onda del estado fundamental en ^{134}Sn, el siguiente paso es obtener las secciones eficaces para la substracción de un neutrón desde los diferentes orbitales de ^{134}Sn. Para ello se han llevado a cabo cálculos usando la teoría de reacciones eikonal [153]. La Fig. 7.10 muestra los resultados obtenidos para la substracción de un neutrón desde los proyectiles ^{133}Sn y ^{134}Sn. Los cálculos para la pérdida de un neutrón desde el proyectil ^{133}Sn han sido incluidos para validar el modelo en la región del ^{132}Sn, donde observamos que la sección experimental para esta reacción σ_{1n}^{exp}=183(21) mb es perfectamente reproducida por el modelo eikonal σ_{1n}^{theo}=200 mb cuando se consideran en los cálculos el espacio N = 50-82 y el orbital $1f_{7/2}$ situado por encima de N=82. Para el caso en que el neutrón es extraído desde el proyectil ^{134}Sn, la situación es algo más compleja debido a la baja energía de separación S_n en ^{133}Sn, ya que a diferencia del ^{132}Sn donde su energía de separación (S_n = 7.343(7) MeV) es lo suficientemente alta para que la substracción de un neutrón desde cualquiera de los orbitales situados en el espacio N=50-82 de ^{133}Sn pueble estados ligados, en el caso del ^{133}Sn la pérdida de un neutrón desde el espacio N=50-82 de ^{134}Sn puebla estados no-ligados en ^{133}Sn que en principio se esperaría que decayesen completamente vía la emisión de un neutrón, pero como hemos observado y mencionado anteriormente, pueden decaer también vía la emisión de radiación γ. De modo

que substrayendo a la sección eficaz experimental para la eliminación de un neutrón desde ^{134}Sn, σ_{1n}^{exp}=69(10) mb, la sección eficaz calculada con el modelo eikonal para la pérdida de un neutrón desde cualquier orbital perteneciente al espacio N>82, σ_{1n}^{val} = 20 mb, obtenemos aproximadamente $\approx$ 49 mb, los cuales son debidos al decaimiento γ de estados no-ligados de neutrones, ya que si estos estados decayeran vía la emisión de un neutrón serían identificados como ^{132}Sn en ZeroDegree. Comparando ahora estos 49 mb con la sección eficaz calculada para la substracción de un neutrón desde el espacio N = 50-82 en ^{134}Sn, σ_{1n}^{core} = 152 mb, podemos obtener el porcentaje de competitividad γ/neutrón para el decaimiento de estado no-ligados de neutrones en ^{133}Sn, obteniéndose un porcentaje de 25-39% para el decaimiento γ de estados no-ligados de neutrones en ^{133}Sn.

Table 7.7: Probabilidad de ocupación de los dos neutrones de valencia situados por encima del cierre de capas N=82 para acoplarse al estado fundamental 0^+ de^{134}Sn.

Probabilidad (%)	$1f_{7/2}$	$2p_{3/2}$	$2p_{1/2}$	$0h_{9/2}$	$1f_{5/2}$	$0i_{13/2}$
Estado fundamental 0_1^+	80.30	5.19	1.55	5.67	4.07	3.19

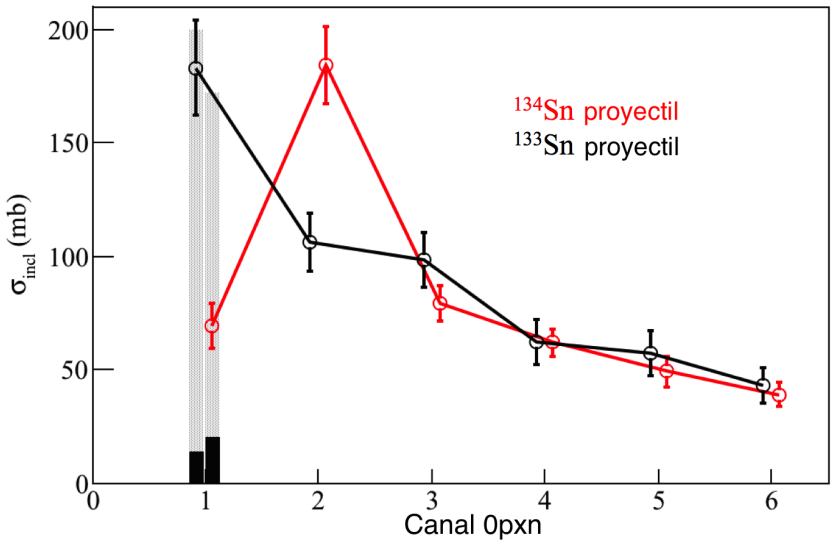

Figure 7.10: Secciones eficaces inclusivas experimentales para la substracción de un neutrón desde los proyectiles ^{133}Sn (línea negra) y ^{134}Sn (línea roja). Las barras verticales representan los cálculos teóricos para la pérdida de un neutrón obtenidos desde el modelo eikonal [153]. Las barras negras indican la sección eficaz para la eliminación de un neutrón perteneciente al espacio de valencia (N>82) mientras que las barras grises representan la sección eficaz para la substracción de un neutrón desde el espacio situado entre N=50-82.

Appendix A

Spectroscopic information for the rest of by-products

In this appendix, the reader can find summarized the Doppler-corrected γ-ray spectra for the rest of by-products produced when the secondary beam interacted with the C target. All the results shown are preliminary and they are presented with the idea of showing the scientific wealth of the data. For each reaction channel, the experimental Doppler-corrected γ-ray spectrum is fitted with two exponential functions to describe the background and simulated response functions of the DALI2 array. In some cases, besides the Doppler-corrected γ-ray spectrum considering all γ-ray multiplicities, which is necessary to obtain the total cross sections, we also display the Doppler-corrected γ-ray spectrum for events with γ-ray multiplicity M_γ = 1 since the γ-ray transitions are more visible due to a background suppression. Each reaction channel is accompanied by a table that contains the energies of the simulated γ rays and the cross sections of each transition. The quoted values are not exclusive cross sections to individual excited states because up to now we have not built the level scheme necessary to obtain exclusive cross sections. In the cases where the energy of the γ ray is well known from literature and we observe a shift with respect to its nominal value, we consider lifetime for the excited state to obtain a better description of the experimental data. Lastly, all the γ spectra have applied the addback algorithm.

A.1 The ^{12}C(^{136}Te,^{135}Te+γ)X reaction

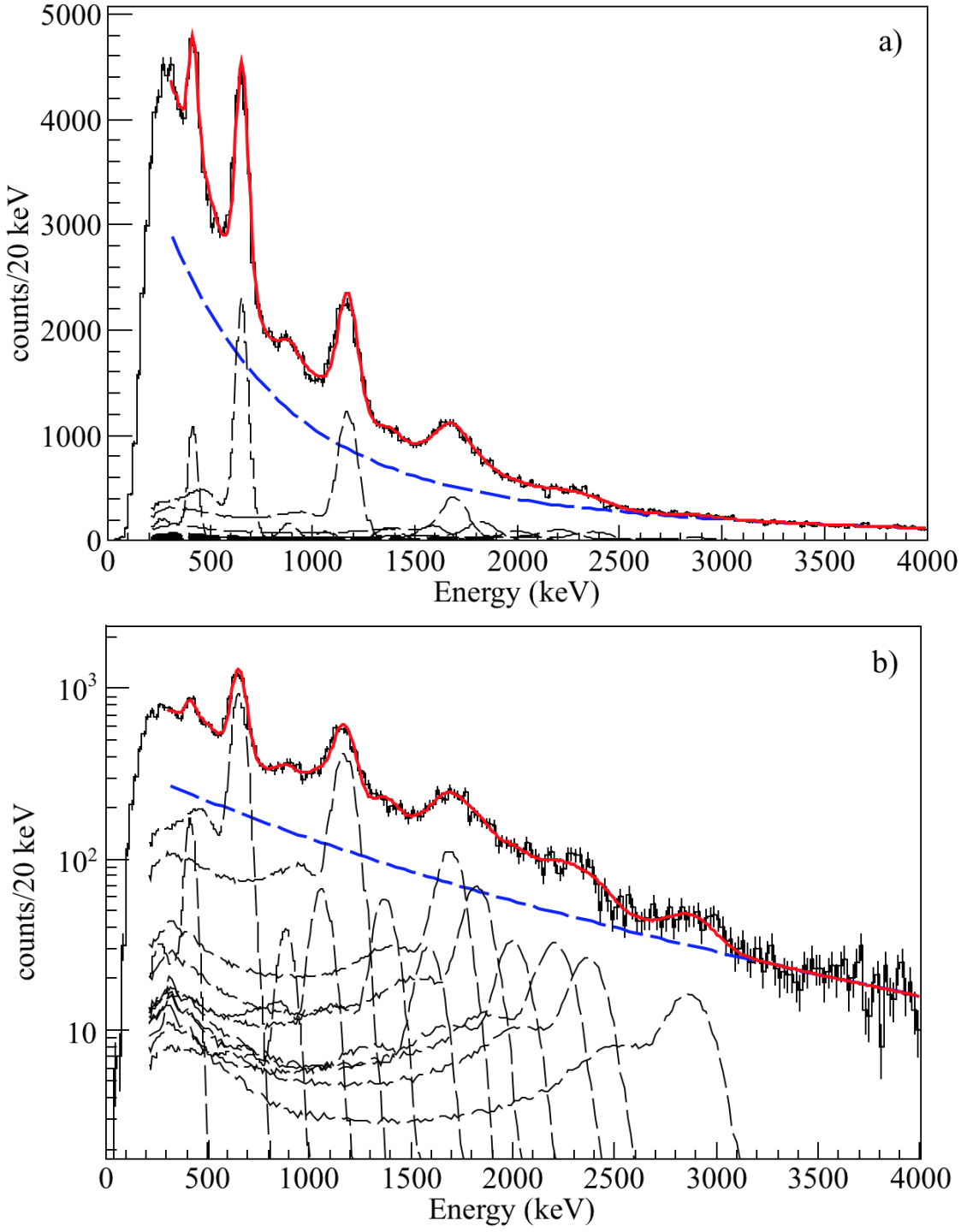

Figure A.1: Doppler-corrected γ-ray energy spectrum for the ^{12}C(^{136}Te,^{135}Te+γ)X reaction a) considering all γ-ray multiplicities and b) only events with γ-ray multiplicity M_γ=1. The addback algorithm was applied.

A.2 The ^{12}C(^{136}Te,^{134}Te+γ)X reaction

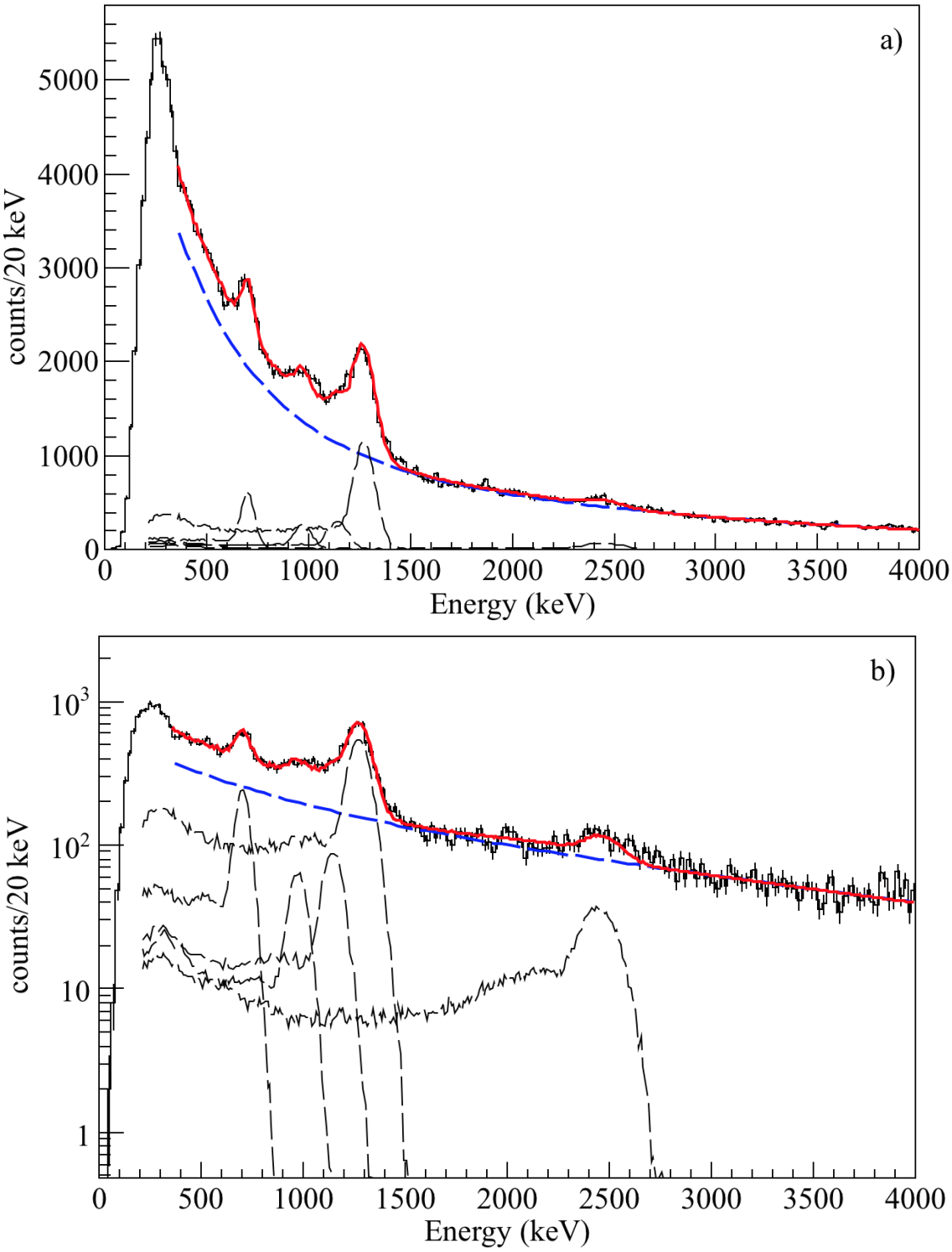

Figure A.2: Doppler-corrected γ-ray energy spectrum for the ^{12}C(^{136}Te,^{134}Te+γ)X reaction a) considering all γ-ray multiplicities and b) only events with γ-ray multiplicity M_γ=1. The addback algorithm was applied.

A.3 The ^{12}C(^{137}Te,^{136}Te+γ)X reaction

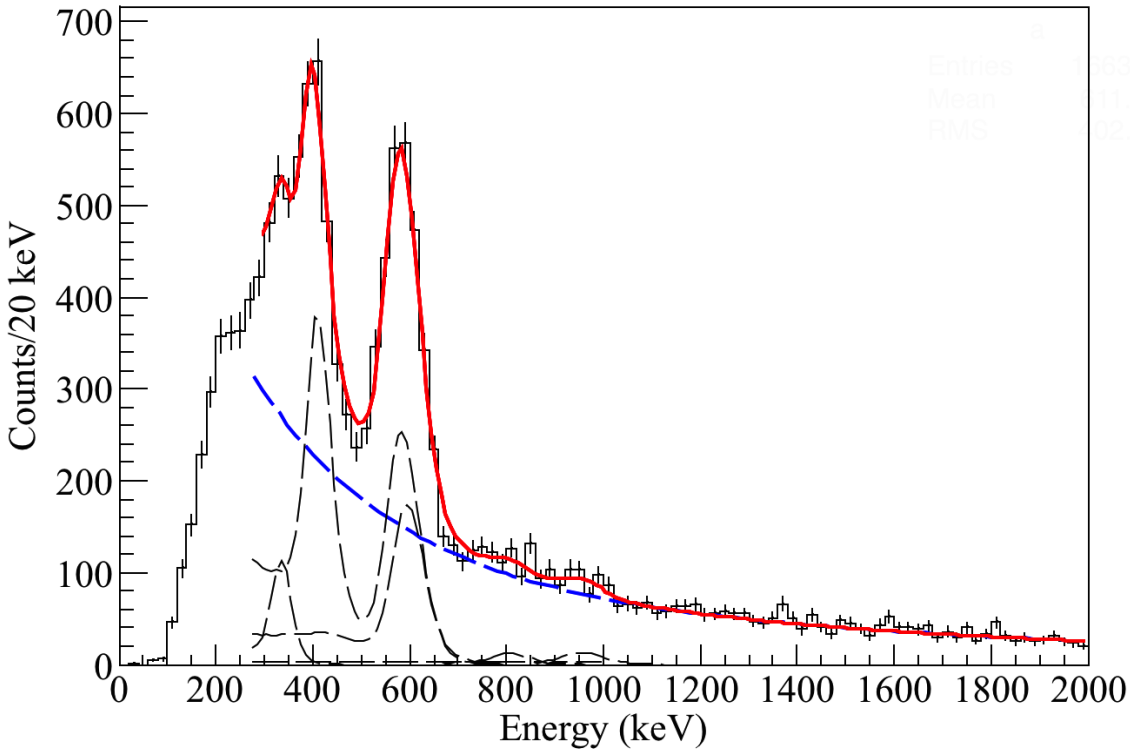

Figure A.3: Doppler-corrected γ-ray energy spectrum for the ^{12}C(^{137}Te,^{136}Te+γ)X reaction considering all γ-ray multiplicities. The addback algorithm was applied. The cascade $4_1^+ \rightarrow 2_1^+ \rightarrow 0_1^+$ and their known lifetimes have been considered in the fit.

Table A.1: Energies and cross sections for the different γ-ray transitions observed in the Doppler-corrected γ-ray spectrum of ^{135}Te populated via one-neutron knockout from ^{136}Te. The inclusive cross section for this reaction is also included in the table.

$E_{transition}$ (MeV)	σ (mb)	$E_{transition}$ (MeV)	σ (mb)
0.419	4.9(7)	1.702	7.64(10)
0.658	15(2)	1.837	3,7(6)
0.892	1.4(3)	2.018	2.1(4)
1.067	0.9(3)	2.219	2.9(5)
1.179	15(2)	2.390	2.4(4)
1.380	1.7(4)	2.900	1.0(2)
1.595	2.5(4)		
σ_{incl} = 100(11) mb			

Table A.2: Energies and cross sections for the different γ-ray transitions observed in the Doppler-corrected γ-ray spectrum of ^{134}Te populated via two-neutrons knockout from ^{136}Te. The inclusive cross section for this reaction is also included in the table.

$E_{transition}$ (MeV)	σ (mb)	$E_{transition}$ (MeV)	σ (mb)
0.706	4.6(7)	1.279	17(2)
0.978	2.9(5)	2.475	2.4(4)
1.150	3.8(6)		
σ_{incl} = 134(15) mb			

Table A.3: Energies and cross sections for the different γ-ray transitions observed in the Doppler-corrected γ-ray spectrum of ^{136}Te populated via one-neutron knockout from ^{137}Te. The inclusive cross section for this reaction is also included in the table. In the case of the 2_1^+ state, the feeding from the 4_1^+ state has been subtracted. The transitions corresponding to the decay of 2_1^+ and 4_1^+ states have been simulated considering their known lifetimes.

$E_{transition}$ (MeV)	σ (mb)	$E_{transition}$ (MeV)	σ (mb)
0.337	4.0(10)	0.810	0.8(5)
0.423^a	13(2)	0.922	1.0(5)
0.606^a	9.0(17)^b		
σ_{incl} = 114(16) mb			

a: assuming lifetime
b: once the feeding from the 4_1^+ *state has been substracted*

A.4 The ^{12}C(^{135}Sb,^{134}Sn+γ)X reaction

Table A.4: Energies and cross sections for the different γ-ray transitions observed in the Doppler-corrected γ-ray spectrum of ^{134}Sn populated via one-proton knockout from ^{135}Sb. The inclusive cross section for this reaction is also included in the table. The transition corresponding to the decay of 2_1^+ state has been simulated considering a lifetime of τ = 70 ps.

$E_{transition}$ (MeV)	σ (mb)
0.310	0.12(3)
0.725^a	0.18(3)
1.281	0.04(2)
σ_{incl} = 2.6(3) mb	

a: assuming a lifetime of τ *= 70 ps*

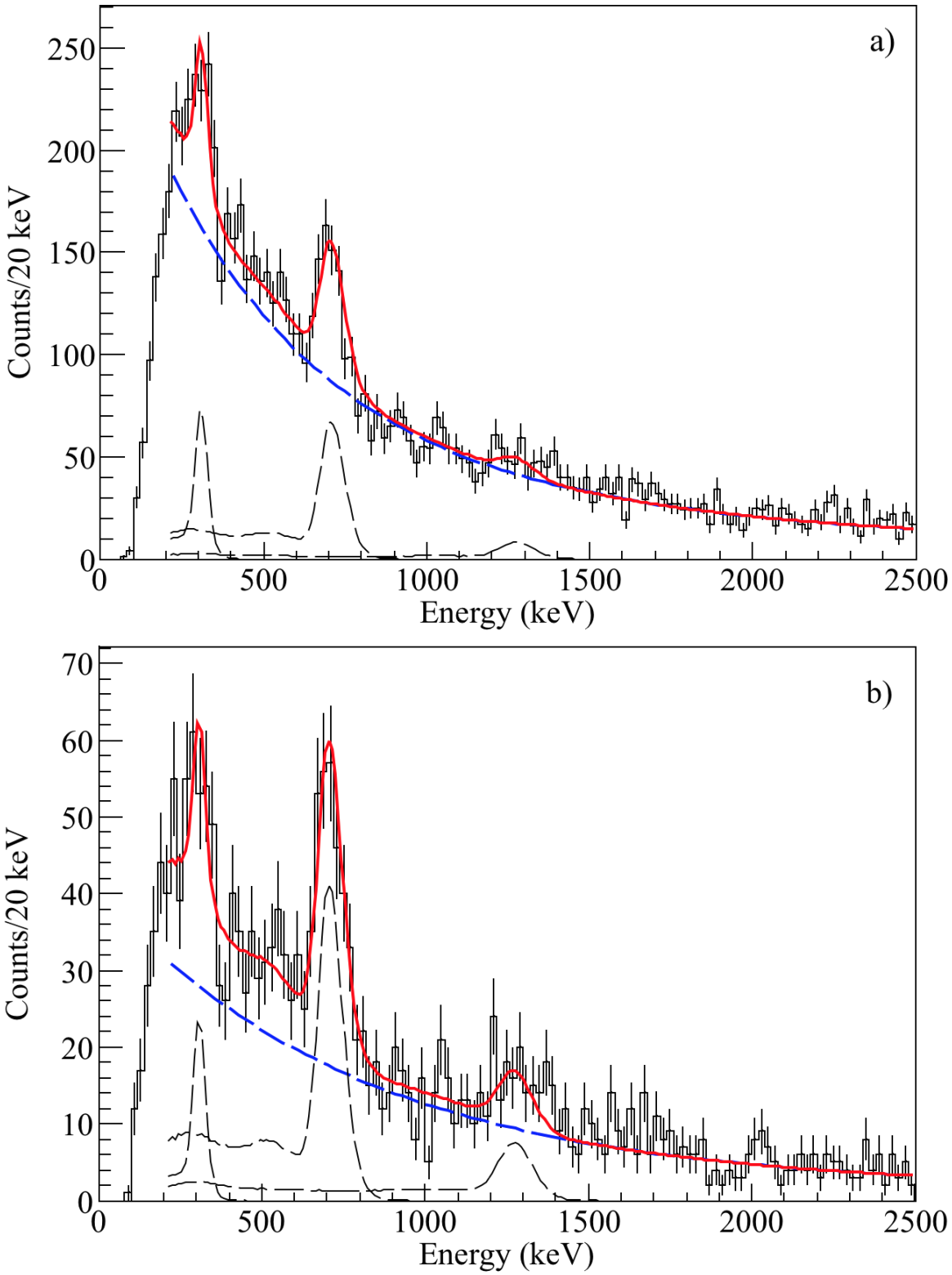

Figure A.4: Doppler-corrected γ-ray energy spectrum for the ^{12}C(^{135}Sb,^{134}Sn+γ)X reaction a) considering all γ-ray multiplicities and b) only events with γ-ray multiplicity M_γ=1. The addback algorithm was applied.

A.5 The ^{12}C(^{134}Sn,^{133}In +γ)X reaction

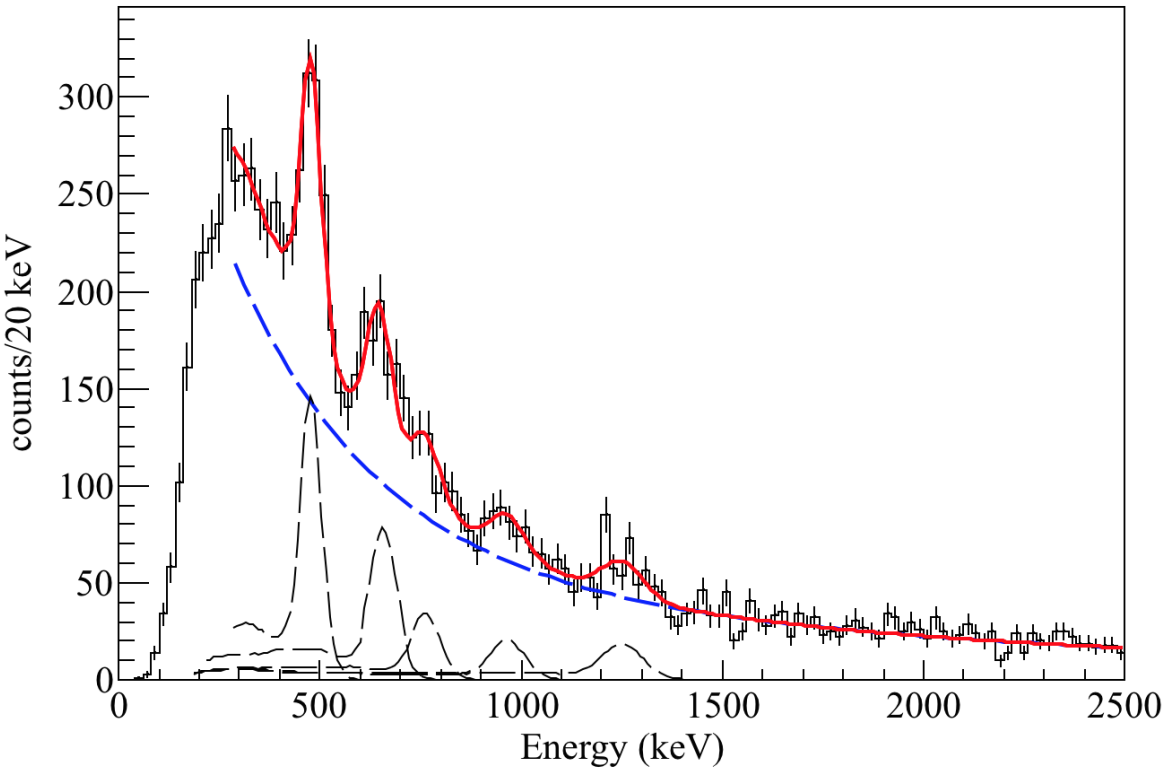

Figure A.5: Doppler-corrected γ-ray energy spectrum for the ^{12}C(^{134}Sn,^{133}In+γ)X reaction considering all γ-ray multiplicities. The addback algorithm was applied.

Table A.5: Energies and cross sections for the different γ-ray transitions observed in the Doppler-corrected γ-ray spectrum of ^{133}In populated via one-proton knockout from ^{134}Sn. The inclusive cross section for this reaction is also included in the table.

$E_{transition}$ (MeV)	σ (mb)	$E_{transition}$ (MeV)	σ (mb)
0.480	1.2(2)	0.970	0.31(10)
0.650	0.83(17)	1.255	0.37(11)
0.765	0.42(12)		
σ_{incl} = 13(2) mb			

A.6 The ^{12}C(^{136}Sb,^{135}Sb +γ)X reaction

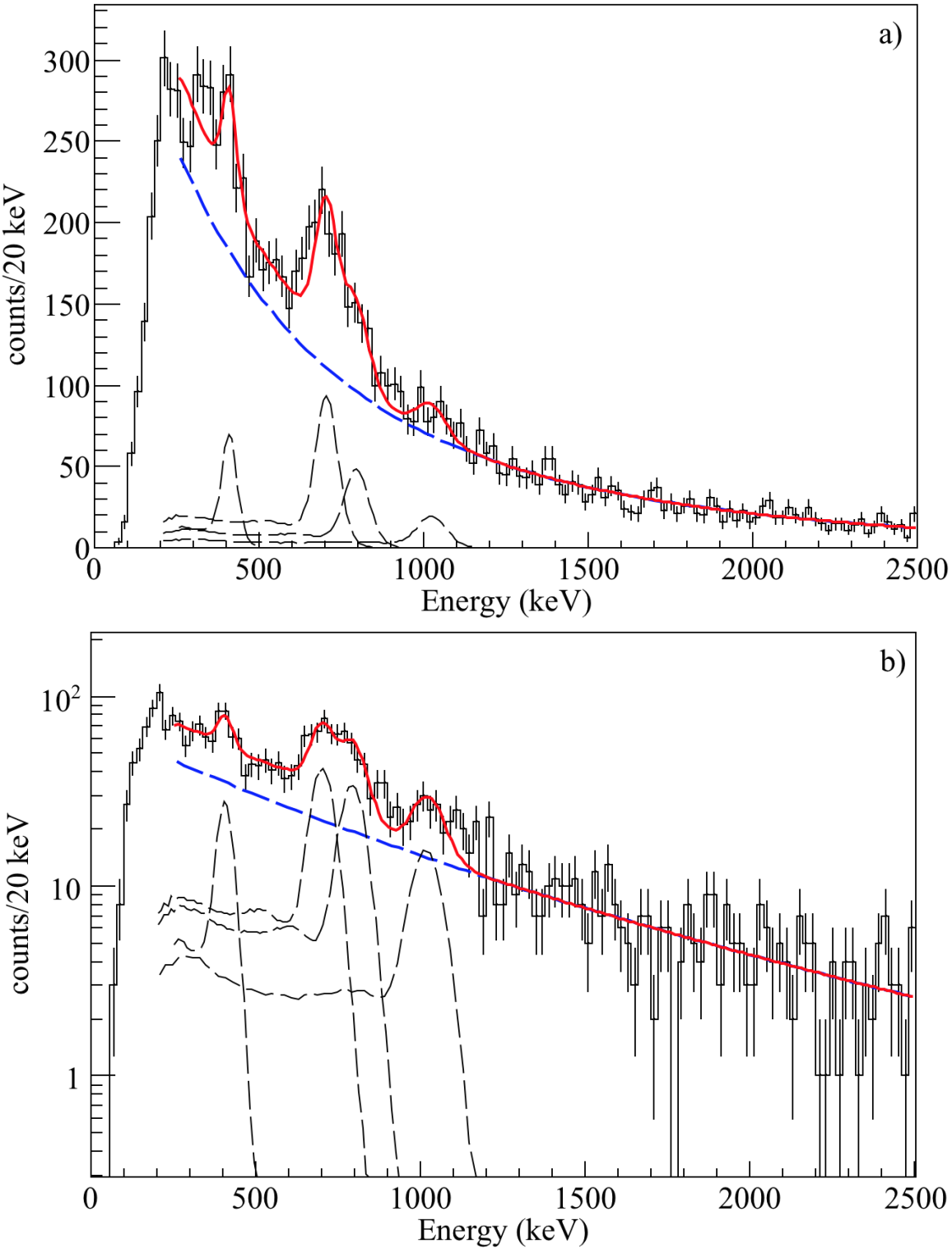

Figure A.6: Doppler-corrected γ-ray energy spectrum for the ^{12}C(^{136}Sb,^{135}Sb+γ)X reaction a) considering all γ-ray multiplicities and b) only events with γ-ray multiplicity M_γ=1. The addback algorithm was applied.

A.7 The ^{12}C(^{136}Te,^{135}Sb +γ)X reaction

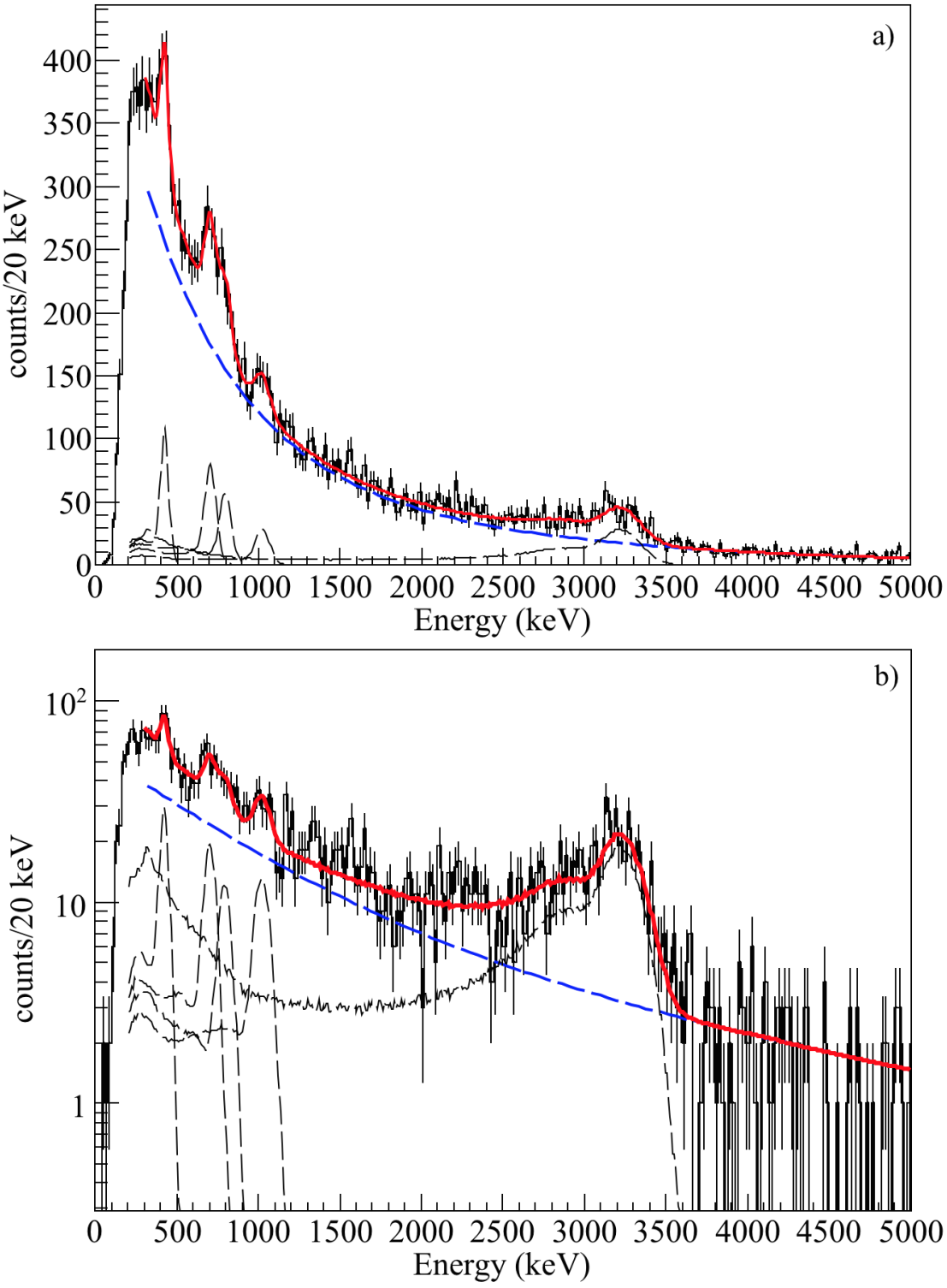

Figure A.7: Doppler-corrected γ-ray energy spectrum for the ^{12}C(^{136}Te,^{135}Sb+γ)X reaction a) considering all γ-ray multiplicities and b) only events with γ-ray multiplicity M_γ=1. The addback algorithm was applied.

Table A.6: Energies and cross sections for the different γ-ray transitions observed in the Doppler-corrected γ-ray spectrum of ^{135}Sb populated via one-neutron knockout from ^{136}Sb. The inclusive cross section for this reaction is also included in the table.

$E_{transition}$ (MeV)	σ (mb)	$E_{transition}$ (MeV)	σ (mb)
0.425	2.4(6)	0.797	2.8(7)
0.707	5(1)	1.027	1.5(5)
σ_{incl} = 180(29) mb			

Table A.7: Energies and cross sections for the different γ-ray transitions observed in the Doppler-corrected γ-ray spectrum of ^{135}Sb populated via one-proton knockout from ^{136}Te. The inclusive cross section for this reaction is also included in the table.

$E_{transition}$ (MeV)	σ (mb)	$E_{transition}$ (MeV)	σ (mb)
0.425	0.52(13)	1.027	0.29(9)
0.707	0.56(13)	3.250	1.2(2)
0.797	0.45(12)		
σ_{incl} = 11(2) mb			

Table A.8: Energies and cross sections for the different γ-ray transitions observed in the Doppler-corrected γ-ray spectrum of ^{132}Sb populated via three-neutrons knockout from ^{135}Sb. The inclusive cross section for this reaction is also included in the table.

$E_{transition}$ (MeV)	σ (mb)	$E_{transition}$ (MeV)	σ (mb)
0.291	1.02(16)	0.993	0.5(2)
0.341	2.7(3)	1.025	3.0(4)
0.401	0.96(16)	1.774	0.39(11)
0.443	0.80(14)	$\approx$ 4.000	1.7(2)
0.529	2.2(3)	$\approx$ 4.500	1,13(17)
0.652	0.64(12)	$\approx$ 5.000	1.10(15)
0.898	1.9(2)	$\approx$ 5.800	0.79(11)
σ_{incl} = 75(7) mb			

A.8 The ^{12}C(^{135}Sb,^{132}Sb +γ)X reaction

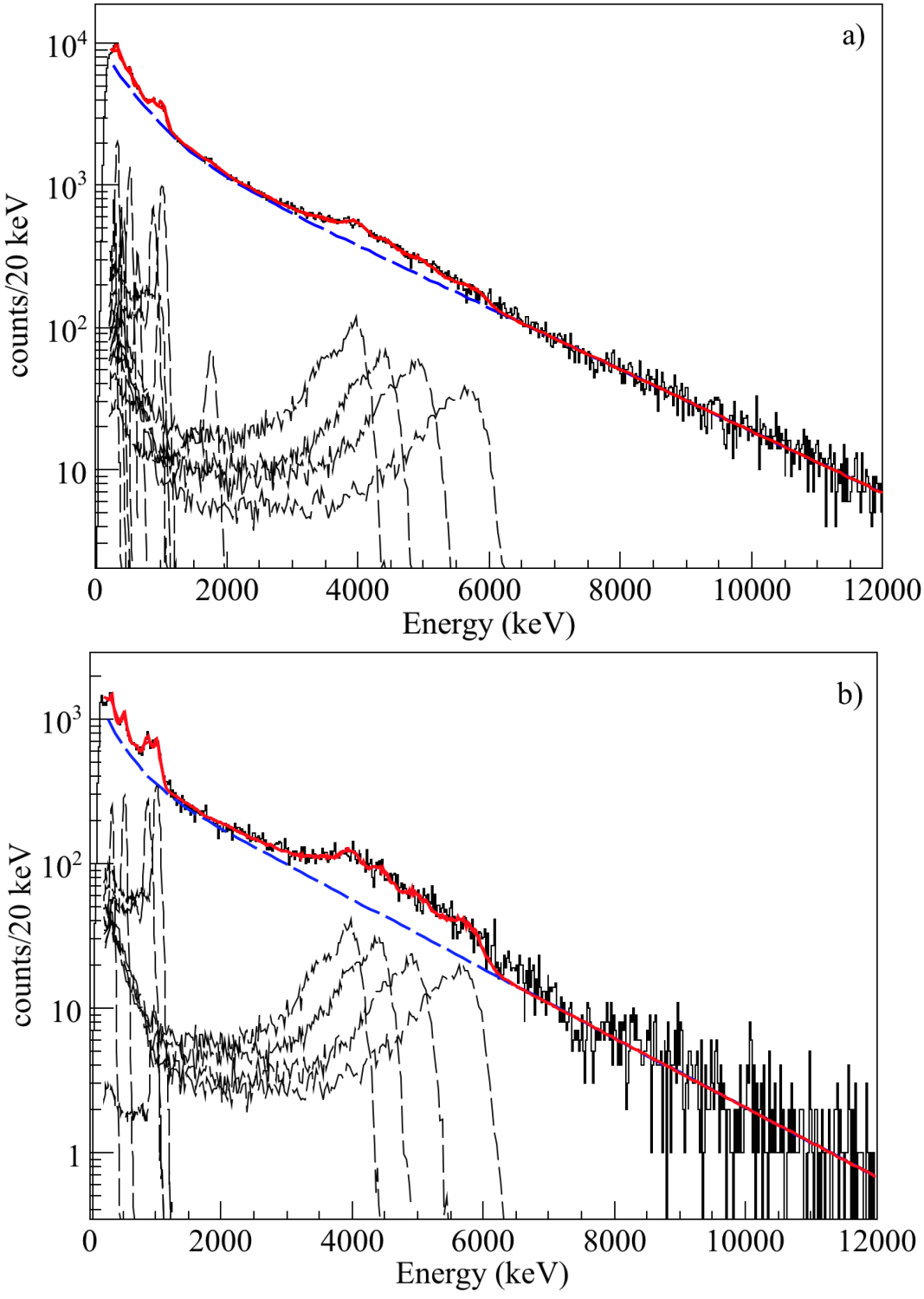

Figure A.8: Doppler-corrected γ-ray energy spectrum for the ^{12}C(^{135}Sb,^{132}Sb+γ)X reaction a) considering all γ-ray multiplicities and b) only events with γ-ray multiplicity M_γ=1. The addback algorithm was applied.

A.9 The ^{12}C(^{135}Sb,^{133}Sn +γ)X reaction

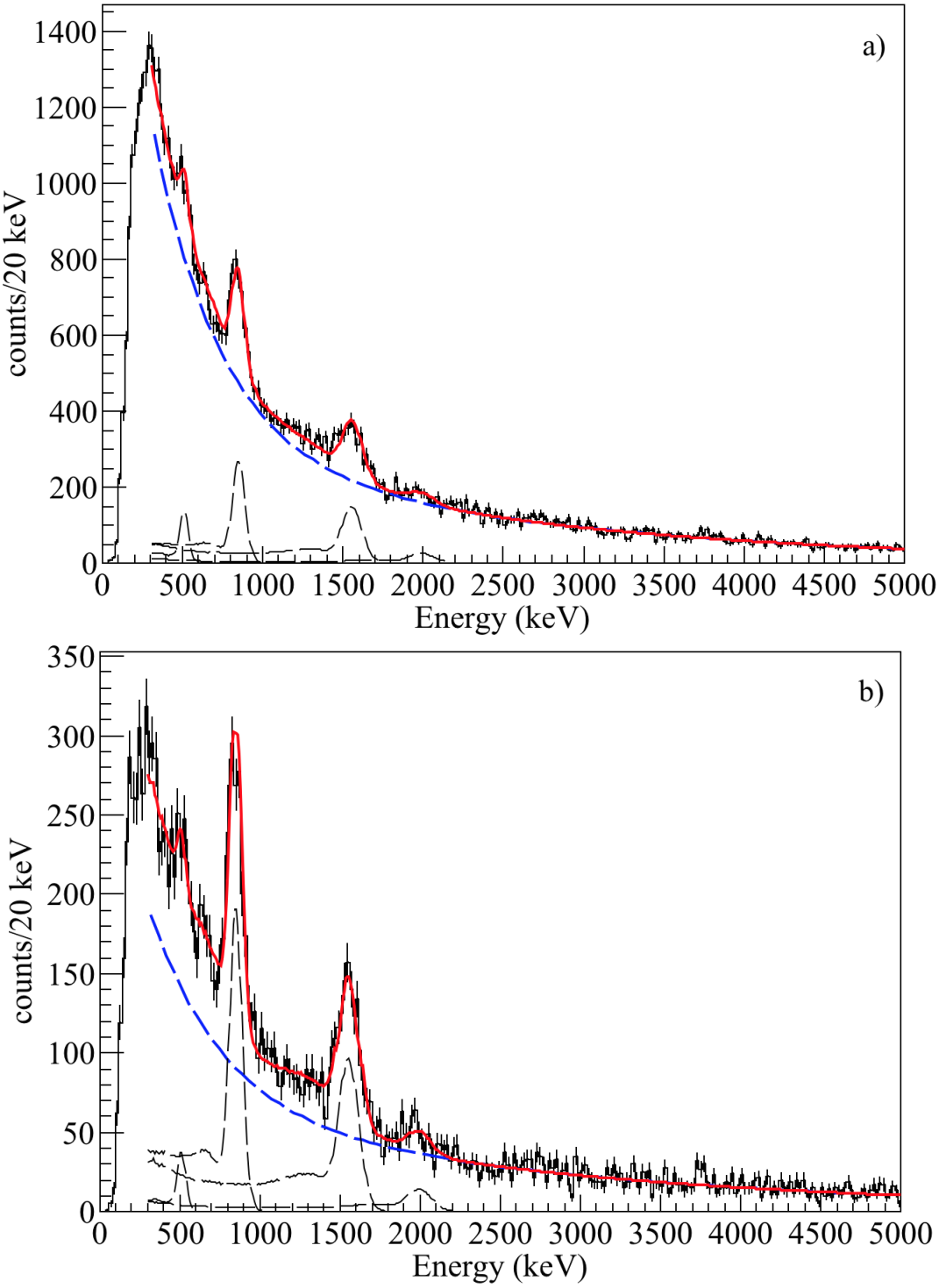

Figure A.9: Doppler-corrected γ-ray energy spectrum for the ^{12}C(^{135}Sb,^{133}Sn+γ)X reaction a) considering all γ-ray multiplicities and b) only events with γ-ray multiplicity M_γ=1. The addback algorithm was applied.

A.10 The ^{12}C(^{133}Sn,^{132}Sn +γ)X reaction

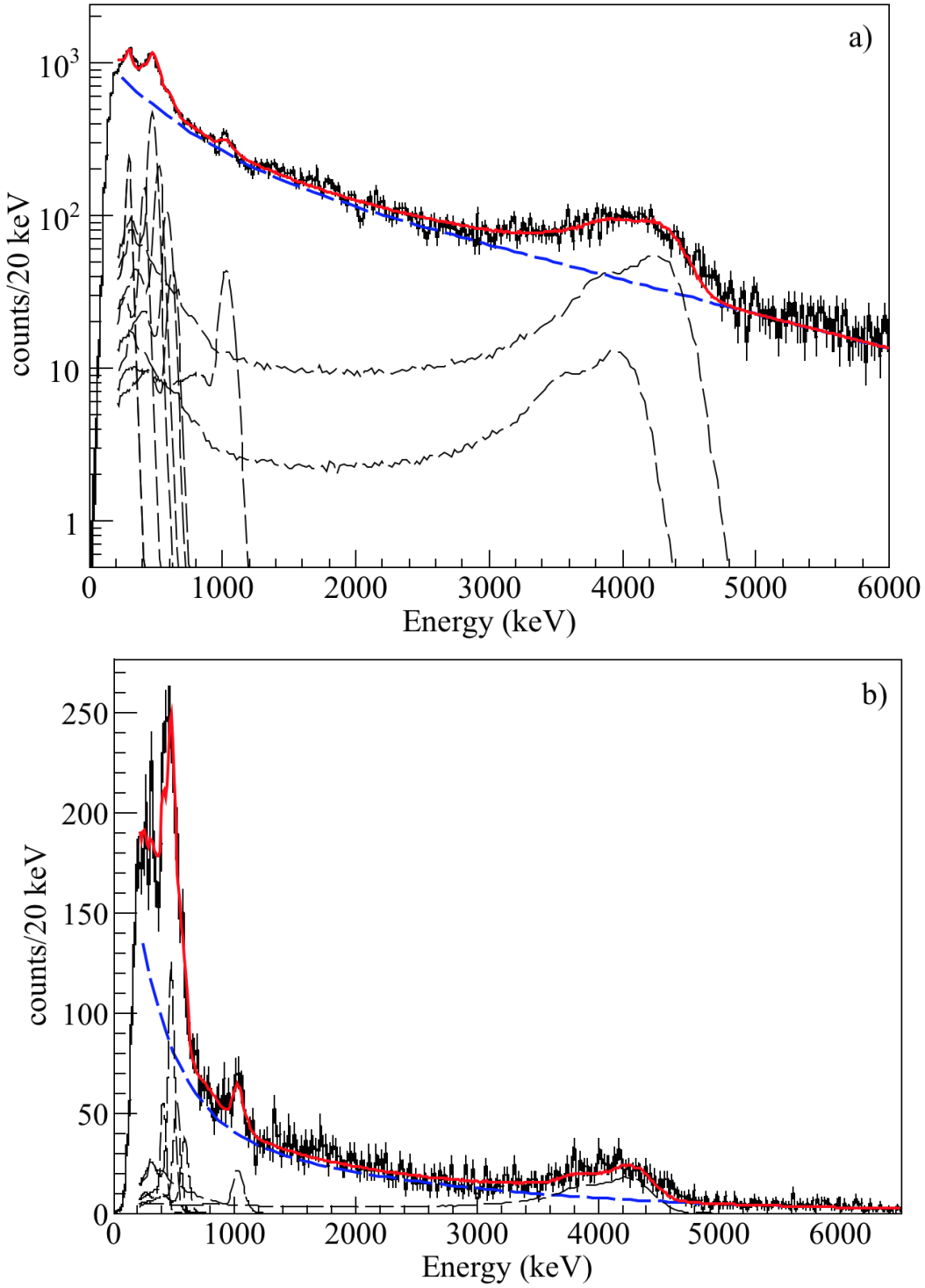

Figure A.10: Doppler-corrected γ-ray energy spectrum for the ^{12}C(^{133}Sn,^{132}Sn+γ)X reaction a) considering all γ-ray multiplicities and b) only events with γ-ray multiplicity M_γ=1. The addback algorithm was applied.

A.11 The ^{12}C(^{135}Sb,^{133}Sb +γ)X reaction

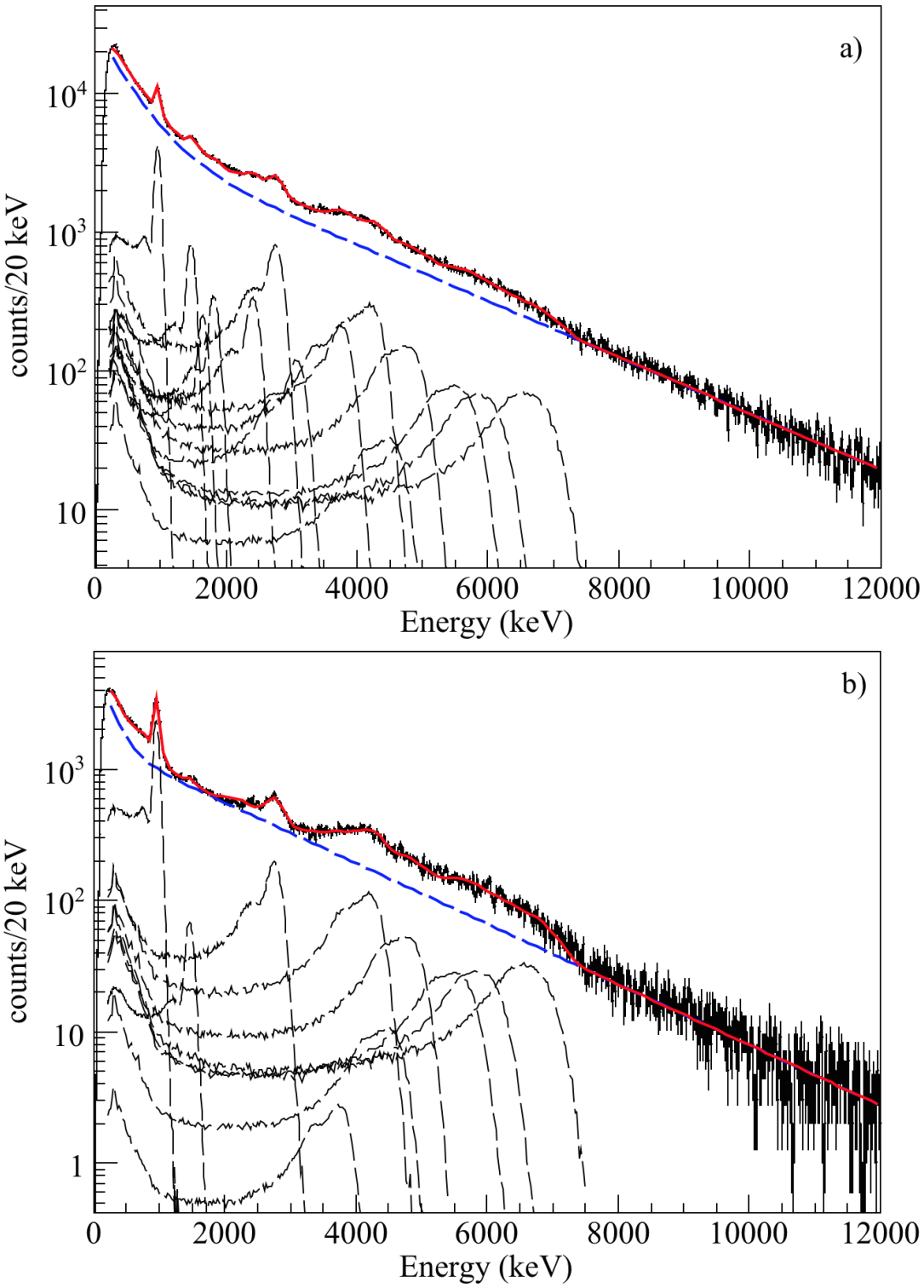

Figure A.11: Doppler-corrected γ-ray energy spectrum for the ^{12}C(^{135}Sb,^{133}Sb+γ)X reaction a) considering all γ-ray multiplicities and b) only events with γ-ray multiplicity M_γ=1. The addback algorithm was applied.

Table A.9: Energies and cross sections for the different γ-ray transitions observed in the Doppler-corrected γ-ray spectrum of ^{133}Sn populated via one-proton one-neutron knockout from ^{135}Sb. The inclusive cross section for this reaction is also included in the table.

$E_{transition}$ (MeV)	σ (mb)	$E_{transition}$ (MeV)	σ (mb)
0.513	0.22(6)	1.561	0.75(16)
0.854^a	0.67(14)	2.002	0.18(5)
σ_{incl} = 16(3) mb			

a: assuming a lifetime of τ = 30 ps

Table A.10: Energies and cross sections for the different γ-ray transitions observed in the Doppler-corrected γ-ray spectrum of ^{132}Sn populated via one-neutron knockout from ^{133}Sn. The inclusive cross section for this reaction is also included in the table.

$E_{transition}$ (MeV)	σ (mb)	$E_{transition}$ (MeV)	σ (mb)
0.300	6.5(12)	0.63	1.9(10)
0.414	4.8(10)	1.035	3.1(9)
0.479	16(2)	4.041	4.9(13)
0.526	7.7(14)	4.352	22(3)
0.591	4.3(12)		
σ_{incl} = 183(21) mb			

Table A.11: Energies and cross sections for the different γ-ray transitions observed in the Doppler-corrected γ-ray spectrum of ^{133}Sb populated via two-neutrons knockout from ^{135}Sb. The inclusive cross section for this reaction is also included in the table.

$E_{transition}$ (MeV)	σ (mb)	$E_{transition}$ (MeV)	σ (mb)
0.962	10.1(12)	2.439	2.5(3)
1.477	3.3(4)	2.791	7.2(8)
1.655	1.2(2)	3.129	1.3(2)
1.829	1.8(3)	3500-7000	$\sum$ 15(2)
σ_{incl} = 176(16) mb			

A.12 The ^{12}C(^{134}Sb,^{133}Sb +γ)X reaction

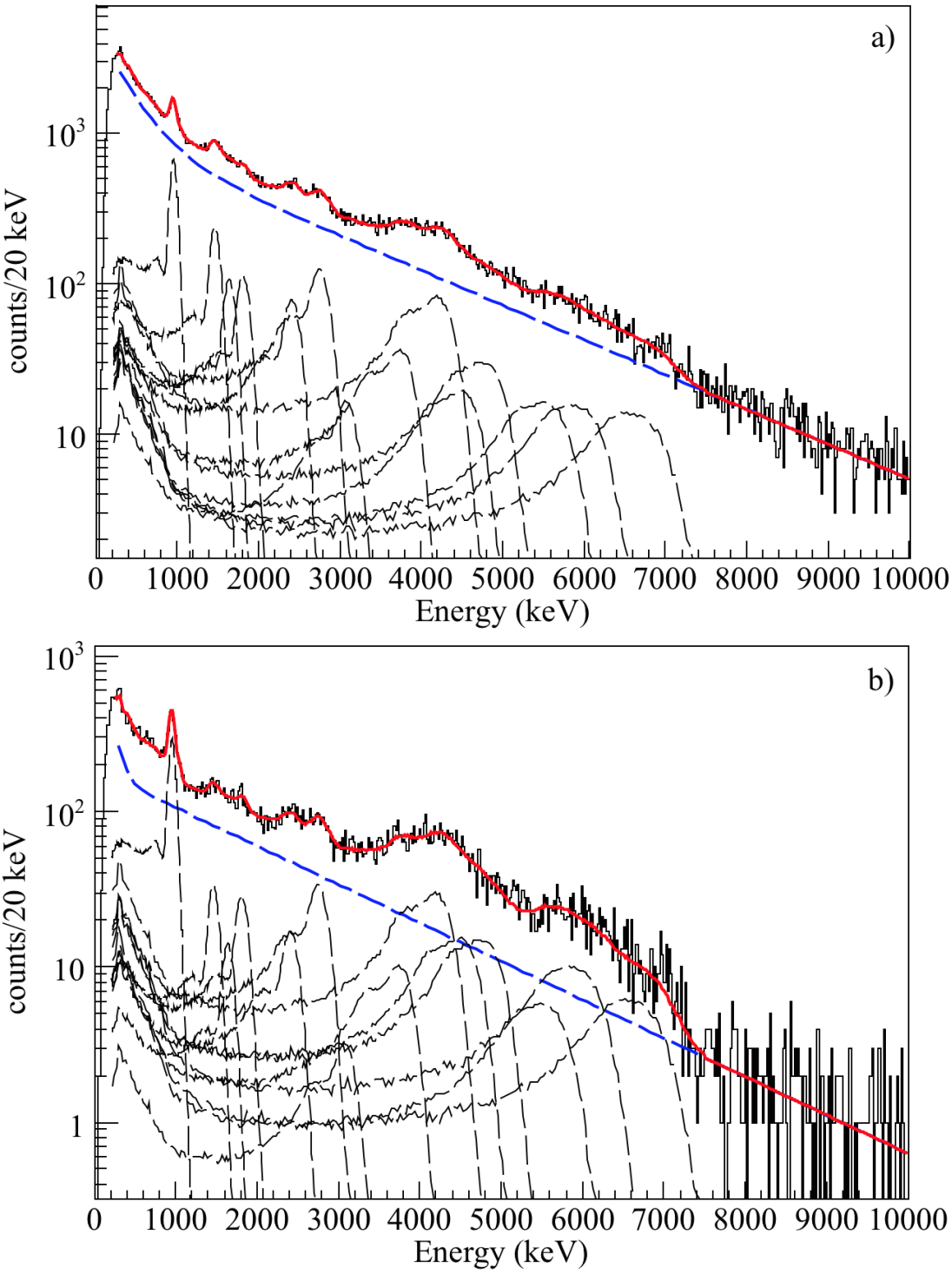

Figure A.12: Doppler-corrected γ-ray energy spectrum for the ^{12}C(^{134}Sb,^{133}Sb+γ)X reaction a) considering all γ-ray multiplicities and b) only events with γ-ray multiplicity M_γ=1. The addback algorithm was applied.

A.13 The ^{12}C(^{135}Sb,^{134}Sb +γ)X reaction

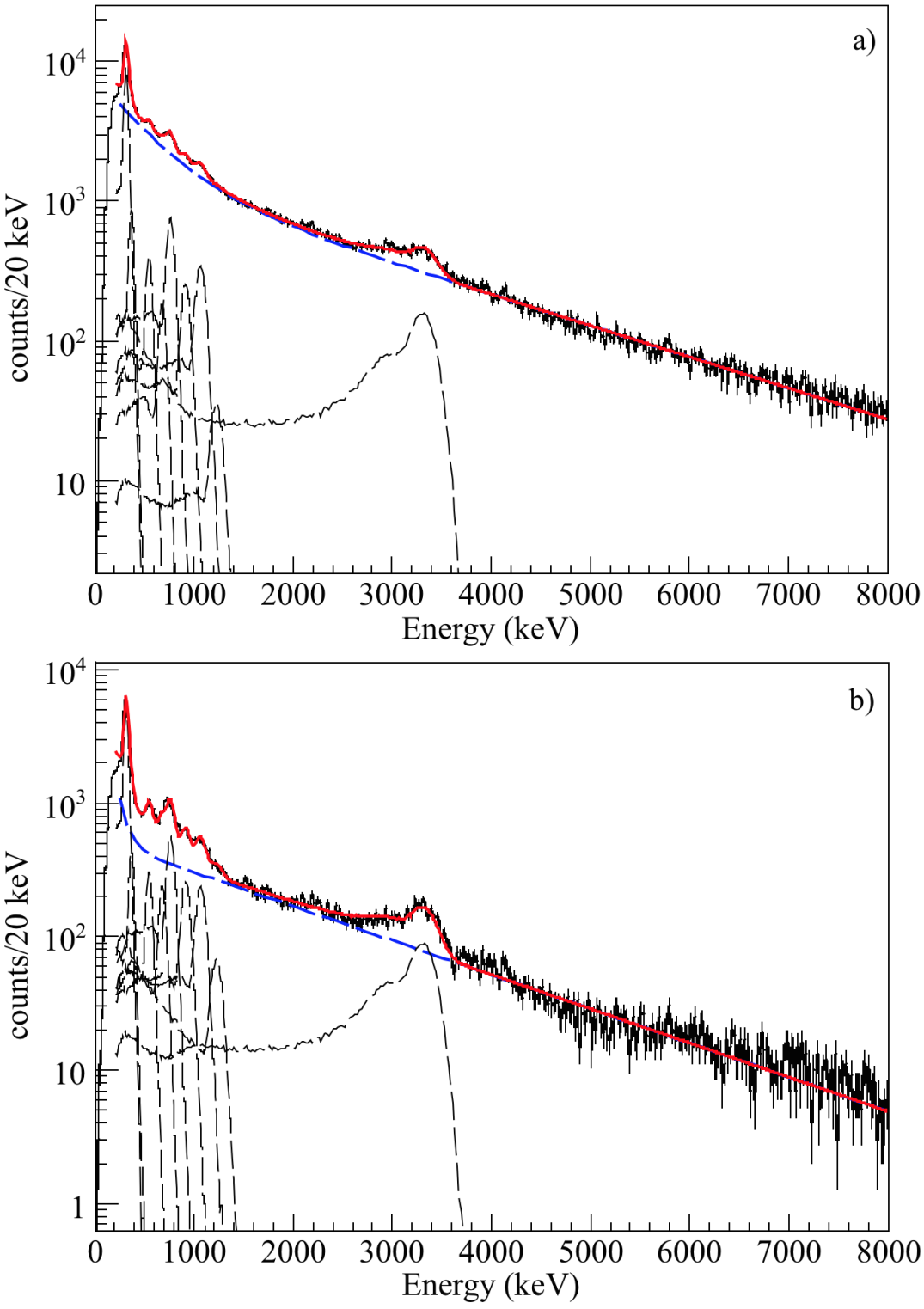

Figure A.13: Doppler-corrected γ-ray energy spectrum for the ^{12}C(^{135}Sb,^{134}Sb+γ)X reaction a) considering all γ-ray multiplicities and b) only events with γ-ray multiplicity M_γ=1. The addback algorithm was applied.

A.14 The ^{12}C(^{135}Sb,^{131}Sn +γ)X reaction

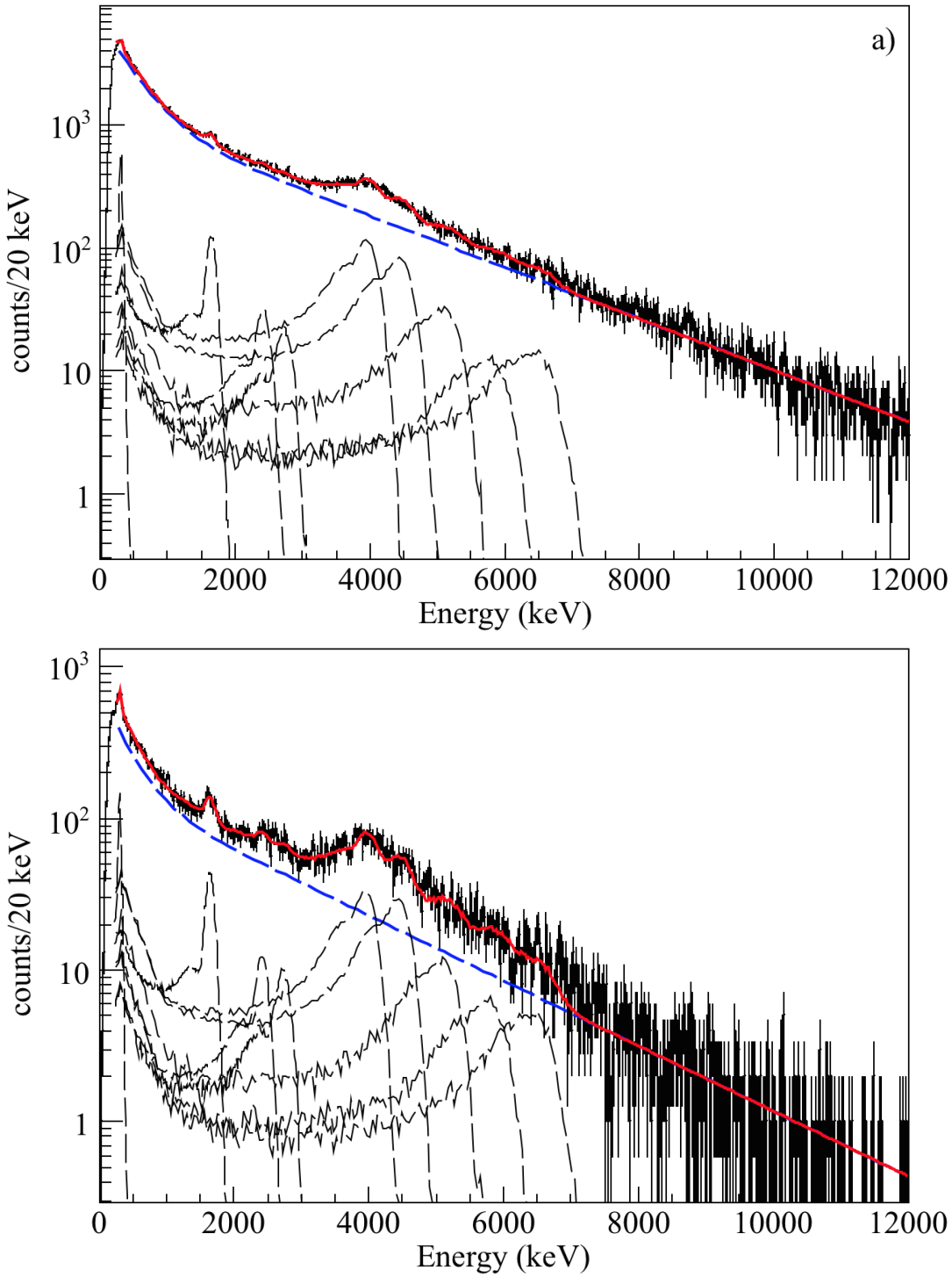

Figure A.14: Doppler-corrected γ-ray energy spectrum for the ^{12}C(^{135}Sb,^{131}Sn+γ)X reaction a) considering all γ-ray multiplicities and b) only events with γ-ray multiplicity M_γ=1. The addback algorithm was applied.

Table A.12: Energies and cross sections for the different γ-ray transitions observed in the Doppler-corrected γ-ray spectrum of ^{133}Sb populated via one-neutron knockout from ^{134}Sb. The inclusive cross section for this reaction is also included in the table.

$E_{transition}$ (MeV)	σ (mb)	$E_{transition}$ (MeV)	σ (mb)
0.962	13.2(18)	2.439	4.9(9)
1.477	7.8(12)	2.791	9.3(14)
1.655	4.1(7)	3.129	1.4(6)
1.829	4.9(8)	3500-7000	$\sum$ 28(3)
σ_{incl} = 169(19) mb			

Table A.13: Energies and cross sections for the different γ-ray transitions observed in the Doppler-corrected γ-ray spectrum of ^{134}Sb populated via one-neutron knockout from ^{135}Sb. The inclusive cross section for this reaction is also included in the table.

$E_{transition}$ (MeV)	σ (mb)	$E_{transition}$ (MeV)	σ (mb)
0.318	10.1(15)	0.922	0.63(12)
0.371	1.0(2)	1.073	1.02(17)
0.551	0.62(11)	1.235	0.13(8)
0.685	0.34(9)	3.340	1.7(3)
0.768	1.6(2)		
σ_{incl} = 61(8) mb			

Table A.14: Energies and cross sections for the different γ-ray transitions observed in the Doppler-corrected γ-ray spectrum of ^{131}Sn populated via one-proton and three-neutrons knock-out from ^{135}Sb. The inclusive cross section for this reaction is also included in the table.

$E_{transition}$ (MeV)	σ (mb)	$E_{transition}$ (MeV)	σ (mb)
0.310	0.73(15)	$\approx$4.500	1.4(3)
1.654	0.63(13)	$\approx$5.200	0.62(12)
2.434	0.26(9)	$\approx$5.900	0.27(7)
2.750	0.21(9)	$\approx$6.600	0.33(7)
$\approx$4.000	1.7(3)		
σ_{incl} = 25(4) mb			

Appendix B

Shell-model study of proton-neutron multiplets in ^{210}Bi, ^{134}Sb and ^{132}In

Nuclei around doubly-closed shells are of great importance for the study of the evolution of nuclear structure. They provide information about two different ingredients used as input, or test of shell models. Nuclei possessing, or lacking only one nucleon (proton/neutron) with respect to doubly-closed shells provide the single-particle (SPE) and single-hole (SHE) energies, respectively, while nuclei with two nucleons outside doubly closed shells give information about the nucleon-nucleon correlations. In odd-odd nuclei, the proton-neutron correlations can be used to obtain the proton-neutron ($\pi\nu$) two-body matrix elements of the effective interaction. As is well known, ^{132}Sn and ^{208}Pb are strong doubly-closed core nuclei located very differently in the nuclear chart. Both regions have similar behavior with respect to individual nucleon and nucleon-nucleon correlations, since every single-particle proton, or neutron state with quantum numbers (n, l, j) in the ^{132}Sn region has its homologous state in the ^{208}Pb region with quantum numbers $(n, l+1, j+1)$. Therefore, in some works [156, 157] both regions have been studied together to obtain information about their similarity of nuclear structure.

In this appendix, we perform a shell-model study of the ^{132}Sn and ^{208}Pb regions using the same type of shell model calculations for both regions. The shell model calculations are compared to the experimental information from literature, in particular for the ^{208}Pb region, for which there is more experimental information available. This comparison was performed with the idea of proposing an experiment in the ^{132}Sn region [158], for which much less experimental information is available. The shell model uses as input the experimental SP/SH energies, while the two-body effective interaction is derived by means of a $\hat{Q}$-box folded-diagrams method from the CD-Bonn NN potential. The shell-model calculations were performed with the ANTOINE shell-model code [132].

Before presenting the shell model calculations for the ^{132}Sn region, we carried out a comparison between the shell model and the experimental results in the ^{208}Pb region. The ^{210}Bi nu-

cleus, with one proton and one neutron outside the doubly-magic ^{208}Pb core, was the selected case. Many experimental spectroscopic information is available for this nucleus [159, 160]. The shell model used considers ^{208}Pb as a closed core, where the valence proton space is formed by $1f_{7/2}$, $2p_{3/2}$, $0h_{9/2}$, $2p_{1/2}$, $1f_{5/2}$ and $0i_{13/2}$ orbitals of the 82-126 space, while let neutrons moving in the $1g_{9/2}$, $0i_{11/2}$, $0j_{15/2}$, $2d_{5/2}$, $3s_{1/2}$, $1g_{7/2}$ and $2d_{3/2}$ levels of the 126-184 space. The single-particle energies are taken from the experimental spectra of ^{209}Bi and ^{209}Pb. The comparison between these shell model calculations and the experimental information of the lowest proton-neutron multiplet in ^{210}Bi, i.e $\pi h_{9/2}\nu g_{9/2}$, was already published [161]. An excellent agreement was observed between the shell model and the experimental values, where the 1p1h excitations are responsible for the ground state being 1^- instead 0^-. Here, the analysis is extended to higher-lying multiplets. For each multiplet, the minimum spin of the band is given by $\left|j^\pi - j^\nu\right|$, where j^π and j^ν are the spin of the proton and neutron, respectively, whereas the maximum spin corresponds to $j^\pi + j^\nu$.

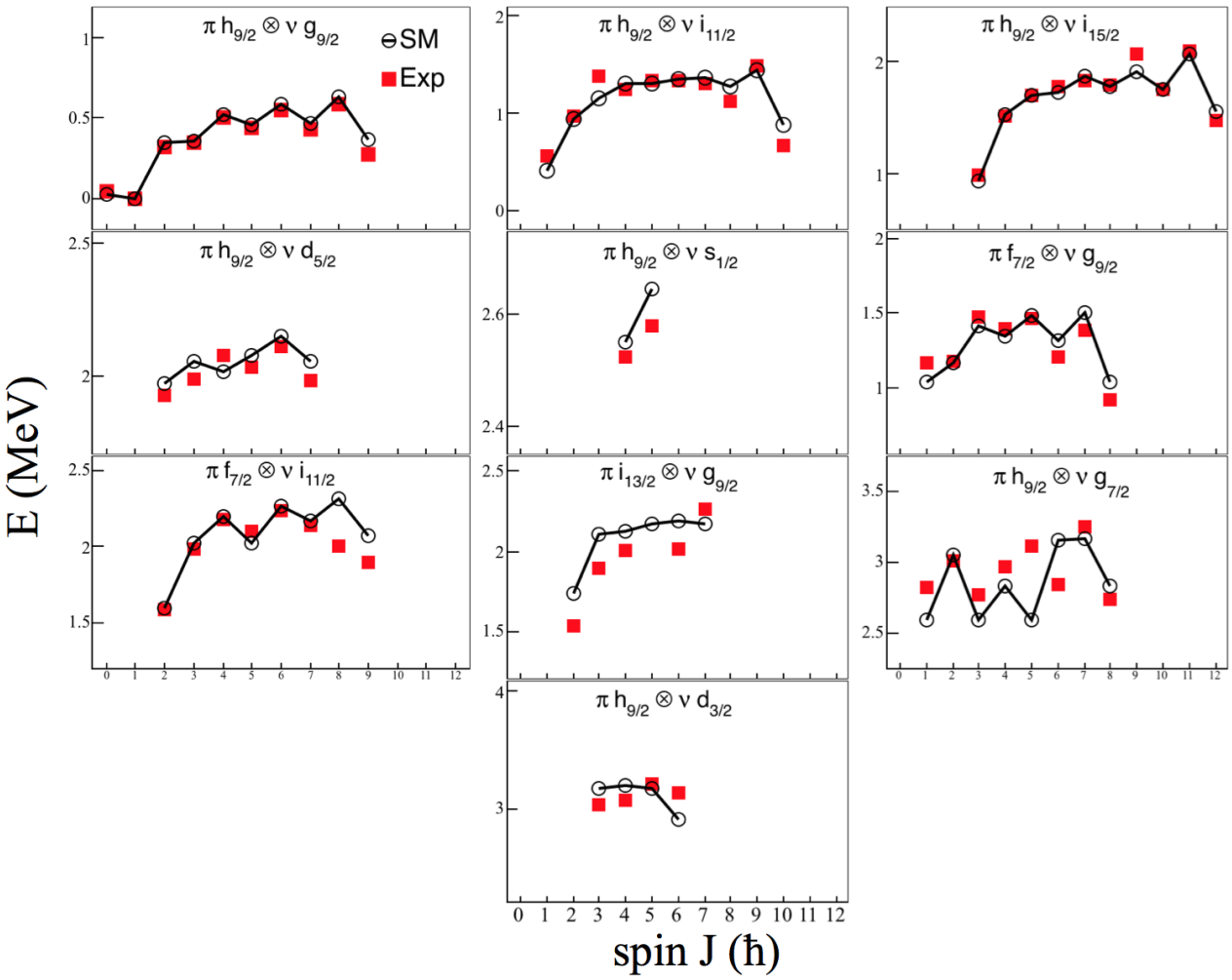

Figure B.1: Experimental excitation energies (red squares) of the proton-neutron multiplets in ^{210}Bi compared to shell model calculations (open circles).

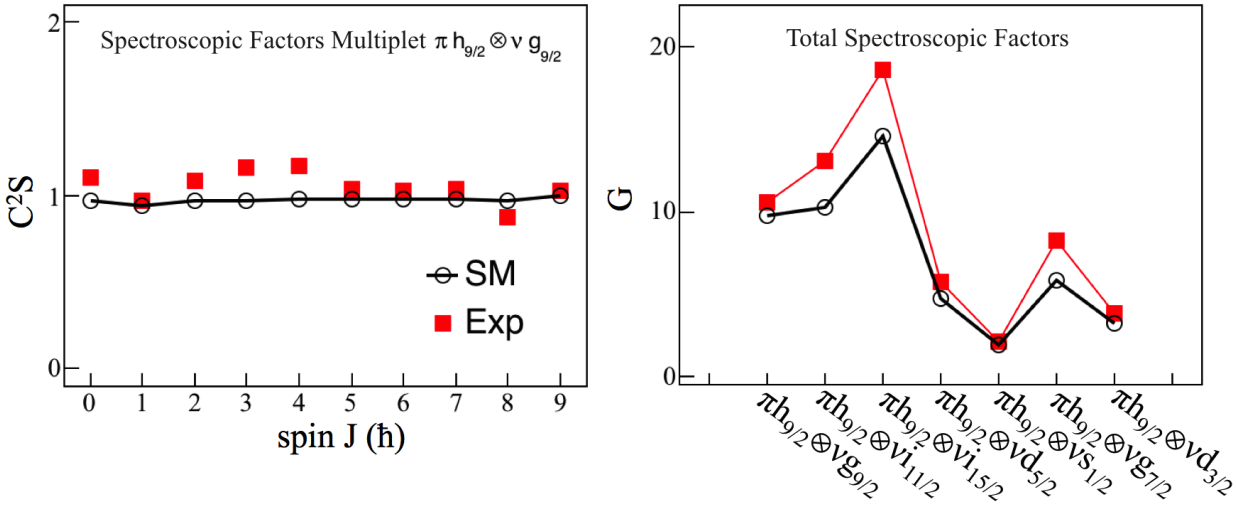

Figure B.2: Left: experimental spectroscopic factors (red squares) for the ten states of the first $\pi h_{9/2} \otimes \nu g_{9/2}$ multiplet populated through the ^{209}Bi(d, p) reaction compared to SM calculations (open circles). Right: total experimental spectroscopic factors of the ^{209}Bi(d, p) reaction for various proton-neutron multiplets in ^{210}Bi (red squares) compared to SM calculations (open circles).

Figure B.1 shows a systematic comparison between the experimental and shell-model (SM) energies for various proton-neutron multiplets in ^{210}Bi. The agreement is quite good, in particular for the lower-lying multiplets, since they are purer proton-neutron multiplets states and the experimental information is clearer. The left of Fig. B.2 shows the spectroscopic factors for the ten states of the first multiplet in ^{210}Bi populated through the ^{209}Bi(d, p) reaction. Again, an excellent agreement is observed. The right of Fig. B.2 shows a comparison between the total experimental spectroscopic factors of various proton-neutron multiplets in ^{210}Bi populated with the same reaction and SM calculations. The summed spectroscopic strength (G) for the different multiplets is given by:

$$G = \frac{1}{2J_i + 1} \sum_{all\ states} (J_f + 1) C^2 S \tag{B.1}$$

where J_i is the spin of the ^{209}Bi ground state (J_i=9/2), J_f is the spin of the excited state in ^{210}Bi and C^2S are the spectroscopic factors. The comparison reveals that this type of shell model is appropriate to describe the experimental information in the quadrant north-east of ^{208}Pb.

The nucleus analogous to ^{210}Bi in the ^{132}Sn region is ^{134}Sb, which has one proton and one neutron outside the doubly-magic ^{132}Sn core. In this case, the shell model space consists in the five orbitals $0g_{7_2}$, $1d_{5/2}$, $1d_{3/2}$, $2s_{1/2}$ and $0h_{11/2}$ of the 50-82 space for the valence protons and the six levels $1f_{7/2}$, $2p_{3/2}$, $0h_{9/2}$, $2p_{1/2}$, $1f_{5/2}$ and $0i_{13/2}$ of the 82-126 space for the valence neutrons. The proton and neutron SP energies are taken from the experimental spectra of ^{133}Sb and ^{133}Sn, respectively, except the $2s_{1/2}$ and $0i_{13/2}$ proton and neutron SP energies,

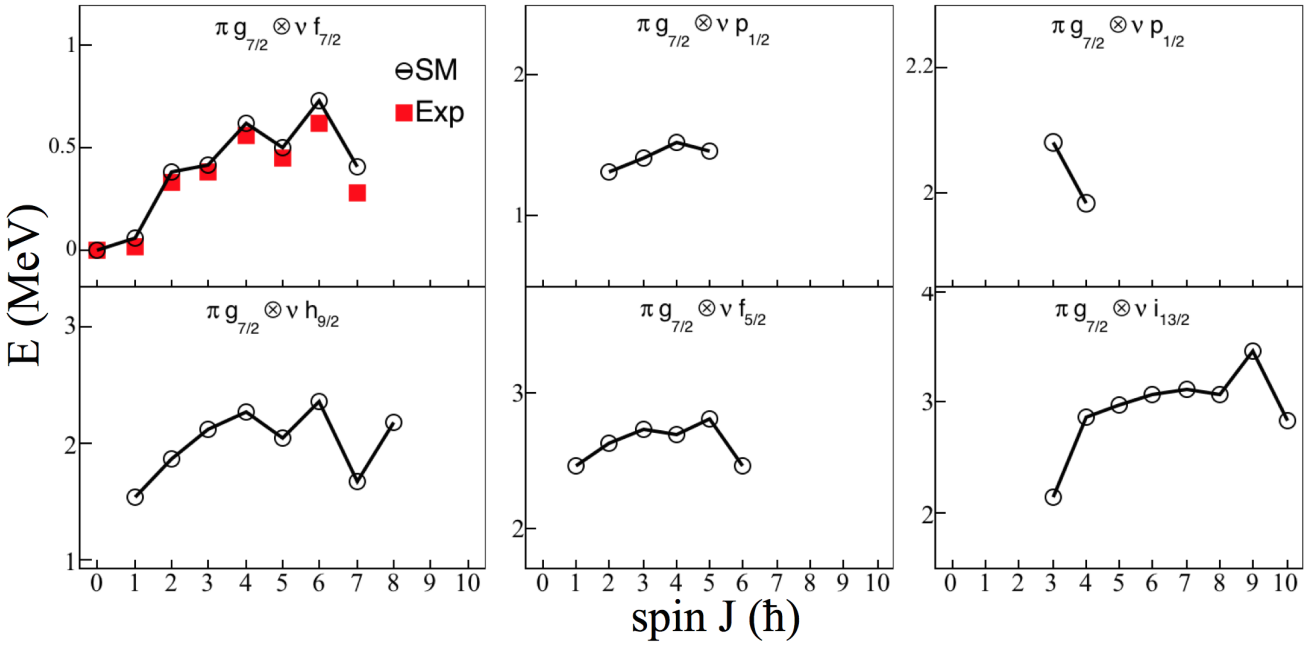

Figure B.3: Experimental excitation energies (red squares) of the proton-neutron multiplets in ^{134}Sb compared to shell model calculations (open circles). The experimental energies are only available for the first multiplet, $\pi g_{7/2} \otimes \nu f_{7/2}$.

which are still missing. Figure B.3 shows a systematic comparison between the experimental and SM energies for various proton-neutron multiplets in ^{134}Sb. The experimental energies are only available for the first multiplets and the comparison between the experimental values and the SM calculations was already published in Ref. [162]. The agreement between the experimental and SM values seems to be slightly worse than in ^{210}Bi. For this reason, it is necessary to extend the experimental information for higher-lying multiplets. In Fig. B.3 are displayed the SM energies for the multiplets of ^{134}Sb in which the proton is always in the $0g_{7/2}$ orbital coupled to any of the six neutron orbitals of the N=82-126 major shell. These multiplets can be populated through the ^{133}Sb(d,p) reaction, since the $\pi 0g_{7/2}$ orbital is the ground state of ^{133}Sb, and the neutron can be transferred to any of the neutron orbitals of the N=82-126 major shell. The cross sections for the population of the different multiplets can be derived from DWBA calculations using global optical potentials [158], while the spectroscopic factors, C^2S, and the pattern decay of the excited states can be derived from SM calculations.

The same type of SM calculations were performed for the one proton-hole and one-neutron particle nucleus in the ^{132}Sn region, i.e ^{132}In. In this case, the proton-hole valence space is formed by the $0f_{5/2}$, $1p_{3/2}$, $1p_{1/2}$ and $0g_{9/2}$ orbitals, while the same neutron valence space as the used for ^{134}Sb is considered. The proton SH energies are taken from the experimental spectrum of ^{131}In, except the $\pi 0f^{-}_{5/2}$ orbital, whose energy is still not known. Figure B.4 shows a systematic comparison between the experimental and SM energies for various proton-neutron

multiplets in ^{132}In. The experimental values are only available for the first multiplet and the comparison between the experimental and the SM results was already published in Ref. [19]. Again, the agreement seems to be slightly worse than in ^{210}Bi, although it must be mentioned that the experimental energies of the first multiplet, obtained in Ref. [19], were derived assuming that one of the lowest transitions within the multiplet was unobserved and adopting an energy of 25$\pm$ 25 keV for this transition. Therefore, the experimental energies are subject to more uncertainty. The rest of multiplets shown in Fig. B.4 can be populated through the ^{131}In(d,p) reaction, since the $\pi 0 g_{9/2}^{-1}$ orbital is the ground state of ^{131}In, and the neutron can be transferred to any of the neutron orbitals of the N=82-126 major shell.

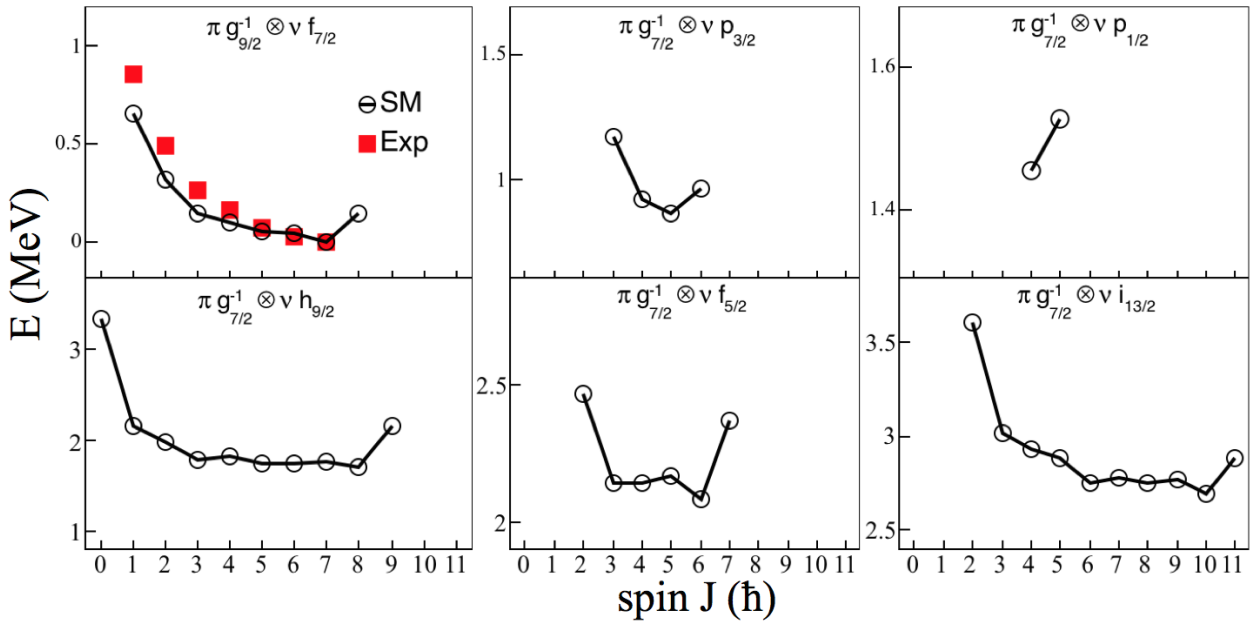

Figure B.4: Experimental excitation energies (red squares) of the proton-hole and neutron-particle multiplets in ^{132}In compared to shell model calculations (open circles). The experimental energies are only available for the first multiplet, $\pi g_{9/2}^{-1} \otimes \nu f_{7/2}$.

Appendix C

Publications

-**"Gamma Decay of Unbound Neutron-Hole States in ^{133}Sn"**, V. Vaquero, A. Jungclaus, P. Doornenbal, K. Wimmer, A. Gargano, J. A. Tostevin, S. Chen, E. Nácher, E. Sahin, Y. Shiga, D. Steppenbeck, R. Taniuchi, Z. Y. Xu, T. Ando, H. Baba, F. L. Bello Garrote, S. Franchoo, K. Hadynska-Klek, A. Kusoglu, J. Liu, T. Lokotko, S. Momiyama, T. Motobayashi, S. Nagamine, N. Nakatsuka, M. Niikura, R. Orlandi, T. Saito, H. Sakurai, P. A. Söderström, G. M. Tveten, Zs. Vajta, and M. Yalcinkaya, *Physical Review Letters* **118**, 202502 (2017).

-**"In-beam γ-ray spectroscopy of ^{136}Te at relativistic energies"**, V. Vaquero, A. Jungclaus, P. Doornenbal, K. Wimmer, A.M. Moro, K. Ogata, T. Furumoto, S. Chen, E. Nácher, E. Sahin, Y. Shiga, D. Steppenbeck, R. Taniuchi, Z. Y. Xu, T. Ando, H. Baba, F. L. Bello Garrote, S. Franchoo, K. Hadynska-Klek, A. Kusoglu, J. Liu, T. Lokotko, S. Momiyama, T. Motobayashi, S. Nagamine, N. Nakatsuka, M. Niikura, R. Orlandi, T. Saito, H. Sakurai, P. A. Söderström, G. M. Tveten, Zs. Vajta, and M. Yalcinkaya, submitted to *Physical Review C* on September 18, 2018.

-**"Inclusive cross sections for one- and multi-nucleon removal from Sn, Sb, and Te projectiles beyond the N=82 shell closure"**, V. Vaquero, A. Jungclaus, J.L. Rodríguez-Sánchez, J.A. Tostevin, P. Doornenbal, K. Wimmer, S. Chen, E. Nácher, E. Sahin, Y. Shiga, D. Steppenbeck, R. Taniuchi, Z. Y. Xu, T. Ando, H. Baba, F. L. Bello Garrote, S. Franchoo, K. Hadynska-Klek, A. Kusoglu, J. Liu, T. Lokotko, S. Momiyama, T. Motobayashi, S. Nagamine, N. Nakatsuka, M. Niikura, R. Orlandi, T. Saito, H. Sakurai, P. A. Söderström, G. M. Tveten, Zs. Vajta, and M. Yalcinkaya, to be submitted to *Physics Letters B* in October 2018.

Gamma Decay of Unbound Neutron-Hole States in ^{133}Sn

V. Vaquero,[1] A. Jungclaus,[1,*] P. Doornenbal,[2] K. Wimmer,[3] A. Gargano,[4] J. A. Tostevin,[5] S. Chen,[2,6] E. Nácher,[1] E. Sahin,[7] Y. Shiga,[8] D. Steppenbeck,[2] R. Taniuchi,[2,3] Z. Y. Xu,[9] T. Ando,[3] H. Baba,[2] F. L. Bello Garrote,[7] S. Franchoo,[10] K. Hadynska-Klek,[7] A. Kusoglu,[11,12] J. Liu,[9] T. Lokotko,[9] S. Momiyama,[3] T. Motobayashi,[2] S. Nagamine,[3] N. Nakatsuka,[13] M. Niikura,[3] R. Orlandi,[14] T. Saito,[3] H. Sakurai,[2,3] P. A. Söderström,[2] G. M. Tveten,[7] Zs. Vajta,[15] and M. Yalcinkaya[11]

[1]*Instituto de Estructura de la Materia, CSIC, E-28006 Madrid, Spain*
[2]*RIKEN Nishina Center, 2-1 Hirosawa, Wako, Saitama 351-0198, Japan*
[3]*Department of Physics, University of Tokyo, 7-3-1 Hongo, Bunkyo, Tokyo 113-0033, Japan*
[4]*Istituto Nazionale di Fisica Nucleare, Complesso Universitario di Monte S. Angelo, I-80126 Napoli, Italy*
[5]*Department of Physics, University of Surrey, Guildford, Surrey GU2 7XH, United Kingdom*
[6]*School of Physics and State Key Laboratory of Nuclear Physics and Technology, Peking University, Bejing 100871, People's Republic of China*
[7]*Department of Physics, University of Oslo, NO-0316 Oslo, Norway*
[8]*Department of Physics, Rikkyo University, Tokyo, Japan*
[9]*Department of Physics, The University of Hong Kong, Pokfulam, Hong Kong*
[10]*Institut de Physique Nucléaire Orsay, IN2P3-CNRS, 91406 Orsay Cedex, France*
[11]*Department of Physics, Faculty of Science, Istanbul University, Vezneciler/Fatih, 34134 Istanbul, Turkey*
[12]*ELI-NP, Horia Hulubei National Institute of Physics and Nuclear Engineering, 077125 Magurele, Romania*
[13]*Department of Physics, Faculty of Science, Kyoto University, Kyoto 606-8502, Japan*
[14]*Advanced Science Research Center, Japan Atomic Energy Agency, Tokai, Ibaraki 319-1195, Japan*
[15]*MTA Atomki, P.O. Box 51, Debrecen H-4001, Hungary*

(Received 28 February 2017; published 17 May 2017)

Excited states in the nucleus ^{133}Sn, with one neutron outside the double magic ^{132}Sn core, were populated following one-neutron knockout from a ^{134}Sn beam on a carbon target at relativistic energies at the Radioactive Isotope Beam Factory at RIKEN. Besides the γ rays emitted in the decay of the known neutron single-particle states in ^{133}Sn additional γ strength in the energy range 3.5–5.5 MeV was observed for the first time. Since the neutron-separation energy of ^{133}Sn is low, $S_n = 2.402(4)$ MeV, this observation provides direct evidence for the radiative decay of neutron-unbound states in this nucleus. The ability of electromagnetic decay to compete successfully with neutron emission at energies as high as 3 MeV above threshold is attributed to a mismatch between the wave functions of the initial and final states in the latter case. These findings suggest that in the region southeast of ^{132}Sn nuclear structure effects may play a significant role in the neutron versus γ competition in the decay of unbound states. As a consequence, the common neglect of such effects in the evaluation of the neutron-emission probabilities in calculations of global β-decay properties for astrophysical simulations may have to be reconsidered.

DOI: 10.1103/PhysRevLett.118.202502

The atomic nucleus offers a unique opportunity to study the competition between three of the four fundamental forces known to exist in nature, namely, the strong nuclear, the electromagnetic, and the weak nuclear interaction. In general, the decay of an excited nuclear state follows the hierarchy of these forces. The emission of one or more particles mediated by the strong interaction dominates the decay of unbound states while bound excited states usually decay by electromagnetic radiation until the ground state is reached. Finally, the latter decays via β decay mediated by the weak nuclear interaction. The different strengths of these interactions are reflected by the time scales of the above mentioned processes, ranging from typically 10^{-22} s for fast particle decays to 10^{7} s for slow β decays and 10^{30} s for double β decays. Of course there are exceptions to this general rule. There are many cases known in which β decay wins against electromagnetic decay because the latter requires the emission of a γ ray of high multipolarity and/or low energy. In the case of the strong force the Coulomb barrier can defer the emission of charged particles and allow electromagnetic decay to compete above the separation energy. In the case of neutron emission on the neutron-rich side of the nuclear chart, in the absence of a Coulomb barrier, only the angular momentum barrier may hinder the neutron emission and thus favor γ decay. Indeed γ-decaying high-spin states above the neutron-separation energy have been identified in several neutron-rich nuclei. In general, however, it is assumed that neutron decay dominates for all low- to moderate-spin states above the neutron threshold. This assumption is commonly used in theoretical calculations of global β-decay properties that are employed for astrophysical calculations, for example, for

the description of the rapid neutron-capture process (r process) of nuclear synthesis.

However, according to Fermi's golden rule the probability of a certain decay process occuring does not only depend on the strength of the interaction and the density of final states, but also on the overlap between the wave functions of the parent and daughter states [1]. By means of this latter ingredient, nuclear structure effects can influence decay rates and thus have an impact, for example, on the competition between neutron emission and γ deexcitation above the neutron-separation energy in neutron-rich nuclei. In recent years several cases have been reported in which electromagnetic decay successfully competes with neutron emission in the decay of unbound states with excitation energies up to more than 2 MeV above the neutron-separation energy [2–5], i.e., well beyond the first few hundred keV where neutron emission is hindered by the low penetrability. In some of these works nuclear structure arguments based on theoretical calculations have been put forward to explain the experimental findings. On the neutron-deficient side of the nuclear chart, the γ decay of isobaric analog states far above the proton-separation energy has been observed in fp shell nuclei and explained by the fact that proton emission is isospin forbidden in these cases [6,7].

In this Letter we investigate the nuclear structure aspect in the decay of unbound states by means of a very simple nuclear system, namely, the nucleus ^{133}Sn. This nucleus has only one valence neutron in the $N = 82$–126 major shell outside ^{132}Sn, which is generally considered as a very robust double magic core. Neutron single-particle energies (SPE) of 854, 1367, 1561, and 2002 keV for the $2p_{3/2}$, $2p_{1/2}$, $0h_{9/2}$, and $1f_{5/2}$ orbitals, respectively, relative to the $1f_{7/2}$ orbital, have been established combining the information from both β decay and (d, p) neutron-transfer experiments [8–11]. For the $0i_{13/2}$ SPE an energy range of 2360–2600 keV has recently been proposed based on the systematics of $13/2^+$ levels in $N = 83$ nuclei in comparison with shell-model calculations [12]. The neutron single-hole states in ^{133}Sn are expected at excitation energies far above S_n. In Ref. [8], a line at 1.26 MeV in the neutron spectrum measured following the β decay of ^{134}In has tentatively been assigned to the decay of the $0h_{11/2}^{-1}$ hole state in ^{133}Sn, positioning this state at an excitation energy of around 3.66 MeV [$S_n = 2.402(4)$ MeV [13]]. The present work reports on the study of the γ decay of excited states in ^{133}Sn populated via one-neutron knockout from ^{134}Sn at relativistic energies.

The experiment was performed at the Radioactive Isotope Beam Factory at RIKEN. Secondary radioactive beams were produced via projectile fission of a 345 MeV/u ^{238}U beam with an average intensity of 15 pnA, impinging on a 4-mm thick Be target. The ions of interest were separated from other reaction products and identified on an ion-by-ion basis by the BigRIPS in-flight separator [14]. The particle identification was performed using the ΔE-TOF-$B\rho$ method in which the energy loss (ΔE), time of flight (TOF) and magnetic rigidity ($B\rho$) are measured and used to determine the atomic number Z and the mass-to-charge ratio A/q of the fragments [15]. The identified ^{134}Sn ions then impinged with a kinetic energy of 165 MeV/u on a 3-mm thick C target. Reaction products created via nucleon removal were identified in the ZeroDegree (ZD) spectrometer [14], employing again the ΔE-TOF-$B\rho$ method. Total reaction cross sections for the removal of x neutrons, σ_{xn}, were determined from the yield of the respective reaction products and the number of incoming projectile ions taking into account the transmission through the ZD spectrometer, losses due to reactions with detector material along the beam line, and the properties of the C target. To detect γ radiation emitted from excited reaction residues the secondary target was surrounded by the DALI2 spectrometer [16]. DALI2 consisted of 186 NaI(Tl) detectors, covering polar angles in the range from 20° to 150°, and had a photo peak efficiency of 15% for the 1.33-MeV γ ray emitted by the stationary ^{60}Co source.

Figure 1 shows the Doppler-corrected γ-ray spectrum measured in coincidence with ^{134}Sn ions detected in BigRIPS and ^{133}Sn nuclei detected in the ZD spectrometer. The three lines at energies of 854, 1561, and 2002 keV correspond to the decays of the $2p_{3/2}$, $0h_{9/2}$, and $1f_{5/2}$ single-particle states to the $1f_{7/2}$ ground state while the 513-keV γ ray depopulates the $2p_{1/2}$ state at 1367 keV to the $2p_{3/2}$ level at 854 keV [11]. Besides these known γ rays, clearly additional γ strength is observed above the

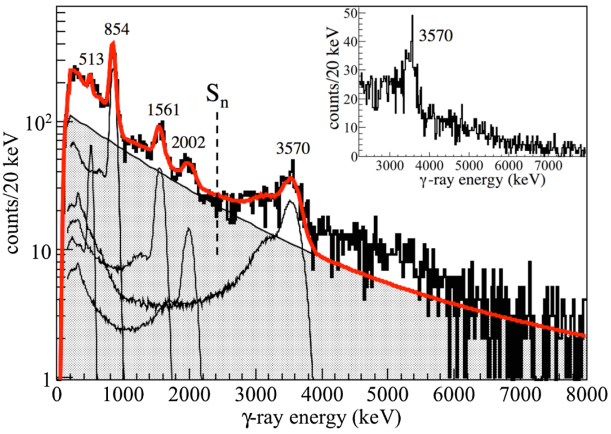

FIG. 1. Doppler-corrected γ-ray spectrum (for γ-ray multiplicity $M_\gamma = 1$ after add back) of ^{133}Sn populated via one-neutron knockout from ^{134}Sn. The response function fit to the experimental spectrum is shown by the thick red line while the individual components are shown as thin black lines. The background is indicated as the gray area. The inset shows the high-energy region of the spectrum on a linear scale.

neutron separation energy, reaching up to about 5.5 MeV. To describe the experimental spectrum the response of the DALI2 array to the incident γ radiation was simulated using GEANT4 [17]. In these simulations the precise γ-ray energies determined in Ref. [11] were employed. To increase the detection efficiency for high-energy γ rays and to improve the peak-to-total ratio over the full energy range an add-back algorithm was applied. All energy depositions registered in NaI crystals within a range of 15 cm from the center of the crystal with the highest energy signal were summed. Doppler correction was performed using the midtarget velocity of $\beta = 0.497$. The background in the spectrum shown in Fig. 1 has been parametrized by the sum of two exponential functions cut off at low energy with an error function. Up to the neutron separation energy the experimental spectrum is well described by the sum of the background and the DALI2 response to the listed γ rays. For the 854-keV line, however, a small shift with respect to the nominal energy was observed when only the most forward crystals of DALI2 were considered as shown in Fig. 2(a). This shift points to a lifetime of a few tens of ps for the 854-keV state because in that case the γ ray emission takes place at a lower average recoil velocity than assumed in the simulation. Comparing the experimental line shapes obtained for two different angular ranges of DALI2 detectors to simulations, a value of $\tau = 30(15)$ ps was deduced for the state at an excitation energy of 854 keV (see Fig. 2). From this lifetime a transition strength of $B(E2) = 1.6(8)$ W.u. is calculated for the $2p_{3/2} \rightarrow 1f_{7/2}$ $E2$ transition in ^{133}Sn. This strength is comparable to that of the $2d_{5/2} \rightarrow 1g_{9/2}$ and $3s_{1/2} \rightarrow 2d_{5/2}$ neutron single-particle transitions in ^{209}Pb [$B(E2) = 2.5(7)$ and $B(E2) = 2.13(8)$ W.u., respectively, [18]]. Coming back to the spectrum shown in Fig. 1, the strongest peak above S_n is well described by the DALI2 response to a single γ ray with an energy of 3570(50) keV. With respect to the γ strength at even higher energy, unfortunately the limited statistics and poor energy resolution prohibit a more detailed analysis.

To interpret the γ-ray spectrum of ^{133}Sn, the reaction process that led to the population of excited states in this

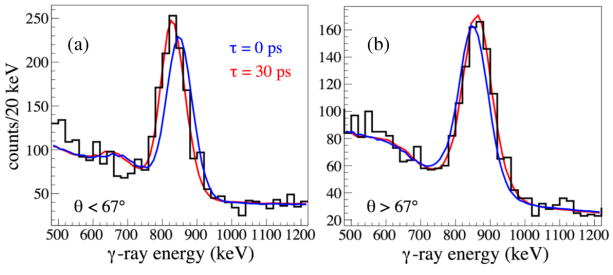

FIG. 2. Comparison between the experimental shape of the 854-keV line observed in the DALI2 detectors at polar angles (a) $< 67°$ and (b) $> 67°$ and simulations assuming lifetimes of $\tau = 0$ (blue) and $\tau = 30$ ps (red) for the 854-keV state.

nucleus has to be considered. In principle, the neutron removal can proceed from any neutron orbital that is occupied in the ground state of the projectile nucleus, in this case ^{134}Sn. Considering the single-particle energies in ^{133}Sn it is expected that the valence-neutron pair in ^{134}Sn occupies dominantly the $1f_{7/2}$ orbital. A knockout from this orbital results in the ground state of ^{133}Sn and, consequently, no γ ray is emitted in this case. However, also the other neutron orbitals of the $N = 82$–126 shell contribute to the composition of the wave function; i.e., there is a certain probability for the neutron pair to occupy the $2p_{3/2}$, $2p_{1/2}$, $0h_{9/2}$, $1f_{5/2}$, and $0i_{13/2}$ orbitals. Shell-model calculations using realistic effective interactions [19] predict an 80% probability for the valence-neutron pair to occupy the $1f_{7/2}$ orbital and contributions between 1.6% and 5.2% for all other orbitals of the $N = 82$–126 shell. One-neutron knockout from the $2p_{3/2}$, $2p_{1/2}$, $0h_{9/2}$, and $1f_{5/2}$ orbitals will populate the known bound single-particle states in ^{133}Sn, which decay via γ-ray emission to the ground state. Consequently, the 513-, 854-, 1561-, and 2002-keV transitions are all clearly visible in the spectrum shown in Fig. 1. With respect to the yet unknown position of the $0i_{13/2}$ orbital we note that in the present experiment no γ ray is observed in the expected energy range ($E_x = 2360$–2600 keV [12]).

Besides the removal of one of the two valence neutrons also the knockout of a neutron from the closed $N = 82$ core can occur. In this case neutron-hole states in ^{133}Sn are populated as illustrated in Fig. 3(a). Although knockout can proceed from all five orbitals of the $N = 50$–82 shell, the largest cross section is expected for the $0h_{11/2}$ orbital since it is close to the Fermi level and occupied by as many as twelve neutrons. We therefore suggest that the 3570(50)-keV transition corresponds to the decay of a $11/2^-$ state to

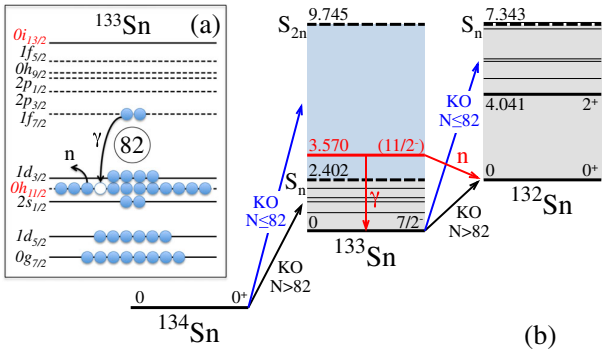

FIG. 3. (a) Schematic of the neutron orbital occupancies after the knockout of a $0h_{11/2}$ neutron from the ^{134}Sn projectile, followed by γ decay or neutron emission; (b) Illustration of the population of bound (gray regions) and unbound (blue region) excited states in ^{132,133}Sn following one-neutron knockout (KO) from either the valence space ($N > 82$) or the $N = 50$–82 core ($N \leq 82$). Energies are quoted in MeV.

the ground state. Note that this energy is close to the 3.66 MeV proposed in Ref. [8]. Since this excited state lies above the neutron-separation energy, it can decay either via neutron emission or electromagnetic decay; see Fig. 3(b). Because of the high excitation energy of the first excited state in ^{132}Sn, $E_x(2^+) = 4.041$ MeV, the presumed $11/2^-$ state at 3570(50) keV can only neutron decay to the ground state of ^{132}Sn, i.e., via the emission of an $\ell = 5$ neutron with a kinetic energy of about 1.2 MeV ($E_n = E_x - S_n$). The expected lifetime for this decay amounts to less than 10^{-17} s. To estimate the lifetime for an $E2$ γ decay to the $7/2^-$ ground state, we assume a transition strength of 2 W.u. in line with the experimental strength of several single-particle $E2$ transitions in ^{133}Sn and ^{209}Pb as discussed above. This estimate yields a lifetime of about 10^{-14} s. Therefore, at the level of pure single-particle transitions, the neutron decay is expected to be roughly 3 orders of magnitude faster as compared to γ-ray emission.

As mentioned above, an additional factor, which can affect the competition between neutron and γ-ray emission, is the overlap of the wave functions of the initial and final states. After the knockout of a core neutron, e.g., a $0h_{11/2}$ neutron, from the projectile ^{134}Sn, ^{133}Sn is populated with a neutron configuration as shown in Fig. 3(a). In the case of γ decay, the hole in the $N = 50$–82 core is filled by one of the two neutrons occupying primarily the $1f_{7/2}$ orbital in the ground state of ^{134}Sn and a 3570-keV γ ray is emitted. The final state corresponds to the ground state of ^{133}Sn. Neutron emission, on the other hand, yields a ^{132}Sn nucleus with two holes in the $0h_{11/2}$ orbital and two neutrons above the $N = 82$ gap, i.e., in a two-particle–two-hole ($2p$-$2h$) state. The ground state of ^{132}Sn, however, is not expected to contain large contributions of $2p$-$2h$ configurations and, consequently, the overlap of the wave function of the parent state with that of the daughter state plus a neutron is small. It is this wave function mismatch which hinders neutron emission and allows electromagnetic decay to compete in the decay of highly excited neutron-hole states in ^{133}Sn. Note that the above reasoning is valid for all hole states in the $N = 50$–82 shell, not only the $0h_{11/2}$ hole.

In order to quantify the average γ-ray branching for states above the neutron-separation energy in ^{133}Sn, we will discuss in the following the total cross sections for one-neutron knockout from ^{133}Sn and ^{134}Sn projectiles, σ_{1n}, which are shown together with the cross sections for multineutron removal σ_{xn} in Fig. 4. The measured cross sections, $\sigma_{1n} = 183(21)$ mb for ^{133}Sn and $\sigma_{1n} = 69(10)$ mb for ^{134}Sn, comprise contributions from both the removal of a neutron from the valence space ($N > 82$) $\sigma_{1n}^{\rm val}$, as well as knockout from the $N = 50$–82 core, $\sigma_{1n}^{\rm core}$, as discussed above. These contributions were calculated using eikonal reaction theory [20,21] and employing the ground state wave functions from the shell model, the known SPE in ^{133}Sn and excitation energies for the neutron-hole states from a spherical Hartree-Fock (HF) calculation. These calculations yield values of $\sigma_{1n}^{\rm val} \sim 14/20$ and $\sigma_{1n}^{\rm core} \sim 186/152$ mb for knockout from ^{133}Sn/^{134}Sn. For removal from ^{133}Sn it is expected that due to the high neutron-separation energy in the daughter nucleus ^{132}Sn, $S_n = 7.343(7)$ MeV [13], most of the highly excited states populated following the removal of a neutron from the $N = 50$–82 core are bound and decay via γ-ray emission as illustrated in Fig. 3(b). Indeed, the calculated value, $\sigma_{1n} = \sigma_{1n}^{\rm val} + \sigma_{1n}^{\rm core} \sim 200$ mb, is in good agreement with the measured cross section. In the case of knockout from ^{134}Sn, in contrast, the residual nucleus ^{133}Sn has a low neutron-separation energy of only $S_n = 2.402(4)$ MeV [13] and, as a consequence, neutron removal from the core populates unbound states which can decay either via neutron or γ-ray emission. In the case of neutron emission the final nucleus is identified as ^{132}Sn in the ZD spectrometer and the corresponding cross section is, therefore, assigned to the two-neutron removal reaction. As a consequence the measured value of σ_{2n} is larger as compared to σ_{1n} (see Fig. 4). The cross section corresponding to γ-decaying unbound states in ^{133}Sn can be estimated by subtracting the calculated cross section for neutron removal from the valence space to bound final states in ^{133}Sn, amounting to $\sigma_{1n}^{\rm val} \sim 20$ mb, from the measured $\sigma_{1n} = 69(10)$ mb. The resulting value of ~49 mb, compared to the calculated value of $\sigma_{1n}^{\rm core} \sim 152$ mb for knockout from the core, suggests that 25%–35% of the decay of unbound states in ^{133}Sn, populated in the one-neutron knockout reaction, proceeds via γ-ray emission. Although this estimate is subject to several uncertainties it clearly shows that the contribution of γ decay is significant.

The effect of nuclear structure on the competition between neutron and γ decay of unbound states may have

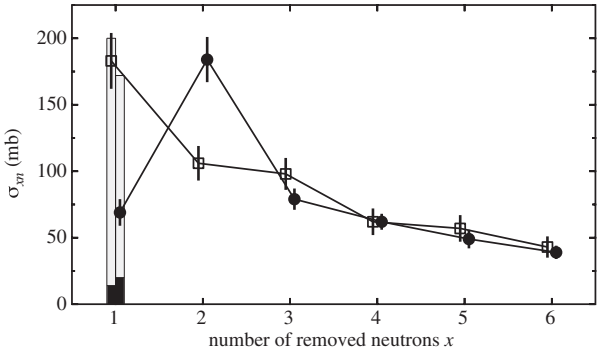

FIG. 4. Total experimental cross sections for the removal of x neutrons, σ_{xn}, from ^{133}Sn (open squares) and ^{134}Sn (filled circles) projectiles. Lines are drawn to guide the eye. The vertical bars for $x = 1$ indicate the cross sections for knockout from the $N > 82$ valence space (black) and from the $N = 50$–82 core (gray) as calculated using eikonal reaction theory. The contribution from the $0h_{11/2}$ orbital to the latter amounts to 67 and 56 mb, respectively.

more general and further-reaching consequences. The β-decay properties of nuclei in the region southeast of ^{132}Sn are of great importance for the description of the r process of nuclear synthesis [22,23]. In this region, the β-decay energies Q_β are large and the neutron-separation energies S_n low, so that unbound excited states in a wide energy window of more than 10 MeV can be populated in the β decays. Experimental information is scarce so that in many cases theoretical calculations of global β-decay properties have to be relied upon. In the latter β-delayed neutron emission probabilities are deduced from calculated strength functions under the assumption that neutron emission occurs whenever it is energetically possible [see, for example, Eq. (21) of Ref. [24]]. It is well known that for nuclei with $Z < 50$ and $N \approx 82$, the β decay is dominated by the $\nu 0g_{7/2} \rightarrow \pi 0g_{9/2}$ Gamow-Teller transition [24,25]. Also the first-forbidden $\nu 0h_{11/2} \rightarrow \pi 0g_{9/2}$ decay is known to play a significant role. Beyond $N = 82$, once the $1f_{7/2}$ neutron orbital starts being occupied, both these transitions populate core-excited states at high excitation energy in the daughter nuclei. In ^{132}Sn and ^{131}In, populated in the β decays of the $N = 83$ isotones ^{132}In [26] and ^{131}Cd [27], excited states comprising a neutron hole in the $0h_{11/2}$ ($0g_{7/2}$) orbital have been identified in the energy range of 4–5 MeV (6–7 MeV). For the decay of these states, the same structure arguments apply, which have been put forward above in the discussion of the decay of highly excited neutron-hole states in ^{133}Sn. It therefore seems advisable to fully elucidate the neutron versus γ-ray competition in the decay of unbound excited states in exotic nuclei southeast of ^{132}Sn in future experiments.

To conclude, we presented clear evidence for the electromagnetic decay of states in ^{133}Sn at excitation energies up to more than 3 MeV above the neutron-separation energy. These excited states are interpreted as neutron-hole states that are populated following the knock-out of a neutron from the closed $N = 50$–82 shell of the ^{134}Sn projectile ion at relativistic energies. The ability of γ-ray emission to compete with neutron decay, despite a hindrance of 3 orders of magnitude at the single-particle level, is explained taking into account the structure of the initial and final states and the resultant wave-function overlap. Our study raises the question whether, due to nuclear structure effects, the γ-ray emission may play a much more significant role than generally assumed in the decay of highly excited states populated following β decay in the region southeast of ^{132}Sn.

A. J. acknowledges fruitful discussions with H. Grawe, S. L. Tabor, and J. L. Tain. We thank the staff of the RIKEN Nishina Center accelerator complex for providing stable beams with high intensities to the experiment. This work was supported by the Spanish Ministerio de Ciencia e Innovación under Contract No. FPA2011-29854-C04 and the Spanish Ministerio de Economía y Competitividad under Contract No. FPA2014-57196-C5-4-P. J. A. T. acknowledges the support of the Science and Technology Facilities Council (UK) Grant No. ST/L005743 and R. O. that of JSPS KAKENHI Grant No. 26887048. G. M. T. gratefully acknowledges funding of this research from the Research Council of Norway, Project Grant No. 222287.

*andrea.jungclaus@csic.es

[1] E. Fermi, *Nuclear Physics* (University of Chicago Press, Chicago, 1950).
[2] S. R. Stroberg *et al.*, Phys. Rev. C **90**, 034301 (2014).
[3] J. L. Tain *et al.*, Phys. Rev. Lett. **115**, 062502 (2015).
[4] R. Dungan *et al.*, Phys. Rev. C **93**, 021302(R) (2016).
[5] A. Spyrou *et al.*, Phys. Rev. Lett. **117**, 142701 (2016).
[6] X. Xu *et al.*, Phys. Rev. Lett. **117**, 182503 (2016).
[7] S. E. A. Orrigo *et al.*, Phys. Rev. C **93**, 044336 (2016).
[8] P. Hoff *et al.*, Phys. Rev. Lett. **77**, 1020 (1996).
[9] K. L. Jones *et al.*, Nature (London) **465**, 454 (2010).
[10] K. L. Jones *et al.*, Phys. Rev. C **84**, 034601 (2011).
[11] J. M. Allmond *et al.*, Phys. Rev. Lett. **112**, 172701 (2014).
[12] W. Reviol *et al.*, Phys. Rev. C **94**, 034309 (2016).
[13] M. Wang, G. Audi, A. H. Wapstra, F. G. Kondev, M. MacCormick, X. Xu, and B. Pfeiffer, Chin. Phys. C **36**, 1603 (2012).
[14] T. Kubo *et al.*, Prog. Theor. Exp. Phys. **2012**, 3C003 (2012).
[15] N. Fukuda, T. Kubo, T. Ohnishi, N. Inabe, H. Takeda, D. Kameda, and H. Suzuki, Nucl. Instrum. Methods Phys. Res., Sect. B **317**, 323 (2013).
[16] S. Takeuchi, T. Motobayashi, Y. Togano, M. Matsushita, N. Aoi, K. Demichi, H. Hasegawa, and H. Murakami, Nucl. Instrum. Methods Phys. Res., Sect. A **763**, 596 (2014).
[17] S. Agostinelli *et al.*, Nucl. Instrum. Methods Phys. Res., Sect. A **506**, 250 (2003).
[18] http://www.nndc.bnl.gov/ensdf/, updated evaluation of data for ^{209}Pb by F.G. Kondev ENSDF 14 June 2015.
[19] L. Coraggio, A. Covello, A. Gargano, and N. Itaco, Phys. Rev. C **88**, 041304(R) (2013), and references therein.
[20] J. A. Tostevin, Nucl. Phys. **A682**, 320 (2001).
[21] P. G. Hansen and J. A. Tostevin, Annu. Rev. Nucl. Part. Sci. **53**, 219 (2003).
[22] G. Lorusso *et al.*, Phys. Rev. Lett. **114**, 192501 (2015).
[23] M. R. Mumpower, R. Surman, G. C. McLaughlin, and A. Aprahamian, Prog. Part. Nucl. Phys. **86**, 86 (2016).
[24] T. Marketin, L. Huther, and G. Martínez-Pinedo, Phys. Rev. C **93**, 025805 (2016).
[25] I. N. Borzov, J. J. Cuenca-García, K. Langanke, G. Martínez-Pinedo, and F. Montes, Nucl. Phys. **A814**, 159 (2008).
[26] B. Fogelberg, M. Hellstrom, D. Jerrestam, H. Mach, J. Blomqvist, A. Kerek, L. O. Norlin, and J. P. Omtvedt, Phys. Rev. Lett. **73**, 2413 (1994).
[27] J. Taprogge *et al.*, Eur. Phys. J. A **52**, 347 (2016).

Submitted to Physical Review C 18/September/2018

In-beam γ-ray spectroscopy of ^{136}Te at relativistic energies

V. Vaquero,[1] A. Jungclaus,[1,*] P. Doornenbal,[2] K. Wimmer,[3,2] A.M. Moro,[4] K. Ogata,[5] T. Furumoto,[6] S. Chen,[2,7] E. Nácher,[1] E. Sahin,[8] Y. Shiga,[9] D. Steppenbeck,[2] R. Taniuchi,[2,3] Z.Y. Xu,[10] T. Ando,[3] H. Baba,[2] F.L. Bello Garrote,[8] S. Franchoo,[11] K. Hadynska-Klek,[8] A. Kusoglu,[12,13] J. Liu,[10] T. Lokotko,[10] S. Momiyama,[3] T. Motobayashi,[2] S. Nagamine,[3] N. Nakatsuka,[14] M. Niikura,[3] R. Orlandi,[15] T.Y. Saito,[3] H. Sakurai,[2,3] P.A. Söderström,[2] G.M. Tveten,[8] Zs. Vajta,[16] and M. Yalcinkaya[12]

[1]*Instituto de Estructura de la Materia, CSIC, E-28006 Madrid, Spain*
[2]*RIKEN Nishina Center, 2-1 Hirosawa, Wako, Saitama 351-0198, Japan*
[3]*Department of Physics, University of Tokyo, 7-3-1 Hongo, Bunkyo, Tokyo 113-0033, Japan*
[4]*Departamento de FAMN, Universidad de Sevilla, Apartado 1065, 41080 Sevilla, Spain*
[5]*Research Center for Nuclear Physics, Osaka University, Ibaraki, Japan*
[6]*Graduate School of Education, Yokohama National University, Yokohama 240-8501, Japan*
[7]*School of Physics and State Key Laboratory of Nuclear Physics and Technology, Peking University, Bejing 100871, People's Republic of China*
[8]*Department of Physics, University of Oslo, NO-0316 Oslo, Norway*
[9]*Department of Physics, Rikkyo University, Tokyo, Japan*
[10]*Department of Physics, The University of Hong Kong, Pokfulam, Hong Kong*
[11]*Institut de Physique Nucléaire Orsay, IN2P3-CNRS, 91406 Orsay Cedex, France*
[12]*Department of Physics, Faculty of Science, Istanbul University, Vezneciler/Fatih, 34134, Istanbul, Turkey*
[13]*ELI-NP, Horia Hulubei National Institute of Physics and Nuclear Engineering, 077125 Magurele, Romania*
[14]*Department of Physics, Faculty of Science, Kyoto University, Kyoto 606-8502, Japan*
[15]*Advanced Science Research Center, Japan Atomic Energy Agency, Tokai, Ibaraki 319-1195, Japan*
[16]*MTA Atomki, P.O. Box 51, Debrecen H-4001, Hungary*

(Dated: September 18, 2018)

The reduced transition probability B($E2$; $0_1^+ \rightarrow 2_1^+$) to the first excited 2^+ state of the neutron-rich nucleus ^{136}Te, with two protons and two neutrons outside the doubly-magic ^{132}Sn core, has been measured via Coulomb excitation at relativistic energies at the RIKEN Radioactive Isotope Beam Factory. A value of B($E2$)=0.191(26) e^{2}b^2 was extracted from the measured inelastic scattering cross section on an Au target taking into account the contributions from both Coulomb and nuclear excitations. In addition, an upper limit for the transition strength to a 2^+ state of mixed-symmetry character in the excitation energy range of 1.5-2.0 MeV has been determined and compared to the predictions of various theoretical calculations. The high statistics gathered in the present experiment allowed for the first time to assess in detail the systematic uncertainties involved in the analysis of Coulomb excitation experiments at beam energies around 150 MeV/u.

PACS numbers: 21.10.Ky, 21.60.Cs, 27.60.+j

I. INTRODUCTION

Since the pioneering study of the neutron-rich Te isotopes by Radford and collaborators [1] using low-energy Coulomb excitation of radioactive beams in inverse kinematics at the Holifield Radioactive Ion Beam Facility (HRIBF) of the Oak Ridge National Laboratory (ORNL) fifteen years ago, significant theoretical effort has been devoted trying to achieve a better understanding of these nuclei close to the doubly magic ^{132}Sn. In particular the low value of the reduced transition probability to the first excited 2^+ state of ^{136}Te at an excitation energy of E_x = 607 keV, B($E2$; $0_1^+ \rightarrow 2_1^+$)=0.103(15) e^{2}b^2 (in the following abbreviated B($E2$)), which implied a significant asymmetry of this quantity with respect to the N = 82 shell closure in the chain of Te isotopes (for ^{132}Te a value of B($E2$)=0.172(17) e^{2}b^2 was measured in the same work), has been considered as a real surprise at that time. Later this low B($E2$) value was confirmed by the preliminary results of a fast timing experiment performed at ISOLDE which yielded B($E2$)=0.122(24) e^{2}b^2 [2]. In 2011 it was reported that the data analysis, which lead to the results presented in Ref. [1], was based on an erroneous assumption on the target thickness [3]. Consequently, corrected B($E2$) values were quoted for ^{132,134,136}Te which, although slightly larger as compared to Ref. [1] (B($E2$)=0.216(22) e^{2}b^2 for ^{132}Te and B($E2$)=0.122(18) e^{2}b^2 for ^{136}Te), still reflected the asymmetry mentioned above. While shell model calculations were not able to reproduce this peculiar behavior of the $E2$ strength [4], the calculations performed by Terasaki et al. using the quasiparticle random phase approximation (QRPA) traced it to a reduced neutron pairing above the N = 82 gap which causes a neutron dominance in the wave function of the 2_1^+ state of ^{136}Te [5].

Very recently a new measurement has been reported upon [6], performed again at the HRIBF using Coulomb excitation in inverse kinematics. This time, however, a

*Electronic address: andrea.jungclaus@csic.es

heavier titanium target was used as compared to the carbon target which had been employed in the first experiment. The new value of B($E2$)=0.181(15) e^{2}b^2 is in clear conflict with the previously reported results.

In view of this inconsistent body of experimental information a re-measurement of the B($E2$; $0_1^+ \rightarrow 2_1^+$) value in ^{136}Te using an independent approach seemed highly desirable. We therefore conducted an experiment at the Radioactive Isotope Beam Factory (RIBF), operated by the RIKEN Nishina Center and the Center for Nuclear Study of the University of Tokyo, using the technique of Coulomb excitation at relativistic energies. An additional motivation for this measurement has been the search for an excited 2^+ state of mixed proton-neutron symmetry in ^{136}Te, which several theoretical studies predict to exist in the excitation energy range of 1.5-2.0 MeV [4, 7, 8]. The study of the decay properties of such a 2^+_{ms} state, the isovector analogue of the 2_1^+ level, in ^{136}Te, in comparison to those of the recently observed 2^+_{ms} state in ^{132}Te [3], constitutes an alternative approach to probe the proton-neutron balance of the nuclear wave function. Note that at relativistic energies the Coulomb excitation cross section for a 2^+ state is nearly independent on the excitation energy. Therefore, the population of a second excited 2^+ state in this experiment is favorable as compared to the studies using low-energy Coulomb excitation, in which the cross section for the excitation of a 2^+ level decreases with its excitation energy.

Finally, the high statistics gathered in the present experiment allowed for the first time to evaluate in detail the validity of the chosen analysis approach. The latter will be described in detail in this article in order to serve as guideline for the evaluation of the different systematic uncertainties involved in the analysis of other experiments using the same technique but accumulating less statistics.

II. EXPERIMENT

The experiment was carried out at the RIBF at RIKEN. A primary beam of ^{238}U at 345 MeV/u bombarded a 4-mm-thick beryllium target located at the entrance of the BigRIPS fragment separator [9]. The fission products around ^{136}Te were selected and purified by employing the Bρ-ΔE-Bρ method through a combination of magnetic rigidity (Bρ) selection and two wedge-shaped aluminium degraders. The particle identification was performed on an event-by-event basis using the ΔE-Bρ-TOF method, where the energy loss ΔE was measured by an ionization chamber located at the focal plane F7, Bρ was determined from position measurements using parallel plate avalanche counters (PPACs) and the time of flight (TOF) was measured with two plastic scintillators located at the focal points F3 and F7. The atomic number (Z) and the mass-over-charge (A/Q) ratio of each ion were determined with this method [10]. The primary beam intensity was kept below 2.5 pnA in order to limit the counting rates in the beam detectors, in particular the ionization chambers, to such a level that a clean particle identification can be achieved. The particle identification plot obtained in this way is shown in Fig. 1a).

After the selection and identification, the secondary beams were transported to the focal point F8 where they impinged in two different runs on reaction targets consisting of 950 mg/cm^2 Au and 535 mg/cm^2 C, respectively. The high-Z Au target ($Z = 79$) was used to induce Coulomb excitation, while the low-Z C target ($Z = 6$) allowed to extract the nuclear contribution to the inelastic scattering cross section measured with the Au target. At the center of the target, the energies of the ^{136}Te ions were 139 MeV/u (corresponding to $\beta = 0.493$) and 140 MeV/u ($\beta = 0.494$) for the Au and C targets, respectively (165/110 and 165/112 MeV/u before/after the target). The scattering angles of the elastically and inelastically scattered ions were measured with two PPACs installed upstream and one PPAC installed downstream of the reaction target. The reaction products were identified by the ZeroDegree spectrometer [9] using again the previously described ΔE-B_ρ-TOF method. Fig. 1b) shows the ZeroDegree particle identification following the interaction of ^{136}Te ions with the Au target. Note that the ^{136}Te ions were detected in the ZeroDegree spectrome-

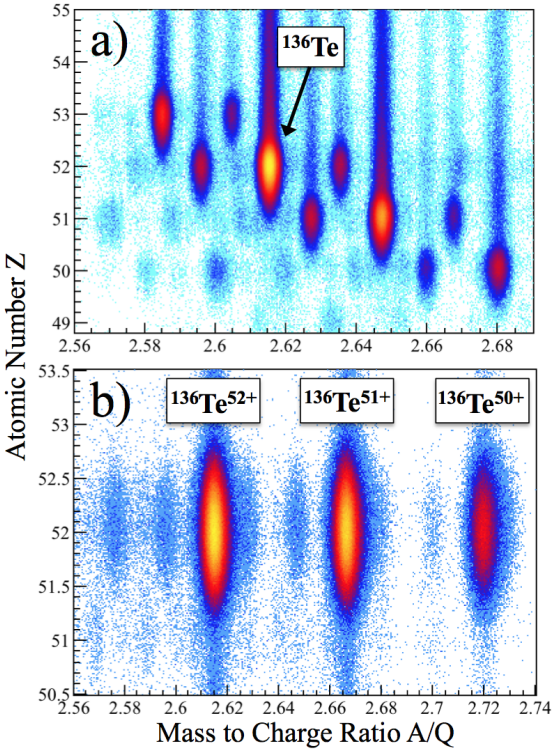

FIG. 1: Particle identification plots for a) BigRIPS and b) the ZeroDegree spectrometer requiring the identification of ^{136}Te ions in BigRIPS obtained with the Au target. Note that the ^{136}Te ions were observed in different charge states in ZeroDegree.

ter in three different charge states, namely 50% fully-stripped, 42% hydrogen-like and 8% helium-like (the corresponding numbers for the C target are 64%, 33% and 3%, respectively).

To measure γ rays emitted following the decay of excited states of the reaction products, the target was surrounded by the DALI2 spectrometer [11], a high-efficiency γ-ray detector array consisting of 186 NaI(Tl) detectors covering angles from 20° to 150°. In order to reduce the low-energy bremsstrahlung background, the beam pipe at the F8 focus was enclosed by 1-mm lead and 1-mm tin shields. A DALI2 energy calibration was performed using ^{60}Co, ^{88}Y and ^{137}Cs sources. The full-energy-peak efficiency and energy resolution (FWHM) were obtained to be around 15% and 6%, respectively, at 1.33 MeV (^{60}Co). This efficiency value is in good agreement with simulations performed using the Geant4 code [12]. To reduce the dead time of the data acquisition system, during the present experiment only the 92 NaI(Tl) crystals placed at forward angles $\theta < 60°$ in the laboratory frame (layers 10 and 11 plus the forward wall [11]) were used. In this angular range, due to the Lorentz boost and the background properties, the peak-to-background ratio was largest. Considering only this sub-array and assuming prompt emission, the efficiency reduced from 24% to 13% for a γ ray with an energy of 600 keV emitted by ions moving with a velocity of β=0.5. To increase the detection efficiency for high-energy γ rays and to improve the peak-to-total ratio over the full energy range an add-back algorithm was applied for the data taken with the C target. All energy depositions registered in NaI crystals within a range of 15 cm from the center of the crystal with the highest energy signal were summed. Doppler correction was then performed assuming that the largest energy deposition corresponds to the first interaction of the γ ray in the array and using the midtarget velocity. Add-back has been applied to increase the statistics of the γ-ray spectra and in particular for the analysis of $\gamma\gamma$ coincidences. However, all cross sections reported in the present work have been determined from γ-ray spectra without add-back. The reason for that is that the γ-ray efficiency applying the add-back algorithm strongly depends on the background which is not included in the Geant4 simulations.

III. RESULTS

A. γ-ray spectra and level scheme

The Doppler-shift corrected γ-ray spectrum from inelastic scattering of ^{136}Te on the C target is shown in Fig. 2a). Five lines at energies around 330, 400, 600, 810, and 960 keV are visible in this spectrum. From spontaneous fission and β-decay studies [13–15], γ rays with 353, 423, and 607 keV are known to form the $6_1^+ \rightarrow 4_1^+ \rightarrow 2_1^+ \rightarrow 0_1^+$ sequence in ^{136}Te and we therefore identify the first three lines in the spectrum of Fig. 2a)

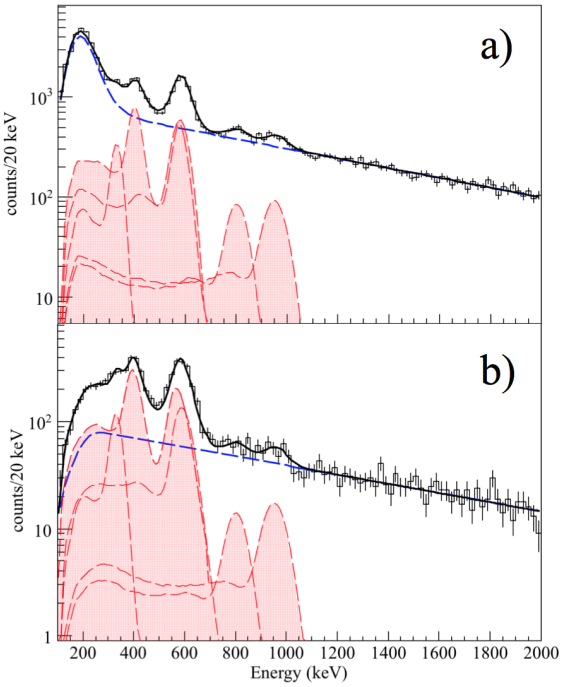

FIG. 2: a) Doppler-shift corrected γ-ray spectrum from inelastic scattering of ^{136}Te on the C target. The fit to the experimental spectrum is shown as thick black line which is the sum of the background (blue dashed line) and the simulated DALI2 response for γ rays with energies of 353, 423, 607, 810, and 962 keV (red dashed lines). No cut on the γ-ray multiplicity has been applied. b) Same as a), but for the one-neutron transfer reaction C(^{137}Te,^{136}Te). Here, only events with multiplicity M_γ<4 are considered. In both parts of the figure add-back was applied.

with these transitions. Furthermore, a 962-keV γ ray was observed in Ref. [14] and assigned as decaying from a 2_2^+ state at 1568 keV to the 2_1^+ level at 607 keV. Most probably this transition corresponds to the highest-energy line observed in Fig. 2a). In addition, a γ ray with an energy of 810(15) keV is observed for the first time in the present experiment. The background in the spectrum shown in Fig. 2a) can be parametrized by the sum of two exponential functions cutoff at low energy with an error function. The experimental spectrum is then nicely reproduced by the sum of this background and the simulated response function of the DALI2 array for γ rays with energies of 353, 423, 607, 810, and 962 keV. Note that the feeding of the 2_1^+ level from the 4_1^+ state is simulated as cascade since the finite lifetime of the 4_1^+ state (see below) affects the position of the line corresponding to the $2_1^+ \rightarrow 0_1^+$ transition. As shown in Fig. 2b), the same five γ transitions are also observed following the population of ^{136}Te via the one-neutron knockout reaction from ^{137}Te, although with different relative intensities. A comparison between the two spectra shown in Fig. 2 nicely illustrates the very different shape of the background, in particular at low energy, in these two reaction channels leading to

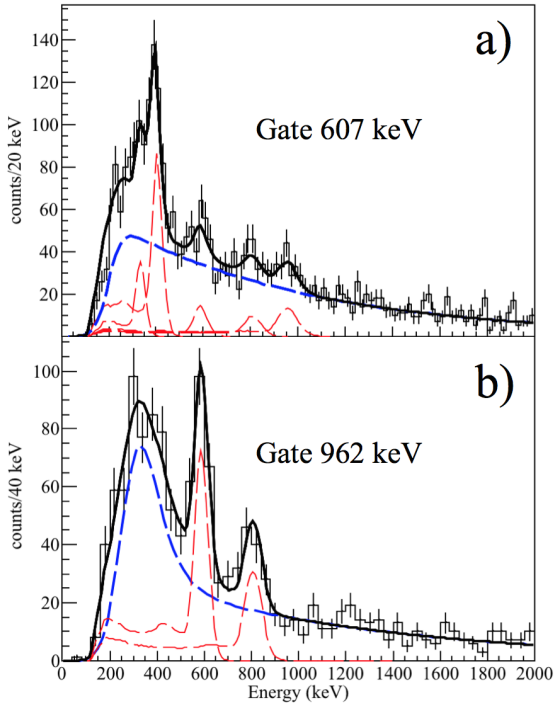

FIG. 3: $\gamma\gamma$ coincidence spectra for ^{136}Te on the C target with gate on a) the 607-keV, $2_1^+ \rightarrow 0_1^+$ and b) the 962-keV, $2_2^+ \rightarrow 2_1^+$ transition. In both parts of the figure add-back was applied and only events with multiplicity $M_\gamma < 6$ were considered.

the same final nucleus.

To obtain information about the placement of the new 810-keV transition in the level scheme of ^{136}Te, $\gamma\gamma$-coincidence spectra were produced using the data from inelastic scattering with a gate on either the 607-keV, $2_1^+ \rightarrow 0_1^+$, or the 962-keV, $2_2^+ \rightarrow 2_1^+$, transition, see Fig. 3. Since the moderate energy resolution of DALI2 does not allow to perform a clean background subtraction, besides the lines corresponding to the 353-, 423-, 810-, and 962-keV transitions, also one at 607 keV is observed in the spectrum shown in Fig. 3a). This self-coincidence has its origin in the contributions from the Compton background of the higher-energy transitions to the energy gate on the 607-keV line (compare Fig. 2). The gate on the 962-keV transition, in contrast, is expected to be much cleaner due to the lower background at higher energies and the fact that no γ rays are observed above 1 MeV. The coincidence spectrum in Fig. 3b) shows that besides the 607-keV ground-state transition also the new 810-keV transition is observed in coincidence with the 962-keV line suggesting its placement on top of the 2_2^+ state as shown in Fig. 4. Included in Fig. 4 is also the relative feeding of the excited states of ^{136}Te populated via either inelastic scattering or one-neutron knockout. Note that the 4_1^+ and 6_1^+ yrast states are stronger populated relative to the 2_1^+ state in the one-neutron knockout reaction while the population of the yrare 2_2^+ level is comparable

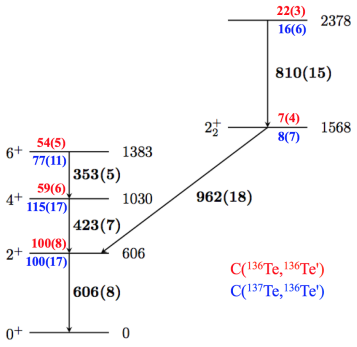

FIG. 4: Level scheme of ^{136}Te including the new transition with an energy of 810(10) keV (see text for details). The feeding (normalized to that of the first excited 2^+ state) of all excited states of ^{136}Te populated in the present experiment via the inelastic scattering (one-neutron knockout) reaction on a C target is quoted above (below) each level.

in the two reactions.

The Doppler-corrected γ-ray spectrum measured in coincidence with ^{136}Te ions detected in both BigRIPS and the ZeroDegree spectrometer for the Au target is shown in Fig. 5a). Only a single line corresponding to the decay of the first excited 2^+ state at 607 keV is observed in the energy range up to 2 MeV. Since for the relativistic beam energies used in the present experiment the probability for multi-step Coulomb excitation is very small, the non-observation of the transitions emitted in the decay of the 4_1^+ and 6_1^+ states is expected. However, a second 2^+ state could have been excited and its decay observed in the present experiment if the B(E2) transition probability would have been sufficiently large.

As mentioned in the introduction several theoretical calculations predict the existence of an excited 2^+ state with mixed proton-neutron symmetry in ^{136}Te in the excitation energy range 1.5-2.0 MeV. Such a mixed-symmetry 2_{ms}^+ state is expected to decay via a strong $M1$ transition to the 2_1^+ and a weak $E2$ to the 0_1^+ level. As illustrated by the difference between the experimental spectrum and the fitted DALI2 response shown in Fig. 5b), besides the 607-keV ground-state transition no additional γ ray is observed in the energy range up to 2 MeV in the present experiment following the excitation of the ^{136}Te beam on the Au target. In particular, we note that the 962-keV $2_2^+ \rightarrow 2_1^+$ transition, which has been observed with the C target (see Fig. 2), is absent in the spectrum shown in Fig. 5a). In order to optimize the resolution for the 607-keV line in this spectrum Doppler correction was performed using β=0.448 corresponding to the velocity of the ^{136}Te ions behind the target. However, the search for additional lines in the spectrum has been performed for a wide range of β values. Based on Monte Carlo simulations and the difference spectrum shown in Fig. 5b) observational lower limits of 10% and 16% relative to the intensity of the 607 keV line

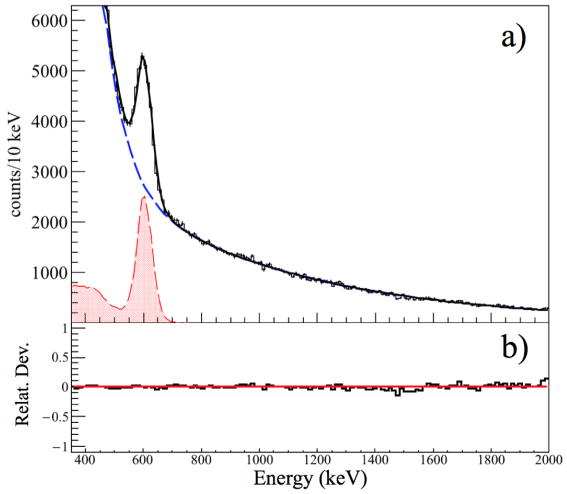

FIG. 5: a) Doppler-shift corrected γ-ray spectrum from inelastic scattering of ^{136}Te on the Au target. The fit to the experimental spectrum is shown by the thick black line, which is composed of a two-exponential function describing the background (blue dashed line) and the simulated response function of DALI2 for the 607-keV $2_1^+ \rightarrow 0_1^+$ transition (red dashed line). No cut on the γ-ray multiplicity and no add-back was applied. b) Relative difference between the experimental and simulated spectra shown in a).

have been determined for hypothetical γ-ray energies of 0.9 MeV and 1.8 MeV, respectively. The estimation of B($E2$; $0_1^+ \rightarrow 2_{ms}^+$) limits from these values will be discussed in section VII.

Finally, we note in passing that in the present experiment, besides the 607-keV $2_1^+ \rightarrow 0_1^+$ transition, two γ rays with energies of 3.6(1) and 4.2(1) MeV, respectively, have been observed for the first time. They depopulate a state at an excitation energy of 4.2(1) MeV and the 3.6(1) MeV γ ray corresponds to a decay branch to the 2_1^+ state. This new excited state will be discussed in detail in a forthcoming publication. It is sufficient to mention here that this indirect feeding of the 2_1^+ level will correctly be taken into account in the determination of the B($E2$; $0_1^+ \rightarrow 2_1^+$) value presented in section VI.

B. Direct lifetime determination based on the observed Doppler shifts

Both the 2_1^+ and 4_1^+ states in ^{136}Te are known to have lifetimes of tens of picoseconds [6]. This implies that the 607- and 423-keV γ rays are emitted mainly after the ions already left the target. If Doppler correction is performed using the midtarget velocity and assuming emission from the center of the target, these lines are shifted to smaller energies as compared to the nominal values (all detectors are placed at $\theta < 60°$). Therefore, as already has been demonstrated in Ref. [16], estimates of the excited-state lifetimes can be obtained from a comparison between the experimental line shapes and Monte Carlo simulations.

In Fig. 6a) the experimental line shape of the 607-keV line measured with DALI2 for the Au target is compared to Geant4 simulations assuming a prompt decay of the 2_1^+ state. Clearly the experimental line shape is not reproduced by these simulations. Only when a finite lifetime around $\tau(2_1^+)$=33 ps is assumed, a good agreement is obtained (see Fig. 6b)). In the spectrum taken with the C target besides the 607-keV line also the 423-keV transition emitted in the decay of the 4_1^+ state is observed (compare Fig. 2a)). Keeping the lifetime of the 2_1^+ state fixed, $\tau(2_1^+)$=33 ps, and considering both a direct population of the 2_1^+ state as well as a cascade of two γ rays emitted following the population of the 4_1^+ level a longer lifetime around 98 ps is needed for the 4_1^+ state in order to describe the experimental spectrum (compare Fig. 6c,d). This value has to be considered as effective lifetime of the 4_1^+ state since the relative intensities quoted in Fig. 4 indicate significant feeding from the 6_1^+ state. Unfortunately, due to the increasing background in the low-energy region of the spectrum and the vicinity to the 423-keV line, it was not possible to deduce any information with respect to the unknown lifetime of the 6_1^+ state from an analysis of the line corresponding to the 353-keV transition. Final values of $\tau(2_1^+)$=33(15)

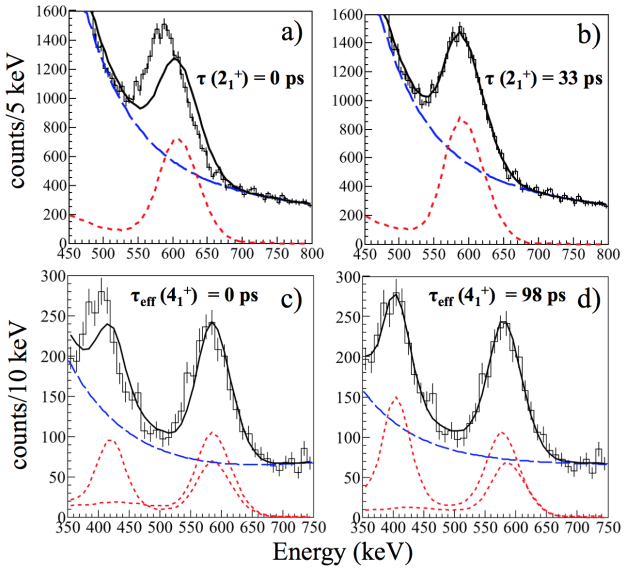

FIG. 6: a) Comparison between the experimental shape of the 607-keV line for the Au target (black histogram) and GEANT4 simulations (black line) assuming $\tau(2_1^+)$=0 ps; b) same as a) but assuming $\tau(2_1^+)$=33 ps; c) comparison between the experimental shapes of the 423- and 607-keV lines (black histogram) for the C target and GEANT4 simulations (black line) assuming $\tau(2_1^+)$=33 ps and $\tau_{eff}(4_1^+)$=0 ps, d) same as c) but assuming $\tau_{eff}(4_1^+)$=98 ps. In parts a),b) no add-back was applied and the γ-ray multiplicity was limited to M_γ=1 while in parts c),d) add-back was applied and only events with M_γ=2 were considered. In all cases Doppler correction performed using the midtarget velocity.

ps and $\tau_{eff}(4_1^+)$=98(50) ps were deduced from the experimental spectra shown in Fig. 6. From the fit of the simulated DALI2 response functions assuming vanishing excited state lifetimes to the two lines observed around 810 and 962 keV in Fig. 2a), γ-ray energies of 810(15) and 962(18) keV have been deduced. The agreement of the latter value with the literature value of 961.72(5) keV [14] suggests that the lifetime of the 2_2^+ level at 1568 keV is short.

Note that while the accuracy which can be achieved using this technique is obviously very limited when unsegmented scintillator arrays such as DALI2 are used for γ-ray detection as in the present experiment, it becomes a precision tool when position-sensitive Ge detectors are employed for in-beam spectroscopy at relativistic energies [17, 18] and will show its full power with γ-ray tracking arrays such as AGATA [19] and GRETA [20] in the future.

IV. DETERMINATION OF EXCLUSIVE SCATTERING CROSS SECTIONS

In order to determine experimental differential inelastic scattering cross sections, the γ-ray yield has to be measured as a function of the scattering angle. In the present experiment the latter is measured using the information from the three PPACs installed in front of and behind the target position. The proper alignment of all beam detectors used in the reconstruction of the incoming and outgoing beam trajectories can be checked by confirming a flat distribution of the azimuthal scattering angle. In Fig. 7a) the angular distributions of the ^{136}Te ions identified in BigRIPS are shown for the runs without target (empty frame) and with the C and Au targets inserted at target position. Note that in the following the expression angular distribution always refers to $d\sigma/d\theta_{lab}$ (which includes the $\sin(\theta)$ and corresponds to what is really measured), in contrast to the differential cross section $d\sigma/d\Omega$. All three distributions can be fitted with Gaussian curves multiplied by $\sin(\theta)$ yielding width parameters σ of 4.8 mrad, 5.4 mrad and 8.8 mrad, respectively. The angular resolution measured without target reflects the uncertainty of the position measurements in the PPAC detectors. The measured value σ=4.8 mrad can be reproduced in Monte Carlo simulations assuming a position resolution of σ_x=σ_y=0.73 mm for all PPAC detectors involved in the measurement of the scattering angle. With the C and Au targets in the beam an additional contribution stemming from the angular straggling, mainly due to multiple elastic scattering in the target material, leads to considerably worse angular resolutions. This angular straggling has been estimated with the code ATIMA [21] based on the energy before the target and the target thickness to 2.3/8.0 mrad for the C/Au targets. Combining the contributions from the position measurement and the straggling, values of 5.3/9.3 mrad are obtained in rather good agreement with the

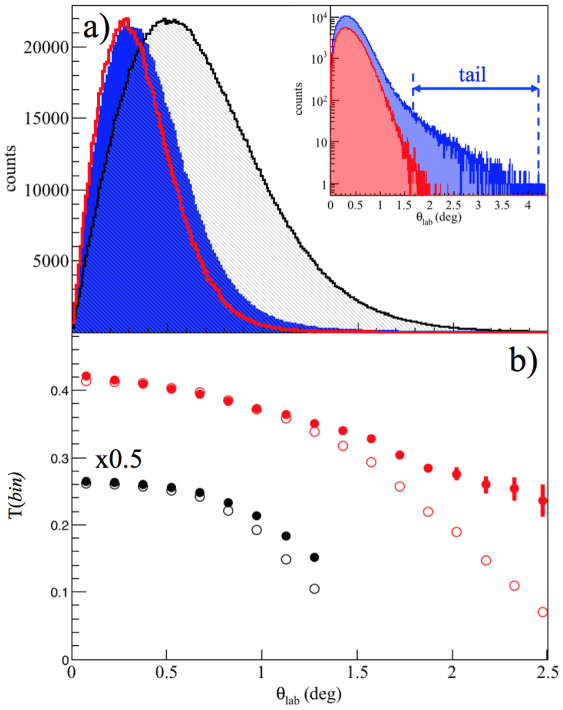

FIG. 7: a) Angular distributions of the ions which have been identified as ^{136}Te in BigRIPS without target (red line) and for the C (blue area) and Au (grey area) targets, respectively. The inset shows the angular distribution of the ^{136}Te ions for the C target (filled blue curve, same as blue curve in a) on a logarithmic scale in comparison to the one obtained when in addition the detection of a fully-stripped ^{136}Te ion in the ZeroDegree spectrometer is required (filled red curve). b) Transmission curves for those ^{136}Te ions which are detected in the ZeroDegree spectrometer in the fully-stripped charge state for the C (black, multiplied by 0.5) and Au (red) targets, respectively, before (open circles) and after correction for reaction losses (bullets). See text for details.

experimental observation.

In the next step, separate γ-ray spectra were produced for different ranges of the scattering angle. To determine the differential cross section for the excitation of the 2_1^+ state, angular bins of $\Delta\theta_{lab}$=0.15° were used. Coincidence conditions were applied on ^{136}Te ions in BigRIPS and on either the fully-stripped or the hydrogen-like ^{136}Te in the ZeroDegree spectrometer (compare Fig. 1). For each of these scattering-angle gated γ-ray spectra the intensity of the 607-keV line was deduced from a fit of the simulated DALI2 response function similar to the ones shown in Fig. 2 for the case of the C target and Fig. 5 for the case of the Au target. In the simulation of the DALI2 response prolate (oblate) γ-ray angular distributions have been assumed for the Coulomb excitation on the Au target (the nuclear excitation on the C target) [22, 23]. A systematic uncertainty of 5%, corresponding to half of the intensity difference between prolate (oblate) and spherical angular distributions for the present detec-

tor geometry, was considered in order to account for possible attenuation effects due to charge state changes and γ decay behind the target. Before the cross section can be calculated for each angular bin, the observed γ yield has to be corrected for i) the scattering-angle dependent losses due to the limited acceptance of the ZeroDegree spectrometer, ii) losses due to reactions which take place on any material in the beam line, both targets and beam detectors, between the identifications in BigRIPS and the ZeroDegree spectrometer, and iii) the charge state fraction. An effective transmission which includes all three contributions can be extracted from the data by comparing the number of ^{136}Te ions which are detected in the ZeroDegree spectrometer (separately for each of the charge states) to the number of ^{136}Te ions identified in BigRIPS as a function of the scattering angle. The resulting transmission curves for the fully-stripped component are shown for both the C and Au targets in Fig. 7b). As illustrated in the inset of Fig. 7a) for the C target, the angular distributions of the ions identified as ^{136}Te in BigRIPS exhibit tails at large scattering angles which correspond to ions which had been identified as ^{136}Te in BigRIPS but lost neutrons and/or protons before their scattering angle was measured in the PPACs. These tails have been parametrized, extrapolated to smaller scattering angles and subtracted from the distributions. Using these corrected angular distributions, new effective transmission curves have been determined as shown in Fig. 7b). After removal of the tail, higher transmission was obtained, in particular for large scattering angles. To acknowledge the uncertainty involved in the subtraction process, an error has been assumed for the experimental points at largest scattering angles which covers the full range between the lower limit of the transmission obtained before the subtraction of the tail and the maximum limit corresponding to the assumption of constant transmission over the whole angular range.

Once the effective transmission $T(bin)$ has been determined, the angular distribution is obtained as:

$$d\sigma/d\theta_{lab}(bin) = \frac{N_\gamma(bin)}{T(bin) \times N_{ions} \times d\theta_{lab}(bin) \times N_{target}} \quad (1)$$

where $N_\gamma(bin)$ is the number of decays of the 2_1^+ state (deduced from the fit to the spectrum for each angular bin), N_{ions} is the number of ^{136}Te ions impinging on the target (number of ions in the BigRIPS gate corrected for the down-scaling factor used in the trigger) and N_{target} is the number of target atoms. Fig. 8a) shows the resulting angular distributions $d\sigma/d\theta_{lab}(bin)$ for the excitation of the 2_1^+ state in ^{136}Te on the Au target, separately for the ions detected in the fully stripped and hydrogen-like charge states, respectively, in the ZeroDegree spectrometer. A good agreement is observed so that finally for each angular bin an average value can be calculated leading to the final angular distribution shown in Fig. 8b). The total cross section for the excitation of the 2_1^+ state is calculated as sum over all bins, i.e., $\sigma_{tot} = \sum_{bin=1}^{n} d\sigma/d\theta_{lab}(bin)$. A comparison between

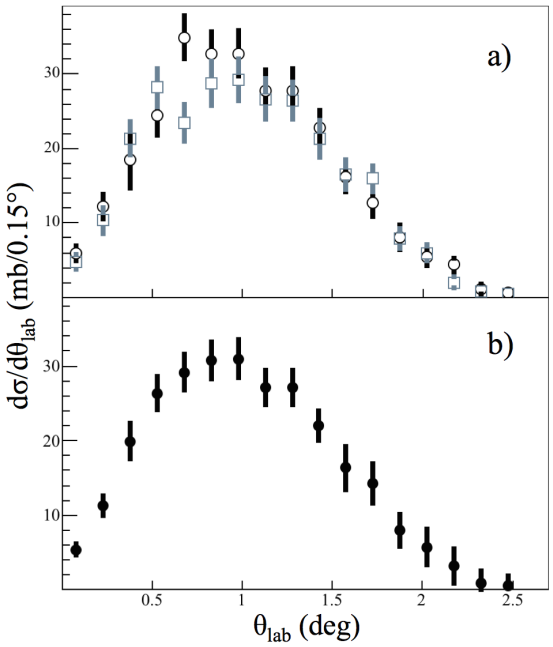

FIG. 8: Experimental angular distributions measured in coincidence with the 607-keV transition in ^{136}Te on the Au target a) separately for the ions detected in the fully-stripped (open circles) and hydrogen-like (open squares) charge states in the ZeroDegree spectrometer and b) after averaging both components.

the Figs. 7b) and 8b) shows that the uncertainty in the determination of the transmission in the angular range θ_{lab}>1.5° does not significantly affect the total cross section since the angular distribution peaks at lower scattering angles.

Note that a too small cross section value is obtained when it is calculated in an integral way from the total number of γ rays, N_γ, and the total transmission $T = N_{ions}^{ZD}/N_{ions}^{BR}$. In the case of the 2_1^+ state in ^{136}Te excited on the Au target, the difference amounts to 9% for the fully-stripped component and 7% for the hydrogen-like ions. In cases in which the statistics is not sufficient to allow for a differential analysis according to Eq. (1), we anticipate that in view of the good agreement between experimental and theoretical angular distributions to be discussed in section VI, the cross sections can be determined based on the experimental transmission curve and the calculated angular distribution. All cross section values measured in coincidence with a discrete γ transition are summarized on the left hand side of Table I.

In order to deduce the exclusive excitation cross section to the 2_1^+ state from the cross sections measured in coincidence with the different γ transitions for the C and Au targets, the indirect population of this level from higher-lying excited states has to be considered. For the C target exclusive cross sections have been calculated on the basis of the level scheme presented in Fig. 4. The result is that only less than half of the observed yield

of the 607-keV transition, namely $\sigma(2_1^+)$=9.5(32) mb, is due to the direct excitation of the 2_1^+ state, while the remaining intensity is due to feeding from the higher-lying states. As mentioned in the last section, two discrete γ rays with energies above 3.5 MeV have been observed following the inelastic excitation of the ^{136}Te ions on the Au target. One of them populates the 2_1^+ state and consequently the cross section of 21(3) mb corresponding to this transition has to be subtracted from the 279(17) mb measured for the 607-keV γ ray (see Table I). In this case the statistics was sufficient to subtract this feeding contribution in a differential way, i.e., separately for each bin of the angular distribution shown in Fig. 8b). In addition, the contribution due to unobserved feeding from higher-lying 2^+ states has to be taken into account. This feeding fraction was estimated in two different ways. First, this quantity was determined for the experimentally very well studied stable N=84 isotones ^{142}Ce and ^{144}Nd [24]. In these nuclei, a total of 7 and 12 excited 2^+ states with known lifetimes, respectively, are reported in the energy range from 1.5 to 3.2 MeV. Taking into account measured half-lives and branching ratios, a feeding of 15% and 11% is obtained for the 2_1^+ states in ^{142}Ce and ^{144}Nd, respectively. Alternatively, shell model calculations employing realistic effective interactions (see Section VII) have been performed to estimate the feeding from 2_x^+ states to the 2_1^+ level at 607 keV. In the same energy range quoted above, a total of 16 2^+ states are predicted to exist and from the calculated decay properties, a feeding fraction of 14% is deduced in nice agreement with the experimental numbers for ^{142}Ce and ^{144}Nd. Based on these estimates it is in the following assumed that 85(5)% of the remaining yield measured for the 607-keV γ ray, $\sigma(2_1^+)$=0.85(5)×258(22) mb=219(23) mb correspond to the direct excitation of the 2_1^+ state in ^{136}Te.

TABLE I: Total cross sections measured in coincidence with γ rays in ^{136}Te on C and Au targets (left) and exclusive inelastic scattering cross sections to individual excited states of ^{136}Te (right). The quoted errors include the uncertainties related to the transmission, the number of γ rays from the fit, the number of detected ions, the target thickness and the downscale factor of the trigger. Additional errors of 5% each are added to account for the uncertainties of the DALI2 efficiency calibration and the angular distribution (see text for details).

E_γ (MeV)	σ^C (mb)	σ^{Au} (mb)	E_x (MeV)	I_i^π	σ^C (mb)	σ^{Au} (mb)
0.353	5.1(7)	–	0.607	2_1^+	9.5(32)	219(23)[a]
0.423	10.7(11)	–	1.030	4_1^+	5.6(13)	–
0.607	23(3)	279(22)	1.383	6_1^+	5.1(7)	–
0.810	2.1(3)	–	1.568	2_2^+	0.7(5)	–
0.962	2.8(4)	–	2.378		2.1(3)	–
3.6	–[b]	21(3)	4.2		–	42(4)
4.2	–[b]	21(3)				

[a]Assuming 15(5)% feeding from high-lying 2_x^+ states.
[b]Contaminated by C target excitations.

V. EXTRACTION OF B($E2$; $0_1^+ \rightarrow 2_1^+$) FROM THE MEASURED $\sigma(2_1^+)$

In scattering off a high-Z target both electromagnetic and nuclear excitations can occur so that both processes, as well as the interference between them, contribute to the measured inelastic scattering cross section. Therefore, the determination of the B($E2$) value from the measured cross section is not a trivial task. For Coulomb excitation experiments at intermediate or relativistic energies (with typical beam energies between 40 and 180 MeV/u) there are in general four different ways to determine the transition probability for the state of interest, e.g., B($E2$; $0^+ \rightarrow 2_1^+$) values, from the measured exclusive inelastic scattering cross section. In the first two, relative measurements are performed. The excitation strength is deduced either by comparison to target excitations with known transition probability (e.g., the 548-keV transition in ^{197}Au, see examples in Refs. [25]) or relative to another nucleus excited under the same experimental conditions [26–28]. In these cases the quality of the obtained result relies mainly on the reliability of the experimental information from literature and the correct evaluation of experimental differences (with respect to transmission, feeding, efficiencies etc.). In cases in which nuclear contributions can not be neglected, in addition also possible differences with respect to the nuclear deformation length, δ_{nucl}, have to be considered. Alternatively, two different approaches have been used in the literature which are based on the measurement of absolute inelastic scattering cross sections. In the analyses of experiments performed at NSCL, using beam energies in the range from 40 to 80 MeV/u, cuts on the scattering angle were applied in order to limit the analysis to peripheral collisions in which nuclear contributions are assumed to be negligible ("safe" impact parameter criterion touching spheres plus 2 fm), see Refs. [29, 30] and overview tables in [31, 32]. At the higher beam energies in the order of 150 MeV/u, which are usually employed for experiments at GSI and RIKEN [27, 28, 33–35], this technique is not valid any longer as will be illustrated below. In these cases, transition probabilities can only be deduced from the measured cross sections when the contributions from both the Coulomb and nuclear interactions to the total cross section are correctly accounted for. This latter approach will be discussed in detail in section VI.

A. The minimum impact parameter (maximum scattering angle) approach

Once the angular resolution of the measurement has been determined (see last section and Fig. 7) we can

demonstrate why at least in the present case of ^{136}Te measured at a midtarget energy of 139 MeV/u, but probably more in general in this energy domain, the approach to apply a cut on the scattering angle in order to suppress nuclear contributions to the measured cross section is no longer valid. Using the criterion which is commonly applied in the analysis of NSCL experiments, namely selecting a minimum impact parameter corresponding to touching spheres plus 2 fm, a maximum scattering angle of θ_{max}=1.2° in the laboratory system is calculated for the Au target. Fig. 9a) shows a schematic angular distribution, $d\sigma/d\theta_{lab}$, in line with the Alder-Winther formalism [36]. Here it is assumed that all events with angles beyond θ_{max} are absorbed, corresponding to a sharp angle cutoff in a simplistic black-disk model. In part b) of the same figure, the corresponding angular distribution is shown for the case of ^{88}Kr excited on a ^{209}Bi target at a midtarget energy of 58.5 MeV/u which has recently been discussed in Ref. [30]. In this case, a significantly larger maximum scattering angle of θ_{max}=3.2° is obtained. Now, in order to compare these theoretical curves with data, they have to be folded with the angular resolution of the experiment which in the present case amounts to σ_{Au}=8.8 mrad as discussed above. This folding is done in three dimensions taking into account independent vectors for the scattering and straggling processes (for more details see Ref. [37]). The comparison between the original and folded curves shown in Fig. 9 legitimates the approach followed by the NSCL group to limit the comparison to angles below a certain limit and only consider the Coulomb part of the interaction. A comparison to the Fig. 3 of Ref. [30] indicates that the angular resolution in that experiment has been similar to the one assumed here. Depending on the resolution indeed a maximum scattering angle can be chosen, here θ=2.4° [30], so that nuclear contributions and absorption effects are negligible (see green dashed line in Fig. 9b). Although proven to be a valid analysis procedure it still has the drawback that for the determination of the transition probability it takes advantage of only part of the statistics gathered in the experiment (roughly 50%). The same comparison for the case of ^{136}Te as shown in Fig. 9a), on the other hand, clearly demonstrates that this technique can not be applied in the present case. To conclude, only when the safe scattering angle is large as compared to the angular resolution of the experiment, a cut on the angular distribution is a valid approach. However, for most of the experiments performed at higher beam energies around 150 MeV/u at GSI and RIKEN this is not the case.

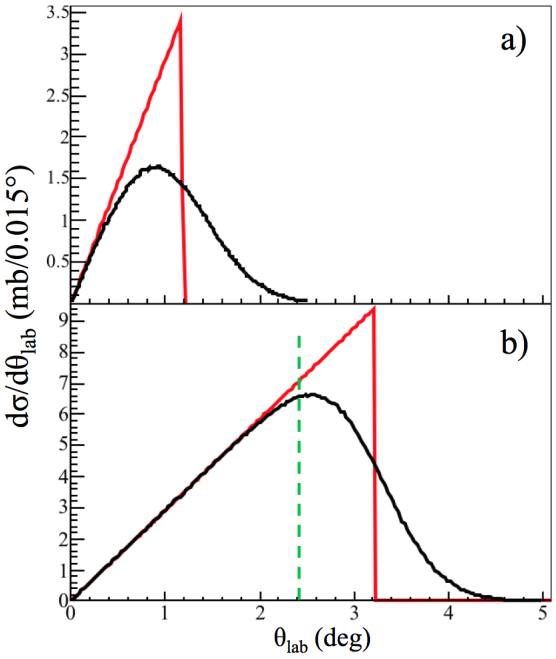

FIG. 9: Illustration of the effect of the limited experimental angular resolution on the measurement of angular distributions for a) the reaction ^{136}Te + ^{197}Au at 139 MeV/u discussed in the present work and b) the reaction ^{88}Kr + ^{209}Bi at 58.5 MeV/u [30]. The red lines correspond to angular distributions calculated within the relativistic Coulomb excitation model of Ref. [36] and cut at θ_{max}, while the black lines show theses theoretical curves after folding with the experimental angular resolution of σ_{Au}=8.8 mrad. The dashed green line indicates the more restrictive scattering-angle cut applied in the analysis presented in Ref. [30].

B. Consistent description of both nuclear and electromagnetic excitations with the reaction code FRESCO

As has been shown in the last section, in the present case it is not possible to determine a B(E2) value from the measured cross section without considering simultaneously the contributions from both Coulomb and nuclear excitations as well as possible interference effects between them. There are several reaction codes on the market which allow to do that, among them ECIS [38], FRESCO [39, 40], and DWEIKO [41]. ECIS and FRESCO are fully quantum-mechanical coupled-channels codes. DWEIKO is also a coupled channels code, designed for inelastic processes, which makes the additional eikonal (i.e., forward-angle, high-energy) approximation to the distorted waves to simplify its solution. The different versions of the ECIS code have widely been used in the past in the analysis of Coulomb excitation experiments [34, 35, 42–45], in some of these cases considering relativistic kinematics. In particular in the cases in which angular distributions have been measured with high angular resolution and thus high sensitivity to the interference pattern between the nuclear and Coulomb interactions, ECIS has proven to well describe the experimental data. Unfortunately, ECIS97 shows convergence problems when applied to heavier systems such as the reaction discussed in the present work and therefore had to be discarded. Before using instead the FRESCO code for the determi-

nation of the B($E2$; $0_1^+ \rightarrow 2_1^+$) value in ^{136}Te we investigated its capability to correctly describe some of the high-resolution measurements reported in the literature, in particular the angular distributions measured for excited states in ^{208}Pb populated in collisions with a ^{17}O beam at 84 MeV/u [42, 45] as well as the data reported in Ref. [34]. Good agreement was found so that it seems legitimate to employ FRESCO instead of ECIS97 in the present analysis. Unfortunately no experimental information on the angular distributions for inelastic scattering were found in the literature for heavier systems and at higher beam energies. In the following results will be presented which have been obtained with a modified version of the FRESCO code [46] that takes into account relativistic kinematics. Before closing this section we would like to mention that we were not able to reproduce the angular distributions measured for the system ^{17}O+^{208}Pb [42, 45] using the DWEIKO code. The analysis of both electric dipole and quadrupole states seems to indicate that, at least in the studied cases, neither the nuclear-Coulomb interferences nor the nuclear absorption are correctly treated.

VI. DETERMINATION OF THE REDUCED TRANSITION PROBABILITY B($E2$; $0_1^+ \rightarrow 2_1^+$)

In order to deduce a reduced transition probability to the 2_1^+ state in ^{136}Te from the experimental exclusive cross section on the Au target determined as discussed in section IV, both the nuclear and Coulomb contributions have to be considered. In all calculations presented in this section, optical potentials were used which were derived from the microscopic folding model with the complex G-matrix interaction CEG07 and a specific global density (for more details see [47]). For the Coulomb part the standard collective-model form factor has been employed. Since in reactions on the C target Coulomb effects are negligible information about the nuclear deformation length can be deduced from the cross sections measured on this light target (compare Table I). The inclusive cross section of σ^C=23(3) mb measured for the 607-keV transition is reproduced with FRESCO using a value for the deformation length of δ_{nucl}^{eff}=1.05(7) fm, while the exclusive cross section to the 2_1^+ state, $\sigma^C(2_1^+)$=9.5(32) mb, is reproduced with a value of $\delta_{nucl}(2_1^+)$=0.68(10) fm. As shown in Fig. 10a) for the C target the cross section is centered at very small scattering angles. As a consequence, the measured angular distribution mainly reflects the experimental angular resolution and is thus very sensitive to the correct folding. The theoretical curve after folding is shown in comparison to the experimental data in Fig. 10b). Nice agreement is observed which validates the folding method. Turning now to the data taken with the Au target, the B($E2$; $0_1^+ \rightarrow 2_1^+$) value can be determined taking into account the effective nuclear deformation length, δ_{nucl}^{eff}. This approach assumes that the relative population of the different excited states due to nuclear interactions is the same for the two targets. Keeping δ_{nucl}^{eff}=1.05(7) fm fixed, the reduced matrix element $M(E2)$ is varied until the experimental exclusive cross section to the 2_1^+ state, $\sigma^{Au}(2^+)$=219(23) mb, is reproduced. In this way, a value of B(E2; $0_1^+ \rightarrow 2_1^+$)=0.195(22) e^{2}b^2 is obtained. Note that the quoted uncertainty is the maximum error due to the experimental error of the cross section (σ=242 mb are obtained assuming B(E2)=0.217 e^{2}b^2 while B(E2)=0.173 e^{2}b^2 corresponds to σ=196 mb). The comparison between the experimental angular distribution and that calculated with FRESCO and folded with the angular resolution is shown in Fig. 10d). As in the case of the C target, the theoretical curve reproduces the shape of the experimental distribution rather well. Note that the theoretical curves shown in Fig. 10 are not adjusted to the experimental data but the result of calculations, which reproduce the measured total cross section taking into account nuclear contributions. So far all calculations have been performed for beam energies corresponding to the average energy of the ions at the center of the target. The influence of the finite target thickness on the resulting reduced transition probability will be discussed in section VI.A.

To illustrate the influence of the nuclear contribution to the total cross section, the calculated total angular distribution as well as those obtained separately for the Coulomb (δ_{nucl}=0 fm) and nuclear ($M(E2)$=0 eb) parts are shown in Fig. 10c). The optical potentials affect the shape of the total angular distribution in two ways. The real part of the potential determines the cross section due to nuclear excitations (blue curve in Fig. 10d)) while the imaginary part is responsible for the absorption, i.e., it defines the right wing of the distribution. The Coulomb and nuclear interactions interfere in a destructive way, thus leading to a shift of the position of the maximum of the distribution to smaller scattering angles. The destructive interference is also reflected by the nuclear and Coulomb contributions to the total cross section. Coulomb and nuclear cross sections of σ_{coul}=224 mb and σ_{nucl}=44 mb lead to a total cross section of σ^{tot}=219 mb. Due to the destructive interference, the B(E2) value is not very sensitive to the nuclear deformation length δ_{nucl}. A smaller value of the latter corresponds to a lower nuclear cross section so that the Coulomb cross section would slightly increase to compensate. However, since also the interference changes, these effects are small. As example we quote here the values σ_{coul}=234 mb and σ_{nucl}=19 mb which are obtained assuming δ_{nucl}=0.68 fm, i.e., the deformation length which reproduces the experimental exclusive cross sections to the 2_1^+ on the C target. In this case, the resulting B(E2) value increases by 4%. Interestingly, assuming δ_{nucl}=0 fm, i.e., no nuclear contribution at all, a 2.5% smaller B(E2) value is deduced from the measured σ^{tot}. Unfortunately, due to the limited angular resolution of the present experiment, the measured angular distribution is not sensitive to the value of δ_{nucl}.

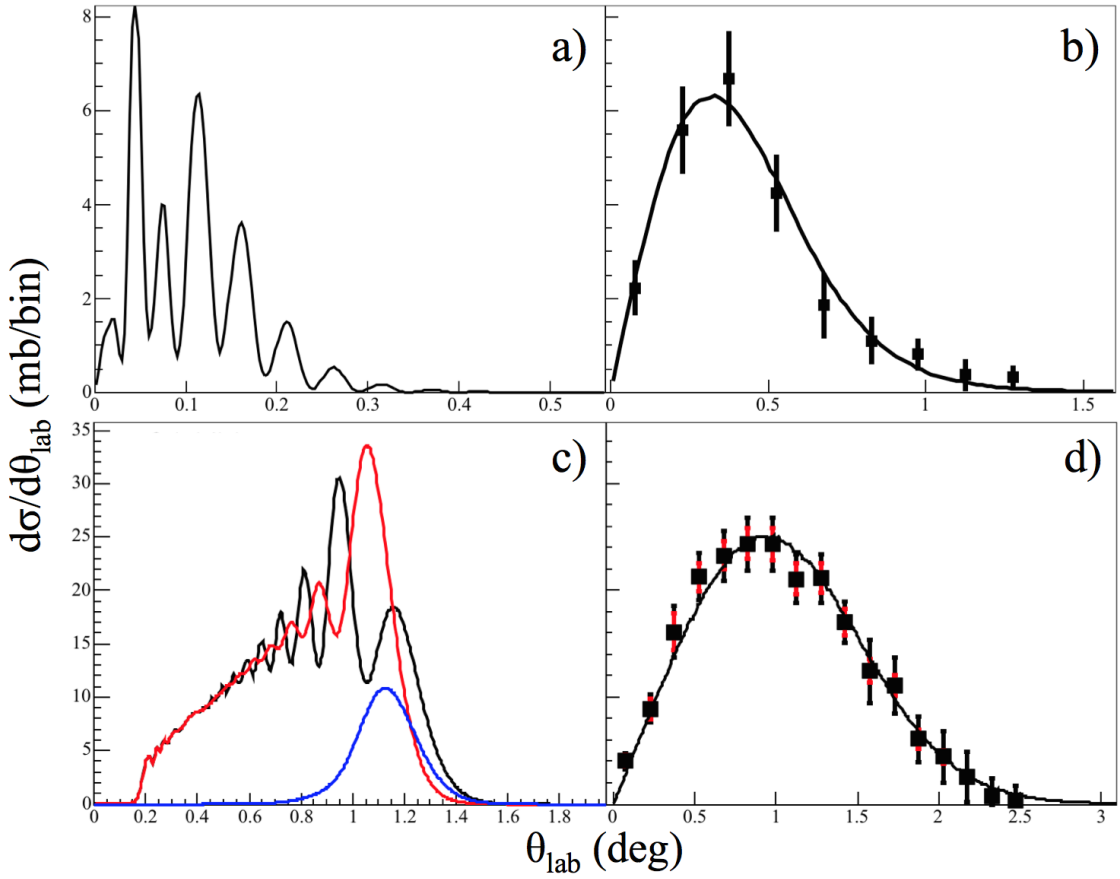

FIG. 10: Theoretical (a) and experimental (b) angular distributions for the excitation of the 2_1^+ state in ^{136}Te on a C target. In b) the theoretical curve was folded with the experimental angular resolution following the procedure discussed in the text. Theoretical (c) and experimental (d) angular distributions for the excitation of the 2_1^+ state in ^{136}Te on a Au target. In c) in addition to the total differential cross section (black line) the Coulomb (red) and nuclear (blue) contributions are also shown separately. In d) the theoretical curve was folded with the experimental angular resolution following the procedure discussed in the text. The red error bars indicate purely statistical errors, while the black bars also include systematical uncertainties added in quadrature. Bins of 0.025°, 0.15°, 0.071°, and 0.15° have been used in parts a), b), c), and d), respectively.

A further test has been made to study the robustness of the result with respect to the optical model potentials used in the calculations. The potentials calculated by Furumoto et al. [47] are based on the Sao Paulo parametrisations of the proton and neutron density distributions which are adjusted to stable nuclei. To test the validity of this prescription when applied to neutron-rich nuclei such as ^{136}Te potentials were calculated based on realistic theoretical density distributions which have been calculated with the Hartree-Fock-Bogoliubov approach and the finite range density dependent Gogny force in the D1S parametrisation [48]. Using these potentials instead of the original ones in the analysis, the resulting B(E2) value changes by less than 2%. Finally, the full analysis has been repeated also using optical potentials which were obtained with the t-$\rho\rho$ approximation [49]. In this case a slightly larger deviation of 5% was found for the final B(E2) value. Thus, to account for the systematic uncertainty related to the choice of the optical potentials a systematic error of 5% has been assumed in the present work.

To close this section, we would like to briefly come back to the minimum impact parameter approach discussed in section V.A. After having discussed the results of the FRESCO calculations shown in Fig. 10c) it is clear now that not only the limited experimental angular resolution due to straggling and position measurement uncertainties, but also the interference between the Coulomb and nuclear excitations prohibits the use of this approach in the analysis of experiments performed at beam energies around 150 MeV/u. Due to the destructive interference, the total integral cross section up to the maximum scattering angle of θ_{max}=1.2° is about 9% smaller as compared to the integral Coulomb excitation cross section in the same angular range (196 vs. 215 mb), so that even in the ideal case of vanishing angular resolution a too small B(E2) value would be obtained when only Coulomb excitation is considered. With respect to

the analysis of experiments performed with beam energies in the range 40-80 MeV, note that although shown to be a valid approach, using this method implies loosing a considerable fraction of the available statistics. At these lower beam energies as compared to the experiment discussed here, the relative contribution of nuclear excitations to the measured cross section is much smaller and consequently also the interference phenomena are less important. The only crucial ingredient for a reliable calculation of the total inelastic scattering cross section is then the correct description of the nuclear absorption process for small impact parameters, i.e., large scattering angles. The comparison between the calculated and measured angular distributions for the 2_1^+ state in ^{136}Te shown in Fig. 10d), together with those for the studied literature examples mentioned in section V.B. and additional experimental cases studied at RIKEN [50], clearly shows that FRESCO calculations using modern optical model potentials provide a realistic description of the measured angular distributions. It would be very interesting to compare the results obtained following the analysis approach presented here and the one employing an scattering-angle cut for a typical experiment such as the one discussed in Ref. [30].

A. Correction due to the significant energy loss in the thick target

In the thick Au target used in the present experiment (950 mg/cm^2) the ions loose more than 30% of their initial energy during the passage through the target. They slow down from 165 MeV/u to 110 MeV/u. Since the increase of the Coulomb excitation cross section with decreasing beam energy is not linear, the error made when considering in the analysis a fixed energy, namely the energy at the center of the target, in the determination of the B(E2) value has to be estimated. The cross sections calculated for the average beam energies at the entrance, the center and the exit of the target are 190, 219 and 267 mb, respectively. To first order the B(E2) value has to be reduced by 2%, leading to a value of B(E2; $0_1^+ \rightarrow 2_1^+$)=0.191(24) e^{2}b^2. An uncertainty of the same order as the effect is assumed. Note that also the shape of the angular distribution of the inelastically scattered ions changes with the beam energy. However, due to the limited angular resolution of the present experiment these effects are nearly washed out once the theoretical curves are folded with the experimental response.

B. Uncertainty due to non-consideration of relativistic reaction dynamics

As mentioned before in the present work, a modified version of the FRESCO code has been used which is taking into account relativistic kinematics. We note that in the present case of the 2_1^+ state in ^{136}Te excited on a Au target at a midtarget energy of 139 MeV/u, a 7% smaller B(E2) value would be deduced when the standard version of FRESCO [39] would have been employed. For a fully consistent description of the excitation process also dynamical relativistic corrections on the nuclear and Coulomb potentials should be taken into account. Based on previous calculations using an eikonal version of the continuum-discretized coupled-channels (CDCC) method [51] these corrections are expected to be rather small in the present case. Choosing a conservative approach, we consider an additional systematic uncertainty of 5% in the determination of the final B(E2) value.

C. Summary of systematic uncertainties

The final result of the analysis and the different contributions to its error are summarized in Table II. After taking into account all possible sources of systematic uncertainties related to the different analysis steps, the final relative uncertainty amounts to 14%. It is important to notice that the systematic uncertainties dominate the final error. Due to the high counting statistics of the present experiment, the statistical uncertainty of the cross section measured for the 607-keV transition on the Au target is only 3%. Already at this point the systematic uncertainty of 5% inherent to the determination of the γ-ray intensities from a fit of simulated spectra to the experimental data, i.e., the uncertainty due to the efficiency calibration of DALI2, is larger than the statistical error. Since the latter uncertainty as well as the other systematic errors considered in this work, related to the choice of the optical potentials, the relativistic corrections and the finite target thickness, are unavoidable and difficult to reduce, the precision for the reduced transition probability reached in the present work can be considered as a limit of what can be achieved using the technique of Coulomb excitation at relativistic energies

TABLE II: Summary of the systematic uncertainties which have been considered in the determination of the final value of B(E2; $0_1^+ \rightarrow 2_1^+$)=0.191(26) e^{2}b^2.

	$\sigma^{Au}(2_1^+)$ (mb)	$\Delta\sigma^{Au}(2_1^+)$ (mb)	error
inclusive	279	9	statistical
γ efficiency	279	17	5%
γ ang. distr.	279	22	5%
feeding	219	23	5%
	B(E2) (e^{2}b^2)	ΔB(E2) (e^{2}b^2)	error
FRESCO	0.195	0.022	$\Delta\sigma^{Au}(2_1^+)$
potentials	0.195	0.024	5%
target thickness	0.191	0.024	2%
rel. dynamics	0.191	0.026	5%

at facilities such as RIKEN or GSI/FAIR.

Note that using the equation [41, 52]

$$B(E\lambda) = (\frac{3}{4\pi} ZeR^{\lambda-1})^2 \delta^2_{coul,\lambda} \quad (2)$$

with the radius at 50% of the central nuclear density R=1.2 $A^{1/3}$ fm and the multipolarity λ=2, a charge deformation length $\delta_{coul,\lambda}$=0.57(4) fm can be calculated from the B(E2) value. This value is in agreement with the nuclear deformation length δ_{nucl}=0.68(10) fm deduced above from the exclusive inelastic scattering cross section to the 2^+_1 state, $\sigma^C(2^+_1)$. Note that any unobserved feeding, which still may contribute to $\sigma^C(2^+_1)$, would further decrease δ_{nucl}. Equality of the nuclear and charge deformation lengths, δ_{nucl}=δ_{coul}, has actually been assumed in the analysis of several experiments in the past [44, 45]. It is expected to be valid when the neutron and proton distributions are similar and the two nuclei interact only at the surface, which is the case for heavy-ion inelastic scattering being dominated by strong absorption [53].

VII. DISCUSSION

The main experimental result of the present work is the value of the E2 transition probability, $B(E2; 0^+_1 \rightarrow 2^+_1)$= 0.191(26) e^2b^2, to the first excited 2^+ state in ^{136}Te. This value is compared to previous results reported in the literature in Table III and Fig. 11. Our measurement, performed using Coulomb excitation at relativistic energies, agrees with the large value which has recently been obtained in Coulomb excitation at safe energies at Oak Ridge [6]. It is, however, in conflict with the low-energy Coulomb excitation measurement of Refs. [1, 3] and the preliminary result of the experiment using the fast timing technique reported by Fraile et al. [2]. We can not comment on the discrepancy between the two low-energy Coulex experiments, both performed at HRIBF, which employed a carbon target in one case and a titanium target in the other.

The conflict between the results of the two recent Coulomb excitation experiments on one side and the fast timing measurement on the other, in case the preliminary result of the latter will be confirmed, is very interesting. There are already several other cases in the literature in which discrepancies between the results from Coulomb excitation experiments and those obtained using experimental techniques which allow to directly extract the lifetime of excited states, e.g., methods based on the Doppler effect, have been observed. One prominent example are the $B(E2; 0^+_1 \rightarrow 2^+_1)$ values of the stable Sn isotopes [58, 59]. Therefore, a new direct measurement of the 2^+_1 lifetime is of highest interest.

With respect to the comparison of the experimental $B(E2; 0^+_1 \rightarrow 2^+_1)$ value for ^{136}Te to different theoretical calculations performed in the framework of the nuclear shell model (SM) and the quasiparticle random phase approximation (QRPA), we refer the reader to the discussion presented in Ref. [6]. In addition to the theoretical work included in Table II of that reference we add in Fig. 11 also the results of recent SM calculations presented in Ref. [57]. We note that all the different SM calculations predict large B(E2) values for ^{136}Te close to the one measured in the present work and Ref. [6], while the two QRPA calculations provide smaller E2 strengths closer to the experimental values extracted in Refs. [2, 3]. On the other hand, all three SM approaches, which allow to calculate B(E2) values also for ^{132}Te, namely SM1, SM2 and NSM, predict larger B(E2) values for the N=84 isotope ^{136}Te as compared to the N=80 ^{132}Te, in contrast to the available experimental information. Note, however, that in all three calculations different configurations spaces and effective interactions have been used to describe the nuclei below and above the N=82 shell

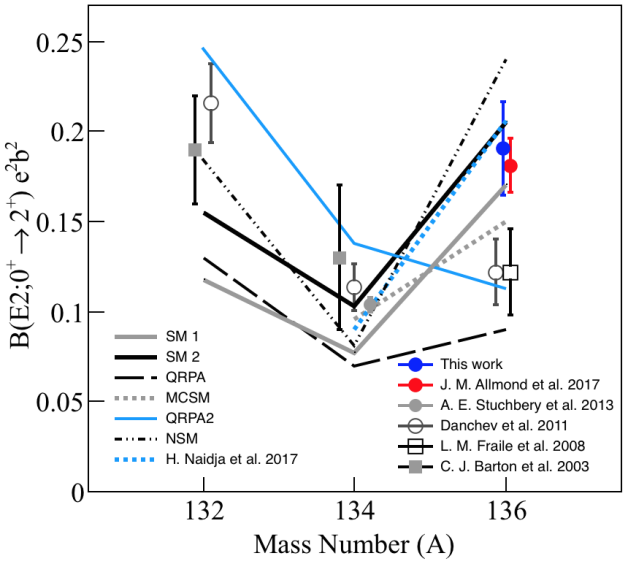

FIG. 11: Comparison of the experimental $B(E2; 0^+_1 \rightarrow 2^+_1)$ value for ^{136}Te determined in the present work to literature values for the ^{132,134,136}Te isotopes [2, 3, 6, 54, 55] and different theoretical calculations [5–8, 56, 57].

TABLE III: Comparison of the transition probabilities in ^{136}Te determined in the present work with those reported in the literature.

B(E2; $I^\pi_i \rightarrow I^\pi_f$) ($e^2b^2$)			Reference
$0^+_1 \rightarrow 2^+_1$	$4^+_1 \rightarrow 2^+_1$	$0^+_1 \rightarrow 2^+_x$	
0.122(18)	–	–	Danchev et al. [3]
0.122(24)	–	–	Fraile et al. [2]
0.181(15)	0.060(9)	<0.02	Allmond et al. [6]
0.191(26)	–	<0.019[a]	present work
0.151(69)	0.061(31)[b]	–	present work, τ

[a]Assuming a 100% 0.9 MeV decay branch to the 2^+_1 state.
[b]From $\tau_{eff}(4^+_1)$, including feeding from the 6^+_1 state.

closure. It will be very interesting to see the results obtained with the most recent SM approaches which consider larger configuration spaces including orbitals above and below the Z=50 and N=82 shell closures and thus allow to describe isotopic chains across the neutron shell closure on equal footing [60, 61].

In section III.A. observational lower limits of 10% and 16% relative to the intensity of the 607 keV line have been determined for γ rays with energies of 0.9 MeV and 1.8 MeV, respectively, decaying from a hypothetical mixed-symmetry 2^+ state in ^{136}Te. These limits correspond to lower limits of either 0.019 e^2b^2 or 0.031 e^2b^2 for the $B(E2;0_1^+ \rightarrow 2_{ms}^+)$ value when the exclusive decay via either a 0.9 or a 1.8 MeV γ ray is assumed. In order to compare the experimental limit to the calculations, in each case the theoretical branching ratio for the decay branches to the 2_1^+ and 0_1^+ states is taken into account. For the MCSM calculation of Ref. [7] with a branching ratio of 4.6:1, a limit of $B(E2;0_1^+ \rightarrow 2_{ms}^+)$<0.023 e^2b^2 is obtained which can be compared to the calculated value of $B(E2;0_1^+ \rightarrow 2_{ms}^+)$=0.03 e^2b^2. The QRPA calculations of Ref. [8] predict a branching ratio of 1.9:1, which leads to an experimental limit of $B(E2;0_1^+ \rightarrow 2_{ms}^+)$<0.029 e^2b^2 as compared to the theoretical value of $B(E2;0_1^+ \rightarrow 2_{ms}^+)$=0.074 e^2b^2. Even more illustrative than this comparison between the absolute experimental and theoretical transition strengths is that for the relative strength, i.e., $B(E2;0_1^+ \rightarrow 2_{ms}^+)/B(E2;0_1^+ \rightarrow 2_1^+)$. In the case of the MCSM calculation, the theoretical value of 20% compares to the experimental limit <12%, while the QRPA prediction of 66% is much larger as compared to the experimental result <15%. We conclude that currently there is no experimental evidence for an enhanced E2 excitation probability to a 2_{ms}^+ state in ^{136}Te. The experimentally determined upper limits are in agreement with the 2_{ms}^+ predictions of the SM calculations of Ref. [4].

VIII. CONCLUSIONS

We reported on the in-beam γ-ray spectroscopy of the neutron-rich nucleus ^{136}Te following inelastic scattering on gold and carbon targets at energies around 140 MeV/u performed at the RIBF facility at the RIKEN Nishina Center. A value of $B(E2;0_1^+ \rightarrow 2_1^+)$=0.191(26) e^2b^2 was derived from the experimental exclusive inelastic scattering cross section on the Au target, taking into account both the Coulomb and nuclear contributions to the measured cross section. Our B($E2$) value is in good agreement with the result of a recent experiment employing low-energy Coulomb excitation [6] but at variance with previously reported values [2, 3]. The origin of this striking disagreement among the available experimental information remains an open question, which calls for additional future investigation. Furthermore, an upper limit for the excitation probability for a hypothetical mixed-symmetry 2_{ms}^+ state has been established on the basis of the experimental sensitivity. Finally, the high statistics gathered in the present experiment allowed to perform a model analysis for the determination of B($E2$) values from measured differential cross sections after inelastic excitation at relativistic energies which can serve as guideline for the analysis of future Coulomb excitation experiments performed at beam energies around 150 MeV/u at GSI and RIKEN.

Acknowledgments

We thank Dirk Weisshaar for valuable discussions and the staff of the RIKEN Nishina Center accelerator complex for providing high-intensity beams to the experiment. This work was supported by the Spanish Ministerio de Economía y Competitividad under contracts FPA2014-57196-C5-4-P and FIS2014-53448-C2-1-P.

[1] D. C. Radford et al., Phys. Rev. Lett. **88**, 222501 (2002).
[2] L.M. Fraile et al., Nucl. Phys. A **805**, 218 (2008).
[3] M. Danchev, G. Rainovski, N. Pietralla, A. Gargano, A. Covello, C. Baktash. J. R. Beene, C. R. Bingham, A. Galindo-Uribarri, K. A. Gladnishki, C. J. Gross, V. Y. Ponomarev, D. C. Radford, L. L. Riedinger, M. Scheck, A. E. Stuchbery, J. Wambach, C. H. Yu, and N. V. Zamfir, Phys. Rev. C **84**, 061306(R) (2011).
[4] A. Covello et al., Prog. Part. Nucl. Phys. **59**, 401 (2007).
[5] J. Terasaki et al., Phys. Rev. C **66**, 054313 (2002).
[6] J.M. Allmond et al., Phys. Rev. Lett. **118**, 092503 (2017).
[7] N. Shimizu et al., Phys. Rev. C **70**, 054313 (2004).
[8] A.P. Severyukhin et al., Phys. Rev. C **90**, 011306 (2014).
[9] T. Kubo et al., Prog. Theor. Exp. Phys. 2012, 03C003 (2012).
[10] N. Fukuda, T. Kubo, T. Ohnishi, N. Inabe, H. Takeda, D. Kameda, and H. Suzuki, Nucl. Instr. Meth. B **317**, 323 (2013).
[11] S. Takeuchi, T. Motobayashi, Y. Togano, M. Matsushita, N. Aoi, K. Demichi, H. Hasegawa, and H.Murakami, Nucl. Instr. Meth. A **763**, 596 (2014).
[12] S. Agostinelli et al., Nucl. Instr. Meth. A **506**, 250 (2003).
[13] K. Butler-Moore et al., J. Phys. G **19**, L121 (1993).
[14] P. Hoff et al., Phys. Rev. C **56**, 2865 (1997).
[15] A. Korgul et al., Eur. Phys. J. A **7**, 167 (2000).
[16] V. Vaquero et al., Phys. Rev. Lett. **118**, 202502 (2017).

[17] J.R. Terry et al., Phys. Rev. C **77**, 014316 (2008).
[18] A. Lemasson et al., Phys. Rev. C **85**, 041303(R) (2012).
[19] S. Akkoyun et al., Nucl. Instr. Meth. **668**, 26 (2012).
[20] I-Yang Lee, AIP Conference Proceedings 656, 343 (2003)
[21] ATIMA code, http://web-docs.gsi.de/weick/atima/
[22] H. Olliver, T. Glasmacher and A.E. Stuchbery, Phys. Rev. C **68**, 044312 (2003).
[23] P. Bednarczyk et al., Acta Phys. Pol. B **40**, 853 (2009).
[24] http://www.nndc.bnl.gov
[25] C. Vaman et al., Phys. Rev. Lett. **99**, 162501 (2007).
[26] V.M. Bader et al., Phys. Rev. C **88**, 051301(R) (2013).
[27] A. Banu et al., Phys. Rev. C **72**, 061305(R) (2005).
[28] G. Guastalla et al., Phys. Rev. Lett. **110**, 172501 (2013).
[29] A. Gade et al., Phys. Rev. C **68**, 014302 (2003).
[30] B. Elman et al., Phys. Rev. C **96**, 044332 (2017).
[31] C.A. Bertulani et al., Phys. Lett. B **650**, 233 (2007).
[32] H. Scheit et al., Phys. Lett. B **659**, 515 (2008).
[33] P. Doornenbal et al., Phys. Rev. C **90**, 061302(R) (2014).
[34] K. Li et al., Phys. Rev. C **92**, 014608 (2015).
[35] P. Doornenbal et al., Phys. Rev. C **93**, 044306 (2016).
[36] A. Winther and K. Alder, Nucl. Phys. A **319**, 518 (1979).
[37] Victor Vaquero Soto, PhD thesis, Universidad Autónoma de Madrid, 2018.
[38] J. Raynal, coupled-channel code ECIS97 (unpublished).
[39] I.J. Thompson, Comput. Phys. Rep. **7**, 3 (1988).
[40] http://fresco.org.uk
[41] C.A. Bertulani, C.M. Campbell and T. Glasmacher, Comp. Phys. Com. **152**, 317 (2003).
[42] J. Barrette et al., Phys. Lett. B **209**, 182 (2008).
[43] P. Roussel-Chomaz et al., Phys. Lett. B **209**, 187 (1988).
[44] T. Motobayashi et al., Phys. Lett. B **346**, 9 (1995).
[45] R. Liguori Neto et al., Nucl. Phys. A **560**, 733 (1993).
[46] A.M. Moro, Phys. Rev. C **92**, 044605 (2015).
[47] T. Furumoto et al., Phys. Rev. C **85**, 044607 (2012).
[48] J.L. Egido, private communication
[49] M.S. Hussein, R.A. Rego, C.A. Bertulani, Phys. Reports **201**, 279 (1992).
[50] T. Arici et al., in preparation
[51] K. Ogata and C. Bertulani, Prog. Theor. Phys. **121**, 1399 (2009).
[52] G.R. Satchler, Nucl. Phys. A **472**, 215 (1987).
[53] D.L. Hendrie, Phys. Rev. Lett. **31**, 478 (1973).
[54] C.J. Barton et al., Phys. Lett. B **551**, 269 (2003).
[55] A.E. Stuchbery et al., Phys. Rev. C **88**, 051304(R) (2013).
[56] D. Bianco et al., Phys. Rev. C **88**, 024303 (2013).
[57] H. Naidja, F. Nowacki and B. Bounthong, Phys. Rev. C **96**, 034312 (2017).
[58] J.M. Allmond et al., Phys. Rev. C **92**, 041303(R) (2015).
[59] A. Jungclaus et al., Phys. Lett. B **695**, 110 (2011).
[60] T. Togashi et al., Phys. Rev. Lett. **121**, 062501 (2018).
[61] D. Rosiak et al., submitted to Phys. Rev. Lett.

Bibliography

[1] E. Rutherford, *Philosophical Magazine* **21**, 669 (1911).

[2] W. M. Elsasser, *Journal de Physique et le Radium* **4**, 549 (1933).

[3] W. M. Elsasser, *Journal de Physique et le Radium* **5**, 389 (1934).

[4] W. M. Elsasser, *Journal de Physique et le Radium* **5**, 635 (1934).

[5] M. Goeppert-Mayer, *Phys. Rev.* **74**, 235 (1948).

[6] M. Goeppert-Mayer, *Phys. Rev.* **75**, 1969 (1949).

[7] O. Haxel, J. Jensen, and H. Suess, *Phys. Rev.* **75**, 1766 (1949).

[8] T. Motobayashi *et al.*, *Phys. Lett. B* **346**, 9 (1995).

[9] C. M. Campbell *et al.*, *Phys. Rev. Lett.* **97**, 112501 (2006).

[10] B. Bastin *et al.*, *Phys. Rev. Lett.* **99**, 022503 (2007).

[11] S. Takeuchi *et al.*, *Phys. Rev. Lett.* **109**, 182501 (2012).

[12] F. Wienholtz *et al.*, *Nature* **498**, 346 (2013).

[13] D. Steppenbeck *et al.*, *Nature* **502**, 207 (2013).

[14] S. Michimasa *et al.*, *Phys. Rev. Lett.* **121**, 022506 (2018).

[15] M. Mumpower, R. Surman, G. C. McLaughlin, and A. Aprahamian, *Prog. Part. Nucl. Phys.* **86**, 86 (2016).

[16] B. Chen *et al.*, *Phys. Lett. B* **355**, 37 (1995).

[17] G. Lorusso *et al.*, *Phys. Rev. Lett.* **114**, 192501 (2015).

[18] Y. Shimizu *et al.*, *J. Phys. Soc. Jpn.* **87**, 014203 (2018).

[19] A. Jungclaus *et al.*, *Phys. Rev. C* **83**, 041301(R) (2016).

[20] H. Wang *et al.*, *Phys. Rev. C* **94**, 051301(R) (2016).

[21] A. Jungclaus *et al.*, *Phys. Rev. Lett.* **99**, 132501 (2007).

[22] H. Watanabe *et al.*, *Phys. Rev. Lett.* **111**, 152501 (2013).

[23] G. S. Simpson *et al.*, *Phys. Rev. Lett.* **113**, 132502 (2014).

[24] H. Watanabe *et al.*, *Phys. Rev. Lett.* **113**, 042502 (2014).

[25] J. Taprogge *et al.*, *Phys. Lett. B* **738**, 223 (2014).

[26] A. Jungclaus *et al.*, *Phys. Lett. B* **772**, 483 (2017).

[27] J. Taprogge *et al.*, *Phys. Rev. C* **91**, 054324 (2015).

[28] A. Jungclaus *et al.*, *Phys. Rev. C* **94**, 024303 (2016).

[29] J. Taprogge *et al.*, *Eur. Phys. J. A* **52**, 347 (2016).

[30] B. Moon *et al.*, *Phys. Rev. C* **95**, 044322 (2017).

[31] P. Hoff *et al.*, *Phys. Rev. Lett.* **77**, 1020 (1996).

[32] K. L. Jones *et al.*, *Nature* **465**, 454 (2010).

[33] K. L. Jones *et al.*, *Phys. Rev. C* **59**, pp. **84**, 034 601 (2011).

[34] J. M. Allmond *et al.*, *Phys. Rev. Lett.* **112**, 172701 (2013).

[35] W. Reviol *et al.*, *Phys. Rev. C* **94**, 034309 (2016).

[36] L. E. D. Geer and G. B. Holm, *Phys. Rev. C* **22**, 2163 (1980).

[37] B. Fogelberg and J. Blomqvist, *Phys. Lett. B* **137**, 20 (1984).

[38] B. Fogelberg and J. Blomqvist, *Nuc. Phys. A* **429**, 205 (1984).

[39] S. Borg *et al.*, *Nuc. Phys. A* **212**, 197 (1973).

[40] K. Sistemich *et al.*, *Z. Phys. A* **285**, 305 (1978).

[41] M. Sanchez-Vega *et al.*, *Phys. Rev. C* **60**, 024303 (1999).

[42] B. Fogelberg *et al.*, *Phys. Lett. B* **209**, 173 (1988).

[43] J. Taprogge *et al.*, *Phys. Rev. Lett.* **112**, 132501 (2014).

[44] T. Rodriguez, J. L. Egido, and A. Jungclaus, *Phys. Lett. B* **668**, 410 (2008).

[45] D. C. Radford *et al.*, *Phys. Rev. Lett* **88**, 222501 (2002).

[46] L. M. Fraile *et al.*, *Nuc. Phys. A* **805**, 218 (2008).

[47] M. Danchev *et al.*, *Phys. Rev. C* **84**, 061306(R) (2011).

[48] L. Grodzins, *Phys. Lett.* **2**, 88 (1962).

[49] A. Covello *et al.*, *Prog. Part. Nucl. Phys.* **59**, 401 (2007).

[50] N. Shimizu *et al.*, *Phys. Rev. C* **70**, 054313 (2004).

[51] J. Terasaki *et al.*, *Phys. Rev. C* **66**, 054313 (2002).

[52] A. P. Severyukhin *et al.*, *Phys. Rev. C* **90**, 011306(R) (2014).

[53] J. M. Allmond *et al.*, *Phys. Rev. Lett.* **118**, 092503 (2017).

[54] C. Barton *et al.*, *Phys. Lett. B* **551**, 269 (2003).

[55] K. L. G. Heyde, *The nuclear shell model*. Springer-Verlag, Second edition, 1994.

[56] P. Ring and P. Shuck, *The nuclear many-body problem*. Springer-Verlag, 1980.

[57] H. Grawe, *Notes Phys* **651**, 33 (2004).

[58] S. Bogner, T. T. S. Kuo, and L. Coraggio, *Nuc. Phys. A* **685**, 432c (2001).

[59] T. Otsuka *et al.*, *Phys. Rev. Lett.* **105**, 032501 (2010).

[60] H. Grawe, *Rep. Prog. Phys.* **70**, 1525 (2007).

[61] T. Otsuka, *Phys. Rev. Lett.* **95**, 232502 (2005).

[62] C. A. Bertulani, *CNS-EFES Summer School*, (2009).

[63] K. Alder and A. Winther, *Electromagnetic Excitation*. North-Holland, 1975.

[64] K. Alder, A. Bohr, T.Huus, B.Mottelson, and A.Winther, *Mod. Phys.* **38** (1956).

[65] A. Winther and K. Alder., *Nuc. Phys. A* **319**, 518 (1979).

[66] C. A. Bertulani and G. Baur, *Phys. Rep.* **163**, 299 (1988).

[67] C. E. Aguiar *et al.*, *Phys. Rev. C* **42** 2180 (1990).

[68] C. A. Bertulani *et al.*, *Phys. Rev. C* **68** 044609 (2003).

[69] https://github.com/miree/nuco.

[70] M. Reese, *PhD thesis TU Darmstadt (2017)*.

[71] A. Gade *et al.*, *Phys. Rev. C* **68**, 014302 (2003).

[72] B. Elman *et al.*, *Phys. Rev. C* **96**, 044332 (2017).

[73] P. Doornenbal *et al.*, *Phys. Rev. C* **90**, 061302(R) (2014).

[74] K. Li *et al.*, *Phys. Rev. C* **92**, 014608 (2015).

[75] D. Cortina-Gil, *The Euroschool on Exotic Beams* **IV**, 183 (2014).

[76] J. A. Tostevin, *Nuc. Phys. A* **682**, 320 (2001).

[77] P. G. Hansen and J. A. Tostevin, *Annu. Rev. Nucl. Part. Sci.* **53**, 219 (2003).

[78] T. Aumann, *Eur. Phys. J. A* **26**, 441 (2005).

[79] A. Gade and T. Glasmacher, *Prog. Part. Nucl. Phys.* **60**, 161 (2008).

[80] A. Gade *et al.*, *Phys. Rev. C.* **77**, 044306 (2008).

[81] C. A. Bertulani and A. Gade, *Comput. Phys. Commun.* **175**, 372 (2006).

[82] T. Nakagawa and Y. Yano, *Rev. Sci. Instrum.* **71**, 637 (2010).

[83] T. Nakagawa and Y. Yano, *Nucl. Instrum. Meth. B* **241**, 935 (2005).

[84] http://www.nishina.riken.jp/RIBF, accessed: 10-06-2018.

[85] O. Kamigaito *et al.*, *Proceedings of IPAC*, Busan, Korea (2016).

[86] H. Geissel and M. Münzenberg, *Nucl. Instrum. Meth. B* **70**, 286 (1992).

[87] J. Gaimard and K. Schmid, *Nucl. Phys. A* **531**, 709 (1991).

[88] T. Kubo, *Nucl. Instrum. Meth. Phys. Res.B* **204**, 97 (2003).

[89] T. Kubo, *IEEE Trans. Appl. Superconductivity* **17**, 1069 (2007).

[90] T. Kubo *et al.*, *Prog. Theor. Exp. Phys.* **03C003** (2012), 637 (2010).

[91] H. Stelzer, *Nucl. Instrum. Meth.* **133**, 409 (1976).

[92] U. Lynen *et al.*, *Nucl. Instrum. Meth.* **162**, 657 (1979).

[93] H. Kumagai *et al.*, *Meth. Phys. Res. B* **317**, 717 (2013).

[94] H. Kumagai *et al.*, *Meth. Phys. Res. A* **470**, 562 (2001).

[95] G. F. Knoll, *Radiation detection and measurement*. John Wiley & Sons, Inc., Fourth edition, 2010.

[96] A. Stolz *et al.*, *GSI Scientific Report* **174** (1998).

[97] W. B. Christie *et al.*, *Nucl. Instrum. Meth. A* **255**, 466 (1987).

[98] K. Kimura *et al.*, *Meth. Phys. Res. A* **538**, 608 (2005).

[99] R. Taniuchi *et al.*, *RIKEN Accel. Prog. Rep.* **48**, 210 (2015).

[100] H. Wang *et al.*, *Prog. Theor. Exp. Phys.* **023D02** (2014).

[101] H. Wang *et al.*, *Phys. Lett. B* **754**, 104 (2016).

[102] T. Nishio *et al.*, *RIKEN Accel. Prog. Rep.* **29**, 184 (1996).

[103] S. Takeuchi *et al.*, *Meth. Phys. Res. A* **763**, 596 (2014).

[104] P. Doornenbal, *Prog. Theor. Exp. Phys.* **03C004** (2012).

[105] S. Agostinelli *et al.*, *Instrum. Meth. Phys. Res. A* **506**, 250 (2003).

[106] H. Baba *et al.*, *Instrum. Meth. Phys. Res. A* **616**, 65 (2010).

[107] O. B. Tarasov and D. Bazin, *Nucl. Instr. Meth. B* **266**, 4657 (2008).

[108] N. Fukuda *et al.*, *Nucl. Instrum. Meth. B* **317**, 323 (2013).

[109] http://www.nucleide.org/Laraweb/index.php, accessed: 17-07-2018.

[110] V. Vaquero *et al.*, *Phys. Rev. Lett.* **118**, 202502 (2017).

[111] L. Coraggio, A. Covello, and N. I. A. Gargano, *Prog. Part. Nucl. Phys.* **62**, 135 (2009).

[112] O. Wieland *et al.*, *Phys. Rev. Lett.* **102**, 092502 (2009).

[113] K. Butler-Moore *et al.*, *J. Phys. G* **19**, L121 (1993).

[114] A. Korgul *et al.*, *Eur. Phys. J. A* **7**, 167 (2000).

[115] P. Hoff *et al.*, *Phys. Rev. C* **56**, 2865 (1997).

[116] https://web-docs.gsi.de/~weick/atima/, accessed: 05-05-2018.

[117] H. Olliver, T. Glasmacher, and A. E. Stuchbery, *Phys. Rev. C* **68**, 044312 (2003).

[118] K. Wimmer, *private communication*.

[119] https://www.nndc.bnl.gov/, accessed: 23-07-2018.

[120] C. Bertulani, C. Campbell, and T. Glasmacher, *Comp. Phys. Com.* **152**, 317 (2003).

[121] J. Raynal, "Coupled-channel code ecis97," *(unpublished)*.

[122] I. J. Thompson, *Comput. Phys. Rep.* **7**, 3 (1988).

[123] J. Barrette *et al.*, *Phys. Lett. B* **209**, 182 (1988).

[124] J. Gibelin *et al.*, *Phys. Rev. C* **75**, 057306 (2007).

[125] T. Motobayashi *et al.*, *Phys. Lett. B* **346**, 9 (1995).

[126] Y. Togano *et al.*, *Phys. Rev. Lett.* **108**, 222501 (2012).

[127] T. Roussel-Chomaz *et al.*, *Phys. Lett. B* **209**, 187 (1988).

[128] A. Moro and K. Ogata, *private communication*.

[129] T. Furumoto *et al.*, *Phys. Rev. C* **85**, 044607 (2012).

[130] M. Hussein, R. Rego, and C. Bertulani, *Phys. Reports* **201**, 279 (1991).

[131] J. L. Egido, *private communication*.

[132] http://www.iphc.cnrs.fr/nutheo/code_antoine/menu.html, accessed: 06-04-2018.

[133] H. Naïdja *et al.*, *Phys. Rev. C* **96**, 034312 (2017).

[134] A. Corsi *et al.*, *Phys. Lett. B* **743**, 451 (2015).

[135] S. Leray *et al.*, *Phys.: Conf. Series* **420** 012065 (2013).

[136] S. Pedoux and J. Cugnon, *Nucl. Phys. A* **866**, 16 (2011).

[137] A. Boudard, J. Cugnon, S. Leray, and C. Volant, *Phys. Rev. C* **66**, 044615 (2002).

[138] A. Boudard *et al.*, *Phys. Rev. C* **87**, 014606 (2013).

[139] D. Mancusi *et al.*, *Phys. Rev. C.* **90**, 054602 (2014).

[140] M. V. R. A. Kèlic, *Proceedings of Joint ICTP-IAEA, Advanced Workshop on Model Codes for Spallation Reactions, ICTP Trieste, Italy, 4-8 February 2008, edited by D. Filges, S. Leray, Y. Yariv, A. Mengoni, A. Stanculescu, and G. Mank (IAEA, Vienna, 2008)*, 181 (2008).

[141] D. Mancusi *et al.*, *Phys. Rev. C* **91**, 034602 (2015).

[142] J. L. Rodriguez-Sanchez *et al.*, *Phys. Rev. C* **96**, 054602 (2017).

[143] L. Audirac *et al.*, *Phys. Rev. C.* **88**, 041602(R) (2013).

[144] J. L. Rodriguez-Sanchez, *private communication*.

[145] E. Fermi, *Nuclear Physics*. University of Chicago Press, 1950.

[146] S. R. Stroberg *et al.*, *Phys. Rev. C* **90**, 034301 (2014).

[147] J. L. Tain *et al.*, *Phys. Rev. Lett.* **115**, 062502 (2015).

[148] R. Dungan *et al.*, *Phys. Rev. C* **93**, 021302(R) (2016).

[149] A. Spyrou *et al.*, *Phys. Rev. Lett.* **117**, 142701 (2016).

[150] L. Coraggio, A. Covello, A. Gargano, and N. Itaco, *Phys. Rev. C* **88**, 041304(R) (2013).

[151] F. Andreozzi, *Phys. Rev. C* **56**, R16 (1997).

[152] L. Coraggio, A. C. A. Gargano, and N. Itaco, *Phys. Rev. C* **65**, 051306(R) (2002), 401 (2007).

[153] J. A. Tostevin, *private communication*.

[154] S. Akkoyun *et al.*, *Nucl. Instr. Meth.* **668**, 26 (2012).

[155] I.-Y. Lee *et al.*, *AIP Conference Proceedings* 656, 343 (2003).

[156] A. G. L. Coraggio, A. Covello and N. Itaco, *Phys. Rev. C.* **80**, 021305(R) (2009).

[157] J. M. Allmond *et al.*, *Phys. Rev. Lett.* **112**, 17270 (2014).

[158] K. Wimmer, A. Jungclaus, V. Vaquero *et al.*, "Study of proton-neutron multiplets in ^{134}Sb populated in the ^{133} Sb(d,p) reaction in inverse kinematics with T-REX and MINIBALL," *Proposal to the ISOLDE and Neutron Time-of-Flight Committee* October (2017).

[159] C. K. Cline, W. P. Alford, and H. E. Gove, *Nuc. Phys. A* **186**, 273 (1972).

[160] J. J. Kolata and W. W. Daehnick, *Phys. Rev. C.* **5**, 2 (1972).

[161] A. G. L. Coraggio, A. Covello and N. Itaco, *Phys. Rev. C.* **76**, 061303(R) (2007).

[162] A. G. L. Coraggio, A. Covello and N. Itaco, *Phys. Rev. C.* **73**, 031302(R) (2006).